The Effect of High Temperature on Polycrystalline Diamond

Thomas Scott

St Catherine's College
University of Oxford

A thesis submitted for the degree of Doctor of Philosophy

Trinity 2019

Abstract

Polycrystalline diamond (PCD) is an important technological material used in the drilling of rock and the machining of high strength, non-ferrous alloys; composites and wood products. For these applications, no other material surpasses its cutting performance. However, PCD suffers from a degradation in its mechanical properties at the high temperatures caused by frictional heating that limits further advances in its capabilities. The literature presents two potential theories to explain this phenomenon: residual stresses due to differential thermal expansion mismatch between diamond and cobalt and, graphitisation of the diamond catalysed by cobalt. As the evidence for neither theory is strong, this thesis presents an in-depth experimental investigation and quantitative analysis of the mechanisms of breakdown of PCD at high temperature. Neutron diffraction is used to measure the residual stresses in diamond and cobalt as a function of temperature. Whilst the compressive stresses in cobalt are found to have a slight toughening effect at room temperature, differential expansion of the two phases is found to have an insignificant effect on the breakdown of PCD at high temperature. The mechanisms of diamond graphitisation are investigated using neutron and X-ray diffraction and an in-situ heating TEM experiment is used to observe graphitisation occurring in real-time. Graphitisation is found to be a two-stage process with nuclei of graphite first forming from η-carbide particles followed by catastrophic graphitisation occurring after an incubation period. A group VII transition metal element is found to increase the length of this period and at some temperatures prevent graphitisation entirely when added to the cobalt binder. An elastic model is presented which explains the sensitivity of this incubation period to temperature and binder chemistry. The literature on the mechanical properties of PCD is also found to contain numerous conflicting reports about the strength of grain boundaries. Microcantilever beam bending is therefore used to show that grain boundaries do not act as weak paths for fracture, that the binder phase is ductile and well adhered to the diamond and that the microstructural features most likely to affect the strength of PCD are processing defects in diamond grains caused by crushing and plastic deformation during manufacture. In summary, this thesis settles some marked inconsistencies and illuminates some poorly understood phenomena in the literature on the room-temperature and high-temperature behaviour of PCD, furthers the mechanistic understanding of graphitisation in PCD and makes possible the design of more thermally robust PCD.

The Effect of High Temperature on Polycrystalline Diamond



Thomas Scott

St Catherine's College

University of Oxford

A thesis submitted for the degree of

Doctor of Philosophy

Trinity 2019

Acknowledgements

Personal

Prof. Richard Todd has been a constant feature throughout my, now, eight years at Oxford and he has kept me on track the whole time. His willingness for me to turn up at his door, to reply to my emails, to answer my phone-calls and to spend hours discussing the minutiae of polycrystalline diamond with me, impressively, seemed to know no bounds and for that I am hugely thankful to him. We would sometimes have disagreements (I think I might have got him to admit to being wrong on one occasion) but his relentless pursuit of the truth usually led us down the path of some good science. More importantly though, despite his heavy workload, he often had time to have a pint of bitter with us lowly students and good times were usually had by all.

Without my wife, Dr. Emma Spence, however, none of this would have been possible. Her ability to remain positive and cheer me up when everything was going wrong, nothing was working and everybody seemed to be actively working against me was surpassed by none. She has remained incredibly patient throughout four years of "I think it should be done pretty soon", has worked to support us both since my funding ran out and has kept me happy when times were tough. Doing a DPhil has been great. It's been awful too but the awful times seemed significantly less bad because of her.

Institutional

The funding for this project was provided by the Engineering and Physical Sciences Research Council (EPSRC) and the Diamond Science and Technology Centre for Doctoral Training at the University of Warwick. Additional funding was also provided by Element Six Ltd and the University of Oxford. Prof. Dave Armstrong was my co-supervisor and provided help and I am thankful for the help and advice that he provided. Samples were kindly manufactured and provided by staff at the Global Innovation Centre (Element Six Limited), in particular by Rod Cruise and Dr. Jon Newland who helped a great deal with sample preparation. Dr. Roger Nilen was immensely helpful throughout the entire project and I am very thankful to have had him as my industrial contact. Many other people at the GIC, Dr. Dave Aldmington, Dr. Brett Lancaster, Dr. Ed Eardley and Dr. Serdar

Özbayraktar also helped with advice, sample acquisition and analysis techniques. Dr Jack Haley, Jesse Singh and Dr. Ian Griffiths of the University of Oxford assisted with electron microscopy techniques.

Abstract

Polycrystalline diamond (PCD) is an important technological material used in the drilling of rock and the machining of high strength, non-ferrous alloys; composites and wood products. For these applications, no other material surpasses its cutting performance. However, PCD suffers from a degradation in its mechanical properties at the high temperatures caused by frictional heating that limits further advances in its capabilities. The literature presents two potential theories to explain this phenomenon: residual stresses due to differential thermal expansion mismatch between diamond and cobalt and, graphitisation of the diamond catalysed by cobalt. As the evidence for neither theory is strong, this thesis presents an in-depth experimental investigation and quantitative analysis of the mechanisms of breakdown of PCD at high temperature. Neutron diffraction is used to measure the residual stresses in diamond and cobalt as a function of temperature. Whilst the compressive stresses in cobalt are found to have a slight toughening effect at room temperature, differential expansion of the two phases is found to have an insignificant effect on the breakdown of PCD at high temperature. The mechanisms of diamond graphitisation are investigated using neutron and X-ray diffraction and an in-situ heating TEM experiment is used to observe graphitisation occurring in real-time. Graphitisation is found to be a two-stage process with nuclei of graphite first forming from η-carbide particles followed by catastrophic graphitisation occurring after an incubation period. A group VII transition metal element is found to increase the length of this period and at some temperatures prevent graphitisation entirely when added to the cobalt binder. An elastic model is presented which explains the sensitivity of this incubation period to temperature and binder chemistry. The literature on the mechanical properties of PCD is also found to contain numerous conflicting reports about the strength of grain boundaries. Microcantilever beam bending is therefore used to show that grain boundaries do not act as weak paths for fracture, that the binder phase is ductile and well adhered to the diamond and that the microstructural features most likely to affect the strength of PCD are processing defects in diamond grains caused by crushing and plastic deformation during manufacture. In summary, this thesis settles some marked inconsistencies and illuminates some poorly understood phenomena in the literature on the room-temperature and high-temperature behaviour of PCD, furthers the mechanistic understanding of graphitisation in PCD and makes possible the design of more thermally robust PCD.

Contents

List of Figures **ix**

List of Tables **xv**

List of Abbreviations **xvi**

1 Introduction and Background **1**
1.1 Brief History of Diamond Synthesis 1
1.2 Polycrystalline Diamond 2
1.2.1 History 2
1.2.2 Modern Synthesis of PCD 3
1.2.3 Leaching of PCD 6
1.3 Motivation for this Work 6

2 Literature Review **7**
2.1 Mechanical Properties 7
2.1.1 Traditional Mechanical Testing of PCD 7
2.1.2 Wear Testing 23
2.1.3 Summary 29
2.2 Residual Stresses 30
2.2.1 Summary 35
2.3 Graphitisation of Diamond 35
2.3.1 Cutter Temperature 35
2.3.2 Thermal Degradation of PCD 36
2.3.3 Graphitisation of Pure Diamond 39
2.3.4 Catalytic Graphitisation 46
2.3.5 Summary 51

3 Mechanical Properties **53**
3.1 Introduction and Aims 54
3.2 Materials and Sample Preparation 54
3.2.1 PCD Materials 54
3.2.2 PCD Sample Preparation Techniques 55

3.2.3 Bend Test Specimens . . . 56
3.2.4 Microcantilever Production . . . 57
3.3 Experimental Techniques . . . 58
3.3.1 Four-point Bending Strength Test . . . 58
3.3.2 Microcantilever Bending Test . . . 59
3.4 Results . . . 61
3.4.1 Strength of Macroscopic Beams . . . 61
3.4.2 Strength of Microcantilever Beams . . . 62
3.4.3 Yield Strength of Cobalt Binder Pools . . . 63
3.5 Discussion . . . 65
3.5.1 Re-analysis of Lammer's Data . . . 65
3.5.2 Macroscopic Strength Results . . . 71
3.5.3 Microcantilever Bending Strengths . . . 71
3.5.4 Cobalt Binder Pool Microcantilevers . . . 79
3.6 Conclusions . . . 82
3.7 Further Work . . . 85

4 Residual Stresses **86**
4.1 Introduction and Aims . . . 87
4.2 Materials and Sample Preparation . . . 87
4.2.1 Polycrystalline Diamond . . . 87
4.2.2 Diamond Powder . . . 89
4.2.3 Metallic Samples . . . 89
4.3 Experimental Techniques . . . 90
4.3.1 General Materials Diffractometer (GEM) . . . 90
4.3.2 High Resolution Powder Diffractometer (HRPD) . . . 93
4.3.3 Laboratory X-ray Diffractometer . . . 94
4.3.4 Lattice Parameter Calculation . . . 94
4.3.5 Defect Analysis . . . 96
4.4 Results . . . 97
4.4.1 Characterisation of Samples . . . 97
4.4.2 General Materials Diffractometer (GEM) . . . 101
4.4.3 High Resolution Powder Diffractometer (HRPD) . . . 108
4.4.4 Laboratory X-ray Diffractometer . . . 112
4.4.5 Defect Analysis . . . 112
4.5 Discussion . . . 115
4.5.1 Understanding the Sintering Process . . . 115
4.5.2 Direct Observation of the Stress-free Temperature . . . 120
4.5.3 Calculation of the Stress-free Temperature . . . 121

4.5.4 Validation of the Model . . . 124
4.5.5 Predicting the Stress-free Temperature . . . 128
4.5.6 Calculated Residual Stresses . . . 132
4.5.7 Effect on Mechanical Properties . . . 137
4.5.8 Lattice Parameter of Diamond Powder . . . 141
4.6 Conclusions . . . 142
4.7 Further Work . . . 143

5 Graphitisation Kinetics 145
5.1 Introduction and Aims . . . 146
5.2 Materials and Sample Preparation . . . 146
5.2.1 PCD Materials . . . 146
5.2.2 Neutron Diffraction Samples . . . 147
5.2.3 Synchrotron X-ray Diffraction Samples . . . 147
5.2.4 Microstructural Analysis . . . 148
5.3 Experimental Techniques . . . 152
5.3.1 Neutron Diffraction . . . 152
5.3.2 Synchrotron X-ray Diffraction . . . 152
5.3.3 Laboratory X-ray Diffraction . . . 157
5.3.4 In-situ Heating TEM Experiment . . . 157
5.3.5 Graphitisation of Mechanical Test Specimens . . . 159
5.4 Results and Discussion . . . 159
5.4.1 GEM Neutron Diffractometer . . . 159
5.4.2 Synchrotron X-ray Diffractometer . . . 169
5.4.3 In-situ Heating TEM Experiment . . . 191
5.4.4 Explanation of Observed Phenomena . . . 198
5.4.5 The Effect of Graphitisation on Mechanical Properties . . . 222
5.5 Conclusions . . . 225
5.6 Further Work . . . 227

Appendices

A Simultaneous Equations for Residual Stress 230

B Extrapolation of Elastic Constants to High Temperature 232
B.1 Young's Modulus and Poisson's Ratio . . . 232
B.2 Diamond . . . 233
B.3 Cobalt . . . 234
B.3.1 Liquid Cobalt . . . 236

C Equations Used in the Calculation of Stresses During Graphitisation **238**
C.1 Fully Elastic Regime 239
C.2 Fully Plastic Regime 240
C.3 Plastic Shell 242

References **244**

List of Figures

1.1 Schematic overview of the main stages of PCD sintering. 5

2.1 Strength against inverse root grain size from Lammer. 9
2.2 Toughness against nominal grain size from Lammer. 10
2.3 Plot of collated strength data from literature sources. 12
2.4 Plot of strength vs. binder content from literature sources. 12
2.5 SEM image of crack path in PCD from Lin. 15
2.6 Higher magnification SEM image of crack path in PCD from Lin. . 15
2.7 Fitting values of critical distance to measured toughness from McNamara. 17
2.8 The effect of leaching on PCD toughness from McNamara. 18
2.9 Plot of toughness vs. grain size collated from literature sources. . . 20
2.10 Plot of fracture toughness vs. binder content collated from literature sources. 21
2.11 SEM image of transgranular fracture in PCD from Marro. 21
2.12 SEM image of crack bifurcation in PCD from Marro. 22
2.13 Residual strength of PCD after Hertzian indentation from Garcia-Marro. 23
2.14 Wear morphologies seen after rock drilling from Hibbs and Lee. . . 24
2.15 SEM images of grain boundaries of PCD after abrasion from Hibbs and Lee. 25
2.16 Micrographs of 'microchipping' wear from Lin. 26
2.17 SEM image of microcracking in PCD from Bai. 30
2.18 Schematic representation of PCD wear mechanisms. 32
2.19 Wear rate of PCD with varying depths of cobalt binder removed. . 37
2.20 Thermal damage of large grained PCD from Miess and Rai 38
2.21 Arrhenius plot from Mehan and Hibbs 39
2.22 Mechanism of direct diamond to graphite transformation from Howes. 41
2.23 Schematic meta-stable carbon phase diagram. 44
2.24 SEM image of graphitisation figures from Khmelnitsky and Gippius. 47
2.25 Structures of graphitic and turbostratic carbon from Oya and Marsh. 48
2.26 TEM image of C-Co-C trilayer after heating from Ramirez. 50

3.1 Schematic diagram of stages of FIB microcantilever production. . . 58
3.2 Schematic diagram of four-point bending jig. 60
3.3 Schematic diagram of custom-made nanoindenter stage. 62
3.4 Height map of cantilever measured with the nanoindenter. 63
3.5 Comparison of strengths of polishing methods. 64
3.6 Strengths of all measured microcantilevers. 65
3.7 Typical load-displacement curve from a cobalt binder pool cantilever. 66
3.8 SEM micrograph of a plastically deformed binder pool. 66
3.9 Plot of transverse rupture strength against inverse root grain size from Lammer. 67
3.10 Replot of toughness values from Lammer with adjustment by 'incipient crack' analysis. 70
3.11 Strength of PCD against inverse, root grain size. 72
3.12 FIB machining defect causing fracture. 73
3.13 Partially eroded binder pool causing fracture. 74
3.14 Barely visible surface crease causing fracture. 75
3.15 Breakdown of cantilevers by their strength and failure location. . . 77
3.16 Breakdown of cantilevers by their strength and the straightness of their fracture paths. 78
3.17 Backscattered electron and cathodoluminescence images of PCD. . . 80
3.18 EBSD and backscattered electron images of PCD. 81
3.19 Abnormal grain growth in PCD from McKie *et al.*. 82
3.20 Slip bands and stable crack in a microcantilever. 83
3.21 Strain bursts in nanoindenter output of a binder pool microcantilever. 84
3.22 Cobalt binder pool holding together fractured microcantilever. . . . 84

4.1 Backscattered electron SEM image of PCD used in neutron diffraction experiments 88
4.2 ICP etching results. 98
4.3 FIB cross-section of leached material. 99
4.4 EDX map of unleached PCD cobalt binder pool. 99
4.5 EDX line scan of atomic composition of cobalt binder pool. 100
4.6 EDX map of unleached PCD cobalt binder pool. 101
4.7 GEM unleached PCD diffractogram. 102
4.8 Diamond {220} neutron diffraction peak. 103
4.9 Diamond lattice parameters calculated by Rietveld refinement from GEM. 103
4.10 Pure cobalt diffractogram at room temperature. 104
4.11 Pure cobalt diffractogram at 600 °C. 105
4.12 Cobalt-tungsten alloy diffractogram at room temperature. 106

4.13 Lattice parameter of bulk cobalt alloys as a function of temperature. 106
4.14 Cobalt {200} peak in unleached PCD diffractogram. 107
4.15 Cobalt tungsten alloy and cobalt peak lattice parameters as a function of temperature. 107
4.16 HRPD diffractogram of unleached PCD at room temperature. . . . 109
4.17 Unleached diamond {111} peak from an HRPD diffractogram. . . . 110
4.18 Diamond powder diffractogram from HRPD. 110
4.19 Diamond lattice parameters as a function of temperature for HRPD. 111
4.20 Cobalt lattice parameter calculated from {200} peak. 111
4.21 Diamond lattice parameter as a function of temperature from lab XRD. 113
4.22 Cobalt lattice parameter as a function of temperature from lab XRD. 113
4.23 Diamond Raman peak position before and after heating. 114
4.24 Single substitutional nitrogen EPR spectrum. 114
4.25 Sintering schematic diagram, stage 1. 116
4.26 Sintering schematic diagram, stage 2. 117
4.27 Sintering schematic diagram, stage 3. 117
4.28 Sintering schematic diagram, stage 4. 118
4.29 Sintering schematic diagram, stage 5. 118
4.30 Repeat measurements of diamond lattice parameter from GEM and HRPD. 120
4.31 Natural log of diamond lattice parameter against temperature. . . . 123
4.32 Plot of calculated stress-free temperature against measurement temperature. 126
4.33 Predicted stress-free temperature against required solidification strain. 130
4.34 Plot of residual stress against temperature. 134
4.35 Cobalt residual stress comparison. 135
4.36 Plot of residual stress vs. temperature in heating and cooling. . . . 136
4.37 Plot of residual stress vs. temperature for WC in WC-Co from Mari *et al.*. 137
4.38 Backscattered electron image highlighting cobalt regions. 139

5.1 Schematic diagram of FIB cross-section manufacture. 149
5.2 FIB lamella partially freed from sample. 150
5.3 Micro-manipulator attached to FIB liftout sample. 150
5.4 In-situ heating TEM sample after final thinning. 151
5.5 Synchrotron experiment infrared furnace. 153
5.6 Furnace power experimental schedule. 155
5.7 Furnace power experimental schedule. 155
5.8 Furnace power experimental schedule. 156

5.9 Furnace power experimental schedule. 156
5.10 Furnace power experimental schedule. 157
5.11 TEM sample attached to DENS heating chip. 158
5.12 GEM isothermal - graphite weight percentage vs. time. 160
5.13 GEM isothermal - diamond lattice parameter vs. time. 161
5.14 GEM isothermal - cobalt lattice parameter vs. time. 161
5.15 Graphite peak with Rietveld fit. 162
5.16 Raman map of graphitised PCD. 163
5.17 Low magnification SEM image of heavily graphitised sample. 164
5.18 Degraded grain boundaries of heavily graphitised sample. 165
5.19 SEM image of multiple graphitised binder pools. 165
5.20 SEM and EDX images of a graphitised region surrounding a binder pool. 166
5.21 Residual binder pools in a leached PCD sample. 166
5.22 EDX image of a residual binder pool in leached PCD after heating. 167
5.23 High angle annular dark field STEM image of graphitised region. . . 169
5.24 Plane spacing of graphite {0002} planes. 170
5.25 TEM image with superimposed EDX map of graphitised region. . . 171
5.26 Offset between HRPD and synchrotron measured lattice parameters. 172
5.27 Temperature calibration curve for synchrotron data. 173
5.28 Comparison of measured and calibrated diamond lattice parameters as a function of time. 173
5.29 Diamond and cobalt lattice parameters as a function of time. 174
5.30 Diamond and cobalt lattice parameters with graphite weight percentage. 175
5.31 Measured temperature of G22-00X sample as a function of time. . . 176
5.32 Diamond and cobalt lattice parameters with graphite weight percentage. 176
5.33 Diamond and cobalt lattice parameters with graphite weight percentage. 177
5.34 Comparison of cobalt lattice parameter drop in sudden vs. gradual heating. 178
5.35 Comparison of measured and calibrated diamond lattice parameters as a function of time. 179
5.36 Diamond and cobalt lattice parameters as a function of time. 180
5.37 Weight percentages of graphite, tungsten carbide and eta-carbide as a function of time. 181
5.38 SEM image of a binder pool after heating. 182
5.39 G75-B-A FIB cross-section with EDX. 182
5.40 SEM image of carbon particles within a binder pool after heating. . 183
5.41 G75-B-B FIB cross-section with EDX. 184

5.42 TEM image from Westraadt *et al.* of graphite paricles within a binder pool. 185
5.43 Graphite formation vs. time for different additive concentrations. . 186
5.44 Effect of additive concentration on incubation time. 187
5.45 Diamond and cobalt lattice parameter, graphite wt% vs. time. . . . 188
5.46 Diamond and cobalt lattice parameter, WC wt% vs. time. 189
5.47 Diamond and cobalt lattice parameter, η-carbide wt% vs. time. . . 189
5.48 Graphite wt% and thermocouple temperature vs. time. 190
5.49 Screenshots of η-carbide dissolving at high temperature. 193
5.50 HAADF STEM image of boundary between cobalt binder pool and diamond. 194
5.51 Screenshots from video of graphitisation in TEM images. 196
5.52 HAADF and DF images of the extent of graphitisation after 9 min at 800 °C. 197
5.53 Binder pool with EDX measurement locations highlighted. 201
5.54 Schematic diagram of "Fully Elastic Regime". 203
5.55 Carbon phase diagram from Bundy. 205
5.56 Graphite and cobalt hydrostatic and cobalt Von Mises stress vs. graphite expansion ratio. 206
5.57 Schematic diagram of "Fully Plastic Regime". 207
5.58 Graphite, cobalt, diamond hydrostatic and diamond hoop stresses vs. graphite expansion ratio. 208
5.59 Comparison of elastic model and measured stresses. 208
5.60 Schematic diagram of "Plastic Shell Regime". 211
5.61 Determination of yield radius in "Plastic Shell Regime". 212
5.62 Graphite, cobalt and diamond hydrostatic stresses with "Plastic Shell Regime". 213
5.63 The effect of yield stress on the yield radius. 214
5.64 Hydrostatic stress in graphite at point of yield vs. cobalt yield stress. 214
5.65 Effect of carbon in solution on "Fully Elastic Regime" cobalt hydrostatic stress. 216
5.66 Effect of carbon in solution on "Fully Elastic Regime" diamond hydrostatic stress. 217
5.67 Effect of carbon in solution on "Fully Plastic Regime" stresses. . . . 218
5.68 Extensive cracking of sample after graphitisation. 219
5.69 The effect of heating on the strength of PCD. 223
5.70 Surface quality of PCD after 1.5 h of heating. 224
5.71 The effect of various levels of heating on the microstructure of PCD. 226

B.1 Cobalt shear modulus as a function of temperature. 235

B.2 Elastic stiffness constant of cobalt alloy as a function of temperature. 235
B.3 Bulk modulus for solid and liquid cobalt. 237

C.1 Schematic diagram of "Fully Elastic Regime". 239
C.2 Schematic diagram of "Fully Plastic Regime". 241
C.3 Schematic diagram of "Plastic Shell Regime" 243

List of Tables

2.1 Critical flaw size vs grain size from Lammer. 9
2.2 Collated strength data from literature sources. 13
2.3 Collated data on fracture toughness of PCD from literature sources. 19
2.4 Literature residual stress values. 34
2.5 Summary of results from Pantea *et al.* 43

3.1 Description of various PCD grades 54
3.2 Dimensions of macroscopic four-point bending specimens. 56
3.3 Strengths and dimensions of four-point bending specimens. 62
3.4 Strength vs inverse root grain size from Lammer with grain size correction. 68

4.1 EDX elemental analysis results. 101
4.2 Cross-over temperatures from GEM and HRPD experiments. 120
4.3 Coefficients for TEC equations. 122
4.4 Calculated stress-free temperatures. 125
4.5 Stress-free temperature, all results. 130
4.6 All components of strain at stress-free temperature. 131
4.7 Summary of measured and calculated diamond lattice parameters. . 133
4.8 Calculated stresses and strains in diamond. 133
4.9 Pre- and post-leach K_{IC} results from McNamara *et al.* 140

5.1 Values for the repeat measurement of diamond lattice parameter. . 170

B.1 Diamond elastic stiffness constant coefficients. 234
B.2 Diamond Young's modulus and Poisson's ratio as a function of temperature. 234
B.3 Cobalt Young's modulus and Poisson's ratio as a function of temperature. 236

List of Abbreviations

PCD . . . . . Polycrystalline Diamond - the main material of study in this thesis.

PDC . . . . . Polycrystalline Diamond Cutter/Compact - confusingly 'PDC cutter' may also be seen. These are often used in industry literature.

GEM . . . . . General Materials [Diffractometer].

HRPD . . . . . High Resolution Powder Diffractometer.

EBSD . . . . . Electron Backscatter Diffraction.

CCD . . . . . Charge Coupled Device.

IPF . . . . . Inverse Pole Figure.

EDX . . . . . Energy Dispersive X-ray [Spectrocopy].

XRD . . . . . X-ray Diffraction/Diffractometer.

SEM . . . . . Scanning Electron Microscope.

TEM . . . . . Transmission Electron Microscope.

STEM . . . . . Scanning Transmission Electron Microscope.

FIB . . . . . Focussed Ion Beam.

EPR . . . . . Electron Paramagnetic Resonance.

SEVNB . . . . Single-Edged V-Notched Beam.

TRS . . . . . Transverse Rupture Strength.

CRS . . . . . Compressive Rupture Strength.

HPHT . . . . . High Pressure, High Temperature.

EDM . . . . . Electrical Discharge Machining.

ICP . . . . . Inductively Coupled Plasma.

FCC . . . . . Face Centred Cubic.

HCP . . . . . Hexagonal Close Packed.

GIC . . . . . Global Innovation Centre

WC/Co . . . . Tungsten Carbide/Cobalt.

alatdiamond . Diamond lattice parameter (used to save space on crowded graphs).

alatcobalt . . . Cobalt lattice parameter (used to save space on crowded graphs).

1

Introduction and Background

Contents

1.1 Brief History of Diamond Synthesis 1
1.2 Polycrystalline Diamond 2
1.2.1 History 2
1.2.2 Modern Synthesis of PCD 3
1.2.3 Leaching of PCD 6
1.3 Motivation for this Work 6

1.1 Brief History of Diamond Synthesis

Almost as soon as diamond was discovered to be an allotrope of carbon in 1797 by Smithson Tennant[1], efforts were made to produce it synthetically. Many claimed success but a distinct lack of evidence and reproducibility suggests that these early reports were fallacious. Simultaneously the most famous and tragic of which was that of Henri Moissan. He attempted to use the solubility of carbon in iron combined with a rapid quench from white heat to induce the pressure required to transform graphite into diamond[2]. Although he claimed success, testimony from his widow stated that one of his assistants had introduced natural diamond flakes into his samples "to please the old man" and cut short his tediously long

experiments[3]. Later cathodoluminescence work confirmed that the diamonds were indeed natural in origin[4].

It wasn't until 1955[5] (with further details given in 1959[6]) that the first credible report of diamond being synthesised was published by researchers at General Electric. They discovered that a molten metal could be used to lower the temperatures and pressures needed to synthesise diamond making it feasible given the technology of the time but did not understand the mechanism of growth. The role of the molten metal was strongly contested until a study in 1981 concluded that it must play a role as both a solvent for graphitic carbon and a catalyst for the re-precipitation of diamondiferous carbon[7], lowering the activation energy barrier of its formation.

1.2 Polycrystalline Diamond

1.2.1 History

The first instance of a sintered, polycrystalline diamond (PCD) compact was published in 1970. This was twelve years after it was predicted that a synthetic form of natural polycrystalline diamond (carbonado) would be a highly desirable material to be able to make[8] by the same author. The following year, it was found that using cobalt as a binder could reduce the temperature and pressure required for successful sintering by up to 24% and 27% respectively[9]. This technological innovation allowed the mass production of PCD to be realised and still accounts for the way in which most PCD is made today.

In 1973, General Electric patented the use of a carbide-supported PCD drill bit for use in oil and gas drilling[10]. From then onwards, PCD cutters made inroads into various material removal industries such as the machining of wood-based products[11], non-ferrous metals[12] and most recently, composites[13]. In 2010, polycrystalline diamond cutters accounted for 65% of the footage drilled by the oil and gas industry[14] and was projected to rise to over 80% by 2016[15] (at the time of the study). Such market domination has been due in large part to the cost savings made possible by PCD's remarkable properties. PCD cutters provide up to two orders of magnitude improvement in tool life over other industry standard

cutting materials such as cemented tungsten carbide depending on the specific application[16][17][18]. This allows far less time and money to be expended on replacing worn tools; something that is particularly costly in drilling applications, leading to vastly reduced operating costs and hence increased profits. Outstanding hardness and abrasion resistance are the two main materials properties of PCD that have allowed such huge performance increases compared to other materials. But, as ever, with high hardness comes low toughness. Although PCD is far less brittle than single crystal diamond, its resistance to impact and shock loading are two of the main issues that must be overcome in improving PCD as a cutting material.

1.2.2 Modern Synthesis of PCD

PCD synthesis begins with diamond powder which can be a single carefully controlled particle size, a wide distribution of particle sizes or multiple single sizes mixed together. The powder is compacted on top of a cemented tungsten carbide substrate which may have a textured top surface to mitigate the residual stresses that develop at the diamond-substrate boundary. This is encapsulated by a metal canister and inserted into a capsule that in turn goes into a high pressure press. There are two common designs of high pressure press: belt and cubic. The cubic press applies pressure along each of the three Cartesian axes whereas the belt press applies pressure circumferentially and from above and below. The presses are capable of applying around 1500°C and 5-10 GPa of pressure. The capsule is designed so that a constituent of it becomes molten at high temperature and distributes the applied pressure hydrostatically.

There are four regimes of the sintering process that occur sequentially and are illustrated in figure 1.1:

1. Cold compaction.
2. Hot compaction.
3. Cobalt infiltration.
4. Liquid phase sintering.

During *cold compaction*, pressure is applied to the capsule at room temperature. Where diamond particles meet at point-like contacts, the local stress becomes exceptionally high causing fracture of the grains. This reduces and widens the average size distribution and causes the density of the green body to increase as fine particles fill in the remaining voids. *Hot compaction* begins when the temperature is raised to the sintering temperature. It is believed that at the sintering temperature, diamond is able to undergo plastic deformation[19]. Where there are remaining point contacts, the diamond plastically deforms, rounding off these corners and reducing the stress concentration. From cathodoluminescence data, it appears that entire grains undergo plastic deformation and that a large proportion of the original diamonds have a resultant high dislocation density[20]. As the temperature rises above the melting point of the cobalt binder phase, *cobalt infiltration* begins. The molten cobalt is drawn from the WC/Co substrate into the diamond compact by capillary forces. Non-diamond carbon and very fine diamond particles are preferentially dissolved into the cobalt as it sweeps through the diamond layer. Finally, during the last stage of *liquid phase sintering*, newly formed diamond precipitates out from the cobalt[20] as the conditions are in the diamond stable region of the carbon-cobalt phase diagram. Diamond grains are strongly bonded together with the remnant binder phase existing in pools between the diamond grains. To be able to understand the macroscopic mechanical properties of PCD, it is important to understand the mechanical properties of these interfaces and so this is one of the areas that this thesis will explore.

The resultant product is a layer of two-phase ceramic material predominantly comprised of micron-sized diamond grains sintered together with a high degree of diamond-diamond bonding (referred to as the "diamond table") atop a thick tungsten carbide/cobalt substrate. The diamond grains retain roughly the same morphology post-sintering and the cobalt binder material occupies the spaces that were not filled by diamond during sintering. The microstructure is a complex combination of the original diamond grains (a proportion of which are heavily

a) Cold Compaction

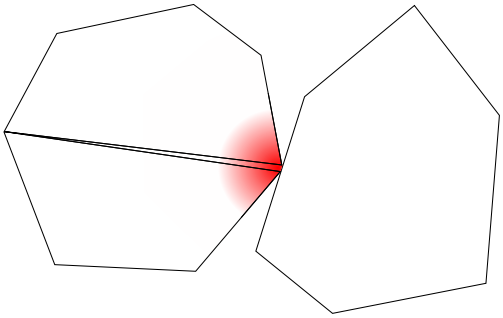

High stresses at point contacts cause fracture of diamond grains and a shift in the particle size distribution to smaller sizes.

b) Hot Compaction

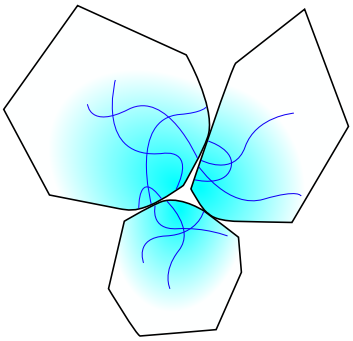

As the heating is applied, the temperature at which plastic deformation occurs is exceeded. Sharp contact points are rounded off and dislocations are introduced into the diamond grains.

c) Cobalt Infiltration

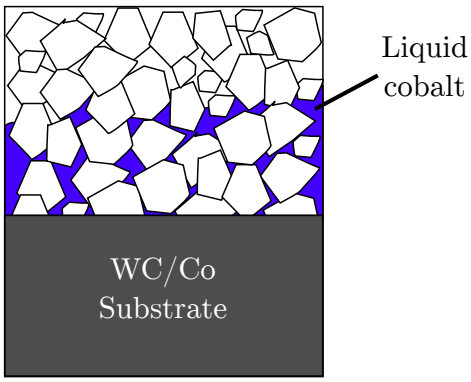

When the cobalt in the substrate melts, a front of liquid cobalt sweeps up through the diamond grains disolving carbon into the liquid as it goes.

d) Liquid Phase Sintering

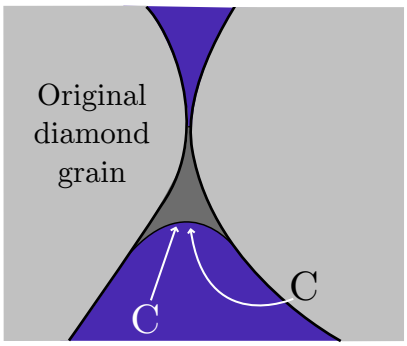

New diamond precipitates from the liquid cobalt pools allowing diamond grains to sinter together. A continuous diamond skeleton is formed.

Figure 1.1: Schematic representation of the four main stages of sintering of polycrystalline diamond by the high pressure, high temperature (HPHT) method.

plastically deformed[19]), newly precipitated diamond[20], now-solidified solvent-catalyst metal binder and various intermetallic phases[21].

1.2.3 Leaching of PCD

Although cobalt is very useful in acting as a catalyst for diamond synthesis, it unfortunately also contributes to the thermal degradation of PCD under the high temperature conditions of drilling[22]. A patent was filed in 1978 describing a method of removal of the cobalt binder phase to increase the thermal stability of PCD, called leaching[23]. Leaching involves heating PCD in a mixture of concentrated nitric and hydrochloric acid for long periods of time to chemically attack and remove the cobalt. Whilst this does increase the thermal stability of PCD, the mechanical properties are degraded[24] and it is a time consuming, costly and hazardous process. Electrolysis has also been used to remove the cobalt from PCD[25] with good results. Only a few studies have been done on the effect leaching has on the mechanical properties of diamond and these will be discussed in later sections.

1.3 Motivation for this Work

Polycrystalline diamond is clearly a very important technological and industrial material. As stronger and stronger structural materials are developed, the performance of the material that is used to cut and machine them also needs to keep pace. PCD already surpasses the performance of most other cutting materials and its room temperature properties are very impressive. However, as cutting applications become more demanding, the temperatures generated during cutting increase and active cooling is not always a viable option. PCD suffers from mechanical breakdown at high temperatures by a process that is not fully understood which places a limit on the performance of PCD as a cutting material. Leaching is an imperfect solution to this problem due to the degradation of the mechanical properties that it causes. In light of this, the aim of this thesis is to understand the mechanisms that control the thermal breakdown process in order to enable the development of a PCD material that is resistant to it.

2
Literature Review

Contents

2.1 Mechanical Properties 7
2.1.1 Traditional Mechanical Testing of PCD 7
2.1.2 Wear Testing 23
2.1.3 Summary 29
2.2 Residual Stresses 30
2.2.1 Summary 35
2.3 Graphitisation of Diamond 35
2.3.1 Cutter Temperature 35
2.3.2 Thermal Degradation of PCD 36
2.3.3 Graphitisation of Pure Diamond 39
2.3.4 Catalytic Graphitisation 46
2.3.5 Summary 51

2.1 Mechanical Properties

2.1.1 Traditional Mechanical Testing of PCD

Techniques such as notched and unnotched beam flexure, ball-on-three ball flexure and diametral compression are discussed in this section. The term "traditional" is taken to mean mechanical deformation of macroscopic samples. Almost all of the work on the mechanical properties of diamond cites the work of Lammer[26] from 1988. A recent review paper entitled "The mechanical and strength properties

of diamond" by Field quotes it as if it is the state of the art[27]. Although Lammer's work made significant improvements over the early work carried out by Gigl[28] and Roberts[29], there are several points to be addressed regarding the conclusions of the paper.

2.1.1.1 The Seminal Paper on the Mechanical Properties of PCD

The first work to examine the mechanical properties of PCD in great depth was written by Lammer in 1988[26]. This paper presented a big step forward in the understanding of this research area and still influences work undertaken today. However, some of its conclusions warrant a re-examination in the light of modern understanding of ceramic materials and given its prominence in the field, the entirety of the present section has been dedicated to doing just that.

Figure 2.1 illustrates the relationship between transverse rupture stress (TRS) and the inverse of the square root of nominal grain size deduced by Lammer for various PCD grades. It shows two distinct regions in behaviour. The bimodal nature of the curve is attributed to an explanation by Rice[30] based on work on other ceramics showing that the inherent critical flaw size c is independent of the grain size d. The argument continues that for fine grained materials, where the inherent flaws may span numerous grains, the strength is controlled by the polycrystalline fracture toughness. For coarse grains, where the critical flaw is *within* a single grain, it is controlled by the single crystal fracture toughness. The crossover point between these two regimes is expected to be where grain size, d, is equal to flaw size, c. From Table 2.1, $c/d = 1$ occurs between 12-30 µm which agrees with the approximate crossover point between "region 1" and "region 2" in Figure 2.1 of 30 µm.

However, the grain size used in this analysis is the average diameter of particles in the powder prior to sintering. During the high pressure sintering process, particles are crushed due to large stresses at point contacts[31], widening the particle size distribution and pushing it to lower diameters. This process is exacerbated with large particles as there are fewer contact points between particles and so the stress at each one is higher. As particle size decreases, the comminution limit is eventually

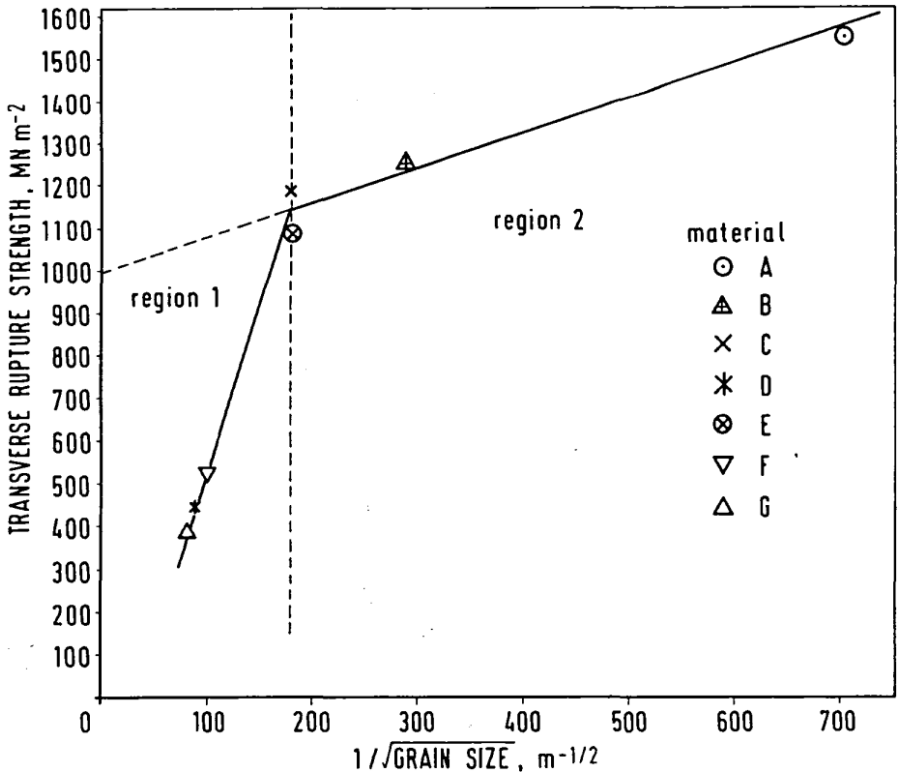

Figure 2.1: Plot of transverse rupture strength against the inverse of the square root of grain size from Lammer[26]. Two distinct regions are shown in the curve transitioning at a value that represents a grain size of approximately 30 µm.

	A	B	C	D	E	F	G
c_{crit}, µm	6	16	18	91	19	68	105
d, µm	2	12	30	125	30	95	150
c/d	3·00	1·33	0·60	0·73	0·63	0·72	0·70

Table 2.1: Critical flaw size calculated from strength and toughness for each grain size material also showing the ratio between the two. From Lammer[26]

reached and so little or no crushing occurs. Therefore, the assertion that the crossover point occurs where $c = d$ is likely untrue as "nominal grain size" largely, but not linearly, overestimates the true grain size.

Additionally, two distinct fracture behaviours would be expected. The "single crystal fracture toughness" for large grain sizes and the "polycrystalline fracture toughness" for small grain sizes. It is also implied that large grained materials should exhibit transgranular fracture whilst small grained materials show intergranular fracture. As can be seen from Figure 2.2, no such clear distinction is evident

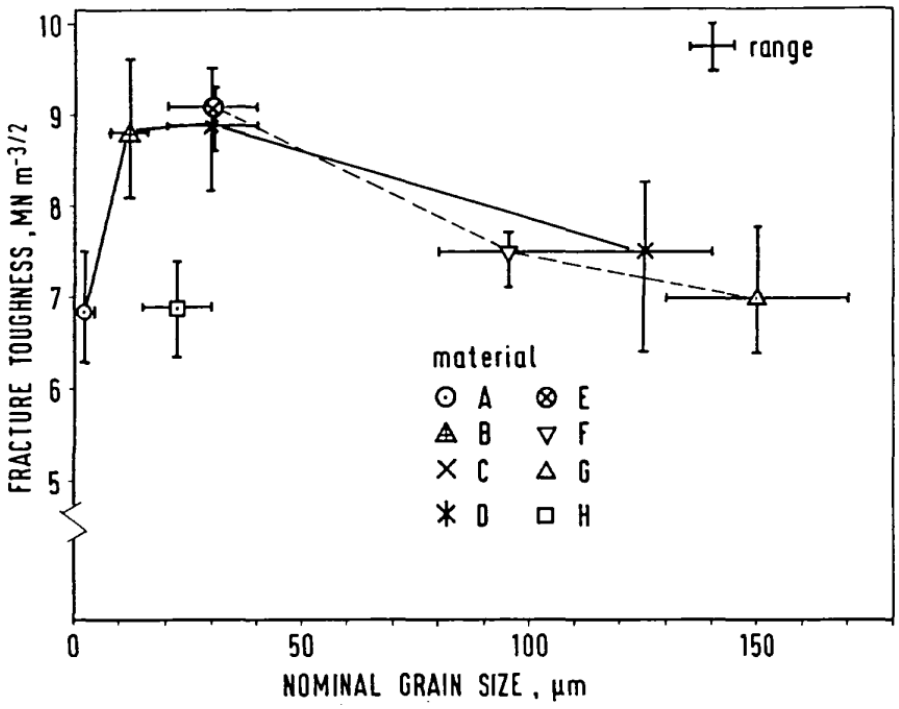

Figure 2.2: Plot of fracture toughness against nominal grain size measured by diametral compression of specimens with laser cut notches in them from Lammer[26]. Given that the drawn trend appears to be on the same order as the scatter in the data, its validity is drawn into question.

and although fracture in large grained ($\geq$ 30 µm) material is described as being transgranular, there is no mention of the fracture mode of fine grained materials and no corroborating SEM images. The explanation given for the observed trend is derived from Rice's work stating that "thermal and elastic anisotropy between diamond and binder phases could result in high interfacial stresses that allow microcracks to propagate along the diamond-cobalt boundaries"[30]. Although high residual stresses have been observed in the diamond layer[32], fracture occurs predominantly transgranularly in PCD[33] so microcracks along the grain boundaries, if they do exist, have minimal effect on the fracture behaviour. He then goes on to say that other factors such as "impurities in the matrix material, the amount and size distribution of the secondary phase, and the degree of plastic deformation and fragmentation of diamond grains during synthesis" could affect the fracture toughness. Some of these postulations are almost certainly true but further work is required to show which hold merit.

2.1.1.2 Strength

Data from other authors measuring the strength of PCD are tabulated in Table 2.2. Belnap and Griffo[34] compared the strength of PCD monoliths and PCD composites with additional tungsten carbide/cobalt admixed. They found that decreasing the diamond content of the composite resulted in a decrease in the flexural strength. The two different grain sizes they used resulted in similar flexural strengths within the bounds of the error. Along with showing that there is a negative strain rate and positive temperature dependence on strength, Petrovic *et al.*[35] found that a larger grain size resulted in a lower strength material. This was ascribed to larger flaws found in the coarser grained material; they noted that the typical flaw size found in the surface of the specimen was proportional to the grain size. Despite reporting the strength of one grade of PCD, Morrell *et al.*[36] do not provide any information on which grade this was. Finally, McNamara *et al.*[37] found that a small decrease in the cobalt content of the PCD resulted in a small decrease in the strength.

The data in Table 2.2 is also shown graphically for grain size and binder content in Figures 2.3 and 2.4. From Figure 2.3, a reasonably clear trend can be seen that decreasing the grain size increases the strength. This agrees with the general trend shown by Lammer but two distinct regions are not obvious in these data. The correlation between flaw size and grain size reported by Petrovic *et al.* disagrees with Lammer's suggestion that flaw size is independent of grain size, however, further results are needed to verify the trend and an investigation into the flaw size distribution for various grades of PCD should be carried out.

In Figure 2.4, a less obvious trend is seen between strength and binder content, although there may be a general positive correlation, the large scatter in the data adds significant uncertainty. As it is difficult to vary the binder content independently of grain size, understanding the role of the binder phase on the mechanical properties from literature data is problematic.

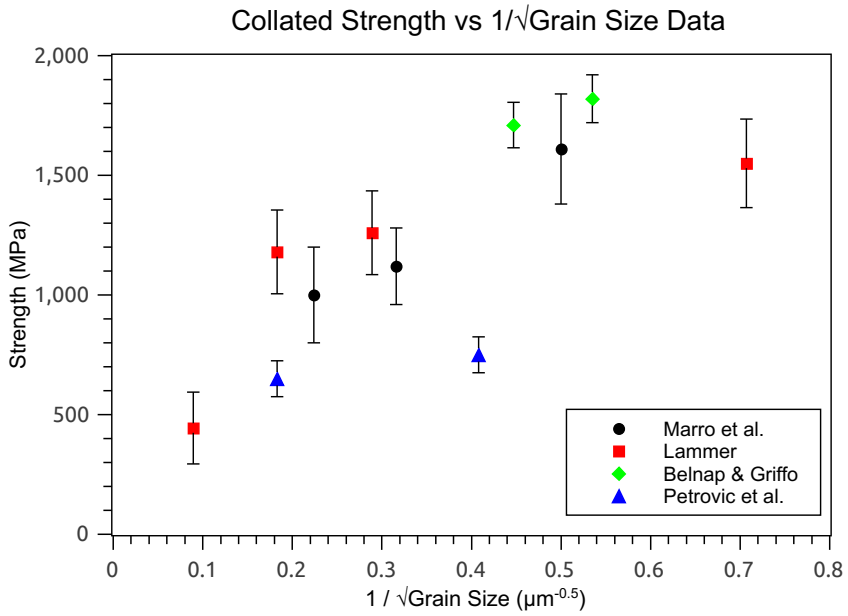

Figure 2.3: Graphical representation of the strength vs grain size data from Table 2.2. Studies were omitted if they did not have sufficient data on grain size. A general positive trend can be seen.

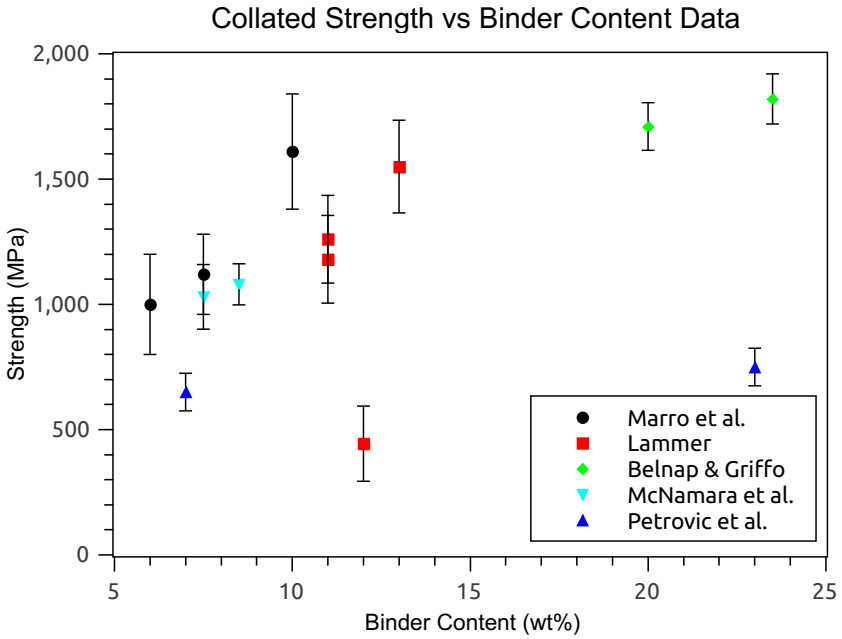

Figure 2.4: Graphical representation of the strength vs binder content data from Table 2.2. Studies were omitted if they did not have sufficient data on binder content. The scatter in the data is large and no obvious overall trend can be seen.

Author	Technique	Strength (MPa)	Weibull Modulus	Grain Size (µm)	Binder Content (wt%)
Petrovic *et al.*[35]	3PB	750 ± 75	-	6	23
		650 ± 75	-	30	7
McNamara *et al.*[37]	-	1075 ± 82	13.4	-	8.5
		1034 ± 129	8.3	-	7.5
Morrell *et al.*[36]	B3B	1453 ± 29	14.5	-	-
Belnap & Griffo[34]	3PB	1815 ± 100	16.0	3.5	23.5
		1714 ± 95	21.9	5	20
Lammer[26]	DC	1550 ± 185	3.4	2	13
		1256 ± 175	4.3	12	11
		1180 ± 175	4.4	30	11
		444 ± 150	3.4	125	12
Marro *et al.*[38]	B3B	1610 ± 230	-	4	10
		1120 ± 160	-	10	7.5
		1000 ± 200	-	20	6

Table 2.2: Strength data for various grades of PCD collated from numerous authors. The following terminology is used for the technique column: 3PB - 3 point bending, B3B - ball-on-three-ball, DC - diametral compression. The error shown in the strength column is the standard deviation except for Lammer where it is the range in the measured results.

2.1.1.3 Fracture Toughness

Miess and Rai[39] investigated the fracture toughness of a wider range of grain sizes using the same method as Lammer. Their results show a plateau in fracture toughness rather than the decrease at larger grain sizes found by Lammer. Along with citing Rice's work, they suggest that as grain boundaries in ceramics are typically weaker than the grains, increasing the area of grain boundary by decreasing the average grain size increases the amount of weak material and hence lowers the

fracture toughness. This argument suffers from the same flaw as that of Lammer - no fracture paths are shown in their work and later work has shown that fracture in PCD occurs predominantly transgranularly.

Double-torsion tests were carried out on various grades of PCD by Lin, Cooper and Hood[40] to measure the fracture toughness and investigate sub-critical crack growth. They measured unusually high values of fracture toughness (13 MPa $\sqrt{\mathrm{m}}$). A review on the technique[41] notes that the use of a guiding groove, as was done in their work, is now recognised to be undesirable as the effects of the stress concentration it causes are poorly understood[42]. It is also noted that crack deflection is a sign of a poorly aligned or balanced loading system. It is therefore unsurprising that Lin *et al.* observed crack deflection as with the exceptionally high stiffness of diamond, even the smallest misalignment will result in large stress gradients. If the alignment of the specimen was slightly off, the stress intensity at the crack tip could be much lower than expected resulting in the unusually high value of fracture toughness observed. However, despite its potential disadvantages, the results of this work are particularly interesting as a natural crack is grown in the sample rather than the artificial notches used in other tests.

Lin *et al.*'s work shows several micrographs of transgranular fracture (figures 2.5 and 2.6), further suggesting that PCD does not preferentially fracture along the grain boundaries. The authors state that crack deflection appears to be a significant toughening mechanism in PCD, however, by examining the micrographs provided it can be seen that this is a minimal effect. It is also explained that in three of the samples tested, the crack advanced in discrete jumps with a stress relaxation occurring after each jump. The authors suggest that this may be due to the presence of the cobalt phase, presumably the plasticity therein, but due to only sporadic descriptions of the microstuctures of the samples tested, it is impossible to form any kind of correlation.

Whilst others have measured the fracture toughness of PCD using single-edged v-notched beam (SEVNB) bending[36][43], the most recent and in-depth study of this type is by McNamara *et al.*[44]. However, the analysis used in this paper, the theory

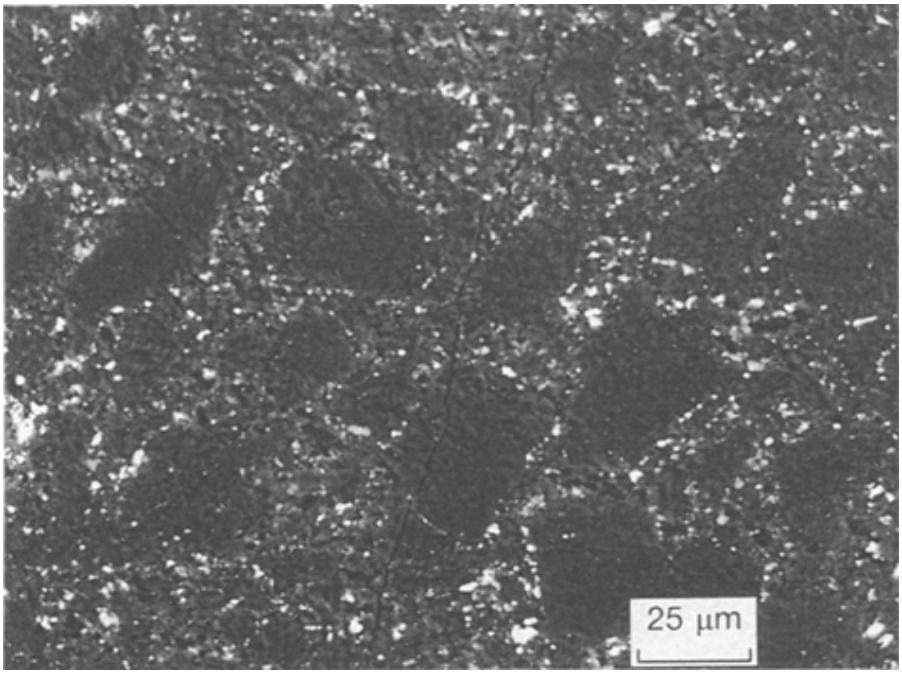

Figure 2.5: Backscattered electron SEM image of a mostly straight crack path showing transgranular fracture. Its microstructure is described as "coarse diamond grains (20-50 µm) embedded in a fine-grained diamond matrix, containing little cobalt". From Lin *et al.*[40]

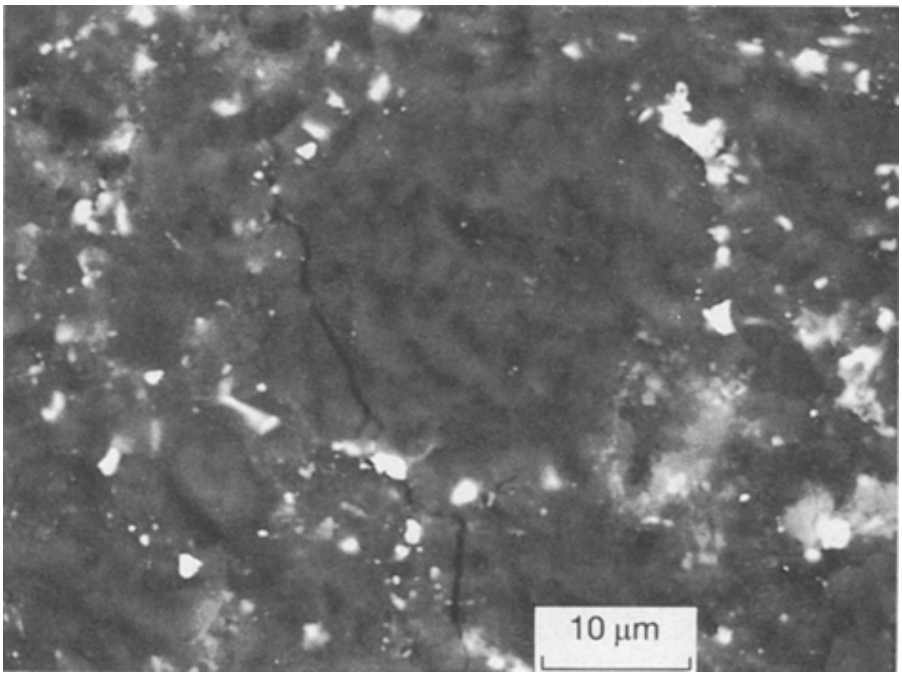

Figure 2.6: Higher magnification backscattered electron SEM image of a crack running through a larger diamond grain. The authors describe this as indicative of crack deflection, however, it appears the degree of deflection is relatively small. From Lin *et al.*[40]

of critical distances, was originally developed for use with metal components[45]. The 'critical distance' r_c is initially taken to be the nominal grain size - a parameter which has been highlighted to be inappropriate when discussing sintered PCD microstructures. Upon realising the difficulty in defining it meaningfully, the authors surmise that it is merely a fitting parameter. Figure 2.7 shows that a small change in r_c results in a large change in the calculated fracture toughness whilst still producing an acceptable fit to the experimental data. The authors note that this is not as catastrophic an issue for fine grained microstructures as it is for coarse grained as the degree of particle crushing is not as great, simplifying the choice of r_c.

McNamara *et al.* also studied the effect that 'residual metal removal depth' (leaching depth) had on the fracture toughness of PCD. Figure 2.8 shows that for coarse grained material, the toughness remains constant until a certain depth and that fine grained material's toughness begins to degrade linearly as soon as leaching begins. It is unclear exactly why this trend exists but the authors suggest fine grained PCD may be more sensitive to leaching as it has a higher volume fraction of cobalt and hence there will be more pores on the surface to act as flaws post-leaching. One possible explanation may be that cobalt leaching only has an effect on toughness once the leaching depth exceeds the grain size and so finer grained materials would show a decrease in toughness with leaching depth sooner than coarse grained materials would.

The collated data on fracture toughness is shown in Table 2.3. Figure 2.9 shows that when aggregated, there is no discernible trend in fracture toughness against grain size. However, within each individual study, a similar trend is apparent - that increasing the grain size increases the fracture toughness but with increasingly diminishing effect. The main conclusion that can be drawn from this is that the changes in fracture toughness as the grain size varies are vastly outweighed by another effect that varies between studies. One possible issue is that three different testing methodologies are used within this data set. Even within a single testing method such as SEVNB bending, different studies can be rendered incomparable if the notch roots are of different radii due to its strong effect on the apparent

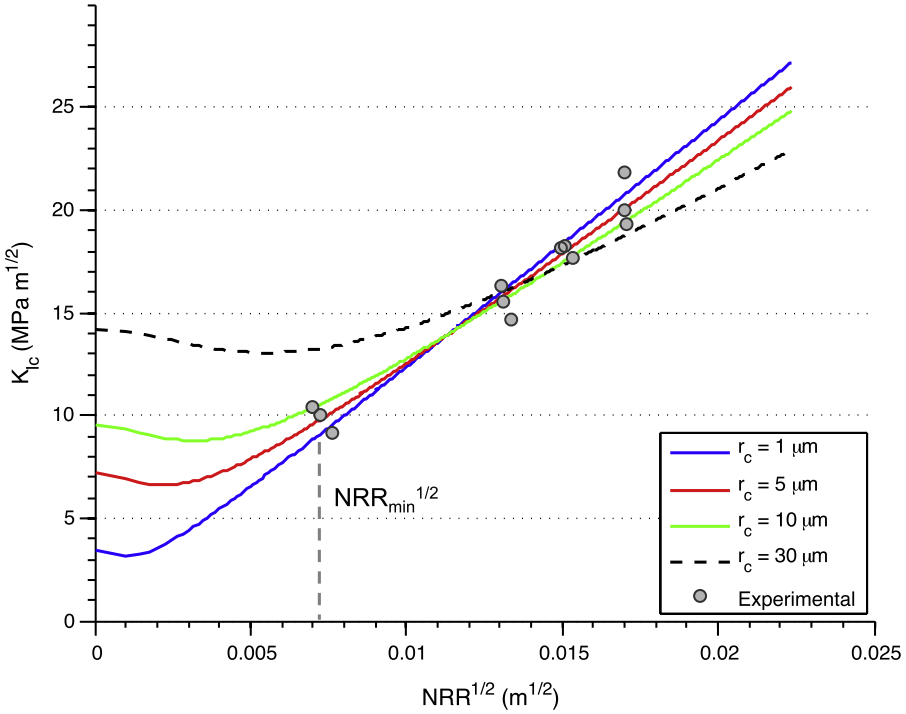

Figure 2.7: Fitting of various values of critical distance r_c to experimental data by McNamara *et al.*[44]. It can be seen that varying r_c from 1 to 30 µm changes the calculated value of fracture toughness K_{Ic} dramatically whilst maintaining an acceptable fit to the experimental data.

toughness[46]. It is highly likely that a similar effect will be present between different testing methodologies.

Figure 2.10, on the other hand appears to tell a completely different story. Of the four plots of collated data from the literature, fracture toughness against binder content appears to be the strongest. There seems to be a strong negative relationship between the toughness and the amount of binder in the PCD which is surprising given that others have suggested[33] that the binder phase contributes a toughening effect. However, the interaction between cracks in PCD, the binder phase and the overall toughness of the material are likely much more complicated than this graph appears to show. For example, the binder content does not vary independently of grain size and the methodology effect may confound the results further. One must be wary of drawing any concrete conclusions from the trend shown in this graph as although there appears to be a low amount of scatter, the results of each study are tightly grouped in binder content-space rather than each showing a similar trend

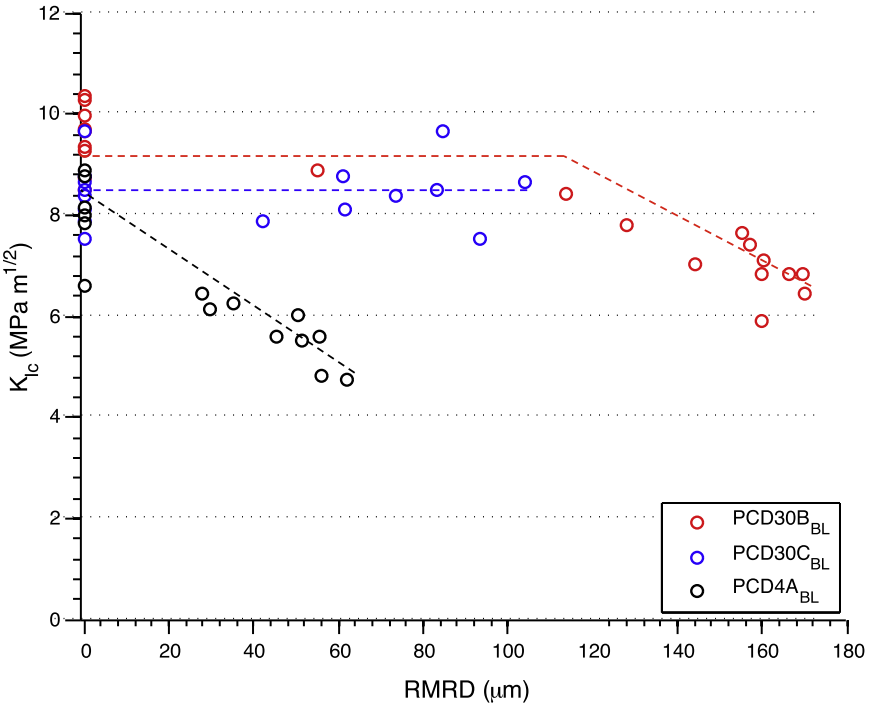

Figure 2.8: Behaviour of the fracture toughness of various grades of PCD as the leaching depth (RMRD) is increased. The number in each label refers to the original diamond particle size. Materials A, B and C contained 8.5, 7.5 and 6.5 % binder phase respectively. It is unclear whether this is volume or weight percentage. From McNamara *et al.*[44]

.

across the whole range. A more carefully controlled investigation into the effect the binder has on fracture toughness is therefore required.

2.1.1.4 Flaw Size Distribution

A piece of information conspicuous by its absence from the literature on PCD is the flaw size distribution. Despite being briefly discussed by Lammer and Petrovic *et al.* and being likely to help explain the trends seen in the strength data, no substantive effort to understand its influence has been published. One such technique that can probe the surface flaw size distribution in diamond is Hertzian indentation[47].

The first example of Hertzian indentation of diamond was by Howes and Tolansky[48] who were attempting to artificially induce the small, polygonal crack figures that Tolansky and Halperin[49] had seen on the octahedral faces of many natural diamonds. Lawn and Komatsu[50] then published a paper explaining that the mechanism behind the deformation that occurred when one of these so called

Author	Technique	Fracture Toughness (MPa $\sqrt{\text{m}}$)	Grain Size (µm)	Binder Content (wt%)
Petrovic *et al.*	SDC	3.4 ± 0.34	2	30
		4.4 ± 0.44	4	-
		2.3 ± 0.23	6	27
		4.5 ± 0.45	16	-
		5.0 ± 0.50	28	18
		6.0 ± 0.60	29	18
		5.0 ± 0.50	30	18
		5.8 ± 0.58	45	-
		5.6 ± 0.56	46	-
		6.4 ± 0.64	76	-
		6.0 ± 0.60	120	-
McNamara *et al.*	3PB	9.55	10	8.5
		9.53	10	7.5
		8.52	10	6.5
Lin, Cooper & Hood	DT	14.28 ± 0.20	30	-
		13.13 ± 0.57	10	-
		13.43 ± 0.66	20	-
		13.03	-	-
		13.12	-	-
Morrell *et al.*	3PB	8.8 ± 0.75	-	-
Lammer	SDC	6.86 ± 0.43	2	13
		8.81 ± 0.46	12	11
		8.89 ± 0.37	30	11
		7.49 ± 0.78	125	12
Devin *et al.*	SDC	5	-	-
		6	-	-

Table 2.3: Fracture toughness data for various grades of PCD collated from numerous authors. The following terminology is used for the technique column: SDC - slotted diametral compression, 3PB - 3 point bending, DT - double torsion. The error shown in the strength column is the standard deviation in the results.

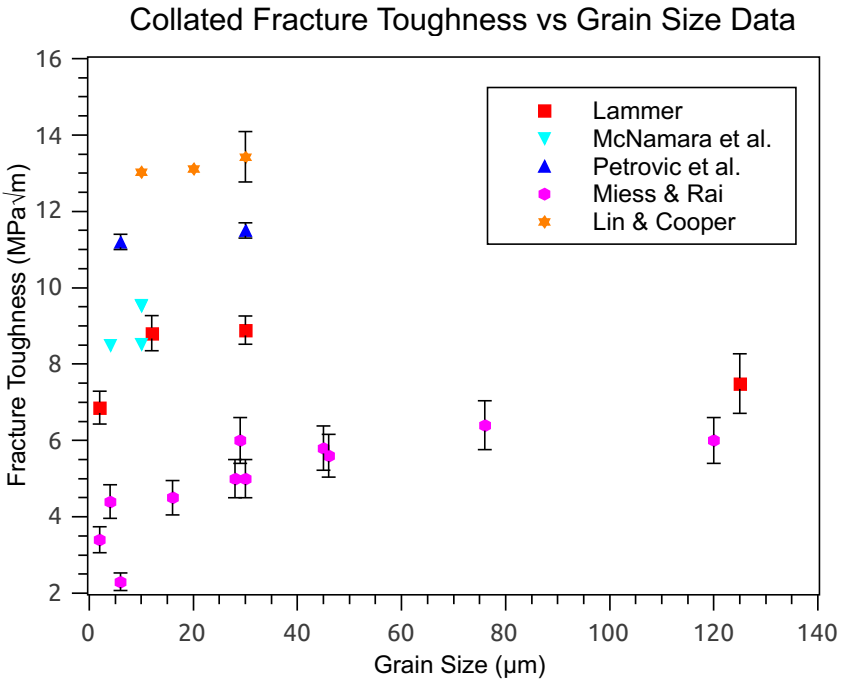

Figure 2.9: Collated data on the variation of fracture toughness with grain size. Although no overall trend can be seen, within each study, a similar trend of initial increase followed by a plateau appears to exist.

'pressure cracks' was formed was completely elastic in nature. Field and Freeman[51] later used Hertzian indentation to measure the fracture toughness of single crystal diamond. By plotting the square of the applied load vs the cube of the cone crack base-radius, something that is considerably easier to measure in transparent materials, the gradient can be used to calculate the fracture energy[52] and hence the fracture toughness. This was calculated as 3.4 MPa $\sqrt{\text{m}}$.

Marro *et al.*[33] performed Hertzian indentation experiments on various grades of polycrystalline diamond under both monotonic and cyclic loading conditions. Although the technique of acoustic emission is reasonably well documented in the literature on Hertzian indentation, it was not used to detect fracture in this study. The authors instead loaded samples of PCD with a spherical indenter up to predetermined loads and then examined them in an optical microscope to determine whether or not fracture had occurred. Although the data they collected was distinctly qualitative in nature, they did find that a fine grained microstructure was more resistant to the initiation of a ring crack as compared

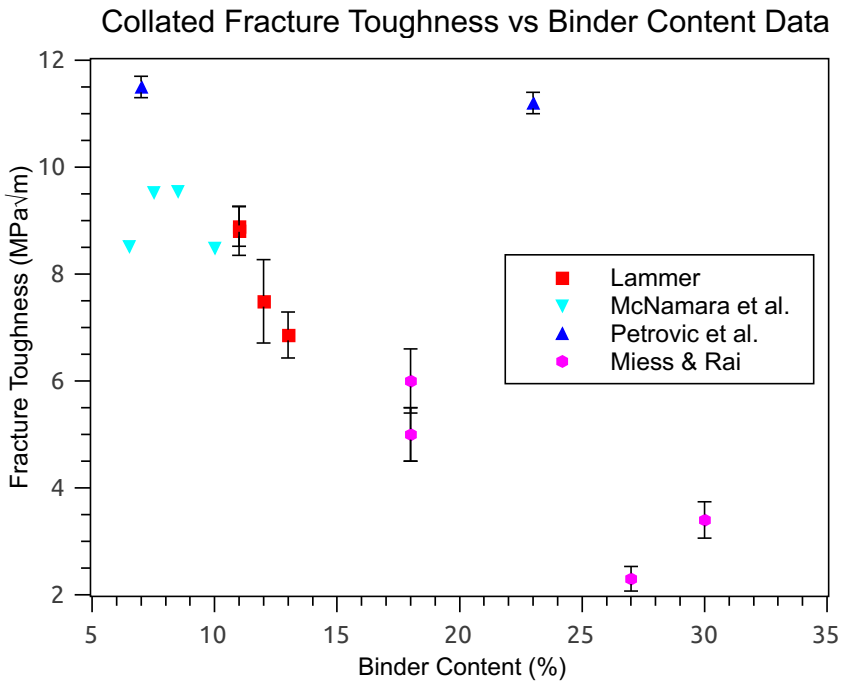

Figure 2.10: Collated data on the variation of fracture toughness with binder content for various studies. Barring a single anomalous point, a reasonably strong negative correlation appears to exist. However, a common trend is not apparent across all of the data sets resulting in data points grouped by study.

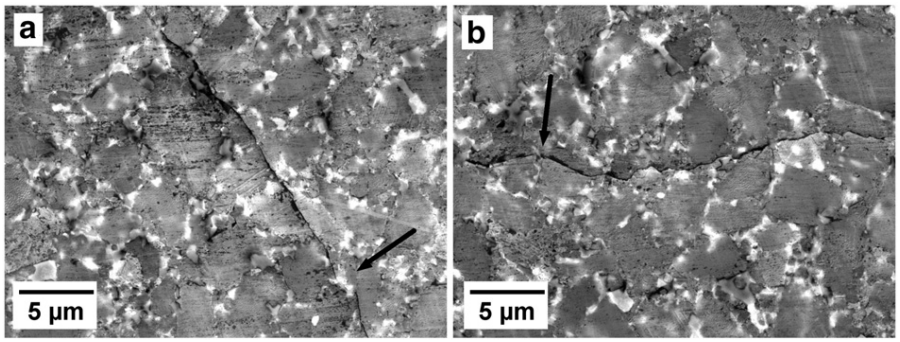

Figure 2.11: Backscattered electron images of a transgranular crack path in finer grained PCD. The arrows show where the author has deemed the binder phase to be showing local toughening by means of a reduced crack opening displacement. From Marro *et al.*[33]

to coarse grained specimens. The authors present micrographs that show local toughening by means of a reduced crack-opening displacement as the crack passes through a binder pool (Figure 2.11). Figure 2.12 shows SEM images of crack paths in a coarser grained microstructure. The crack bifurcates as it passes through a large diamond grain. From the information given and the background literature, it is unclear why this might happen.

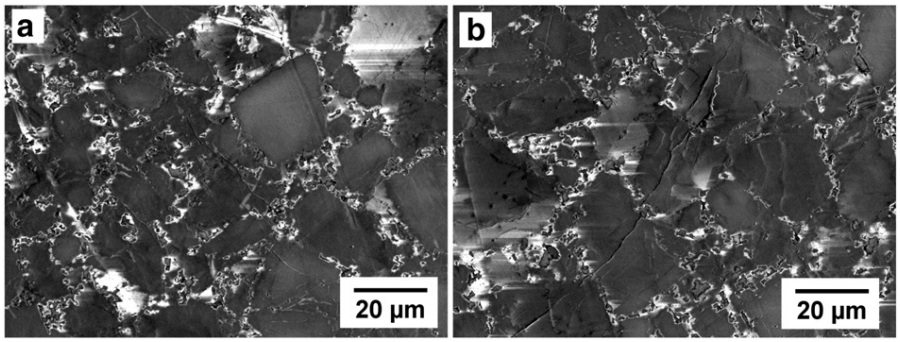

Figure 2.12: Backscattered electron image of a transgranular crack path through a coarse grained PCD material. The crack exhibits bifurcation as it passes through particularly large grains. From Marro *et al.*[33]

The second paper on this topic published by Marro *et al.* deals with the damage tolerance of PCD materials after indentation by measuring the residual strength by means of ball-on-three-ball flexure[38]. This is a very relevant topic for PCD research as one can imagine Hertzian-like fractures being caused by loaded contact with rock asperities during drilling which could then lead to catastrophic failure of the cutter. The authors found that all materials retained their strength with indentations of up to 400 N, likely due to no ring crack or damage of any form being evident at this load. At 1000 N, the fine grained material experiences a drop in strength of around 65% to a strength below that of the coarse grained material (Figure 2.13).

A simple explanation for this effect can be made by comparing the size of the flaw created by the induced Hertzian ring crack to the initial flaw-size distribution for the different grain size PCD materials. If the flaws do scale proportionally with the grain size as suggested by Petrovic *et al.*[35] then the lower initial strength of the coarse grained material can be explained by larger initial flaws. After Hertzian indentation, if the ring crack produced a flaw much larger than the grain size of the fine grained material but of a similar size to coarse grained material, the fine grained material would experience a large drop in strength whereas the coarse grained material would not. Essentially, the coarse grained material is less sensitive to the introduction of large flaws because its inherent average flaw size is already quite large. However, without a measure of the initial flaw size distribution, it is difficult to tell if this explanation is correct.

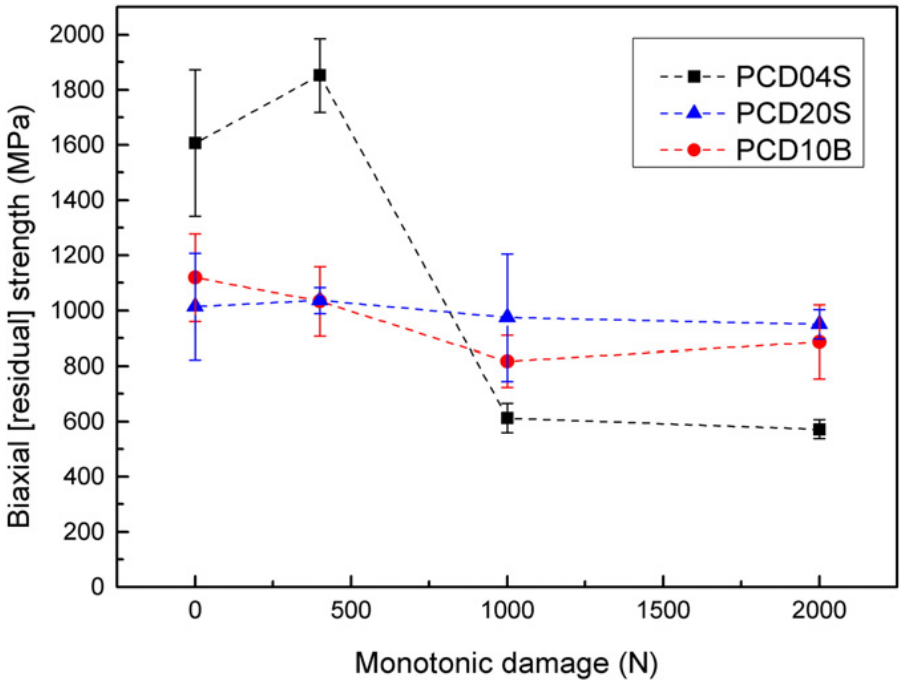

Figure 2.13: Graph showing the residual strength of various grades of PCD after varying Hertzian indentation loads were applied. The number in each label refers to the starting diamond particle size and the terminating letter denotes the modality: S - single mode, B - bimodal. The strength of PCD20S and 10B remain roughly constant regardless of the Hertzian load applied but PCD04S experiences a large drop in strength above 1000 N. From Marro *et al.*[38]

2.1.2 Wear Testing

The vast majority of the applications of PCD involve wear between two bodies; drilling of rock, machining of metal, wood and composites being the most common. In light of this, an understanding of how PCD behaves when it is subjected to wear is highly important if we are to improve its wear resistance.

2.1.2.1 Drilling of Rock

Hibbs and Lee conducted a study into the wear mechanisms that operate when PCD is used in a rock removal process[53]. They used very coarse grained PCD, approximately 100 µm grain size, to cut a helical groove in a mortar rock cylinder containing hard particles of quartz. Figure 2.14 shows the two distinct wear morphologies that they found on the surface of the PCD after testing. The authors put forward an interesting hypothesis explaining the two differing morphologies.

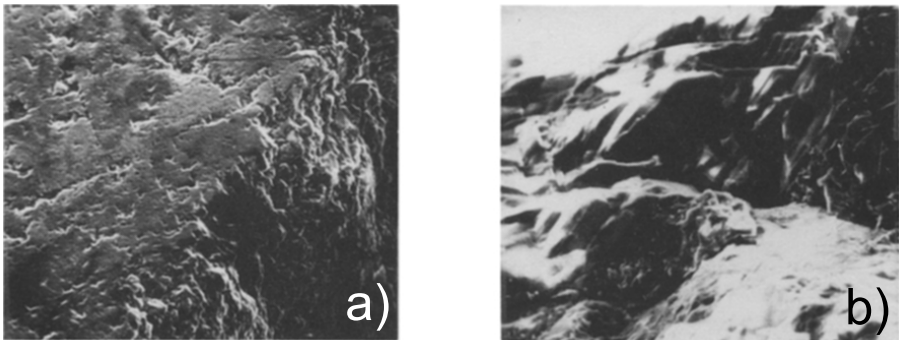

Figure 2.14: Wear morphologies seen after rock drilling by Hibbs and Lee[53]. Panel a) shows sub-grain chipping and panel b) shows transgranular fracture of multiple grains.

During sintering, the diamond grains undergo a large amount of plastic deformation due to the effect of high pressure combined with high temperature. It is suggested that this plastic deformation prevents easy cleavage of grains due to the disruption it causes to the lattice resulting in the chipping of small pieces of diamond from grains as seen in Figure 2.14a. However, some grains may not be plastically deformed to the same degree by the chance arrangement of grains around them causing a bridging effect and preventing them from experiencing the same high stresses. These grains then retain their easy cleavage planes and can fracture transgranularly as seen in Figure 2.14b. As there have been no studies on the effect of plastically deforming diamond on its fracture behaviour to the author's knowledge, this remains an interesting hypothesis to test.

Another significant conclusion from their work is with regards to the wear resistance of the grain boundaries. The authors found that grains contained heavy scratch damage in the grinding direction. Cobalt pools had been preferentially removed from the surface layer but grain boundaries neither preferentially fractured even when they were very close to the active cutting edge (Figure 2.15a) nor were preferentially abraded even when they were parallel to the cutting direction (Figure 2.15b). This gives further evidence that the grain boundaries do not represent a significantly weaker link as part of the PCD microstructure even if the cobalt pools along them are removed, contrary to what many authors have suggested. When a large area *was* found to have broken away, a particularly large grain or evidence

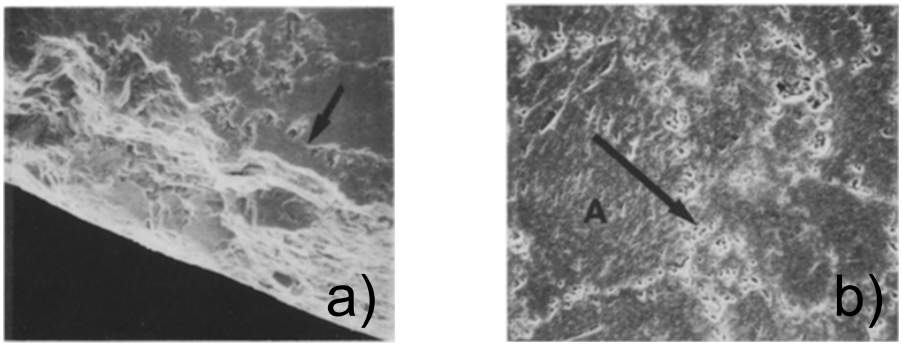

Figure 2.15: Resistance of grain boundaries to fracture and abrasion after rock drilling shown by Hibbs and Lee[53]. Panel a) shows that a grain boundary has not preferentially fractured despite being close to the cutting edge and panel b) shows that there is no preferential abrasion of a grain boundary parallel to the cutting direction.

of poor intergranular bonding was often found showing that inhomogeneities in the sintering of PCD may act as critical flaws for fracture.

Lin *et al.*[54] identified three mechanisms of wear in a detailed study of cutters damaged in both laboratory rock-cutting tests and field operations. 'Smooth wear' occurred where diamond grains appear to have peen polished to a flat surface with no significant fracture occurring. This type of wear was predominantly seen in cutting through strong, abrasive, homogeneous rock where the drill head had a large number of bits distributed over its surface. Grooves oriented in the direction of cutting were also observed similar to those shown in other work[55][56]. The rock being cut contained hard quartz particles but given the considerably higher hardness of diamond even to a very high temperature[57][58], these grooves could not have been caused in a typical abrasive manner. The authors suggested that a combination of thermal and mechanical load on the diamond must have allowed either oxidation or graphitisation to occur causing these grooves to form.

The second wear morphology was labeled 'microchipping'; although it may sound similar to one of the morphologies shown in Hibbs and Lee's work, it can be seen by looking at Figure 2.16 that it is in fact quite different. This wear mechanism is characterised by small flakes of material chipping off where the plane of fracture is roughly parallel to the direction of cutting. The mechanism only appeared when cutting rock with a higher uniaxial compressive strength but low

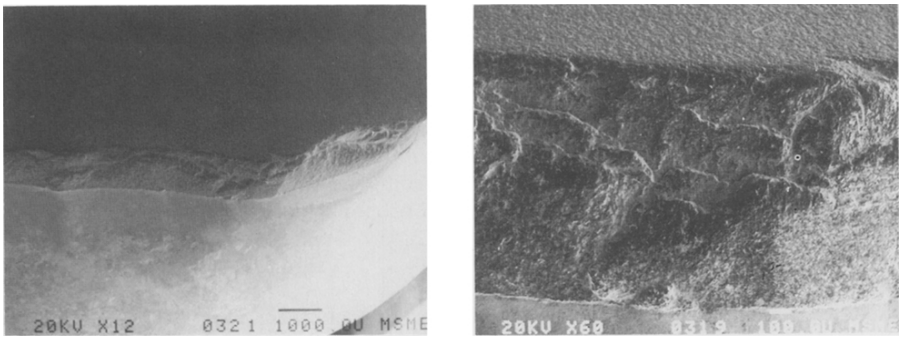

Figure 2.16: Micrographs of the wear morphology labeled 'microchipping' by Lin *et al.*[54].

abrasiveness and after varying the cutting depth a number of times. The authors therefore concluded that this morphology was caused by some thermal or mechanical fatigue mechanism, citing work by Dunn and Lee who showed that the fracture stress of PCD cutters was significantly lowered by cyclic loading[59]. They noted that a higher negative rake angle (associated with higher forces in the direction of the cut) resulted in worse damage by microchipping. The mechanism proposed is that the cracks develop from tensile failure of the top face of the cutter. With a higher negative rake angle (the axis of symmetry of the cutter moving further away from parallel with the direction of cut) there is less material able to support the cutting edge and so larger tensile stresses are present on the cracks that develop here leading to increased microchipping.

The final morphology seen was that of gross fracturing. This involved large chunks of the cutter being removed instantaneously and represents the most problematic wear/fracture mechanism for drilling operations. Gross fractures were found to initiate on the curved surface of the PCD cutter rather than on the top face. Given that this type of fracture often occurred slightly after a change in rock formation during drilling[60], the authors suggested that it was as a result of mechanical overloading. To test this hypothesis, they loaded cutters against a steel plattern in a similar geometry to that of rock cutting. They found that this loading condition caused fractures very similar to the 'gross fractures' seen in operationally-used cutters and that by using a harder steel plattern (causing an increased stress at the cutter's edge), gross fracturing occurred at lower loads.

Yahiaoui *et al.*[61] performed a study comparing the wear resistance of fine (6 ± 1 µm) and coarse (17 ± 4 µm) grained PCD sintered using two HPHT regimes. A standard regime (HPHT1) and one with a higher pressure but shorter dwell time. In the introduction, the author states that it is "well known by the manufacturers [that] PDC cutters with a fine grain distribution are more resistant to abrasion than cutters with coarse grains" citing a review paper on the current state of PDC bit technology[15]. However, the results of the study did not agree as it was found that the coarse grained PCD was more wear resistant than fine grained. The authors did not look for a mechanistic difference in the wear behaviour and suggested that other microstructural parameters might be more important to the wear behaviour than simply average grain size.

In a study of microstructural characterisation of the thermal degradation of PCD after milling of granite, Westraadt *et al.*[62] found that volume expansion due to graphitisation was a major contributor to failure of the cutter. This finding contradicts much of the industrial wisdom that it is the thermal expansion of the cobalt that causes thermally induced cracking. They found through comparison with static annealing experiments that the temperatures generated at the cutting interface must have exceeded 800 °C which is sufficient to cause the cobalt-catalysed conversion of diamond to graphite. Another interesting finding of their work is that much of the cracking they observed was intergranular. This suggests that there may be a different fracture mechanism activated when PCD is used for drilling applications compared to pseudo-static mechanical tests at room temperature. If cobalt along the grain boundaries is causing conversion of diamond to graphite at high temperature resulting in it expanding, it seems logical that the material would fracture along these grain boundaries rather than transgranularly as is seen at low temperature.

2.1.2.2 Machining of Titanium

A growth area for PCD is in the machining of high strength titanium alloys that are particularly difficult to machine with traditional carbide and high strength steel tooling. Turning tests of five different grain sizes on a billet of titanium

found that the tool life increased as grain size increased from 1.3 to 14 µm[63]. Although, the largest grain size of 39 µm performed the worst by far, experiencing grain-pullout and "sub-grain transgranular fracture".

A study was conducted to measure the effect of cutting speed on the wear behaviour of PCD when used to turn Ti-6Al-4V titanium alloy[64]. It was found that the predominant wear mechanism depended on the cutting speed used. At the lower cutting speed, the wear mechanism was described as attritional with a rough, discontinuous wear surface and a complete lack of adhered material to the tool. At the higher cutting speed, a smooth wear surface was found characteristic of diffusive/dissolutional wear. The presence of adhered material on the cutter would seem to support this. Finite element modeling (FEM) simulations were used to calculate the expected temperatures at the cutting interface, the results of which predicted a temperature of 897 °C for the lower cutting speed and 991 °C for the higher. The authors point out that a temperature difference of only 100 °C is not enough to explain a difference in diffusivity so large that it would cause the completely different wear mechanisms seen between the two cutting speeds. It was therefore suggested that a temperature induced phase change in the chip material caused the diffusivity of tool elements into the titanium to increase by orders of magnitude. This hypothesis appears to be backed up by the alloy's phase diagram (taking pressure into account). A secondary argument is that the HCP α phase of titanium contains only six facile slip systems whereas the BCC β phase has twelve. This means that at the lower cutting speed where the chip material is predicted to be of the α phase, the chip will not plastically deform as easily, increasing the stress on the cutting edge and causing it to fracture more frequently.

2.1.2.3 Machining of Wood Composites

Bai *et al.*[65] performed tests involving the machining of laminate wood composites using four different PCD grain sizes (2, 10, 25 and 75 µm diamond powder particle size). Microcracks were observed in the 10 µm grain size material (Figure 2.17). It was suggested that it is the formation of these microcracks that are responsible

for the "rupture and disintegration of the PCD tool". The authors also suggest that these microcracks can propagate along grain boundaries. It may be that this occurs in larger grained microstructures, being responsible for the often mentioned "grain pullout" but it has been shown on numerous occurrences that the grain boundaries do not act as a preferential path for failure so this statement seems unlikely without any evidence provided to support it. An interesting claim is made that the "inherent cleavage cracks generated in HTHP synthesis also contribute to the formation of cleavage wear", however, as the paper cited against this claim is in Chinese[66], further investigation has proven difficult. The final conclusion of this paper is that middle sized diamond grains (10 µm) have the highest wear resistance over both large and small grain sizes, further highlighting the error in what is "known by all manufacturers".

Philbin and Gordon[11] analysed the wear mechanisms that operated when cutting two different types of wood composite with PCD. They found that when cutting a more homogeneous material, abrasive wear was dominant with voids where individual grains had been pulled out were seen. When a material with a protective, hard layer was cut, multi-grain chips were observed at the cutting edge instead. A summary of all of the wear mechanisms described herein is given in schematic form in Figure 2.18.

2.1.3 Summary

The literature on the ambient-condition mechanical properties of PCD was found to often come to conclusions that were at odds with the actual results reported. The most pervasive conclusion being that grain boundaries act as weak paths for fracture despite evidence to the contrary. This claim will therefore be directly tested in an attempt to provide clarity on the issue. Several problems with the conclusions of an important and often-referenced paper were found and so an attempt will be made to re-examine these conclusions. Lastly, studies that tested PCD under conditions that involved heating reported a change from the almost exclusively transgranular fracture reported at room temperature to intergranular fracture and

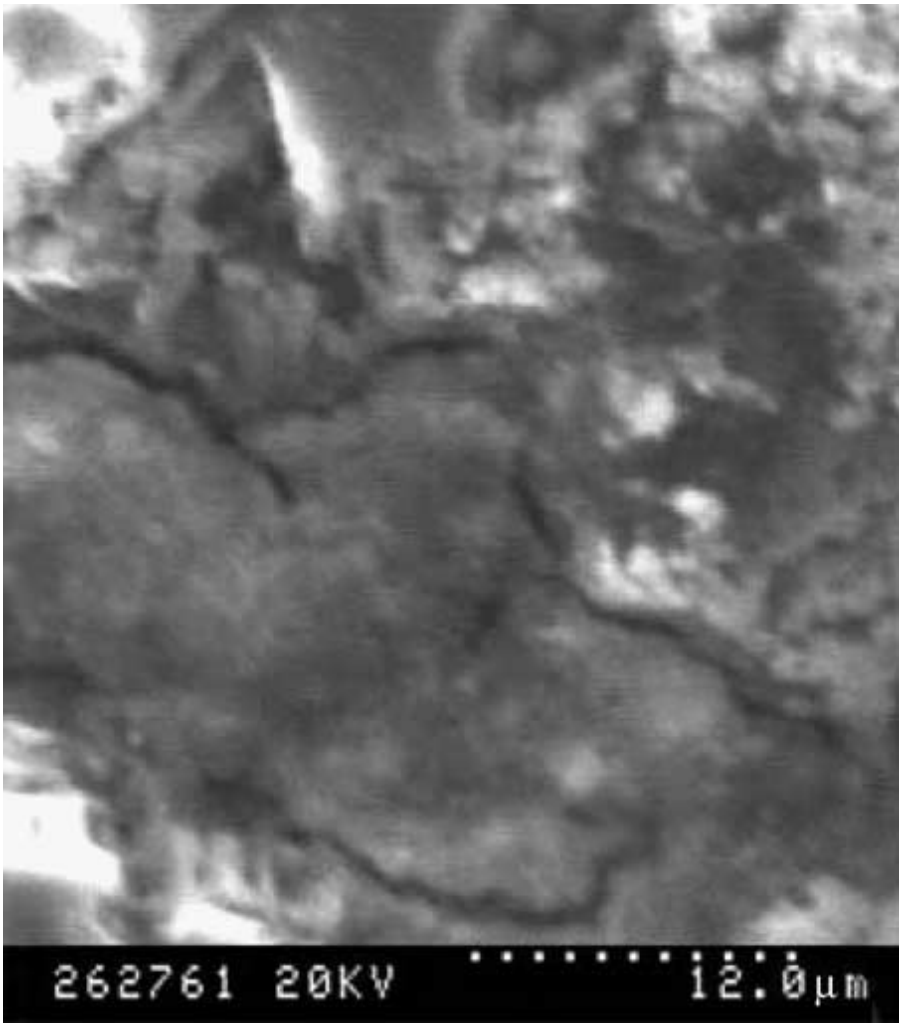

Figure 2.17: Microcracks observed in 10 µm grain size PCD after machining of a laminate composite by Bai *et al.*[65]

whole-grain pull-out at high temperature. It is suspected that this behaviour is due to graphitisation of diamond and so the impact of this phenomenon on the mechanical properties of PCD will also be tested.

2.2 Residual Stresses

PCD consists of a connected network of sintered diamond grains with the spaces in between occupied by a tungsten and carbon-rich cobalt alloy. Additional tungsten carbide precipitates do exist but are not suggested to contribute to the microscopic residual stresses.

Much of the literature focuses on the macroscopic residual stresses present in

[h!]

Sub-grain microchipping **a**
- Hibbs and Lee

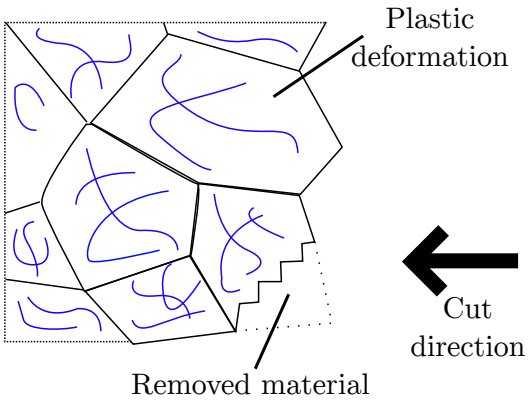

Whole-grain fracturing **b**
- Hibbs and Lee

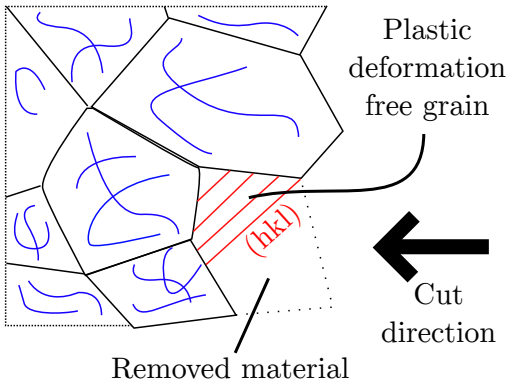

Smooth wear **c**
- Lin *et al.*

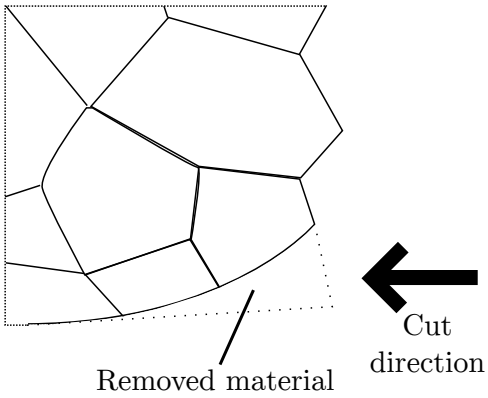

Microchipping **d**
- Lin *et al.*

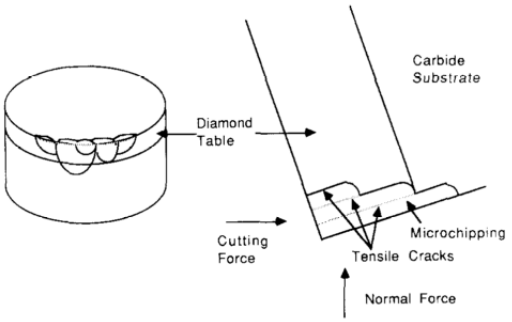

Gross fracturing **e**
- Lin *et al.*

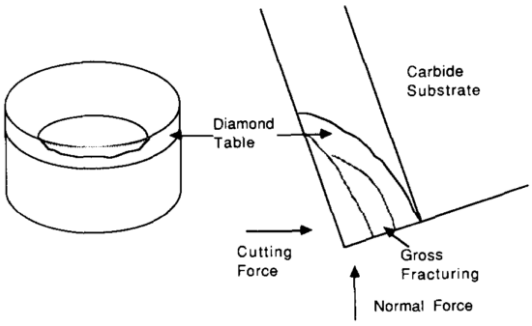

Grain pullout **f**
- Pretorius

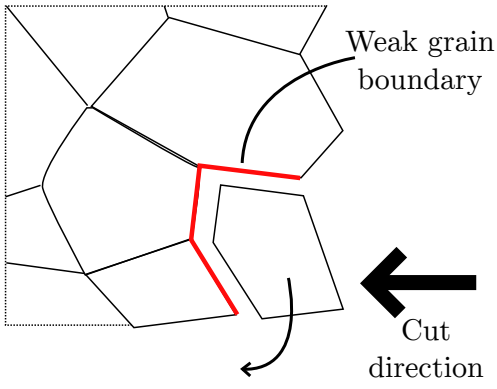

polycrystalline diamond cutters because in service, the PCD layer is connected to a thick tungsten carbide-cobalt cermet substrate. As the WC/Co substrate has a higher thermal expansion coefficient than the diamond, as it cools down from the high temperature at which sintering occurs, it contracts more than the diamond layer thereby putting it into compression. Using a combination of finite difference code modelling and measurement of surface strain with a strain gauge as the carbide backing was progressively ground away, Lin *et al.*[67] found that as expected, a compressive stress is present in the diamond layer with an average of 1.4 GPa (compared to the compressive rupture strength (CRS) of diamond of 1.9–6.9 GPa[26]) and a tensile stress in the carbide layer of 500 MPa (CRS of 1–3 GPa). Increasing the carbide thickness increases the magnitude of these stresses but counter-intuitively, reducing the thickness below 1.5 times the diamond layer thickness reverses the magnitude of the stress on the top face of the diamond layer before dropping to zero as all of the carbide is removed. Increasing the carbide thickness also increases the magnitude of the shear stress at the diamond-carbide interface which can be very detrimental to the integrity of the cutter due to the increased likelihood of delamination of the two layers. These conclusions are confirmed and the values of residual stresses updated by neutron diffraction measurements made by Krawitz *et al.* in a later study [68]. In both cases, the authors assumed that all stresses above 1000°C would be alleviated due to plastic deformation with Krawitz *et al.* suggesting that this effect may extend to lower temperatures to explain their lower measured residual stress values. Where the plastic deformation was expected to occur was not specified. Gasc *et al.*[69] measured a flow stress of 6 GPa and 8 GPa for the (111) and (220) directions in diamond respectively at 1000°C[69], showing

Figure 2.18 *(preceding page)*: Schematic representation of all of the wear mechanisms of PCD described above. a) subgrain microchipping due to plastic deformation blocking easy cleavage planes[53], b) bridging of individual grains prevents plastic deformation allowing single grains to fracture along easy cleavage planes[53], smooth wear caused by dissolution of carbon into the work piece and/or chemical attack[54], d) Microchipping caused by tensile cracks opening up on the PCD table[54] (figure taken from reference) e) gross fracturing caused by excessive normal force on the cutter[54] (figure taken from reference), f) pullout of an entire grain caused by a weakening of the grain boundary[63].

that plastic relaxation is unlikely to occur in the diamond phase. It would be much more likely in the substrate due to its lower yield stress which could reduce the macroscopic (but not microscopic) residual stresses. There are a large number of studies using a variety of techniques such as Raman peak position analysis, diffraction techniques and modelling to spatially map the macroscopic residual stresses in the diamond layer (Table 2.4) [32, 70–73]. The large range of values seen in the data show that the exact value of the residual stress measured varies from author to author but common themes are as follows:

- There is a large compressive, radial stress on the surface of the PCD table.
- Models predict a 200-300 MPa tensile, radial stress near the outer edge of the surface of the PCD table but this is difficult to measure experimentally.
- The interface between PCD and WC/Co is under a shear stress which is damaging to the cutter's longevity.
- A reasonably large axial, tensile stress may exist near the edge of the PCD table which promotes highly damaging spallation during service.

All of the data in Table 2.4 refer to cutters with flat interfaces. A number of studies[72, 76] have examined how these stresses can be reduced through changing the shape of the interface. Although this information is valuable to solving the engineering challenges involved in PCD cutter design, few studies concentrate on understanding the microscopic residual stresses. Much of the literature mentions that the thermal expansion coefficient of cobalt is greater than that of diamond and explain that this will cause large stresses in the diamond due to differential expansion under heating. None qualify this claim but the most likely initiation of the idea is a technical report by Ortega *et al.* that cites earlier unpublished work by Hibbs. The report states:

> It was noted that polycrystalline sintered diamond compacts are subject to gross thermal damage if heated above approximately 750 °C due to the stress generated by the difference in thermal expansion between the diamond and trapped islands of residual metal inclusions along diamond

ID	Radial	Hoop	Axial	Shear	Biaxial	Hydrostatic	Interface Shear
1	-1200	-	690	-421	-	-	383
2	*	-	*	*	-	-	*
3	-	-	-	-	-600†	-	-
4	-	-	-	-	-1300†	-	-
5	-	-	-	-	-	-220†	-
6	-	-	-	-	-	-250†	-
7	-350	-470	-	-	-462	-	700
8	-1250	-1250	0	-	-	-	300
9	180	-	840	671	-	-	-
10	260	-	-	-	-	-	-
11	-	-	-	-	-1250†	-	-

ID	Author	Measurement Technique
1	Chen *et al.*[71]	Finite Element Analysis
2	Yahiaoui *et al.*[72]	Finite Element Analysis
3	Erasmus *et al.*[73]	Raman Microscopy
4	Catledge *et al.*[32]	Raman Microscopy
5	Jia *et al.*[70]	Raman Microscopy
6	Jia *et al.*[74]	Raman Microscopy
7	Krawitz *et al.*[68]	Neutron Diffraction
8	Lin *et al.*[67]	Finite Difference Analysis
9	Cao *et al.*[75]	Finite Element Analysis
10	Bertagnolli and Vale[76]	Finite Element Analysis
11	McNamara *et al.*[77]	Raman Microscopy

Table 2.4: Literature values of various components of absolute residual stress in the diamond layer of a PCD cutter. All values are in megapascals with negative denoting compressive stress. - represents components not measured, * values measured but not clearly reported and † values measured at the surface only. The authors and measurement techniques are shown in the lower table.

> grain boundaries. Boundary failure can occur under these conditions, resulting in whole grain pullout. Gross thermal damage of this type has been observed under conditions of dry cutting, where frictional temperatures were estimated to be on the order of 750 °C[78]. (Ortega *et al.*[79])

In a later paper by Sneddon and Hall[80] citing this work, a distinction is made between this "thermo-physical failure" occurring above 730 °C and leading to "severe intergranular cracking, macrochipping, and rapid failure of the PDC cutter" and "thermo-chemical failure" above 875 °C due to "rapid graphitisation

in the presence of oxygen".

2.2.1 Summary

The topic of macroscopic residual stresses is one that is discussed at length in the literature but with large amounts of scatter in the reported values. Although this issue is undoubtedly important, it is one that can be quantified and potentially solved through finite element modelling and engineering solutions such as modification of the design of the substrate-diamond interface. However, these solutions will not be able to take account of microscopic residual stresses that may or may not arise due to differences in thermal expansion between the diamond and the cobalt binder which are microstructurally intermixed. This difference in thermal expansion coefficient is often used as an explanation for the thermal breakdown of PCD but no evidence for or quantification of its effect is gievn. Furthermore, there is suggestion that graphitisation is actually the process which has the greatest effect on this thermal breakdown. The thermal residual stresses will therefore be analysed to determine if they have a significant impact on the mechanical properties of PCD at high temperature.

2.3 Graphitisation of Diamond

2.3.1 Cutter Temperature

In most real applications of polycrystalline diamond, frictional heating between the tool and work piece (usually rock) cause the PCD to become heated to considerable temperatures. Lathe-turning of concrete tests with PCD suggest bulk cutter temperatures can reach 300–500 °C[81], however, cutter tip temperatures likely exceed this due to the large carbide backing acting as a heat sink and spreader. Reports from mining research suggest that during drilling operations, tool temperatures can reach 1000 °C[39]. In turning tests where a thermocouple was placed 1.27 mm from the cutting face, temperatures of 700°C[82] were measured. However, although single crystal diamond has a very high thermal conductivity of around 2000 $\mathrm{W\,m^{-1}\,K^{-1}}$[83], the polycrystalline nature and inclusion of a second

phase in PCD significantly reduces this[79] meaning that there will be a thermal gradient over a distance of 1.27 mm and so even this is likely an underestimate of the cutting interface temperature.

2.3.2 Thermal Degradation of PCD

Yahiaoui *et al.*[61] tested PCD cutters in a vertical lathe grinding test with manufactured mortar rock counterfaces (designed to be highly abrasive). Using Raman microscopy, they detected graphite on the wear flat generated on a cutter after approximately 79 minutes (based on a sliding distance of 8500 m and a sliding speed of $1.8\,\mathrm{m\,s^{-1}}$). XRD analysis was also performed but graphite was not detected, possibly due to additional peaks from the rock material that was transferred to the PCD cutter obscuring the diffractogram. Although graphitisation is identified as a potential wear mechanism, the dependence of wear on interface geometry and processing conditions is the main focus of this paper, rather than extent of graphitisation.

Liu *et al.* measured the mass and volume wear ratios (mass/volume of work piece removed to mass/volume PCD removed) of PCD samples with varying degrees of cobalt binder removed by electrolysis during turning of granite work pieces[25]. It was found that the greater the cobalt removal depth, the more resistant to wear the PCD was (figure 2.19). The authors attribute this behaviour to a number of factors including increased heating in the unleached material due to a greater friction coefficient between work piece and tool, a self-sharpening behaviour of leached tools and graphitisation of the diamond. XRD analysis found that graphite was present on the worn surface of the unleached tool but not on the leached. The authors note that whilst the force caused by differentially thermally expanding cobalt is not sufficient to fracture diamond-diamond bonds, it does cause metal to be extruded into the wear interface, further increasing the temperature due to increased friction. They then point to a study by Moseley *et al.*[81] which, whilst providing very sparse data due to commercial secrecy, suggested that a transition from intra-granular brittle fracture to whole grain pullout at high temperature occurs.

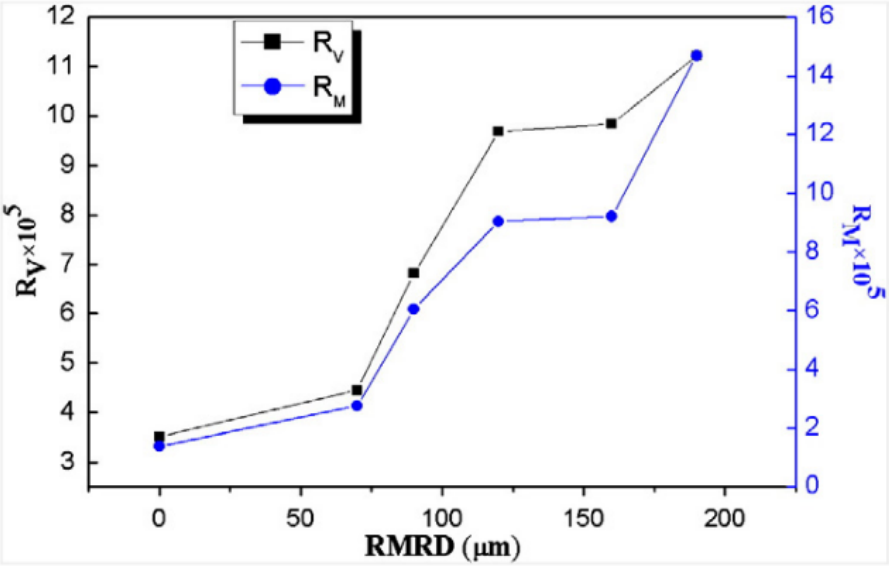

Figure 2.19: Graph showing that the amount of work piece material per unit of PCD removed increases strongly as a greater depth of cobalt is removed from the PCD.

Miess and Rai heated PCD specimens of varying grain sizes in nitrogen, hydrogen and air atmospheres at temperatures of 600, 700, 750 and 800 °C. Above 700 °C, large "stress relief cracks" are seen in the microstructure (figure 2.20) which the authors attribute to relief of the thermal expansion mismatch stress between diamond and cobalt[39]. This is an explanation that is often used in the literature to explain this thermal degradation despite not having any evidence to support it and so this topic will be covered in a later section.

Mehan and Hibbs[22] measured the occurrence of acoustic events when sintered diamond compacts were heated to temperatures in the range 700-900°C. They found that the onset of these events had an incubation period that followed an Arrhenius-type behaviour with temperature and calculated an activation energy for the process of 327 kJ mol^{-1} (Figure 2.21). The same behaviour was observed in both unleached and leached samples; the differences being that the total number of acoustic events was lower by an order of magnitude and no degradation in wear properties was apparent for leached materials. The following mechanism is offered to explain this behaviour:

> [In] both [(leached and unleached)] cases graphitization begins at about the same time, but for the unleached material, cobalt (as well as

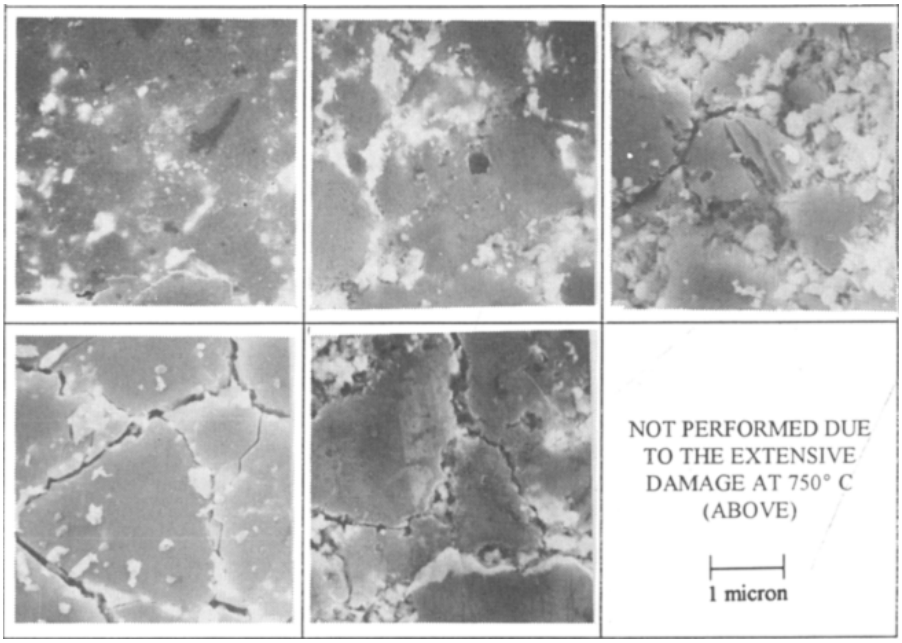

Figure 2.20: So called "stress relief cracking" in large grained (30 µm PCD in hydrogen, nitrogen and air atmospheres (from left to right) at temperatures of 750 and 800 °C (top to bottom)[39].

> the diamond-to-graphite volume change) was available to expand and fracture the weakened diamond network. For the leached case, fewer nucleation sites were present (some metallic elements were not removed in spite of acid leaching) and there was only the diamond-to-graphite volume change to disrupt the diamond structure. (Mehan and Hibbs[22])

The authors then go on to note that Voronov *et al.* [84] put forward that graphitisation was the major contributor to this mechanical breakdown but do not directly explain the suspected mechanism behind their observations.

Work was carried out by Westraadt *et al.*[62] looking into the damage mechanisms that operate when PCD is thermally soaked at temperatures above 500°C in argon. Their experiment used ex-situ X-ray diffraction and TEM microscopy to monitor graphite formation at different temperatures for varying amounts of time. They detected graphite using electron energy loss spectroscopy (EELS) in samples heated to 800°C for 30 minutes despite it not appearing in the X-ray diffraction patterns. The cobalt lattice parameter was also found to decrease with both time and temperature. The TEM analysis also showed the presence of a secondary η-phase

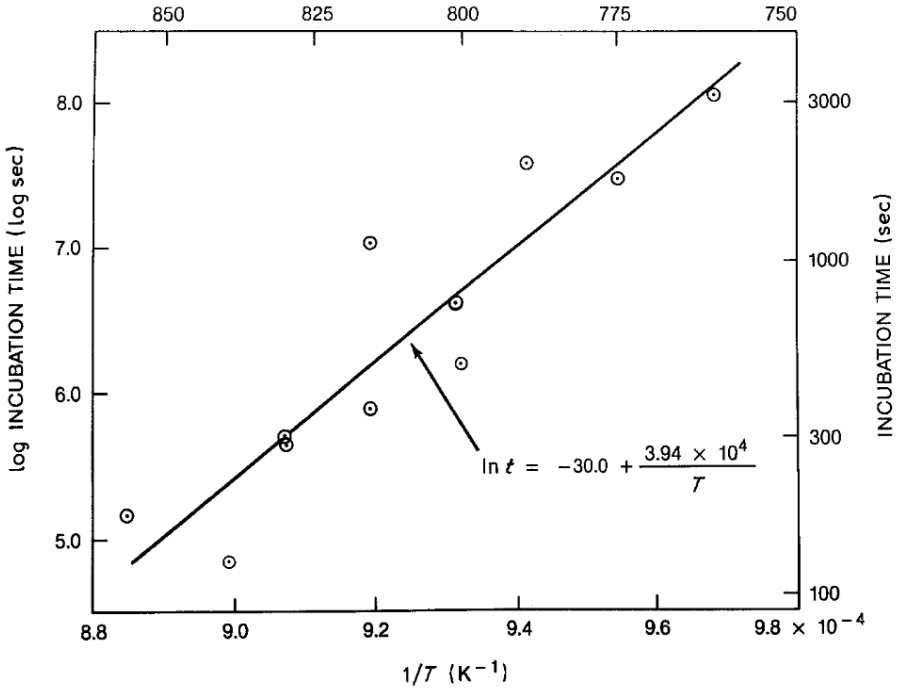

Figure 2.21: Incubation time of graphite formation against the inverse of temperature[22].

carbide identified as $(Co,W)_6C$. Due to the extensive cracking throughout mechanical wear specimens and the presence of graphite in samples heated to 800°C and higher, the authors conclude that the main degradation mechanism is the volume expansion of the diamond to graphite transformation.

2.3.3 Graphitisation of Pure Diamond

Under very high temperatures, diamond has been shown to undergo an allotropic transformation to graphite without the presence of a catalyst. Heating of macroscopic grains of diamond powder in dry helium and subsequent X-ray diffraction analysis showed "superficial" graphitisation occuring at 1300 °C and up to 2 weight % at 1400 °C[85]. Evans and Sauter showed that octahedral faces of diamond graphitised when exposed to air at varying pressures up to atmospheric pressure in the temperature range 900–1400 °C[86]. The graphite formed a thin layer at the surface with a matt, porous appearance. The degree of etching and graphitisation increased with both gas pressure and temperature and by using reflected electron diffraction, the resultant graphite was found to have its c-axis parallel to the

diamond {111} surface. The presence of carbon dioxide also produced similar surface graphitisation.

Howes heated a number of diamond samples in high vacuum at temperatures up to 2000 °C[87]. Different morphologies of graphite were formed either side of 1700 °C. Below this temperature, graphite only formed at the surface of the diamond, was matt-black in appearance, was easy to remove with liquid etchants and did not propagate into the bulk. The orientation relationship was found to be identical to that of graphite formed by gas etching in the work of Evans and Sauter. Due to these similarities, it was determined that even in high vacuum, graphite formation below 1700 °C must be mediated by residual reactive gas species in the vacuum chamber. Above 1700 °C, well adhered graphite that was difficult to remove by liquid etching formed that given sufficient time, progressed into the bulk of the diamond until complete transformation of the diamond to graphite occurred. Using reflection electron diffraction, this graphite was shown to have both its c and a-axes lying within the plane of the {111} diamond surface. This type of graphite formed in characteristic 3-pronged 'propeller' shapes with each of their prongs lying along a ⟨112⟩ direction. Howes suggested that the mechanism for direct transformation of diamond to graphite involved the puckered hexagonal sheets seen within the {111} diamond planes shown in figure 2.22 flattening out to become graphite basal planes. This would then propagate in the ⟨112⟩ type directions as indicated by arrows in the figure. Although this mechanism explains the orientation relationship of the graphite that was observed to form above 1700 °C, the spacing of the newly formed graphite basal planes would be much smaller than the the large 3.35 Å spacing of {0002} graphite planes indicating that there would be significant strain in the resultant graphite.

Evans and James performed similar experiments on highly thinned diamond mackles prepared for TEM analysis and found a similar threshold for the morphology of graphite at 1700 °C [88]. They found that graphite formed above this temperature not only had the same orientation relationship to the diamond as found by Howes but also exhibited extensive, fine cracking; corroborating the large strain necessary

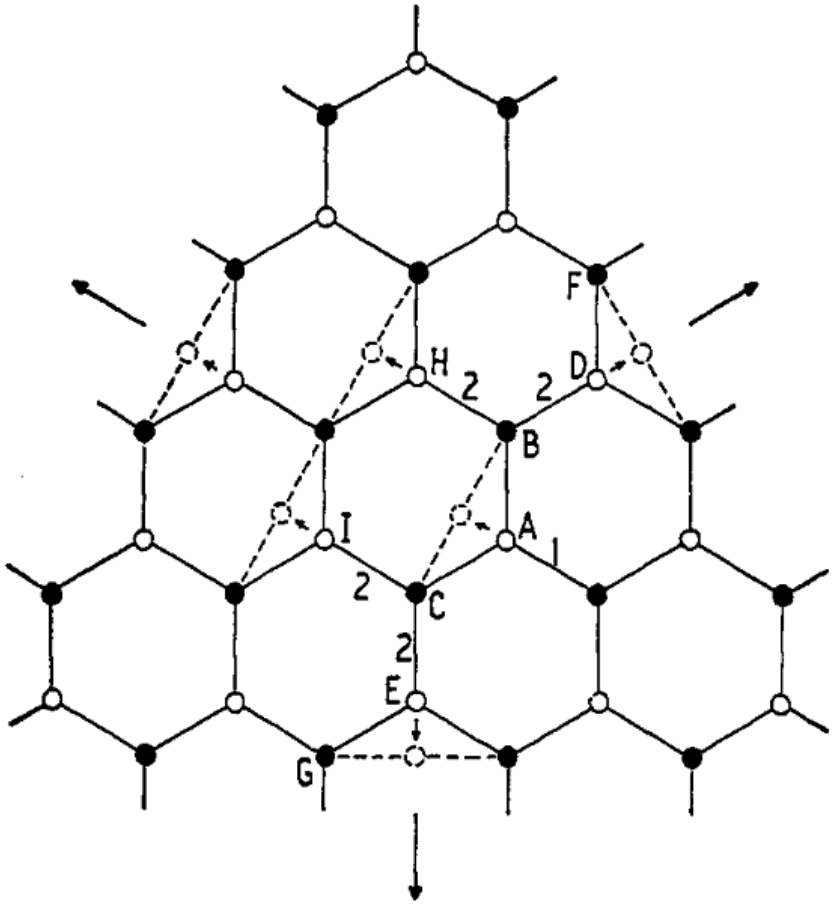

Figure 2.22: A diamond {111} surface is shown parallel to the page with puckered, hexagonal diamond rings. Filled circles indicate lower atoms with their fourth bond going into the page with open circles representing upper atoms with their fourth bond coming out of the page. It is supposed that a flat hexagon begins to form on atoms B and C with atom A breaking the bond labelled 1 and swinging up in the direction shown by the small arrow. If this process weakened the bonds labelled 2, it is suggested that two more flat hexagons could form by atoms D and H moving in the direction indicated by their small arrows. These flat hexagons are now basal planes of graphite that grow in directions marked by the three large peripheral arrows whose crystallographic directions are in the ⟨112⟩ family. Both the a and c-axes of the newly formed graphite being in the {111} plane of the diamond. From ref [87].

in the graphite formed by this mechanism. Both authors put forth that this reaction only begins at a site where there is free volume present due to the large expansion necessary when graphite transforms to diamond necessitating inclusions or free surfaces as nucleation sites.

Davies and Evans measured the rate of graphite formation at ambient and high (4.8 GPa) pressure[89]. By treating the reaction as an Arrhenius-type process, they calculated activation energies for the graphitisation of {111} and {110} surfaces as $(1159 \pm 75)\,\mathrm{kJ\,mol^{-1}}$ and $(728 \pm 50)\,\mathrm{kJ\,mol^{-1}}$ respectively. By finding pairs of temperatures that gave the same graphitisation rate at low pressure as at high pressure, they calculated an atomic activation volume of $0.0166\,\mathrm{nm^3}$ corresponding to a cube of side length 0.255 nm which they compare to the lattice parameter of diamond of 0.3567 nm. Although they do not claim to understand the exact activation volume calculated, they reason that this value is not consistent with previous suggestions that graphitisation occurs by detachment of several hundred diamond atoms at a time[90] and hence a single atom process is more likely. Furthermore, they compare the measured activation energies of the {111} surface ($(1159 \pm 75)\,\mathrm{kJ\,mol^{-1}}$) involving the breaking of 3 atomic bonds per surface atom, that of the {110} surface ($(728 \pm 50)\,\mathrm{kJ\,mol^{-1}}$) involving breaking 2 atomic bonds per surface atom with the vaporisation energy of diamond ($732\,\mathrm{kJ\,mol^{-1}}$) which also involves the breaking of 2 atomic bonds per surface atom. These three mechanisms have activation energies per bond of $(386 \pm 25)\,\mathrm{kJ\,mol^{-1}}$, $(364 \pm 25)\,\mathrm{kJ\,mol^{-1}}$ and $366\,\mathrm{kJ\,mol^{-1}}$ respectively, supporting the hypothesis that it is indeed a single atom process.

Pantea *et al.*[91] heated both synthetic and natural diamond crystals possessing {111} and {100} faces to temperatures in the range 1770–2400 K under pressures of 0.1 GPa, 1 GPa and 2 GPa. As the combinations of pressures and temperatures used were not wholly systematic, the data from which trends can be drawn are shown in table 2.5. As discussed previously, Howes[87] and, Evans and James[88] showed that two different morphologies of graphite formed above and below 1973 K(1700 °C),

Pressure (GPa)	Extent of graphitisation (low temperature[1])	Extent of graphitisation (high temperature[2])
0.1	Small amount near surface defects.	Large amount of disordered graphite; detectable in Raman and XRD.
1.0	None formed.	Some ordered graphite; only detectable with Raman
2.0	None formed.	Large amount of weakly adhered, ordered graphite; detectable with Raman and XRD.

Table 2.5: Summary of comparable results for the extent of graphitisation on {111} faces as a function of pressure and temperature from Pantea *et al.*[91]. Low and high temperature refers to temperatures either side of 1973 K, the threshold suggested by Howes[87] and Evans and James[88] between two different morphologies of graphite formation. Exact temperatures and heating times were as follows in order of ascending pressure: [1]1770 K, 20 min; 1800 K, 2 min; 1870 K, 2 min. [2]2200 K, 2 min; "slightly less than" 2200 K, 2 min; 2200 K, 2 min.

subsequently referred to as high-temperature and low-temperature graphite. The properties of these morphologies are summarised as:

Low-temperature graphite Typically small in quantity, weakly adhered, matt-black, having its c-axis perpendicular to the surface of {111} diamond surfaces.

High-temperature graphite Strongly adhered, having its c-axis lying in the plane of the {111} diamond surface and propagating along ⟨112⟩ directions (of which there are three in each {111} plane)

Pantea *et al.*[91] refer to "ordered/orientated" graphite as that which has its c-axis orientated perpendicular to the {111} surface as measured by XRD analysis and "disordered/disorientated" graphite as that which does not. The "orientated" graphite was also easily scraped off of the diamond surface and therefore appears to be similar to "low-temperature" graphite. Although the other form of graphite is referred to as "disorientated" due to it producing polycrystalline diffraction rings in X-ray diffractograms, it is also described as being well adhered to the surface of the diamond indicating that it may be similar to the "high-temperature" graphite.

From the results of Pantea *et al.* shown in table 2.5, under low pressure, the graphite formed at low temperature was insufficient in quantity for any meaningful analysis and the graphite formed at high temperature was disordered and difficult to remove. Suggesting that this "high-temperature" graphite is the same as that forming from {112} planes described by Howes and, Evans and James.

The summary of results in table 2.5 show that increasing the pressure makes the graphitisation reaction less favourable and allow a schematic, meta-stable phase diagram to be drawn (figure 2.23). At room temperature, the activation barrier is too high for any meaningful transformation of diamond to graphite (even if it is thermodynamically favourable). Increasing the temperature results first in "low-temperature" graphite and then "high-temperature" graphite forming. Increasing the pressure at any given temperature moves the reaction in the direction of "high-temperature" graphite → "low-temperature" graphite → diamond.

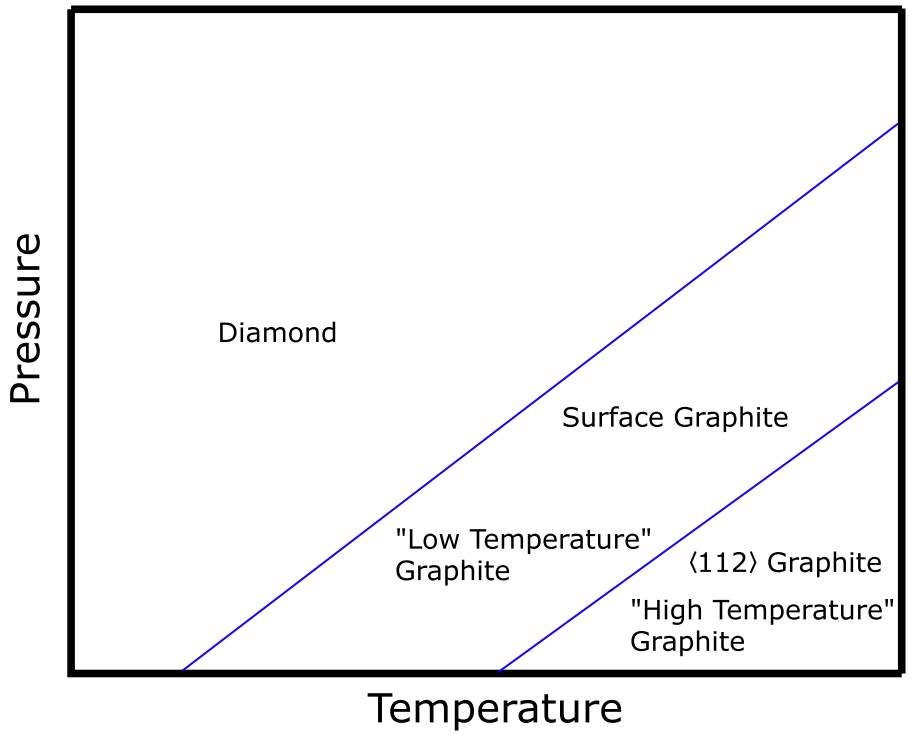

Figure 2.23: Schematic meta-stable pressure-temperature phase diagram for diamond/graphite. This diagram has been drawn from the summary of the work of Pantea *et al.*[91] shown in table 2.5.

This behaviour can be understood by looking at the rate equation that Davies

and Evans[89] used to describe the graphitisation reaction at high pressure:

$$\frac{dx}{dt} = Ce^{\frac{-\Delta E + P\Delta V}{RT}} \tag{2.1}$$

where $\frac{dx}{dt}$ is the rate of reaction, ΔE is the activation energy, P is the applied pressure (compression being negative), ΔV is the activation volume, R is the molar gas constant and T is the temperature. As they calculated a positive activation volume of $10\,\mathrm{cm^3\,mol^{-1}}$, an increase in compressive pressure increases the size of the activation barrier and hence decreases the rate of reaction. From the morphologies of the two forms of graphite described, the reason for this dependence on pressure becomes obvious. The "low-temperature" graphite is described as forming on the surface with little propagation into the bulk. The only barrier to formation due to pressure is that graphite is less dense than diamond, the expansion of the transformation will do work against the applied external pressure making it less favourable. "High-temperature" graphite has been described as forming by transformation of {111} diamond planes to graphite {0002} planes and has been observed propagating into the bulk of the diamond. A large strain is expected to be a consequence of this transformation due to the much larger graphite plane spacing and constraint of the surrounding diamond. This mechanism has both the transformation strain and the plane spacing mismatch strain having to do work against an applied external pressure making it even less favourable as the pressure is increased.

Khmelnitsky and Gippius[92] graphitised a number of natural and synthetic diamonds in vacuum with a total of fifteen different low index crystallographic planes as their surfaces. They conclusively showed that {112} are the only diamond planes that are weak to graphitisation and it is along these planes that the graphite propagates into the bulk of the diamond, supporting the mechanism suggested by Howes. They explained that this is because the {112} diamond planes contain atomic hexahedra and the surface density of this plane differs from that of the graphite {0001}/{0002} planes by only 0.1 % at 1600 °C. They concluded that at temperatures above 900 °C, a homogeneous coating of graphite 5–10 nm thick covers the surface of the diamond as a result of interaction with residual gas molecules

such as oxygen (and possibly other species)[86][93][94]. Above 1600 °C, rounded graphite nuclei which can migrate around the surface of the diamond form. For these rounded nuclei, from both theoretical and experimental studies, it appears that below 10 nm in size these nuclei are ephemeral as diamond is the energetically stable phase. It is suggested that nuclei of graphite above this critical size can only form above a threshold of 1600 °C. SEM analysis showed that in all cases where graphite had propagated into the bulk of the diamond, it had originated from an aggregation or "nest" of these nuclei. Figure 2.24 shows a graphitisation figure emerging from a nuclei "nest" on a (110) face of a diamond crystal. The authors note that how these nests of spherical graphite nuclei cause graphitisation of the adjacent diamond is still unknown. From analysis of the shape of symmetrical graphitisation figures on various crystallographic faces, it was found unambiguously that the {211} plane of diamond is the only 'weak' plane to graphitisation. As suggested in the mechanism by Howes (figure 2.22), the diamond {211} face is highly symmetric and contains atomic hexahedra. Comparing the atomic densities of the diamond {211} and graphite {0001} at 1600 °C gives answers that agree to within 0.1 %. As previously suggested, the authors explained that restraining pressure due to the vastly smaller plane spacing of the diamond {211} planes compared to the newly formed graphite {0002} planes is the main limiting factor on the propagation of graphite into the bulk of the diamond after growth has begun.

2.3.4 Catalytic Graphitisation

Catalytic graphitisation is a topic with much interest surrounding it due to the importance of graphite as a technological material and the large amounts of energy required to heat carbon sources to produce it acatalytically and hence great benefit in finding a lower energy pathway to achieve this. However, most literature is concerned with heating non-diamond carbon to transform it into graphite. Oya and Marsh[95] summarised the two main types of graphite formed using cobalt as a catalyst as follows (their structures are also shown in figure 2.25):

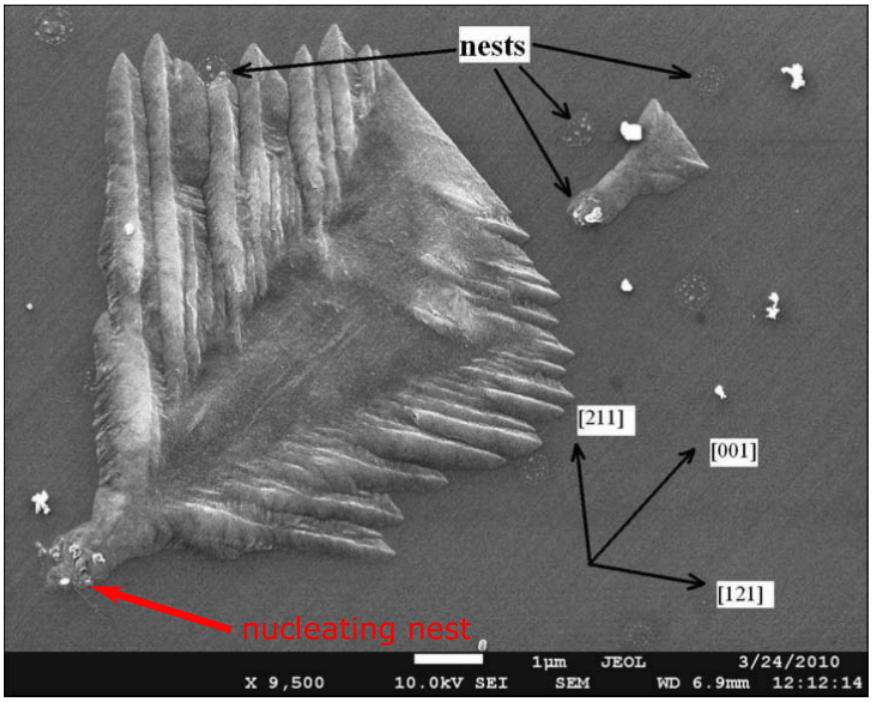

Figure 2.24: From ref [92]. SEM image of graphitisation figures emerging from "nests" of aggregated graphite nuclei on a (110) face of a diamond crystal after annealing at 1650 °C. The normal to the surface of the plate deviates from vector [110] by several degrees approximately in direction [001]. The nest that has resulted in the nucleation of a graphitisation figure is highlighted with a red arrow.

Graphitic Carbon Highly crystalline, ordered graphite with an approximate d_{002} plane spacing of 3.354 Å and a crystallite height of greater than 50 nm. X-ray diffraction peaks from this form of graphite are typically sharp. The mechanism of formation is described as being heterogeneous and arising from large catalyst particles, greater than 100 nm. For transition metals, such as cobalt, it is suggested that graphite is formed by material in a high-energy state (such as disordered or amorphous carbon) dissolving into the catalyst, forming a saturated solid solution and then reprecipitating as the lower energy crystalline graphite[96].

Turbostratic Carbon This form of carbon is quite close to crystalline graphite but typically has lower long-range order. Turbostratic carbon forms with finely divided catalyst particles (on the order of 20 nm) and results in graphite crystallite size of 6–20 nm with a range of d_{002} plane spacings of 3.38–3.42 Å. At the time the review was written, the mechanism of formation of this form of graphite was not

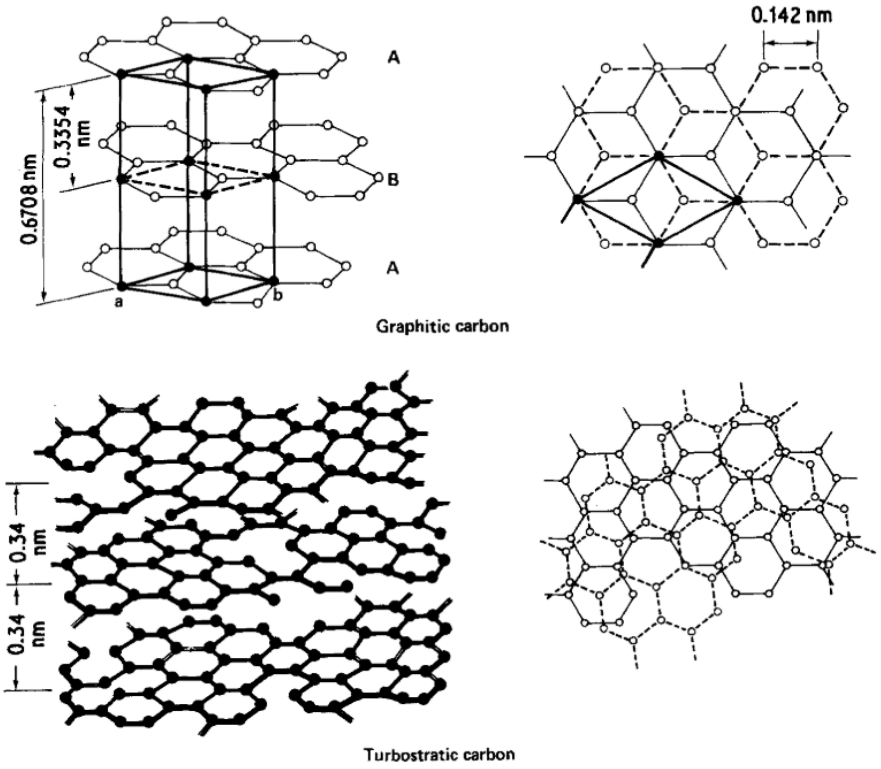

Figure 2.25: Representation of the different morphologies of graphitic and turbostratic carbon adapted from ref [95].

clear but there was evidence to suggest that either dissolution-reprecipitation[97] or formation and subsequent breakdown of a carbide into graphite[98] could be the cause dependent on the catalyst, initial carbon source and their morphologies.

Derbyshire *et al.* evaporated carbon to form an amporphous layer on cold cobalt foils and subsequently heated the bilayer structure causing graphite to form by two different mechanisms at different temperatures[99]. The bilayer was first heated to a range of target temperatures, slowly cooled and then the metal layer was dissolved away by soaking in hydrochloric acid. When heated to temperatures between 600 and 800 °C, the resultant carbon film had reorganised into islands of amorphous carbon surrounded by a material that produced a diffraction pattern characteristic of crystalline graphite. The proportion of amorphous carbon in the film decreased with increased temperature. After heat treatment at 900 °C, no film was produced, indicating that the entirety of the carbon layer had dissolved into the cobalt foil. A sample was then heated to 1000 °C to allow the carbon to dissolve

into the cobalt. Upon rapid cooling, a graphite film was found to grow on both sides of the foil. The lower temperature graphite was found to be disorganised and the reprecipitated material was found to be organised with respect to the underlying foil. This shows that the dissolution-reprecipitation mechanism caused graphite growth on samples heated to higher temperatures and cooled slowly but that another mechanism, that the authors described as "presumably a surface process[, and] that the metal surface provided a medium for the diffusion of mobile carbon atoms, thus facilitating crystallite growth", was active at lower temperatures.

Konno and Sinclair[100] criticised the work of Derbyshire *et al.* stating that as their TEM observations were only carried out in plan view, this made analysis of the mechanism of graphitisation difficult. They created a trilayer of amorphous carbon (a-C):cobalt:a-C and performed in-situ TEM on cross-sections of the film whilst heating it to temperatures between 500 and 620 °C. They discovered that the cobalt layer in the centre split and migrated to the outside of the trilayer through both a-C layers leaving behind crystalline graphite, strongly textured to have its {002} planes parallel to the plane of the film. They suggest that the migration of the cobalt layer indicates that a dissolution-reprecipitation mechanism must be the cause of the graphite formation and it is difficult to see how this could not be the case. Of the two forms of graphite formed in the work of Derbyshire, this mechanism appears to explain the formation of the highly ordered graphite formed by slow cooling from 1000 °C. However, in the case of disordered graphite that was formed at lower temperatures, there was no mention of it forming on the opposite face of the bilayer. With no migration of the cobalt in this case, the mechanism behind the formation of this graphite is still not adequately explained by dissolution-reprecipitation.

Finally, a trilayer of a-C:74.5%Co, 8.5%Cr, 16.1%Pt:a-C was created and annealed at temperatures of 400 and 600 °C (whether it was atomic or weight percentage was unclear) by Ramirez *et al.*[101]. The trilayer was imaged after manufacture using high resolution TEM showing the polycrystalline cobalt-alloy layer sandwiched between two amorphous carbon layers (figure 2.26, panel 'a)'). It was then heated to 400 °C, cooled and imaged again. After the first heating, it

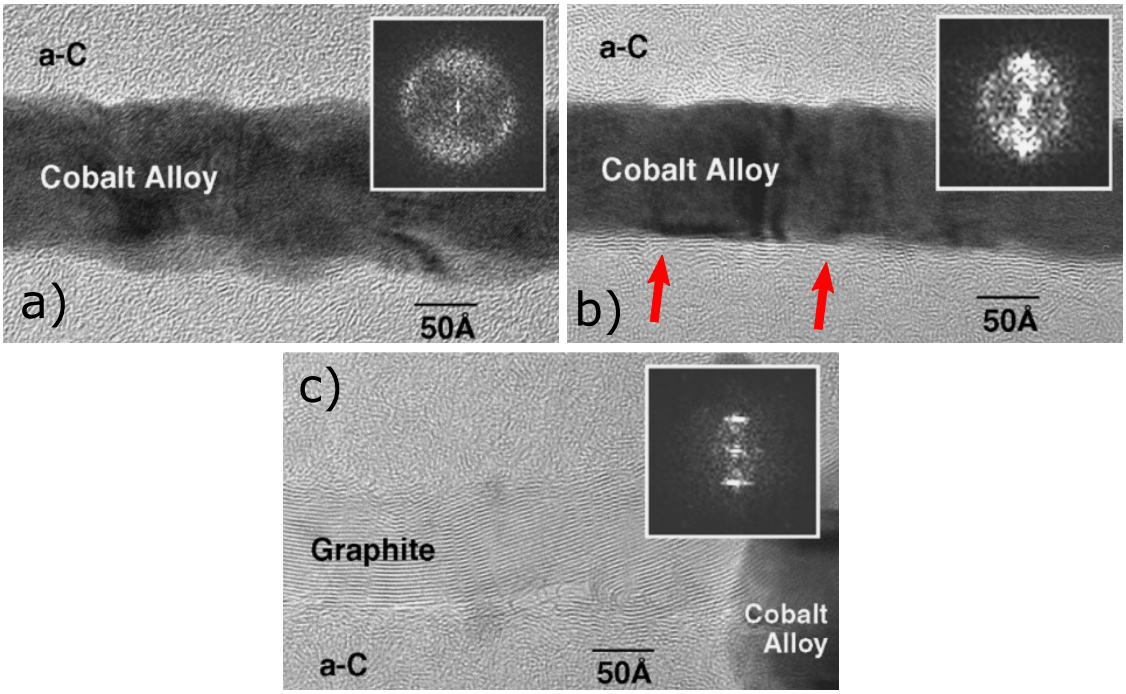

Figure 2.26: TEM micrographs of the a-carbon, cobalt, a-carbon trilayer after various amoutns of heating adapted from Ramirez *et al.*[101]. Panel 'a)' shows the trilayer at room temperature. panel 'b)' shows the trilayer after heating to 400 °C where layers of organised carbon atoms (red arrows) can be seen to have formed adjacent to the cobalt alloy layer. Panel 'c)' shows the trilayer after heating to 600 °C. The cobalt alloy has migrated to the right and has left a trail of graphite in its wake.

appeared that immediately adjacent to the cobalt layer, carbon atoms had arranged into a crystalline structure with a computed diffractogram indicative of graphite (figure 2.26, panel 'b)' - red arrows). The sample was then heated to 600 °C, cooled and imaged again. After this stage, the cobalt layer appeared to have spherodised leaving a train of highly crystalline graphite where the cobalt layer was previously (figure 2.26, panel 'c)'). The partial crystallisation of a-C at 400 °C with no apparent migration of the cobalt layer could be explained by either dissolution-reprecipitation or the surface mechanism suggested to operate at lower temperatures by Derbyshire *et al.* and the spherodisation of the cobalt alloy at higher temperatures clearly shows the former mechanism in action similar to the work of Konno and Sinclair. Although more compelling evidence for the dissolution-reprecipitation mechanism causing recrystallisation of amorphous carbon to form graphite has been shown, the other, surface mediated mechanism cannot be ruled out.

Unfortunately, there is very little research available on the propensity of cobalt to graphitise diamond. Pantea *et al.*[91] found that both ordered and disordered graphite grew around solvent-metal (the particular solvent metal was not specified) inclusions in synthetic diamonds heated to 2200 K under 2 GPa of pressure. The graphite was in the form of plates orientated along {111} planes. Possibly the best evidence of a mechanism behind diamond to graphite catalysation by cobalt is drawn from a study by Tomita *et al.* involving the formation of graphitic layers on the outer surface of cobalt nanoparticles from an initial mixture of these nanoparticles with nanodiamond[102]. The authors found that once the coating of cobalt oxide on the cobalt nanoparticles decomposed at 600 °C graphite formation began immediately suggesting that physical contact between the diamond and cobalt nanoparticles was necessary for the reaction to proceed. They found that once graphitisation had occurred, the number of graphite layers remained constant on further heating and cooling cycles. They therefore concluded that the cobalt acts as a template on which graphite can form allowing the release of energy stored by the thermodynamically unfavourable diamond phase.

2.3.5 Summary

It has been clearly shown in the literature that diamond in PCD graphitises at high temperature and that this is detrimental to its mechanical properties. Progressive removal of the cobalt causes a reduction in the extent of graphitisation and so cobalt is the likely cause. The work of Westraadt *et al.* makes a significant step forward in the understanding of the phenomena surrounding graphitisation but it is a preliminary work and there is clear scope for more of an understanding of the mechanisms behind graphite formation to be explored.

The mechanism of {112} diamond to {0002} graphite conversion has very strong evidence supporting it in pure diamond, dissolution-reprecipitation has clear evidence for the conversion of non-diamond carbon to graphite mediated by cobalt and some evidence was presented to suggest that cobalt nanoparticles may graphitise diamond nano-particles by a surface-mediated “templating” mechanism.

These reports provide a good starting point for the investigation of the observed graphitisation of PCD at high temperature and so one of the major aims of this thesis will be to continue this line of enquiry.

3

Mechanical Properties

Contents

3.1 Introduction and Aims 54
3.2 Materials and Sample Preparation 54
3.2.1 PCD Materials 54
3.2.2 PCD Sample Preparation Techniques 55
3.2.3 Bend Test Specimens 56
3.2.4 Microcantilever Production 57
3.3 Experimental Techniques 58
3.3.1 Four-point Bending Strength Test 58
3.3.2 Microcantilever Bending Test 59
3.4 Results 61
3.4.1 Strength of Macroscopic Beams 61
3.4.2 Strength of Microcantilever Beams 62
3.4.3 Yield Strength of Cobalt Binder Pools 63
3.5 Discussion 65
3.5.1 Re-analysis of Lammer's Data 65
3.5.2 Macroscopic Strength Results 71
3.5.3 Microcantilever Bending Strengths 71
3.5.4 Cobalt Binder Pool Microcantilevers 79
3.6 Conclusions 82
3.7 Further Work 85

3.1 Introduction and Aims

There was shown to be some confusion both about the macroscopic mechanical behaviour of PCD and the influence that some of the features in the microstructure have on this behaviour in section 2.1 of the literature review. These points will be addressed in this chapter. Firstly, some basic macroscopic strength measurements will be made to both see how they fit into the collated literature data and to aid in re-examining some of the conclusions of Lammer's seminal paper on the mechanical properties of PCD. Microcantilever beam bending tests will be performed on various elements of the microstructure such as grain boundaries and cobalt binder pools to examine their mechanical behaviour. These results will then be analysed quantitatively in terms of the strength of these features and qualitatively with regards to how PCD fractures macroscopically.

3.2 Materials and Sample Preparation

3.2.1 PCD Materials

A summary of the properties of the PCD used in these experiments is given in table 3.1. Material was sintered at 1450 °C. All sample preparation was done by Element Six at the Global Innovation Centre, Harwell, UK. The exact particle size distribution of the multi-mode powders cannot be revealed due to commercial sensitivity.

Designation	Average Particle Size (µm)	Mode	Sintering Pressure (GPa)
G4-S	4	Single	5.5
G30-S	30	Single	5.5
G12-M-HP	12	Multi	7.7
G17-M-HP	17	Multi	7.7
G27-M-HP	27	Multi	7.7

Table 3.1: Details of the diamond powder particle size, modality and sintering pressure of the grades of PCD used in the mechanical tests described in the current section.

3.2.2 PCD Sample Preparation Techniques

The sections below detail the various stages of sample preparation for making PCD mechanical test specimens. Preparation techniques have been declared high priority areas for confidentiality for Element Six, the supplier of all the material used in this thesis and so it will not be possible to give specific details allowing the reproduction by other researchers of the materials used here. However, qualitative descriptions of the processes will be given.

3.2.2.1 Electrical Discharge Machine (EDM) Cutting

The conductive nature of PCD due to its contiguous cobalt binder pool network is exploited to cut it as traditional abrasive cutting would be too slow. A wire forms one electrode whilst the PCD workpiece forms the other and a very high voltage is applied between the two with the whole assembly being submerged in a dielectric fluid. When the wire is brought close to the workpiece, the electric field between the two eventually becomes large enough for dielectric breakdown of the fluid to occur causing a large current to flow between the two electrodes. The rapidly recurring current discharge ablates material with each spark which is then carried away from the workpiece with the addition of more dielectric fluid. Material is also removed from the wire electrode which puts a minimum size requirement on it to avoid it instantly breaking and so the minimum radius of a notch cut with this method is around 500 µm.

3.2.2.2 Grinding

This technique is used to remove the largest amount of material as quickly as possible. The sample is pushed with a high load against a rapidly rotating resin-bonded wheel that is impregnated with large diamond particles. The wheel has to be dressed frequently to keep it sharp and wear occurs by a two-body process as the grit particles are bonded to the wheel. Water is used as a lubricant.

3.2.2.3 Lapping

Lapping involves introducing the sample to a cast iron plate rotating at relatively low speeds with a load of 5 kg. An abrasive slurry is used to remove material from the sample and as such wear takes place by a three-body mechanism. A G30-S sample had a measured arithmetic mean roughness, Ra, of 1 µm after preparation with this technique. The mean roughness was measured be Element Six.

3.2.2.4 Polishing

Polishing is the final surface finishing technique used. A resin bonded wheel is used rotating at high speed. A 5 kg sample load is used to avoid sub-surface damage and the process is cooled with air. Two-body wear occurs due to the diamond grit being bonded into the wheel and wear of the wheel is extremely low. A G30-S sample had a measured arithmetic mean roughness, Ra, of 0.1 µm after preparation with this technique. The mean roughness was measured be Element Six.

3.2.3 Bend Test Specimens

After sintering of the cutters, the PCD tables were removed by EDM cutting and approximately 2 mm was ground away from the bottom face to remove any macroscopic residual stresses. The PCD table was then sectioned into five beams and lapped on each side to achieve the dimensions required. The final stage was to polish either just the tensile face or the tensile and the two adjacent faces of each beam. The dimensions of the beams are shown in table 3.2.

Test Type	Length (mm)	Width (mm)	Height (mm)
Single-mode	> 12	1.2	1.0
Multi-mode	10	2.0	1.0

Table 3.2: Dimensions of macroscopic four-point bending specimens. Non-heated beams were cut straight from the cylindrical diamond table and so their lengths varied depending on which part of the cutter they came from.

3.2.4 Microcantilever Production

Samples used for microcantilever testing were marked using a laser with a grid of dots to aid in locating specific regions between different instruments. If the microcantilever was being made on a specific microstructural feature, the first stage was to map the grain orientations of the area of interest using electron backscatter diffraction (EBSD) to highlight the locations of the grain boundaries as these are not directly visible in secondary or backscattered electron contrast. This was performed either using a JEOL 6500f or a Zeiss Merlin EBSD SEM.

After a region was chosen, the sample was transferred to a focussed ion beam (FIB) microscope (FEI FIB200, Zeiss Auriga or Zeiss NVision) and the same location found using the laser-marked grid and SEM images of the area. A 'U-shaped' trench was then excavated with the surface of the sample perpendicular to the FIB beam using a high milling current of 16–20 nA (panel 'a', figure 3.1). The sample was then tilted to 45° to make the first undercut using a lower milling current of 4 nA and then tilted to 45° the other way to make the other undercut (panel 'b', figure 3.1). At this point a rough cantilever shape had been created with highly rounded and FIB-damaged edges due to the high beam currents used having beam tails that extended a large distance from the centre of the beam. Also, due to the propensity of carbon to redeposit milled material back onto itself, most surfaces were covered in a thick layer of redeposited material so it was often necessary to tilt back and forth between the two undercut angles to clean this off. The last stage, shown in panel 'c', was to use increasingly small beam currents stepping down from 1 nA to 200 pA and the so-called 'cleaning cross-section' pattern which rasters the beam back and forth along a single line to the required depth before advancing an incremental distance into the material to remove as much FIB-damaged material from the faces of the cantilever and create as sharp a profile as possible. SEM images of the top and end face of the cantilever were then taken to measure its dimensions.

The first set of microcantilevers were produced in random locations to give a good overview of the mechanical behaviour of PCD and subsequent microcantilevers had either a cobalt binder pool, a visbly defect-free diamond grain or a grain

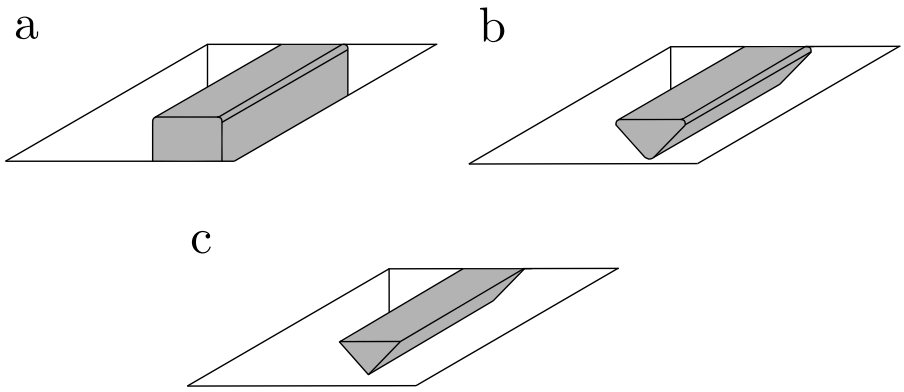

Figure 3.1: Schematic diagram showing the three main stages of microcantilever production by FIB machining. a) A U-shape trench is created with the surface of the sample perpendicular to the beam. A large beam current is used for this stage. b) The sample is rotated by 45° to make the undercuts and create a triangular cross section. The beam current is lower than the first stage but still relatively high and so edges are significantly rounded. c) The final stage involves fine finishing of the faces to produce sharp edges and so a low beam current is used.

boundary at their root. A further set of microcantilevers with grain boundaries at their roots were produced and notched in an attempt to force fracture to occur at the grain boundary. Notching was performed with a very low FIB current of 10 pA to produce as sharp a notch as possible in accordance with the updated solution of the Raju-Newman equation[103] for the stress intensity factor of a surface breaking semi-elliptical crack provided by Strobl *et al.*[104] (subsequently corrected by the same authors in ref [105]). Notches were made with a width of one third of the cantilever width and a depth to width ratio of 0.4. Semi-elliptical notches were used rather than the more conventional for microcantilevers straight-through notch as although every effort was made to accomplish this, grain boundaries were rarely completely straight or perpendicular to the sides of the cantilever and so a narrower notch ensured most of it would fall on the grain boundary.

3.3 Experimental Techniques

3.3.1 Four-point Bending Strength Test

Four point bending strength tests were performed using a stainless steel loading jig with 1 mm diameter tungsten carbide rollers on a screw-driven Shimadzu loading

frame. Force was transferred to the jig by a stainless steel rod attached to the 50 kN load cell that came into contact with a stainless steel ball bearing seated in a depression in the centre of the top of the jig. The upper and lower blocks of the jig that held the rollers were housed in a rectangular slot machined into two halves of a solid stainless steel cylinder. This whole assembly was then inserted into a close-bottomed stainless steel tube with a circular hole cut in the front so that the specimen and rollers were visible during the test (a schematic of this assebly is shown in figure 3.2). The jig was designed to be self-balancing so that any misalignment would be automatically corrected as much as possible on loading. The sample was placed in the centre of the rollers with the polished face downwards. Loading was done in displacement control with an initial displacement rate of $0.01\,\mathrm{mm\,s^{-1}}$ until a load of 4 N was detected followed by loading until failure at $0.02\,\mathrm{mm\,s^{-1}}$. The load-displacement data was recorded digitally at a measurement rate of 100 Hz and the maximum load before failure was found by viewing this data. The strength of the beam was calculated using the following equation[106]:

$$\sigma_f = \frac{3F_f\,(L_o - L_i)}{2wh^2} \tag{3.1}$$

where F_f is the load at fracture, L_o and L_i are the inner and outer loading spans, w is the width of the beam and h is the height of the beam.

Strength tests were performed on non-heated beams made from G4-S, G30-S, G12-M-HP, G17-M-HP and G27-M-HP materials. Two sets of beams were produced with the G4-S and G30-S materials one of which had been polished on the tensile face and the two adjacent faces as per the standard ASTM C1161 - 18. The other set was only polished on the tensile face and lapped on all other faces. As the additional polishing stages were very time consuming, it was important to ascertain whether it would make a meaningful difference to the strength results obtained.

3.3.2 Microcantilever Bending Test

All microcantilever tests were performed on an Agilent G200 nanoindenter. The sample was first loaded onto a custom designed stage to give precise control over

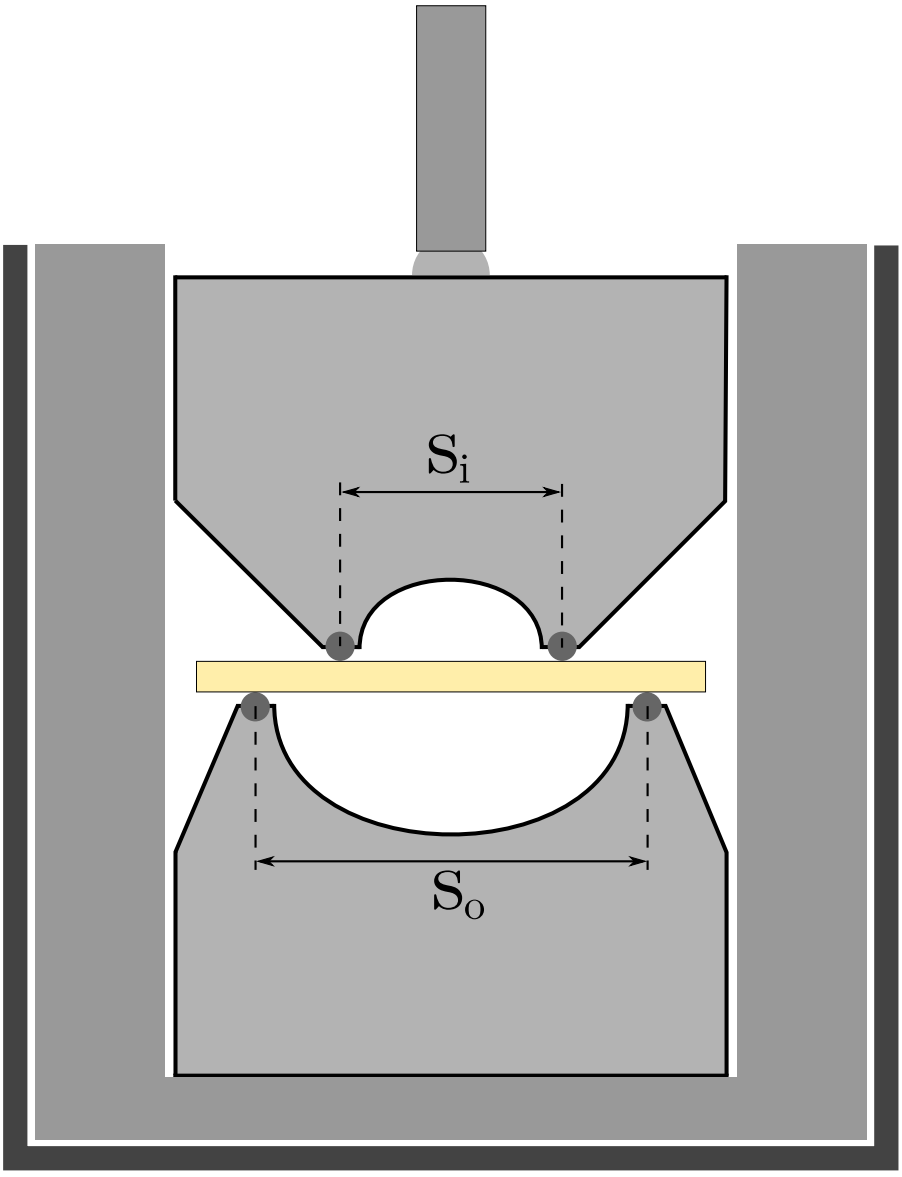

Figure 3.2: Schematic diagram of a cross-section through the four-point loading jig. The outer shell is a hollow cylinder with a window cut to make the sample and rollers visible. The next component is two halves of a cylinder with a rectangular slot machined in it to guide the loading components. The loading components each hold two tungsten-carbide rollers with a diameter of 1 mm. Two sets of loading components were made for the two different sample lengths where S_i and S_o equalled either 5 and 10 mm or 4 and 8 mm.

the sample height to within around 5 µm (shown schematically in figure 3.3) and rotated so that the cantilever to be tested was in the preferred orientation for the nanoindenter scanning direction. A microscope to indenter calibration was performed on the tungsten carbide part of the sample as the diamond indenter was unable to indent the diamond sample. The topography of the region surrounding the cantilever was then scanned by the indenter tip operating in a similar mode to an atomic force microscope with a low load of 0.5 µN to avoid damaging the cantilever and a horizontal scan time of 5 s. This data was shown as a height map (an example of which is shown in figure 3.4). The location to place the indenter tip was then chosen on the scanned image to be approximately in the centre of the width of the cantilever and a distance equal to half the width from the free end. Loading was then performed in displacement control at a rate of $500\,\mathrm{nm\,s^{-1}}$ and the load recorded as a function of displacement. The test was then halted manually as soon as fracture was detected (by a sudden drop in the load) or, the cantilever made contact with the bottom of the trench or the indenter made contact with the sides of the trench (indicated by a steep increase in the load).

The fracture strength of cantilevers was determined by the following equation for the stress at the tensile face of a triangular cross-section beam loaded at one end and constrained at the other[106]:

$$\sigma_f = \frac{12 F_f L_f}{w h^2} \tag{3.2}$$

where F_f is the failure force, L_f the distance between the indenter location and where the cantilever failed, w the width and h the height of the cantilever. The length at which the cantilever failed was determined by SEM analysis after fracture had occurred.

3.4 Results

3.4.1 Strength of Macroscopic Beams

Figure 3.5 shows the comparison between beams polished on only the tensile face and on three sides for G4-S and G30-S materials. Table 3.3 shows the four point

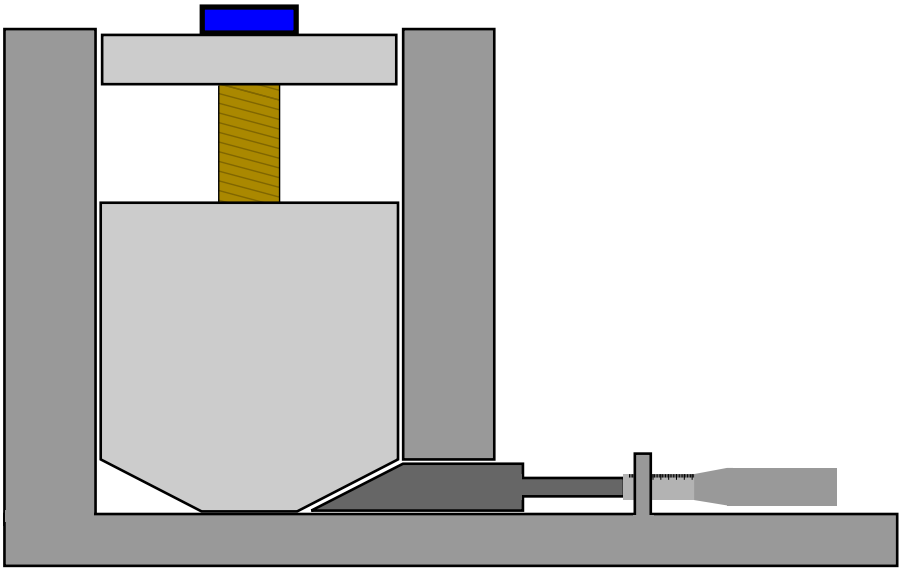

Figure 3.3: Schematic diagram of the stage that was made to precisely adjust the sample height in the nanoindenter. The light grey component had a threaded rod that could be screwed in and out of a tapped hole to coarsely adjust the height of the sample (blue). To adjust the height finely, the micrometer could be adjusted to push a wedge into the bottom of the light grey component to push it up by a small amount per revolution. It was possible to adjust the height of the sample with an accuracy of around 5 µm.

bending strengths and associated standard error for all PCD beams.

Designation	No. Tested	Strength (MPa)	Width (mm)	Height (mm)	Powder Particle Size (µm)
G4-S	5	2246 ± 106	1.2	1.0	4
G30-S	5	1350 ± 36	1.2	1.0	30
G12-M-HP	5	1606 ± 75	2.0	1.0	12
G17-M-HP	9	1223 ± 40	2.0	1.0	17
G27-M-HP	7	1153 ± 17	2.0	1.0	27

Table 3.3: Strengths in mega pascals (with the standard error in the measurement) for the five different grades of PCD tested in four-point bending.

3.4.2 Strength of Microcantilever Beams

The strengths of the four different types of microcantilever are displayed in figure 3.6. None of the notched cantilevers described in section 3.2.4 showed fracture that originated from the notches cut in them and hence these were simply treated as strength measurements and have been included alongside the other results of this kind. Due to the large spread in the results and relatively low number of test

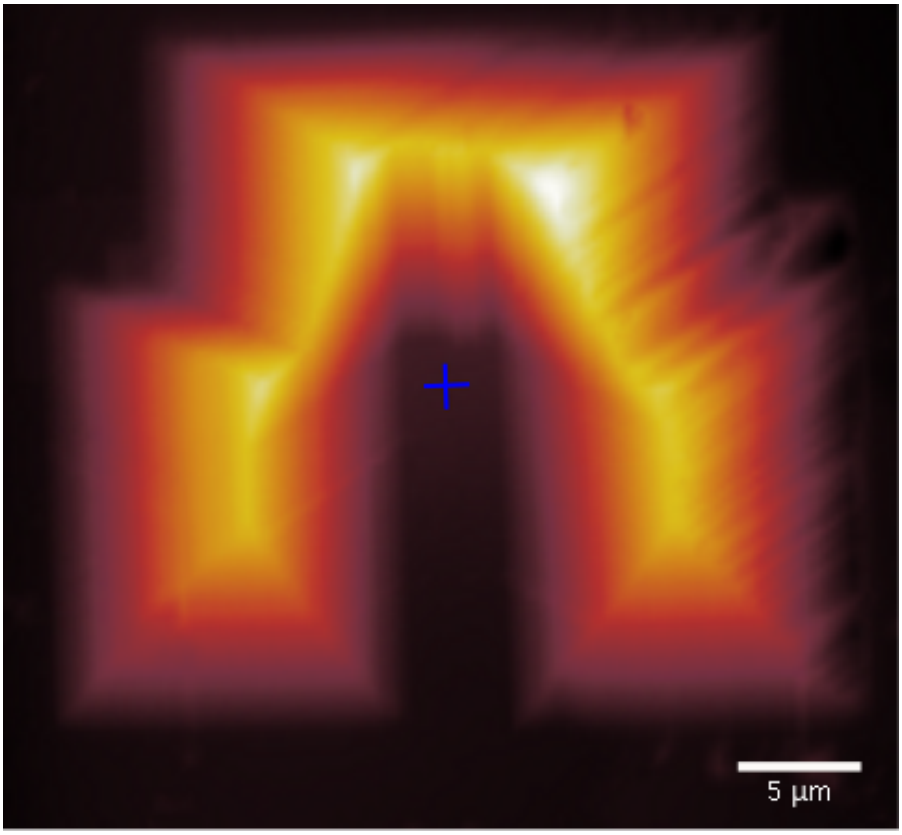

Figure 3.4: Height map of a cantilever measured using the scanning mode of the nanoindenter. Darker colours indicate higher regions and lighter (white/yellow) regions indicate lower regions. The blue cross indicates the location of the indenter tip during testing.

specimens (for a strength test) each individual result has been shown as a point on the graph rather than an average value with its associated error.

3.4.3 Yield Strength of Cobalt Binder Pools

A typical result from a bending test of a cantilever with a large cobalt pool at its root is shown in figure 3.7. The force initially increases linearly with indenter displacement while the cobalt remains in the elastic regime. Eventually, the elastic limit is reached, the cobalt begins to deform plastically and the force-displacement graph curves over as permanent deformation is done. As the cantilever continues to deform plastically, it eventually reaches the point where it either touches the bottom of the trench or the indenter makes contact with the rest of the sample and a sharp increase in the force is seen. The cantilever was unloaded at this point. All five

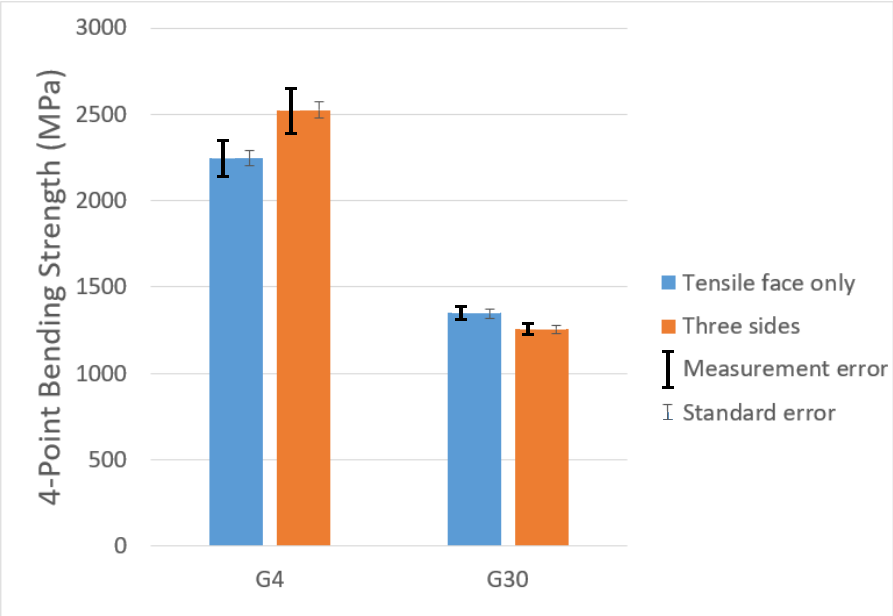

Figure 3.5: Comparison of the strength of beams that were polished on the tensile face and the two adjacent faces (orange) and only the tensile face (blue) for two different grades of PCD, G4-S and G30-S. The bold error bar shows the standard error in repeat measurements and the normal error bar shows the uncertainties in measured quantities propagated through equation 3.1. The difference in strength appears to be just at the bounds of the error in both cases. For the G4-S material, the 3-sides polished sample is stronger and for the G30-S the tensile face only sample is stronger. As a result, it is concluded that there is no strong difference between the two polishing techniques.

cantilevers tested plastically deformed in this manner and no gross fracturing was observed either in the nanoindenter data or on subsequent SEM analysis. The limit of proportionality was chosen as the point at which yield was determined to have happened (indicated by the red arrow in figure 3.7). Based on five microcantilevers the yield stress of the binder was calculated to be (3070 ± 242) MPa. This was calculated as twice the value calculated by equation 3.2 as the compressive stress at the apex of the cantilever is twice that of the tensile stress at the top face and unlike ceramics, metals fail plastically both in tension and compression.

Figure 3.8 shows a binder pool at the root of one of the cantilevers after it had been tested. Slip bands can clearly be seen in the cobalt confirming that plastic deformation had occurred.

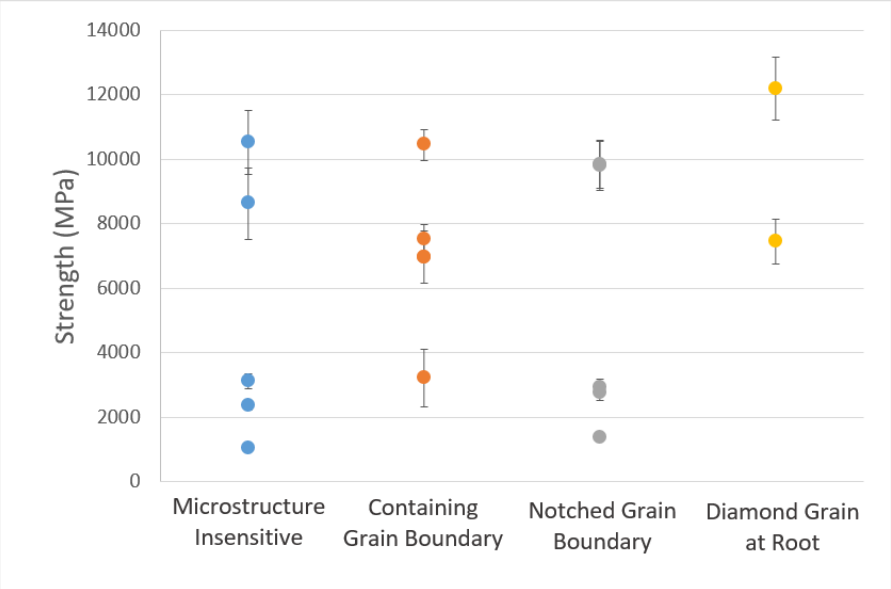

Figure 3.6: Plot showing all results for the bending strength of microcantilever beams. Error bars show the uncertainties in measured quantities propagated through equation 3.2. Four different categories of cantilever were tested: 'Microstructure Insensitive' were made in a grid pattern with no regard for the microstructural features of the PCD, 'Containing Grain Boundary' were made with a grain boundary near the root of the cantilever but were not notched, 'Notched Grain Boundary' also had a grain boundary near their root and a notch a third of the width of the cantilever was machined into it and 'Diamond Grain at Root' were made to have a pristine diamond grain at the root of the cantilever with no visible flaws. The two last results (yellow points) did not break before touching the bottom of the trench and so these values represent minimum strength values.

3.5 Discussion

3.5.1 Re-analysis of Lammer's Data

As the work of Lammer is still the most comprehensive analysis of the strength and fracture toughness of PCD published and its analysis is based on two assumptions that appear not to hold true (namely that the flaw size is independent of the grain size and that the starting diamond powder particle size is equal to the final sintered grain size in the PCD), this section re-analyses this work making an attempt to correct for these two errors.

It is commonly found that in ceramics with large grain sizes, the individual grains act as critical flaws and so the fracture behaviour follows Irwin's modification

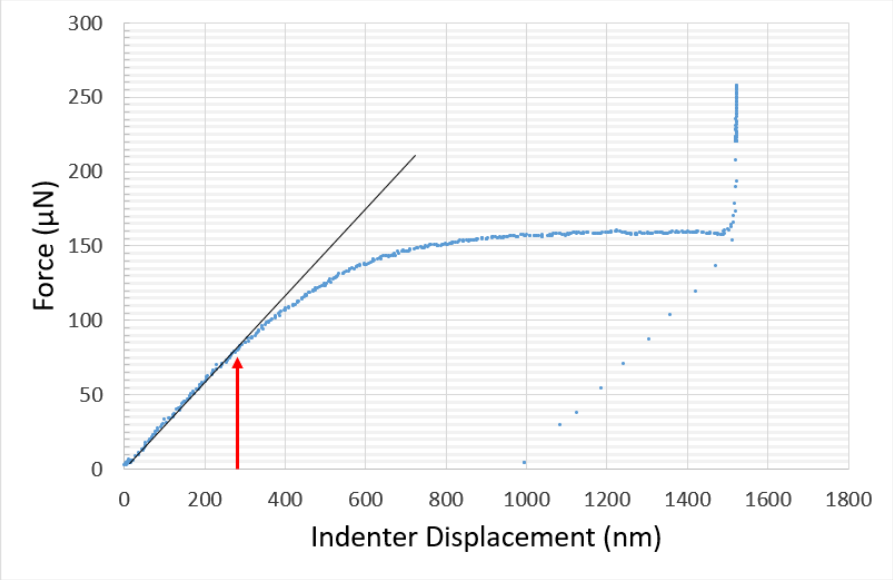

Figure 3.7: Typical load-displacement curve from the nanoindenter bending strength test of a microcantilever with a cobalt binder pool at its root. The black line shows the initial, elastically deforming regime and the red arrow shows where the limit of proportionality was exceeded which was the point chosen to represent the yield stress of the material. The curve flattens out before the load sharply increases indicating that the cantilever had bent until it was touching the bottom of the trench without breaking. The cantilever was then unloaded showing a large, permanent deformation.

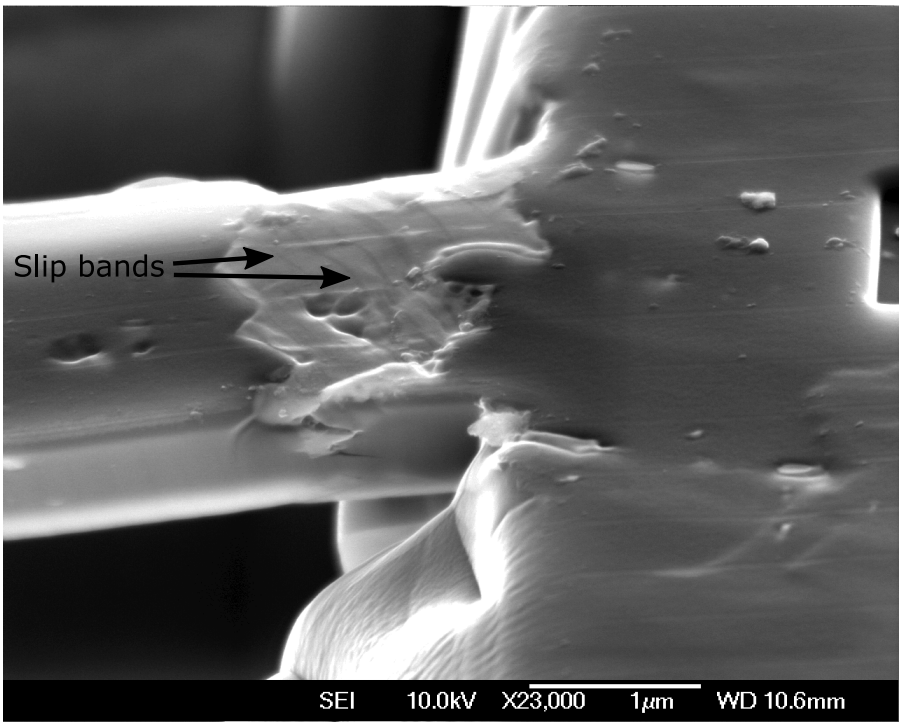

Figure 3.8: Secondary electron image of a plastically deformed binder pool at the root of a microcantilever. Slip bands can be seen within the cobalt indicating that plastic deformation has occurred.

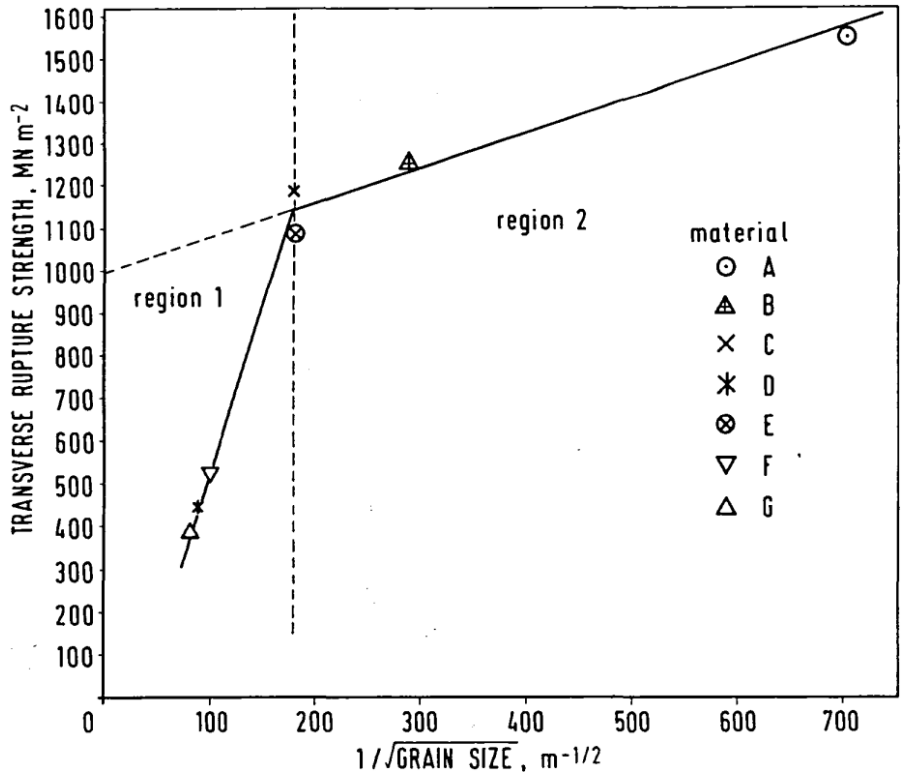

Figure 3.9: Plot of transverse rupture strength against the inverse of the square root of grain size from Lammer[26]. Two distinct regions are shown in the curve transitioning at a value that represents a grain size of approximately 30 µm.

of the Griffith equation[107]:

$$\sigma_c = \frac{K_{Ic}}{Y\sqrt{\pi c}} \tag{3.3}$$

where σ_c is the fracture strength, K_{Ic} is the critical mode-I fracture toughness, Y is a geometrical factor and c is the flaw size. "Region 1" in the graph of strength (σ_c) vs. inverse root grain size ($d^{-\frac{1}{2}}$) (figure 3.9, repeated from section 2.1.1.1) is a straight line that passes approximately through the origin suggesting that this typical behaviour is indeed followed.

Assuming that the largest grains act as critical flaws and that they are semi-elliptical and surface breaking ($d = 2c$ and $Y = \frac{\pi}{2}$) the gradient of "region 1" can be compared to equation 3.4 giving an expression for the implied toughness derived from this graph of:

$$K_{Ic}^{imp} = 1.12 \cdot m\sqrt{\frac{2}{\pi}} \tag{3.4}$$

where m is the gradient of "region 1". However, this data was plotted using values of starting diamond powder particle size which has been shown to be significantly different to the actual grain size of the material. Nilen[108] provides an equation derived empirically from many years of industry analysis of PCD microstructures to convert diamond powder particle size to sintered grain size:

$$d_{sintered} = 0.6 * d_{powder} + 2.9 \tag{3.5}$$

The equation gives the average number-weighted, diamond grain equivalent circle diameter in microns in the final sintered microstructure from the nominal number-weighted diamond powder particle size (typically measured by laser diffraction particle size analysis). This equation is clearly a gross estimate and is only valid for equiaxed, mono-modal powders. At very small grain sizes, abnormal grain growth has been reported (0.5 µm[109] and 2 µm[110]) and so below this limit, the equation is invalid. The reality of the sintering process is that there is competition between grain crushing reducing the average particle size and grain growth increasing it. Empirically, the above equation accounts for Ostwald-ripening of fine-grained material as below a particle width of 7.25 µm, it states that the sintered grain size will be larger than the initial powder size.

With the very approximate nature of equation 3.5 the powder particle size values from figure 3.9 can be tentatively adjusted to fine the equivalent sintered diamond grain sizes which is shown in table 3.4.

Strength (MPa)	Powder Particle Size (µm)	True Grain Size, d (µm)	Inverse, Root Grain Size $\mu m^{-\frac{1}{2}}$
1188	30	21	0.22
1090	30	21	0.22
520	95	60	0.13
444	125	78	0.11
389	150	93	0.10

Table 3.4: Data of strength against inverse, root grain size from Lammer[26] with powder particle sizes converted to true grain size using the empirical formula provided by Nilen[108]

The gradient of these data adjusted for true grain size against strength is $m = 6.62\,\mathrm{MPa}\sqrt{\mathrm{m}}$ which can be used with equation 3.4 to give a value of implied toughness from Lammer's data of $K_{Ic}^{imp} = 5.91\,\mathrm{MPa}\sqrt{\mathrm{m}}$.

Lammer also measured the fracture toughness of these materials following the work of Devin *et al.*[111] using laser cut notches in the centre of diametral compression samples. If the notch created by this technique has a much greater radius than the inherent flaw size of the material, it is considered blunt and will overestimate the toughness[112]. A treatment by Fett and Munz[113] calculates the true fracture toughness from the apparent value by assuming a small, incipient, sharp crack protrudes from the blunt notch using the following equation:

$$K_{true} = K_{app}\, tanh\left(2Y\sqrt{\delta\alpha/\rho}\right) \tag{3.6}$$

where Y is the geometrical shape factor, $\delta\alpha$ is the incipient crack length and ρ is the notch-root radius. Lammer did not measure the root-radius of the laser cut notches and so it is impossible to correct the toughness measurements with absolute certainty. McNamara *et al.*[44] in their aforementioned work using the theory of critical distances to calculate the fracture toughness of PCD created notches in PCD using EDM cutting. They measured root radii ranging from 170–300 µm but this technique generally produces blunter notches than laser cutting due to the greater minimum size requirement of a physical wire as opposed to a focussed spot of light. The only other authors to allude to notch root radius in PCD are Miess and Rai[39] who mention that the diameter of the laser beam used to cut the notches in their samples was approximately 80 µm which would have almost certainly produced a notch with a root-radius bigger than half of this diameter. As the actual notch root radii are not given, a value of 80 µm (diameter 160 µm) has been chosen and the adjusted values are shown in figure 3.10 along with the implied toughness calculated previously. Rather than calculating an accurate value of toughness from these values, this treatment shows that the strength and toughness values measured by Lammer can be made consistent with one another and the idea that a single value of toughness exists and that the strength is controlled by the

grain size is confirmed. This adjustment is shown to produce a consistent toughness value across a range of grain sizes in figure 3.10 ('Incipient Crack - Region 1' data points) that agrees with the implicit toughness calculated from the strength results ('Implied Fracture Toughness' horizontal line).

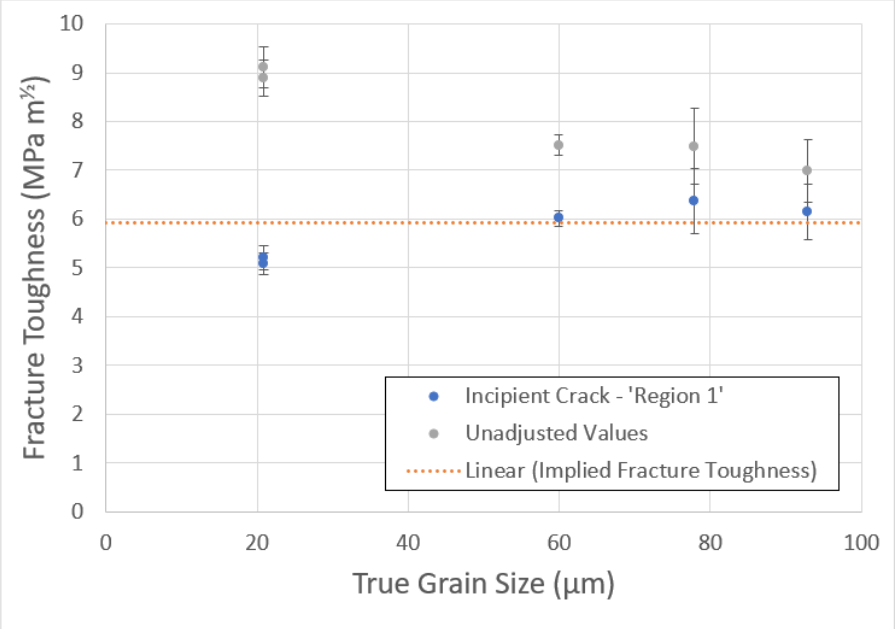

Figure 3.10: Replot of toughness values for materials C-G from Lammer[26]. The data points show the true toughness values calculated with equation 3.6 using a notch root-radius of 80 µm. The orange line shows the "implied" toughness calculated for these materials from the strength data using equation 3.4

If the materials in "region 2" had a different value of fracture toughness, the line would still be expected to pass through the origin just with a different gradient as suggested by equation 3.3. As this is clearly not the case, it is suggested that the small grain size materials used in this study contained an additional source of defects somewhat independent of and larger than the grains, explaining the much weaker dependence and lower than expected strength for smaller grain size materials. It is possible that these were processing defects (perhaps a few larger diamond grains making it into the initial mix and acting as large flaws) or that this is the effect of the cobalt binder on the strength as a larger proportion of binder is an unavoidable consequence of smaller diamond particle size.

3.5.2 Macroscopic Strength Results

The macroscopic strength results measured in this study are shown alongside those collated from the literature in figure 3.11. The strengths measured in this experiment appear to be slightly higher than the literature values with slightly less scatter. One of the likely reasons for this is that constant research and development has been conducted to improve the strength of these materials since the literature results were published and many of the contributions to this (such as diamond-diamond bonding, binder chemistry, proportion of binder in the PCD) are not represented simply by the grain size of the material. Secondly, the test specimens used in these experiments were quite small compared to the large diametral compression samples that are generally used in the studies from the literature. As brittle fracture is a probabilistic phenomenon, the larger the sample is, the more likely it is that a large flaw exists within it and hence the lower its strength is measured to be. Cobalt pool size, which is controlled by a number of factors including the diamond grain size, will likely also have a big impact on the macroscopic strength of PCD. The cobalt pools on the surface are preferentially removed during polishing and can act as surface flaws, the size of which depend on the initial size of the binder pools and the aggressiveness of the polishing technique. To understand this complicated relationship, much further work is required but this was not one of the aims of the present work.

3.5.3 Microcantilever Bending Strengths

The strength results shown in figure 3.6 show a large degree of scatter as is generally expected for strength measurements of a brittle material due to the dependence of the strength of an individual cantilever on the flaw size present within it which is determined by a wide statistical distribution. The results appear to be split into two groups with average strengths of (9033 ± 568) MPa (n = 8) and (2401 ± 327) MPa (n = 7) although it is unclear whether this grouping would disappear with more samples tested. Some of the results in the lower strength group have strengths similar to that of the strongest macroscopic test specimens but some of the higher strength group had strengths up to five times that of the strongest macroscopic

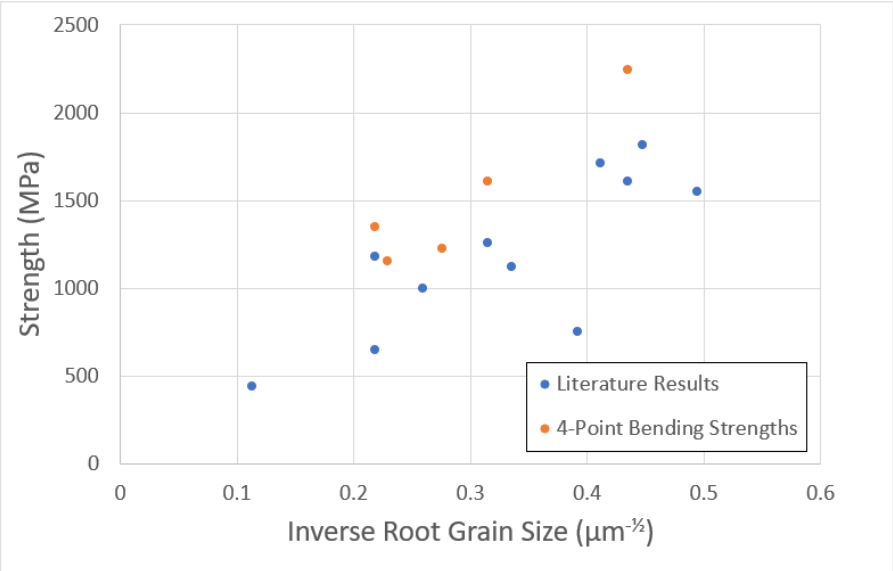

Figure 3.11: Plot showing the collated literature values of strength of PCD (blue) and the results calculated in this study (orange) against inverse root grain size. The results from this study all have slightly higher strengths than the literature values but they fit into the general trend. All of the data in this graph have had their grain size values adjusted using equation 3.5.

beams. The reason behind this is likely that the flaws causing failure in the macroscopic test samples are much bigger than those in the microcantilevers. As the cantilevers ranged from 1 to 5 µm in width, this limits the maximum size of flaw possible within them thereby increasing their strength. SEM images were taken of the cantilevers before and after testing and so it was possible to analyse the likely cause of fracture in each cantilever.

3.5.3.1 Fracture Origin

Three main types of suspected fracture origin were observed and examples of each are given below. The first was a manufacturing defect which was either caused by an error in the FIB machining process such as that shown in figure 3.12 (especially prevalent in the 'Microstructure Insensitive' cantilevers which were the first set made on an older microscope which was much more prone to beam drift) or by preferential milling of some microstructural feature. This caused sections of some cantilevers to be narrower than the rest of the beam causing stress to be concentrated and increasing the likelihood of fracture.

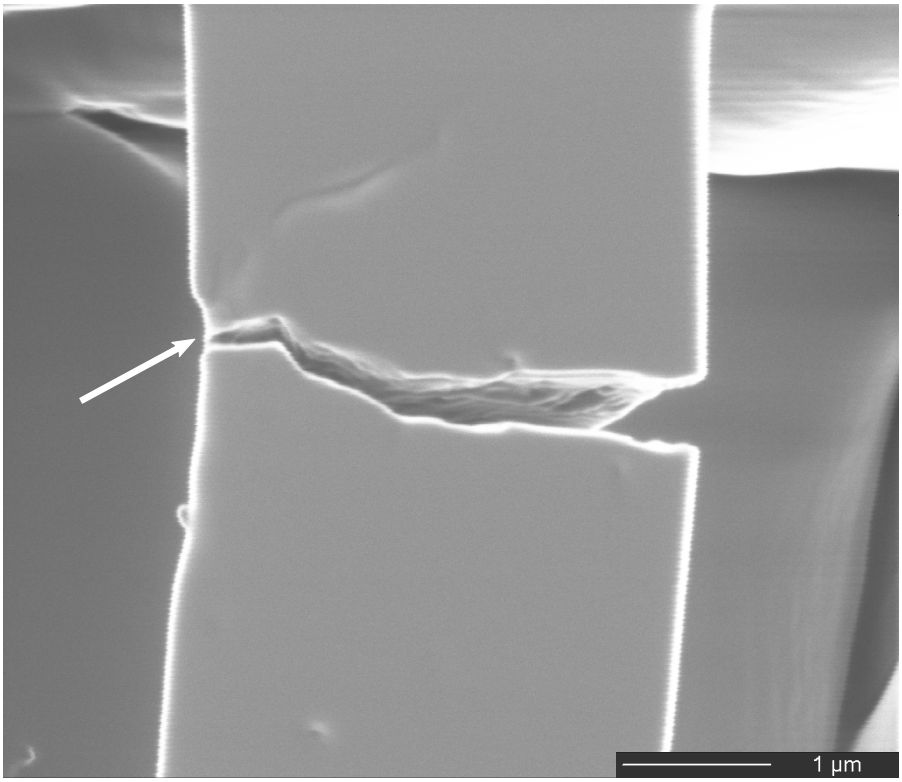

Figure 3.12: FIB image of the top of a microcantilever showing the machining defect (white arrow) that is suspected to have caused fracture.

The second type was a partially eroded binder pool (figure 3.13). As cobalt is removed by the gallium beam at a much greater rate than the diamond, areas of cobalt on the surface quickly became recessed, again this was especially prevalent with cantilevers manufactured using the FEI FIB200 as this was a single column instrument and did not have an SEM column for imaging. It is likely that these features would have still acted as stress concentrators due to the much lower stiffness of the cobalt even if preferential milling had not taken place.

The third type of fracture origin was a barely visible crease on the surface of a seemingly pristine diamond grain (figure 3.14). These features ranged from being almost imperceptible in secondary electron contrast to being slightly preferentially milled. The features were generally quite straight and the fracture followed their path almost exactly.

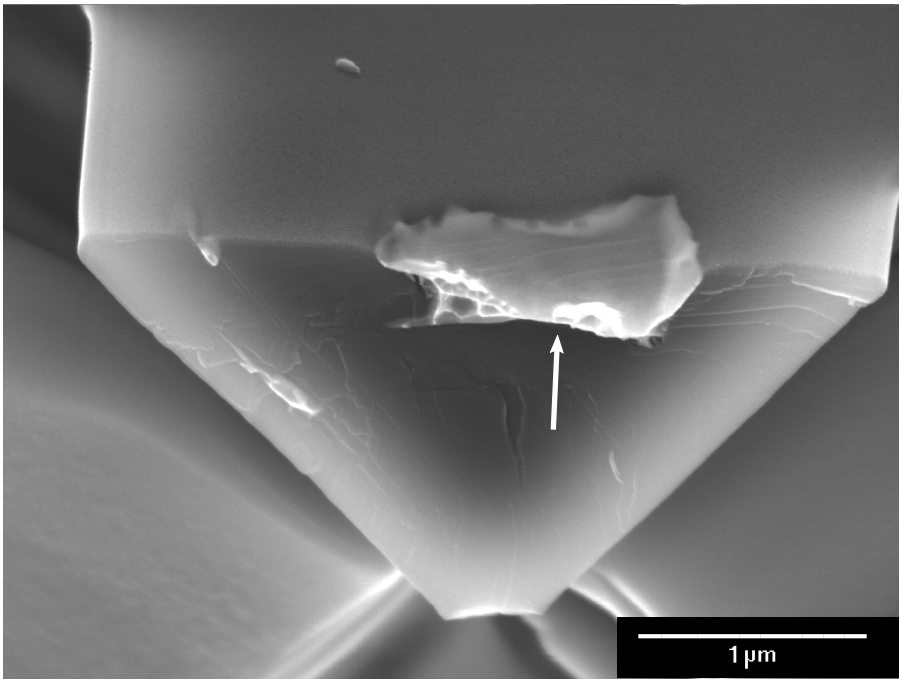

Figure 3.13: SEM image with the sample tilted to 45° showing a partially eroded binder pool (white arrow) in the fracture surface of a microcantilever that is believed to have caused fracture.

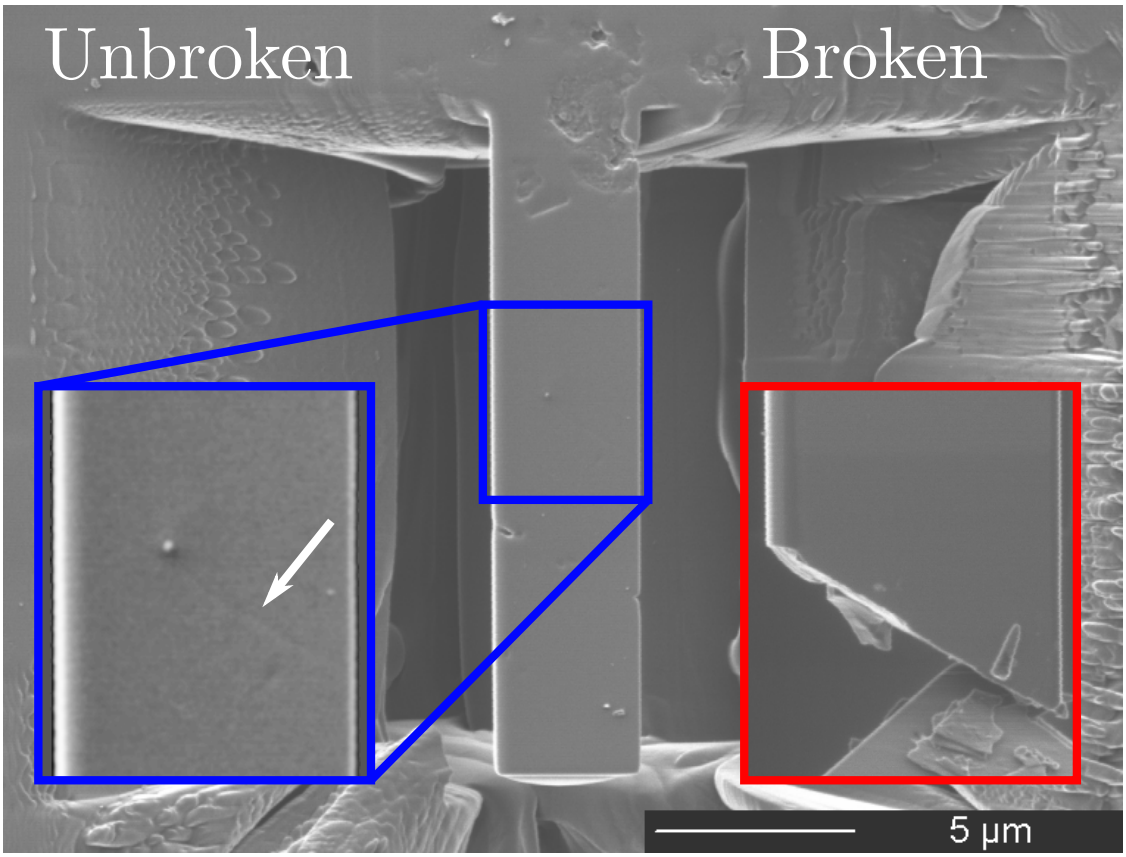

Figure 3.14: SEM image of the top of a cantilever that has failed along a barely visible surface crease. The blue box shows an expanded view of the top face of the cantilever with a white arrow indicating the defect along which the cantilever fractured that crosses the width of the cantilever at approximately 45°. The red box shows a picture of the same region after fracture.

3.5.3.2 Grain Boundaries

The results have been categorised as either high or low strength and whether fracture involved a grain boundary (that is the fracture path passed along a grain boundary, determined by SEM analysis, for greater than half its length) or not and are shown in figure 3.15. It can be seen that for cantilevers that fractured at grain boundaries, there is a roughly equal number that had a high and low strength. There were also a similar number of cantilevers that had high strength and did not fracture at a grain boundary. The only case that stands out is the lower incidence of low strength cantilevers that did not fracture at grain boundaries. The two cantilevers that were made with pristine diamond grains at their root were omitted from these results as they did not fracture. As they reached stresses of 7444 and 12 190 MPa, if they had fractured, they would have been added into either of the high strength categories and therefore would not have changed the overall gist of the results. This information coupled with the average strength of a cantilever that fractured at a grain boundary being (5105 ± 709) MPa and that of a cantilever that did not fracture at a grain boundary being (6924 ± 700) MPa, it would appear that grains are slightly stronger than grain boundaries but that the effect is weak and that grain boundaries do not act as significantly preferential paths for fracture as is suggested by much of the literature. As none of the notched cantilevers fractured at the notches, it is suggested that a more reliable way of notching the cantilever be experimented with so that this finding can be further evaluated by measuring the toughness of the grain boundary and comparing it to that of the grains.

3.5.3.3 Character of Fracture Path

Another way of characterising the fracture of the cantilever was by the straightness of the fracture path. A number of cantilevers exhibited completely straight fracture paths with either very clean or stepped fracture surfaces, an example of which is shown in figure 3.14. The results were categorised as either high or low strength and the fracture path as 'straight' or 'not straight' and the results are shown in figure 3.16. In this case, the strength data seems to show a higher dependence

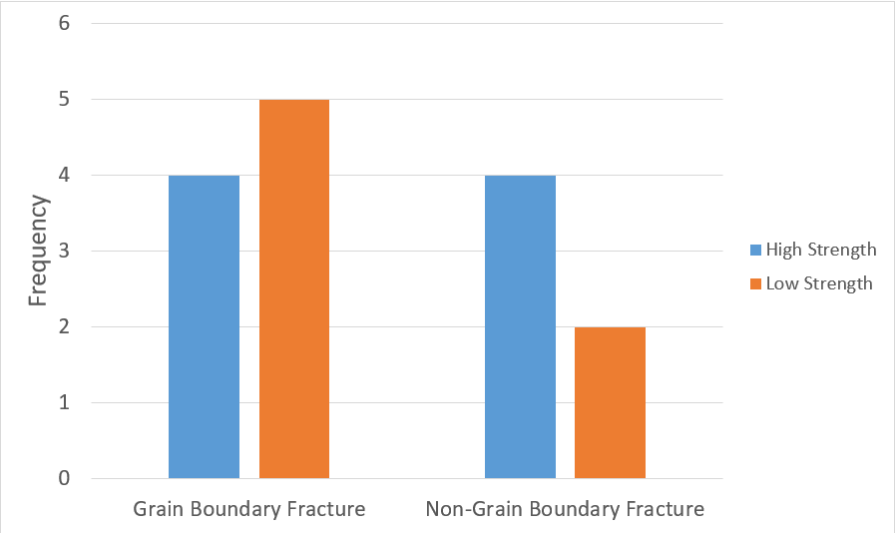

Figure 3.15: Plot showing the occurrence of cantilevers that did and did not fail at grain boundaries separated by whether they belonged to the "high strength" or "low strength" groups described at the start of this section. Cantilevers that failed at grain boundaries were split approximately equally into the high and low strength groups whereas cantilevers which did not fail at grain boundaries had a slightly higher number of high strength cantilevers.

on whether the fracture path was straight or not with more of the 'straight fracture path' cantilevers having a low strength and the 'not straight fracture path' cantilevers having a high strength and there are multiple possible explanations for this. Diamond has long been known to cleave preferentially along the low energy {111} planes[114] but the diamond grains in PCD are also known to plastically deform during hot-pressing which will introduce dislocations to potentially disrupt these easy cleavage planes. Hibbs and Lee[53] suggested that some grains could be protected from this plastic deformation preserving their easy cleavage planes, however, dislocations are not thought to significantly toughen ceramic materials and so this is unlikely to be the main reason between the difference in strengths between the two fracture morphologies.

Cathodoluminescence is a phenomenon where high energy electrons incident on an atom (or atom-like defect) can cause one of its electrons to be excited to a higher energy state and when this electron relaxes, it emits a photon of light equal to the difference in energy levels. Diamond contains many different types of these atom-like optical defects, often involving substitutional nitrogen atoms and/or

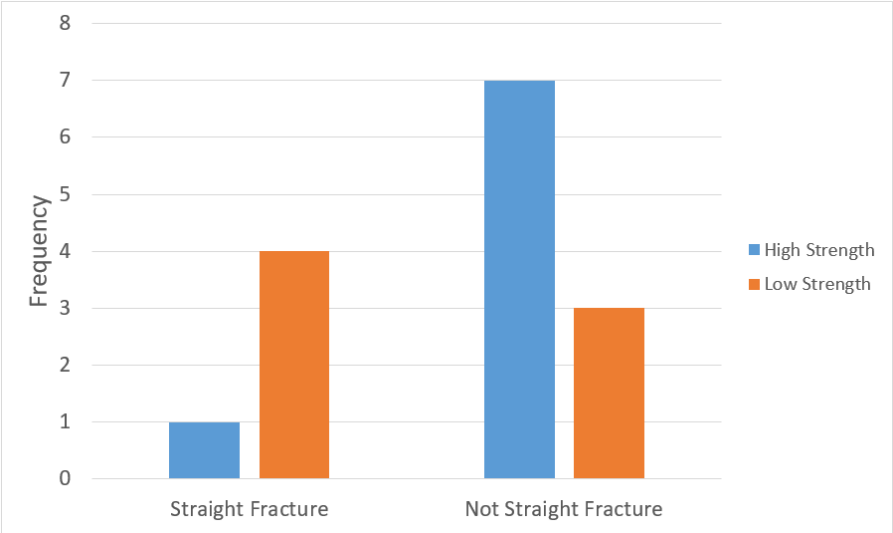

Figure 3.16: Plot of the occurrence of cantilevers that had either straight or non-straight fracture paths. There is a clear trend of cantilevers that had straight fracture paths being mainly low strength and cantilevers with non-straight fracture paths being high strength.

vacancies and the spatial distribution of these defects can be observed by their cathodoluminescent emissions during scanning electron microscopy if a suitable detector is present. Using this technique, a significant amount of the internal defect structure of the diamond grains can be seen that is invisible in both secondary and backscattered electron contrast (as shown in the top panel of figure 3.17). Several reasonably straight structures can be seen within the diamond grains but as the entire spectrum of visible light was collected in this image, it is impossible to tell which optical defects are causing this contrast. Figure 3.18, a combined backscattered electron image and EBSD inverse pole figure of the same region, helps to explain what these structures might be. In region '1', a single diamond grain appears to have been fractured into two separate grains with the EBSD image (right panel) showing a slight rotation between the grains and the backscattered electron image (left panel) showing that a small amount of cobalt has been able to ingress into the fracture. Region '2' shows an area of multiple small grains separated by relatively large binder pools that all have a similar orientation from the EBSD inverse pole figure. The similar orientation of many seemingly distinct grains could be caused by grain growth (normal or abnormal) as shown in the work of McKie *et al.*[109]. They showed that cobalt could become incorporated into these larger

grains by the grain growth front moving through the microstructure faster than the cobalt move along with the boundary. However, figure 3.19 shows a comparison of secondary electron and EBSD IPF images of a region that has experienced abnormal grain growth from their work. Thick regions of cobalt that have been pushed out from the growing grain are seen around the single orientation regions that are not seen in figures 3.17 and 3.18 from the present work. Furthermore, the average grain size of the diamond powder used in these authors' work (0.5 µm) was much smaller than that used in this work (30 µm) and so it is determined that abnormal grain growth has not occurred in this work. Although it is suggested that abnormal grain growth is not the cause, these features may still have been caused by Ostwald ripening. Grain crushing is determined to be the more likely cause of what is seen in the EBSD images, however, more work would be required to confirm this.

It is suggested that the straight line structures seen in the cathodoluminescence image (figure 3.17) could be grains that have fractured during cold pressing but because of the stresses on them, have not separated sufficiently for cobalt to enter the space between the two halves. Both cases are examples of low angle grain boundaries. Where the cobalt catalyst has been able to access the boundary, it has allowed for better diamond regrowth forming a strong, well bonded grain boundary but in the case that it hasn't, poor diamond-diamond bonding has occurred and so a weak interface is produced. It is suggested that these poorly repaired fractures that occur during cold pressing are a possible explanation for the weaker, straight-fracturing microcantilevers.

3.5.4 Cobalt Binder Pool Microcantilevers

The results in section 3.4.3 show that the yield stress of the binder ((3070 ± 242) MPa) is considerably higher than the 400 to 800 MPa measured for bulk, model alloys of cobalt, tungsten and carbon by Roebuck *et al.*[115]. This is due to the well known 'size effect' when measuring strength as a function of sample size that has been studied specifically for the case of microscale mechanical tests by Wheeler *et al.* [116]. Tarragó *et al.*[117] measured the first strain bursts (or "pop-ins") in

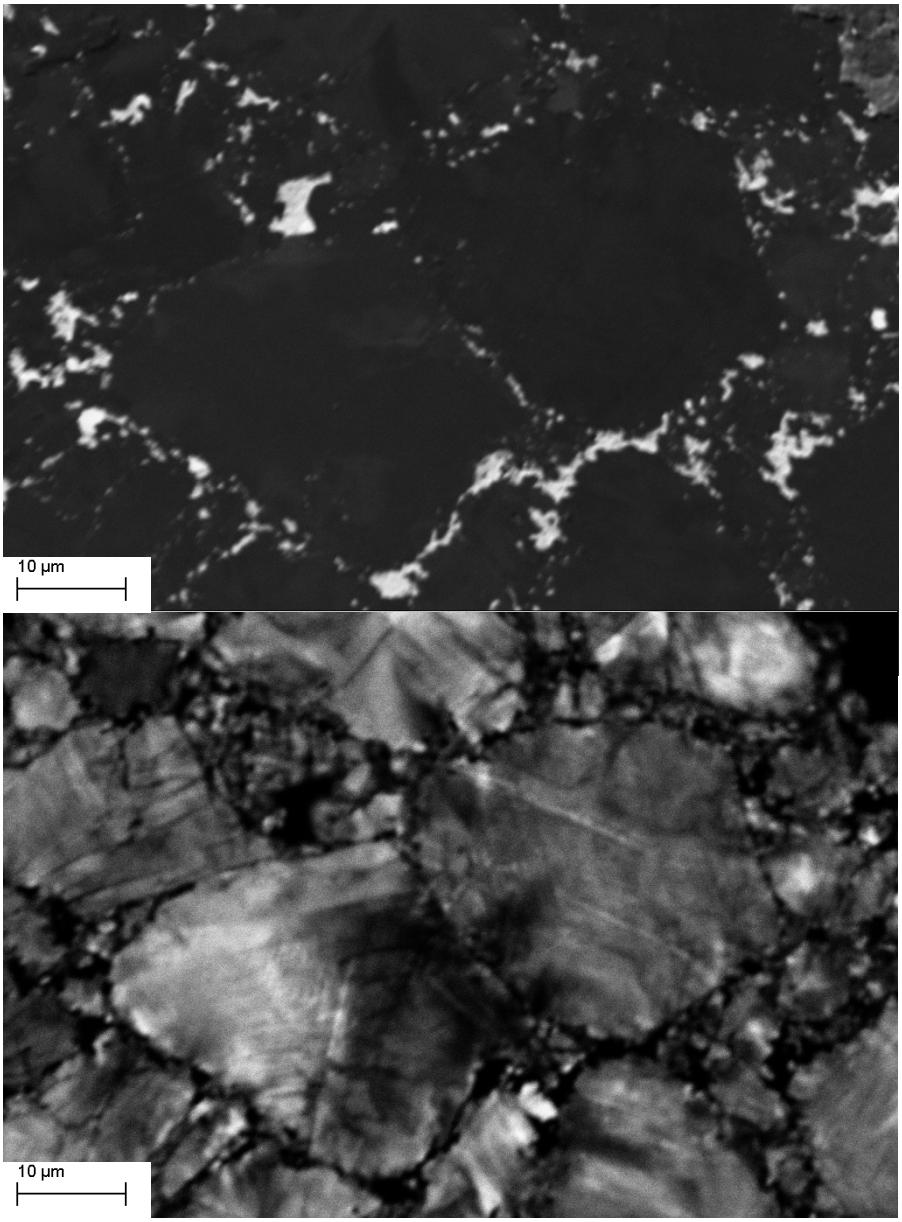

Figure 3.17: The top panel shows a backscattered electron image of the microstructure of a PCD sample (black regions are diamond and lighter regions are mainly cobalt binder pools). The bottom panel shows a cathodoluminescence image of the same region. The contrast in this image is derived from the light emitted by optical defects that are luminescing due to interaction with the electrons from the SEM. A number of linear features are seen in this image. Whilst it is not clear exactly what these features are, it is suggested that they may be connected with the straight fracture path seen in figure 3.14.

uniaxial compression of micropillars manufactured from WC/Co hardmetals to be between 600 and 1700 MPa which is considerably lower than the yield stress measured here. Figure 3.20 shows the likely reason for this discrepancy. Due to the three-dimensional and asymmetrical nature of the binder pools, most of the

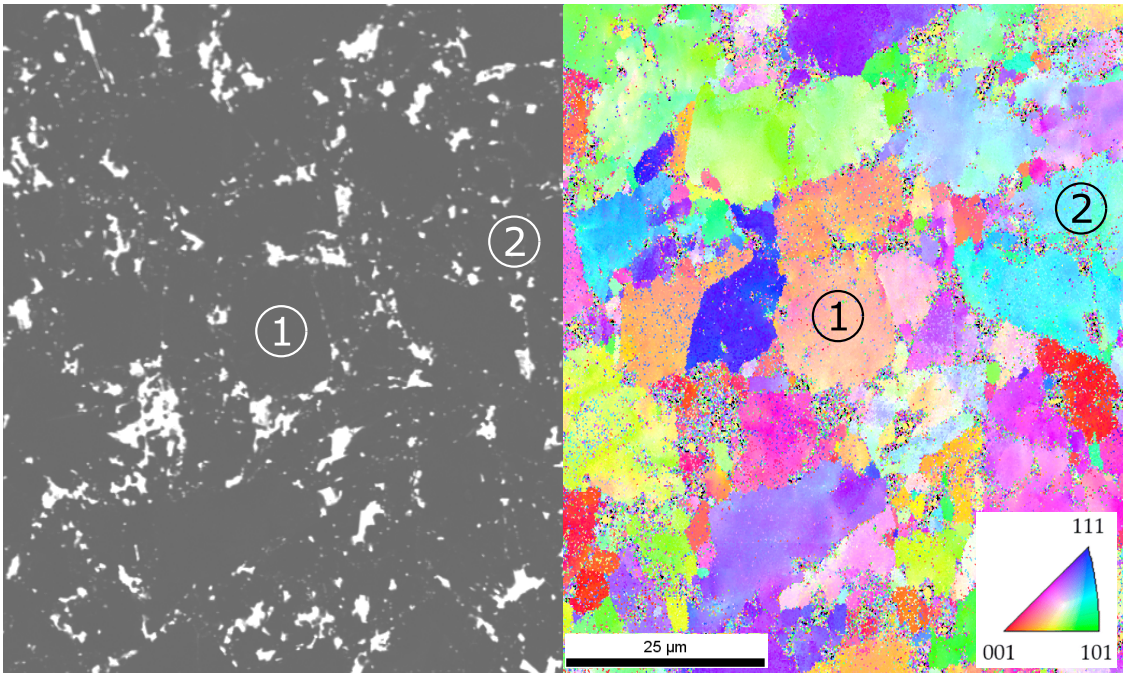

Figure 3.18: The left panel shows a backscattered electron image of the microstructure of a PCD sample (grey regions are diamond and lighter regions are mainly cobalt binder pools). The right panel shows an EBSD, inverse pole figure (IPF) image of the same region. The number '1' shows the same grain in both images that appears to have fractured along a straight path and allowed cobalt to infiltrate during sintering. In the IPF image the two parts of the grain can be seen to have rotated slightly with respect to each other due to their different colours. The number '2' shows what was once a single large grain (indicated by the uniform light blue colour in the IPF image) that has clearly fractured into many parts and allowed a large amount of cobalt to infiltrate which can be seen in the backscattered electron image.

cantilevers with binder pools at their roots actually contained a mixture of diamond and cobalt. In this case, two issues will cause the true yield stress to be lower than that measured: firstly the diamond bridge, being a much stiffer and stronger phase, will support a greater proportion of the stress thereby reducing the stress in the cobalt and secondly as the stress varies as a function of position away from the neutral axis and the diamond exists right at the apex of the cantilever (the furthest from the neutral axis), the level of stress where the cobalt actually exists will be lower. This is slightly counteracted by the preferential milling of the binder causing its cross-sectional area to be reduced compared to the overall cantilever dimensions.

Although an accurate value of yield stress cannot be calculated from these results a reasonable upper bound has been established. Furthermore, these results show

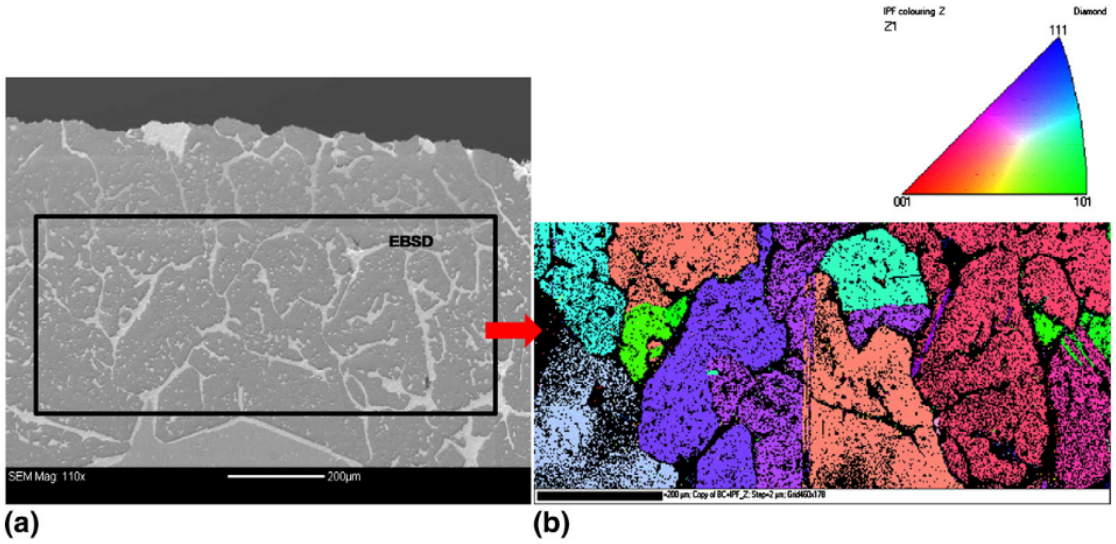

Figure 3.19: Images of abnormal grain growth in a 0.5 µm diamond particle size PCD from the work of McKie *et al.*[109]. Panel 'a)' shows a secondary electron image and panel 'b)' shows an inverse pole figure image from EBSD from the same region. Large grains can be seen to have formed in the IPF image with thick boundaries of cobalt surrounding them.

that the binder does yield as evidenced by the slip bands seen in figure 3.20 and the strain bursts that are seen in (some but not all of) the load-displacement data (figure 3.21) and therefore can display a toughening effect in PCD. No instances of separation of the binder from the diamond have been seen with these tests and none of the binder pool-cantilevers fractured indicating that the binder is strongly bonded to the diamond and that fracture does not take place at the interface between the two. Furthermore, the binder acts as a crack-bridging element to provide some residual toughness after fracture of the diamond grains has occurred as seen by the stable crack indicated by a red arrow in figure 3.20 and figure 3.22 which shows a binder pool holding together a cantilever where the diamond portion has fractured completely.

3.6 Conclusions

The explanation given by Lammer regarding the strength and fracture toughness of PCD has been re-analysed in the light of the current, conventional thinking on the behaviour of brittle materials. It has been shown to be likely that a single

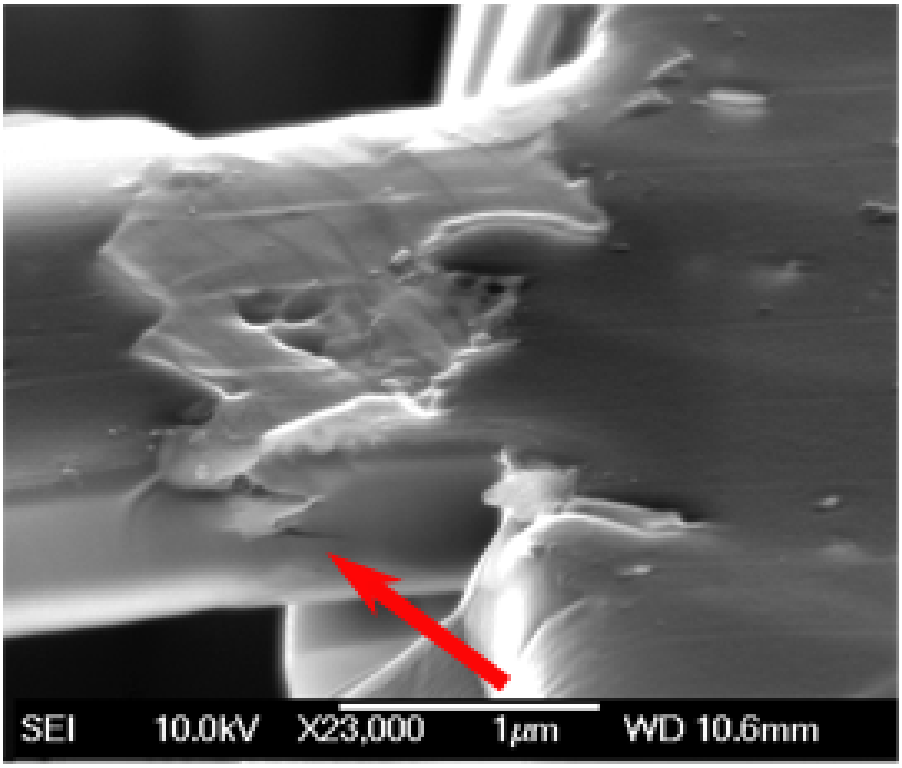

Figure 3.20: Secondary electron image of a microcantilever with a cobalt binder pool at its root. Slip bands can be seen within the cobalt and a stable crack can be seen to have grown towards the underside of the cantilever (red arrow) which is presumably being held together by the binder.

value of fracture toughness exists for PCD and that the strength is controlled by the flaw size. For larger grained materials, this appears to be similar to the grain size (which is quite different to the original diamond powder particle size) and for smaller grained materials, flaws appear to be bigger than the grain size. Clearly, the understanding of this behaviour would benefit from flaw size distribution analysis.

Microcantilever beam bending tests showed strengths that were roughly grouped into high and low strengths. No significant tendency was found for a cantilever with a grain boundary to belong to one of these groups. Therefore grain boundaries do not appear to act as a weaker part of the microstructure contrary to what is stated in much of the literature on this topic. The most convincing finding was that there are straight, linear features that exist in the microstructure that are significantly weaker than other parts. These features are almost imperceptible in standard electron microscopy but it is suggested that they can be seen using

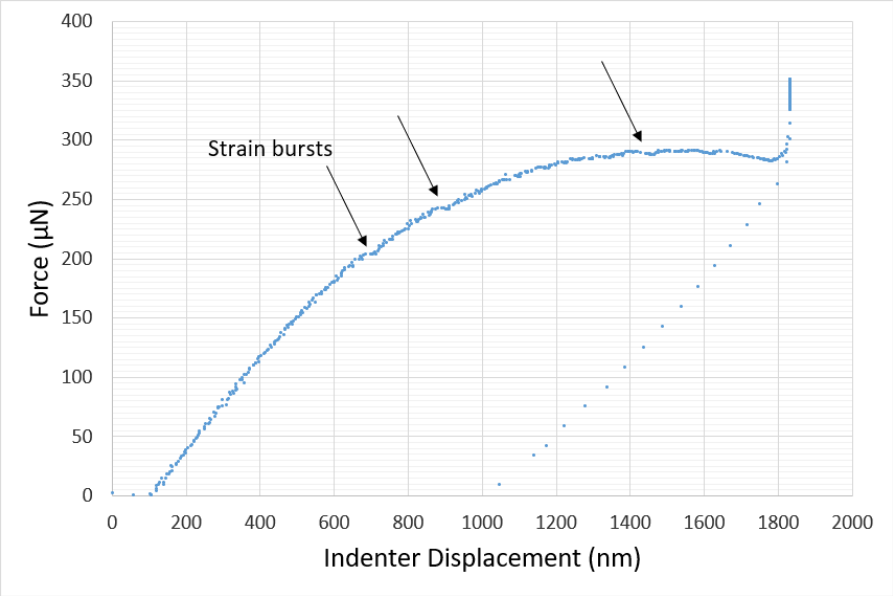

Figure 3.21: Plot of force against nanoindenter tip displacement for a microcantilever with a cobalt binder pool at its root. Several strain bursts or 'pop-ins' can be seen highlighted with black arrows. The force rapidly rises at high displacements because the cantilever has bent until contact with the rest of the sample is made preventing the indenter tip from any further movement.

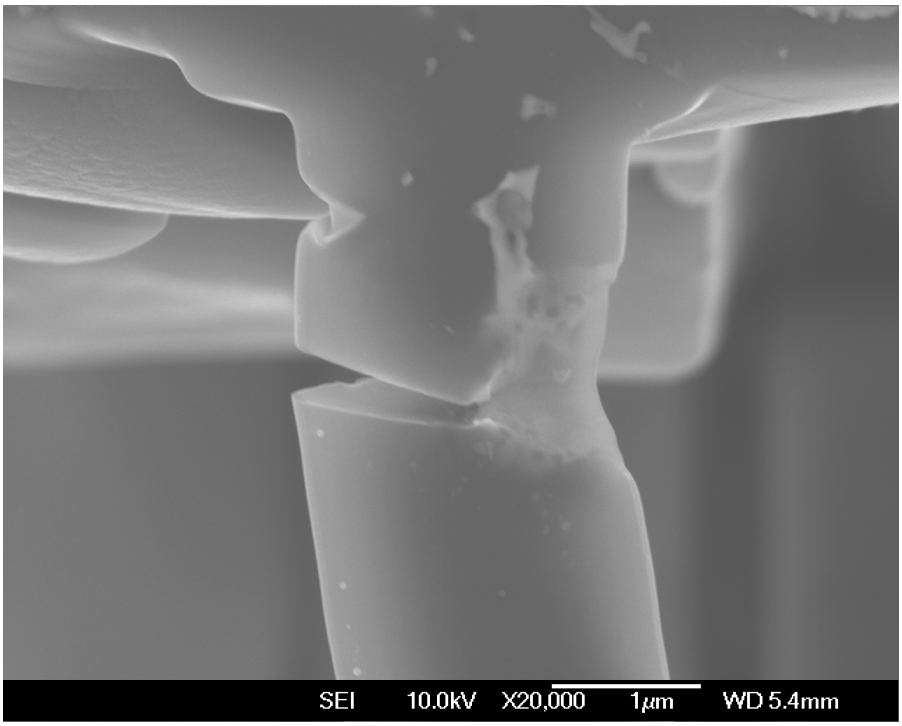

Figure 3.22: FIB image of a fractured microcantilever with a cobalt binder pool at its root. The binder pool can be seen holding the fractured diamond part of the cantilever to the rest of the sample.

cathodoluminescence. Further work is therefore suggested to investigate the origin of these features and more quantitatively measure their mechanical properties.

3.7 Further Work

More work is required to understand the source of flaws in macroscopic strength samples. Although the work presented outlines a potential explanation for the results described here and in the literature, using fractography to identify flaws and how their size changes as a function of microstructure would be very useful. It is suggested that industry is the best place for this study to take place to allow for the vast number of samples that would need to be produced and also to fully control the manufacturing process (including surface finishing) to avoid introducing additional unknown parameters to the problem.

The strength measurements made of microstructural features are the first step to understanding their influence on macroscopic mechanical properties. Attempting to use different micro-notching techniques, including chevron notches, would be highly beneficial in measuring the fracture toughness of these features. It has also been suggested that the features seen in cathodoluminescence spectroscopy may be related to plastic deformation of diamond during manufacture and that these features may have a large influence over the mechanical properties. Firstly, which defects are causing the cathodoluminesence seen in figure 3.17 should be investigated using a cathodoluminescence SEM with a CCD camera for analysing the emission spectrum as a function of position. Secondly, these features would make good candidates for investigation with microcantilever bending tests to verify the suggestion that they are the source of the linear, low strength features observed in this thesis. Finally, further work should be done to understand the factors that affect the degree of plastic deformation in the diamond of sintered PCD and how this affects the macroscopic mechanical properties.

4
Residual Stresses

Contents

4.1 Introduction and Aims 87
4.2 Materials and Sample Preparation 87
4.2.1 Polycrystalline Diamond 87
4.2.2 Diamond Powder 89
4.2.3 Metallic Samples 89
4.3 Experimental Techniques 90
4.3.1 General Materials Diffractometer (GEM) 90
4.3.2 High Resolution Powder Diffractometer (HRPD) 93
4.3.3 Laboratory X-ray Diffractometer 94
4.3.4 Lattice Parameter Calculation 94
4.3.5 Defect Analysis 96
4.4 Results 97
4.4.1 Characterisation of Samples 97
4.4.2 General Materials Diffractometer (GEM) 101
4.4.3 High Resolution Powder Diffractometer (HRPD) 108
4.4.4 Laboratory X-ray Diffractometer 112
4.4.5 Defect Analysis 112
4.5 Discussion 115
4.5.1 Understanding the Sintering Process 115
4.5.2 Direct Observation of the Stress-free Temperature . . . 120
4.5.3 Calculation of the Stress-free Temperature 121
4.5.4 Validation of the Model 124
4.5.5 Predicting the Stress-free Temperature 128
4.5.6 Calculated Residual Stresses 132
4.5.7 Effect on Mechanical Properties 137
4.5.8 Lattice Parameter of Diamond Powder 141
4.6 Conclusions 142
4.7 Further Work 143

4.1 Introduction and Aims

The literature discussed in section 2.2 often makes mention of thermal breakdown of PCD at high temperature due to differences in the thermal expansion coefficient of diamond and cobalt. This effect is never explained quantitatively and no evidence for it operating is given. The present chapter will therefore attempt to quantify the effect and assess whether it is a viable damage mechanism at high temperature. The lattice parameter of diamond in unleached and leached PCD will be measured as a function of temperature using neutron diffraction techniques and a model will be applied to calculate the stresses in the two phases. Finally, the effects of this quantified residual stress on the mechanical properties of PCD will be assessed.

4.2 Materials and Sample Preparation

4.2.1 Polycrystalline Diamond

4.2.1.1 Disc Samples

A number of PCD cutters were manufactured by Element Six Ltd at their Global Innovation Centre (GIC) facility in Harwell, UK. The PCD was pressed at a pressure of 5.5 GPa and a temperature of 1450°C; the grain size of the starting material was 75 microns which was chosen to produce large binder pools, making leaching as easy as possible. All cutters were made with flat interfaces between the WC/Co substrate and the diamond table. After removal from the metal cans, cutters were roughly ground to external dimensions falling within given tolerances. The PCD table was then roughly lapped with a suspension of 20 to 40 µm diamond grit in isopropanol, finely lapped with a suspension of 6 to 15 µm diamond grit and finally polished. Polishing was performed dry with air cooling on a resin bonded scaife containing large diamond particles. PCD tables were then removed from the substrate using electro-discharge machining (EDM) and their back faces roughly lapped to remove

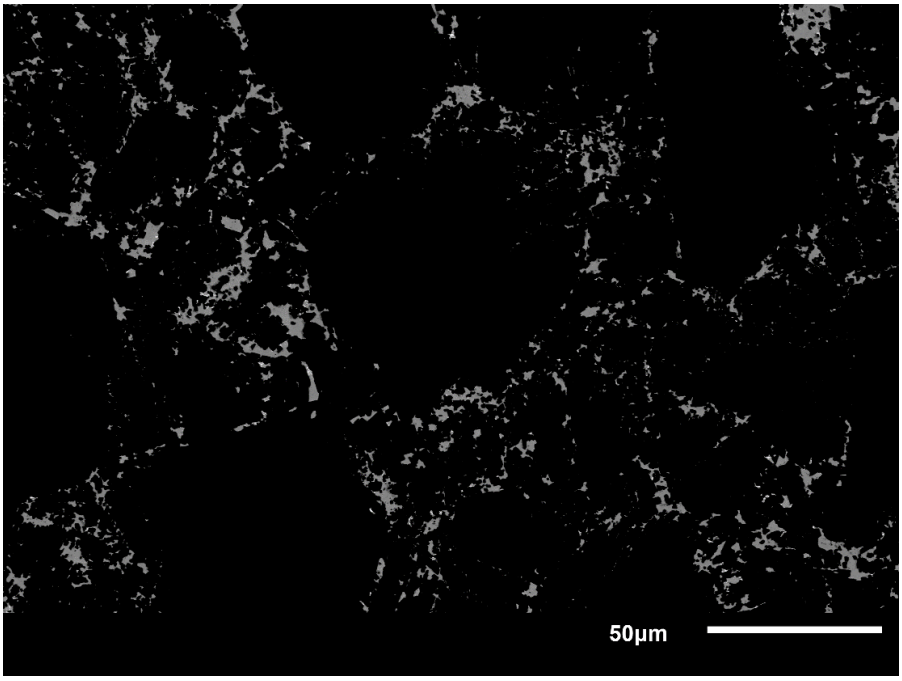

Figure 4.1: Backscattered electron SEM image of the sintered microstructure of the PCD used in HRPD and GEM experiments. Black areas are diamond and grey areas are cobalt. Significant crushing of the starting 75 µm diamond powder can be seen in the reduced size of the larger grains and presence of many small grains.

any residual WC/Co substrate material. Half of the discs were then leached by heating in hydrochloric acid at 109°C for several hundred hours[1]. Final diamond samples were in the form of 16 mm diameter discs with a thickness of approximately 2 mm. Samples of this type were used in experiments on the General Materials Diffractometer (GEM) beamline as described in section 4.3.1. A backscattered electron SEM image of the sintered microstructure is shown in figure 4.1.

4.2.1.2 Bar Samples

Bar samples were first prepared as disc samples identically as described in Section 4.2.1.1. The discs were then EDM cut into beams, typically 5 per disc such that their total length was not less than 12 mm. The thickness of the beam was then reduced by fine lapping such that their final cross-section was 1.5 mm by 1.5 mm. Each beam was left with one polished face that could be used for orientation and

[1]The exact leaching time is commercially sensitive and hence is not included.

three finely lapped faces. These samples were used in experiments on the High Resolution Powder Diffraction (HRPD) beamline as described in a following section.

4.2.2 Diamond Powder

As it was suspected that leached samples would still contain a small amount of residual cobalt and therefore not be perfectly stress free, diamond powder samples were also tested. It is likely that the diamond powder still contains small cobalt defects remnant from the manufacturing process but it was thought that this amount would be much smaller than that in leached PCD and hence diamond powder would be far closer to a stress-free reference. In the GEM experiment (section 4.3.1) 75 µm diamond powder was used and in the HRPD experiment (section 4.3.2) 4 µm powder was used as it was found that the fewer number of grains per unit volume of 75 µm powder produced spotty diffraction patterns.

4.2.3 Metallic Samples

A preliminary diffractogram indicated that only the most intense cobalt peak from the binder phase could be seen and that it had a height of less than one tenth that of the surrounding diamond. This is due to the much weaker neutron scattering cross-section of cobalt in comparison to carbon[118] and its much lower volume fraction in PCD. This problem is further compounded by the similarity in lattice parameters between diamond (3.568 Å) and β-cobalt (3.552 Å) and also the similarity between the diamond cubic structure which consists of two interpenetrating face centred cubic lattices separated along the body diagonal by a quarter of its length and β-cobalt which also has a face centred cubic lattice[119]. As such, it was determined that separate metallic samples were necessary to measure the changes in lattice parameter of cobalt during heating and to act as a stress-free reference sample for the binder phase.

4.2.3.1 Pure Cobalt

A sample was machined from a sheet of 99.9% pure cobalt as a reference to be used to identify the cobalt peaks visible in the neutron diffractograms. The sample was made with a diameter of approximately 16 mm and a thickness of 4 mm.

4.2.3.2 Cobalt/Tungsten Alloy

An Energy Dispersive X-ray (EDX) analysis was performed on a cobalt binder pool in a polished PCD sample to ascertain the relative composition of cobalt and tungsten present in the binder. Although a large amount of carbon is likely dissolved in the binder, EDX is not a reliable technique to measure the amount. Surface contamination with carbonaceous species and the interaction volume generally being larger than the size of the binder pools includes a significant amount of the surrounding extraneous carbon into the measurement volume. Therefore, only the ratio between cobalt and tungsten was considered and a bulk sample was made with this composition using an Arcast Arc200 arc melting furnace from 99.9% pure cobalt and tungsten metals.

4.3 Experimental Techniques

4.3.1 General Materials Diffractometer (GEM)

The experiment, RB1710430, was carried out on the General Materials Diffractometer (GEM) instrument at the ISIS Neutron & Muon source in Harwell, UK. A vacuum furnace was installed on the beamline capable of heating to 1100°C. Samples were held in a hand-made vanadium envelope on the end of a sample stick and had two K-type thermocouples in contact with the outside of the envelope. The samples were held at a 45° angle to the incident beam.

Samples were heated in a "stepped heating" regime as follows: 25°C 30 minutes, 200°C 30 minutes, 400°C 30 minutes, 600°C 30 minutes, 700°C 1 hour, 800°C 1 hour, 900°C 1 hour, 1000°C 1 hour, 800°C 1 hour, 600°C 30 minutes, 400°C 30 minutes. The uneven time steps were chosen as it was expected that only temperatures above

700°C were of particular interest and the limited nature of the beamtime available necessitated time saving wherever possible. Cooling back to room temperature was also unfortunately not possible due to time constraints and long cooling times at lower temperatures in a vacuum. After the last measurement, the sample was cooled rapidly to room temperature by flooding the chamber with helium.

Samples were illuminated with a polychromatic pulse of neutrons at a frequency of 50 Hz; the aperture, or 'jaws', were set at 10 x 10 mm so that the entire beam was incident on the sample. The neutrons diffract according to Bragg's Law:

$$\lambda = 2d_{hkl}sin\theta \tag{4.1}$$

where λ is the neutron wavelength, d_{hkl} the plane spacing and 2θ the scattering angle.

The time-of-flight is recorded and can be used with the de Broglie relationship to calculate the wavelength of the neutrons:

$$\lambda = \frac{ht}{m_n L} \tag{4.2}$$

where h is Planck's constant, t is time-of-flight, m_n is neutron mass and L is the total flight path. These two equations are then combined to find the spacing of the diffracting planes. Software written by ISIS beamline scientists is used to focus the data from the area detectors recorded to produce data in the form of intensity against d- spacing. Diffracted intensity was collected and integrated over the entire time at each temperature. The Rietveld refinement software package TOPAS was used to calculate lattice parameters and weight percentages of the phases present. Yttria and silicon standards whose lattice parameters are known very accurately were run before the experiment began to find calibration constants to accurately convert time-of-flight to d-spacing. Six different banks covering different angular ranges were available and a separate diffractogram could be produced from each one. The most accurate lattice parameter was obtained from bank six due its high backscattering angle of 153.5° removing as much positional inaccuracy of the sample from the measured lattice parameter. The presence of the cobalt peaks did have a noticeable effect on the shape of the diamond peaks and hence it was

included as a phase in the analysis. Due to the additional structure factor rule "hkl all even and h + k + l ≠ 4n" for the diamond cubic lattice versus a simple fcc lattice, a systematic absence forbids the {200} reflection for the diamond phase and hence it is visible for the cobalt phase. Although the addition of the cobalt phase lead to a significant increase in the quality of fit of the entire pattern, as all but one of its peaks overlap strongly with the greater intensity diamond peaks, the value calculated from Rietveld refinement was not deemed sufficiently accurate to determine the lattice parameter of cobalt in PCD. In light of this, single peak fitting was used on the cobalt {200} peak.

4.3.1.1 Calibration

Calibration of the diffractometer was performed immediately before the start of the experiment using two separate calibrants, pure silicon and Ce_2O_3 whose lattice parameters were known very accurately. Machine deadtime (the time-delay introduced by the electronics), instrument geometry and peak shape are the three main quantities that were calibrated. Machine deadtime is a simple time offset that does not vary and is included in the time-of-flight of the neutrons. Instrument geometry varies slightly from the ideal geometry of the designed instrument and this variation is determined using the standard samples with the 'Mantid' software package. This package determines the offsets required to convert time-of-flight from each of the individual detectors to a single d-spacing value. The 'CrossCorrolate' algorithm is used to calculate these and the values calculated are used in the rest of the experiment. Finally, the peak shape must be determined from the actual material of study as this will be significantly different from the reference sample peak shape due to different absorbance of the neutron beam. The reference sample was first refined with known offsets and lattice parameter to get an approximate peak shape. Using this approximate shape, a PCD sample was refined to give the minimal error in peak shape and then this peak shape was fixed for the rest of the refinements.

4.3.2 High Resolution Powder Diffractometer (HRPD)

A follow-up experiment, RB1810570, was conducted on the HRPD instrument at the ISIS Neutron & Muon source with a vacuum furnace installed. PCD samples (as described in section 4.2.1.2) were held in a hand-made vanadium holder with alignment fins to ensure positional and rotational accuracy between differing samples. A single K-type thermocouple contacted the vanadium holder near the sample and the samples were inserted into the furnace at 45° to the incident neutron beam.

The following heating schedules were used:

1. Stepped heating to 900°C:
    - unleached.
    - leached.
    - 4 µm diamond powder.
2. Stepped heating to 600°C:
    - unleached.
3. No heating, repeat room temperature measurements:
    - unleached.
    - leached.

Diffracted intensity was integrated over 15 minute intervals for all heating schedules. Lattice parameter and graphite weight percentage was calculated using the GSAS Rietveld refinement software package.

To assess the error in repeat measurements due to positioning error, a single sample was loaded into the furnace, measured at room temperature and unloaded multiple times. This was also done for nominally identical but physically different samples to assess sample-to-sample variations and at 180° to determine how straight the hand-made sample holder was. Repeat measurements were also made at 90° to determine whether there was significant anisotropy between perpendicular and parallel directions to the surface of the diamond table in the original PCD cutter.

4.3.2.1 Calibration

The calibration of the diffractometer for the HRPD experiments was almost identical to that described in section 4.3.1.1 but LaB_6 was used as the reference sample.

4.3.3 Laboratory X-ray Diffractometer

An attempt was made to remeasure the lattice parameters of diamond powder and the bulk cobalt alloy using a laboratory x-ray diffractometer to calculate the thermal expansion coefficients as a function of temperature. Samples were heated in an Anton Paar HTK-1200N vacuum furnace installed on a Pan Analytical XPERT-PRO diffractometer from room temperature to 900 °C. Diffracted intensity was collected for approximately 40 min in temperature steps of 20 °C. Each diffractogram was then analysed using Rietveld refinement to calculate the lattice parameter of the sample at each temperature.

4.3.4 Lattice Parameter Calculation

4.3.4.1 Rietveld Refinement

Rietveld refinement[120] was used to calculated lattice parameters and weight percentages from neutron diffraction data using either the TOPAS[121] (for data from GEM) or GSAS[122] (for data from HRPD) software package. Rietveld refinement uses an iterative least-squares minimisation routine to approximate a diffractogram from a collection of given inputs such as the crystal structures of the known phases, experimental geometry (flight path length, Bragg angle) and instrumental parameters. The instrumental parameters are determined by performing a diffraction experiment on a standard sample whose properties are known with a high degree of precision. There are three main instrumental parameters (referred to as 't0', 't1' and 't2' in TOPAS; 'ZERO', 'DIFC' and 'DIFA' in GSAS) that are used in converting the time of flight of neutrons into the d-spacing of the atomic planes they diffracted from. 'ZERO' is a term constant with d-spacing that accounts for small differences between timing signals within the particle accelerator. It is instrument dependent and so is calculated from the standard sample and

then fixed. 'DIFC' ('t2') is the relationship between time-of-flight and d-spacing derived from equations 4.1 and 4.2:

$$t = \left(\frac{2m}{h}\right) Lsin\theta\, d$$
$$t = 505.56 L \sin\theta\, d$$
$$DIFC = 505.56\, L \sin\theta$$

(definitions as above) and after being calculated from the standard, this is held constant for each detector bank (each value of L and θ). 'DIFA' accounts for the fact that the neutron absorption cross-section of an atom is wavelength dependent and as pulses of neutrons from the ISIS beamline are polychromatic, a range of wavelengths are present in each pulse. This parameter has a quadratic dependence on d-spacing and is sample dependent and hence is a refined parameter.

The peak shape used is a pseudo-voigt peak convoluted with two back-to-back exponential functions which have parameters that can vary independently to account for the inherently asymmetrical peak shape of the neutron beam at ISIS. Initial values of peak-shape parameters were found from the standard sample but then refined for each measurement sample at room temperature and fixed for the duration of each experiment. A Gaussian and Lorentzian broadening were also applied to each peak to account for broadening due to strain.

4.3.4.2 Single Peak Analysis

A bespoke peak fitting routine was written using the Python 2 programming language to determine an equivalent lattice parameter from the {200} peak of cobalt in the PCD diffractograms. A polynomial background was fit to the region between the two adjacent diamond peaks and a pseudo-Voigt peak used to fit the cobalt peak. The centre of this peak was taken to be the {200} plane spacing and an equivalent lattice parameter was calculated using:

$$a_{Co} = d_{hkl}\sqrt{h^2 + k^2 + l^2} \tag{4.3}$$

where in this case, $h = 2$, $k = 0$ and $l = 0$.

4.3.5 Defect Analysis

A sample of the 75 µm diamond powder used in the GEM experiments was partially sealed in a quartz tube to allow gas to escape but to keep the powder particles inside and heated to 800 °C in a vacuum furnace for 3 h. This sample was then compared with an unheated sample of the same powder.

4.3.5.1 Raman Analysis

Samples of the heated and unheated powders were placed on glass slides and examined in a Horiba Scientific LabRAM ARAMIS Raman microscope with a 532 nm Helium-Neon laser. The instrument's spectrometer was calibrated to a silicon wafer standard using the automatic calibration routine giving an accuracy of the measured Raman shift of $\pm$ 0.5 cm^{-1}. This calibration was done once at the start of the experiment and all measurements used this calibration.

A 50x magnification super long working distance objective lens was used to focus the laser spot on the top face of each diamond grain. The numerical aperture of 0.45 gave a spot size of approximately 1.5 µm. The diffraction grating used had a line density of 600 mm^{-1} and a slit width of 180 µm was used. The laser power was set to 10 % and each measurement consisted of 10 separate exposures to both prevent saturation of the CCD and achieve an acceptable signal-to-noise ratio in the spectrum.

Raman spectra were collected from twenty individual grains from each sample. The peak position of the main diamond Raman peak (typically centred around 1332 cm^{-1}) was measured using a custom peak fitting routine written in the Python programming language.

4.3.5.2 Electron Paramagnetic Resonance

Diamond has many optical defects, typically involving some combination of nitrogen atoms and/or carbon vacancies. One of the simplest of these defects is the single substitutional nitrogen defect where a nitrogen atom replaces a carbon atom in the diamond crystal structure. Electron paramagnetic resonance (EPR) spectroscopy is

a technique that uses the tendency for defects with non-zero magnetic moments (such as the single substitutional nitrogen defect in its neutral charge state, N_s^0) to align their spins either parallel or anti-parallel with an applied magnetic field (Zeeman Effect[123]), thereby creating a splitting in the energy level of the defect whose magnitude is dependant on the magnetic field applied. Due to the Maxwell-Boltzmann distribution, the majority of defects will exist in the lower energy state so that when the sample is exposed to electromagnetic radiation whose photons have an energy equal to the difference in energy between the two states (typically radio waves of frequency 9–10 GHz) these defects will be promoted to the higher energy state causing a net absorption of energy. Each optical defect will have a characteristic absorption spectrum determined by the energy levels of the defect and their degeneracy caused by the Zeeman effect. The spectrum of each defect can be mapped by taking the first derivative of the absorbance of electromagnetic radiation as the magnetic field is scanned. In this particular experiment N_s^0 was the only defect of interest and its quantification was achieved by comparison with a well characterised single crystal HPHT diamond with an N_s^0 concentration of 270 ppm and the fact that the double integral of the EPR signal (single integral of the absorbance) is directly proportional to the number of magnetic spins in the sample. A Bruker EMX spectrometer with a 4122 HS cylindrical cavity resonator was used with radio waves of 9.75 GHz frequency. The data collection and quantification of N_s^0 concentration was performed by Dr Ben Breeze, University of Warwick, UK using in-house written software[124].

4.4 Results

4.4.1 Characterisation of Samples

4.4.1.1 PCD Cobalt Content

Inductively coupled plasma (ICP) etching of leached and unleached materials (figure 4.2) indicates that after leaching there is approximately 2.1 weight percent cobalt remaining. Even after a much more aggressive hydrofluoric- nitric acid etch, this remaining amount is mostly unchanged. The reduction in tungsten content

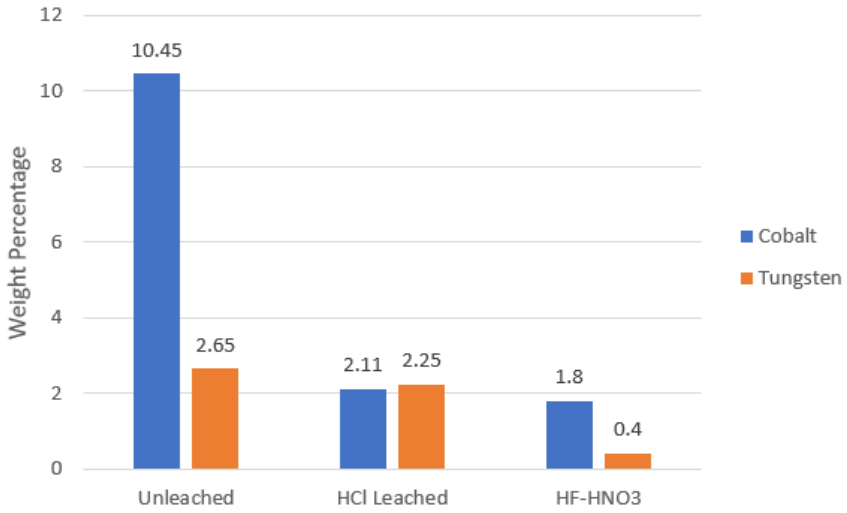

Figure 4.2: ICP etching results showing weight percentages of cobalt and tungsten after no leaching, a standard HCl leach and a more aggressive HF-HNO_3. The error in weight percentage measured by this technique is 0.1 wt%.

after the more aggressive etch is caused by hydrofluoric acid being capable of dissolving WC precipitates whilst hydrochloric acid being incapable. The lack of significant change in cobalt content is due to a small fraction of binder pools being completely enclosed by diamond and hence impossible to remove with a liquid etch regardless of its potency.

4.4.1.2 Scanning Electron Microscopy

Figure 4.3 shows a focussed ion beam (FIB) milled cross-section of the leached material with an overlain EDX map showing cobalt pools that still remain after leaching.

4.4.1.3 Cobalt Phase Elemental Composition

Figure 4.4 shows an EDX map of a binder pool in unleached PCD. Several regions showing high concentrations of tungsten can be seen (thought to be tungsten carbide). An area visibly free from these precipitates was chosen for the elemental composition analysis as it was the bulk alloy composition that was of interest and these precipitates would skew the results towards tungsten. Figure 4.5 shows an EDX line scan of such an area with the calculated amounts of cobalt and tungsten.

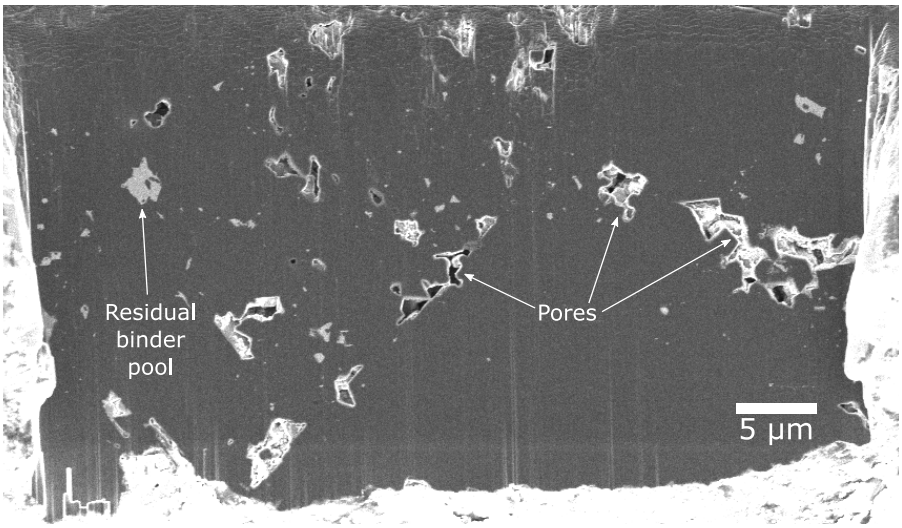

Figure 4.3: Secondary electron image of a FIB-milled cross-section in a leached sample with an EDX overlay showing cobalt content (cyan). Both pores where binder pools have been leached out and isolated pores containing retained cobalt can be seen.

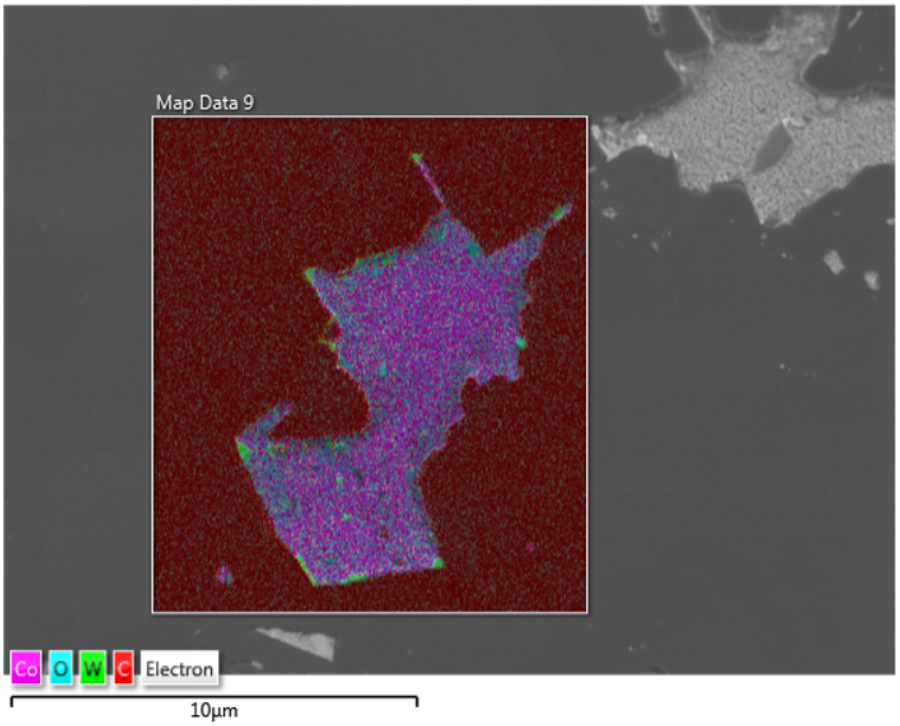

Figure 4.4: EDX map of a cobalt binder pool showing several high tungsten concentration regions. An area that was visibly free of the precipitates was chosen to measure the bulk tungsten concentration of the cobalt phase.

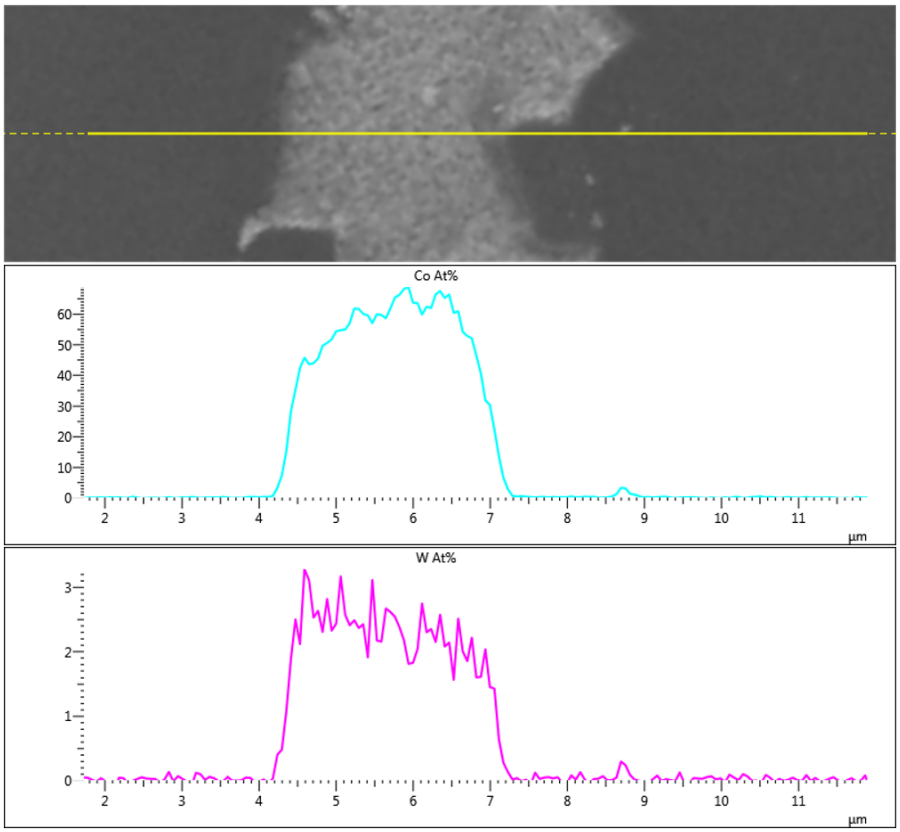

Figure 4.5: Line scan of a region of the EDX map shown in figure 4.4 showing atomic concentrations of cobalt and tungsten as a function of position along the line. The cobalt (cyan) and tungsten (magenta) concentrations can be seen to vary slightly across the width of the binder pool.

A bulk alloy was made using the relative concentration of cobalt and tungsten taken from figure 4.5. Figure 4.6 shows an EDX map of a polished section of the resultant alloy with table 4.1 showing the calculated amounts of tungsten and cobalt compared to those in the PCD binder pool. The EDX map shows a uniform distribution of all elements but as the boiling point of cobalt (2900°C [125]) is below the melting point of tungsten (3422°C[126]) it is likely that a significant proportion of the cobalt boiled off during melting. A surplus of cobalt was added for this reason but the resulting alloy still has an enrichment of tungsten compared to cobalt and time restraints on the beamline experiment prevented another attempt at manufacture of this sample.

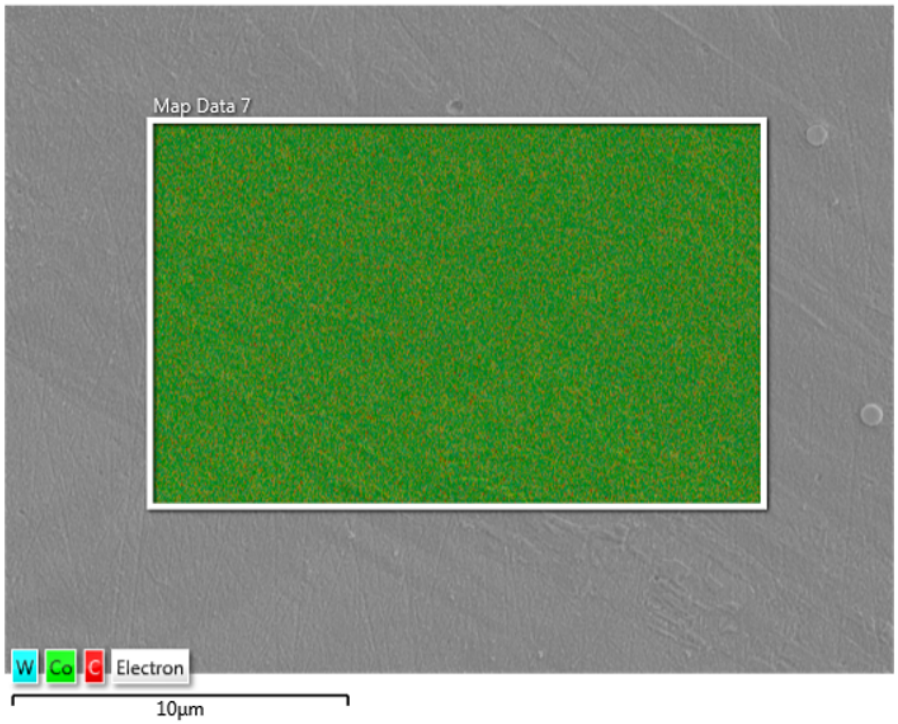

Figure 4.6: EDX map of a polished cross-section of the bulk alloy showing a uniform distribution of tungsten and cobalt. Several regions were tested and no concentrated regions of tungsten were found.

	Carbon	Oxygen	Cobalt	Tungsten	W:Co Ratio
PCD Binder Pool	49.2	5.1	43.9	1.8	0.038
Bulk Alloy	12.1	2.0	82.2	3.8	0.044

Table 4.1: Table of atomic percentages of elements within a PCD binder pool and the bulk cobalt-tungsten alloy calculated from EDX data.

4.4.2 General Materials Diffractometer (GEM)

4.4.2.1 Diamond Lattice Parameter

Figure 4.7 shows a neutron diffractogram from the backscattering bank displayed as intensity against time-of-flight with the difference curve between calculated and measured intensities shown below in grey. A higher magnification view of the (220) diamond peak is shown in figure 4.8 showing the good agreement between the Rietveld model and the measured diffraction intensity.

For each temperature, the lattice parameter of diamond was calculated using Rietveld refinement and this is plotted in figure 4.9. The statistical error in fitting

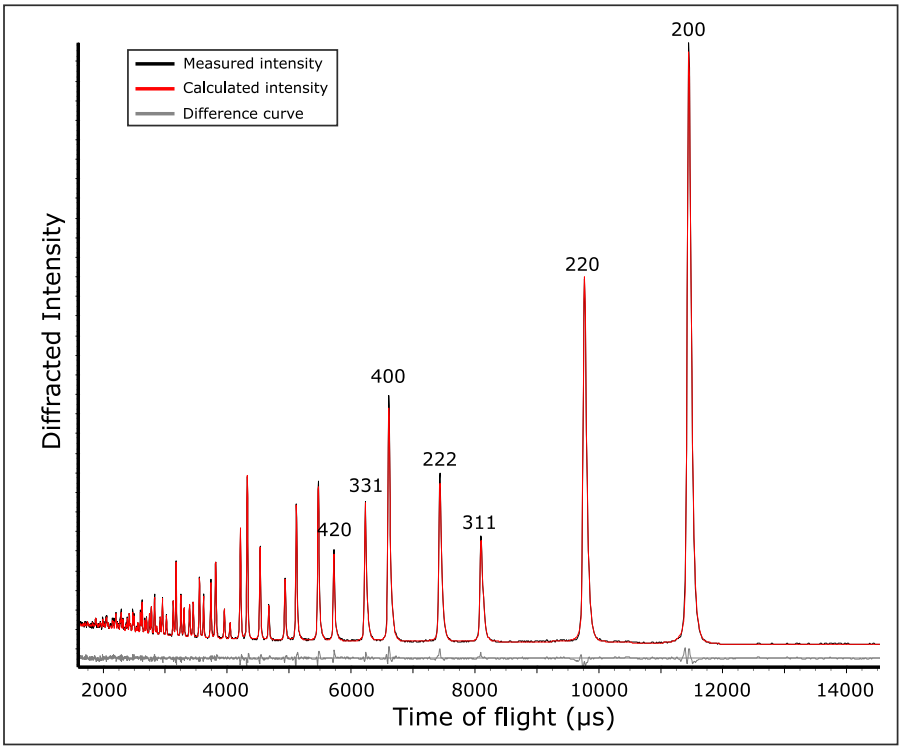

Figure 4.7: Unleached PCD diffractogram from GEM bank 6 (backscattering bank) also showing Rietveld refinement calculated diffraction intensity. Several diamond diffraction peaks are labelled. The small difference between the measured and calculated diffraction intensities is shown by the grey difference curve.

the predicted peak shape to the measured data calculated by the refinement software was on the order of 0.000 03 Å for all diamond lattice parameters. The unleached material (blue) begins at room temperature with a lower lattice parameter than the leached material (orange) but between 600 and 700°C a cross- over is observed. At all temperatures, the diamond powder lattice parameter (grey) is significantly below that of both leached and unleached PCD. The "room temperature" lattice parameter measurements were actually taken at temperatures ranging between 22°C and 74°C. This was due to the large thermal mass of the vacuum furnace having insufficient time to cool down exactly to room temperature (approximately 22°C) between heating runs due to time constraints.

4.4.2.2 Cobalt Lattice Parameter

A diffractogram of the pure cobalt sample at room temperature is shown in figure 4.10. At room remperature, the hexagonal close packed phase makes up the

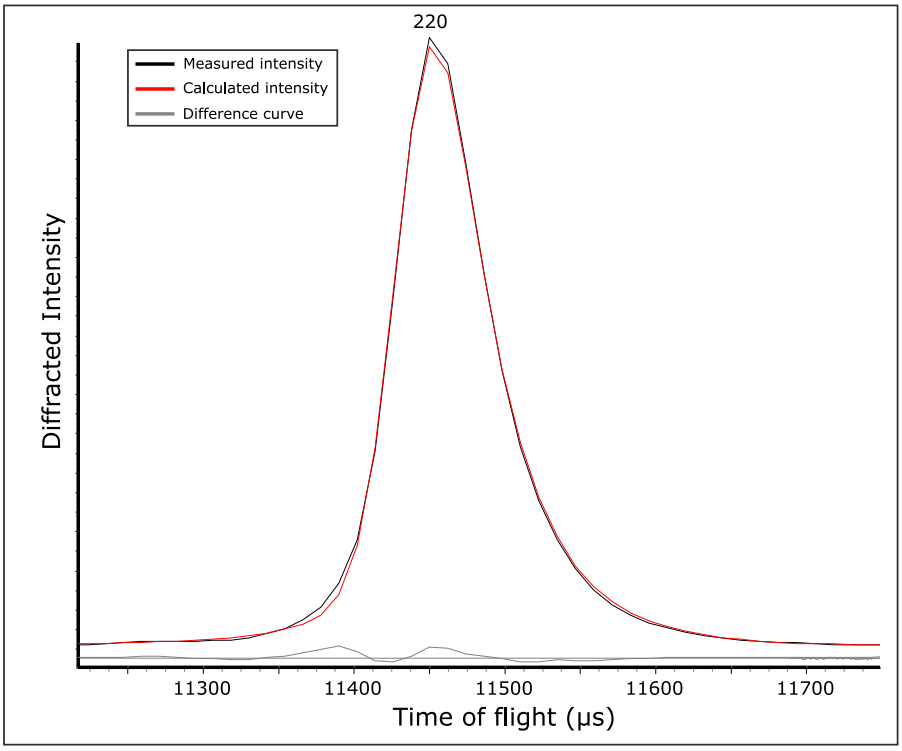

Figure 4.8: Zoomed in view of the diamond {220} diffraction peak from figure 4.7 showing good agreement with the Rietveld refinement calculated and measured diffraction intensities.

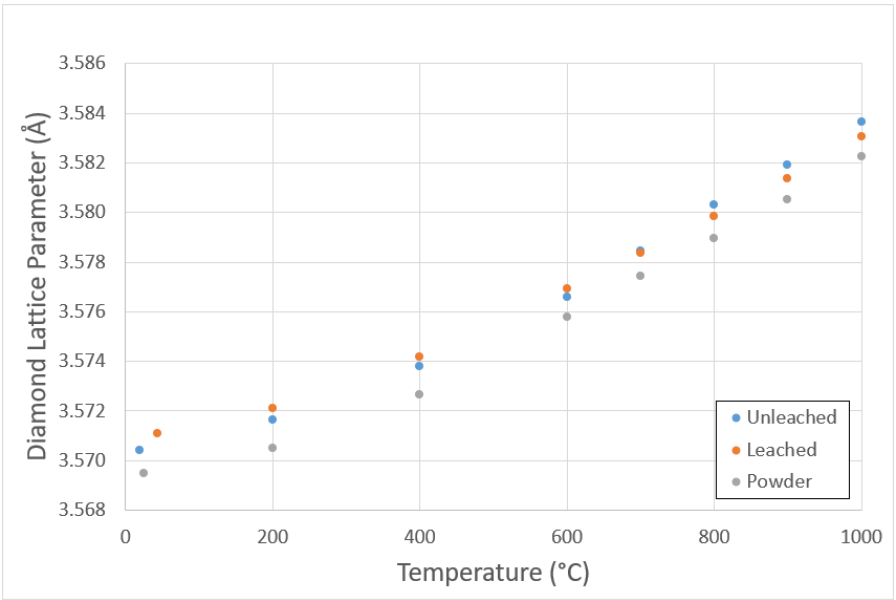

Figure 4.9: Diamond lattice parameters of unleached PCD, leached PCD and diamond powder as a function of temperature from the GEM experiment calculated by Rietveld refinement. Statistical peak fitting error was on the order of 0.000 03 Å for all diamond lattice parameters.

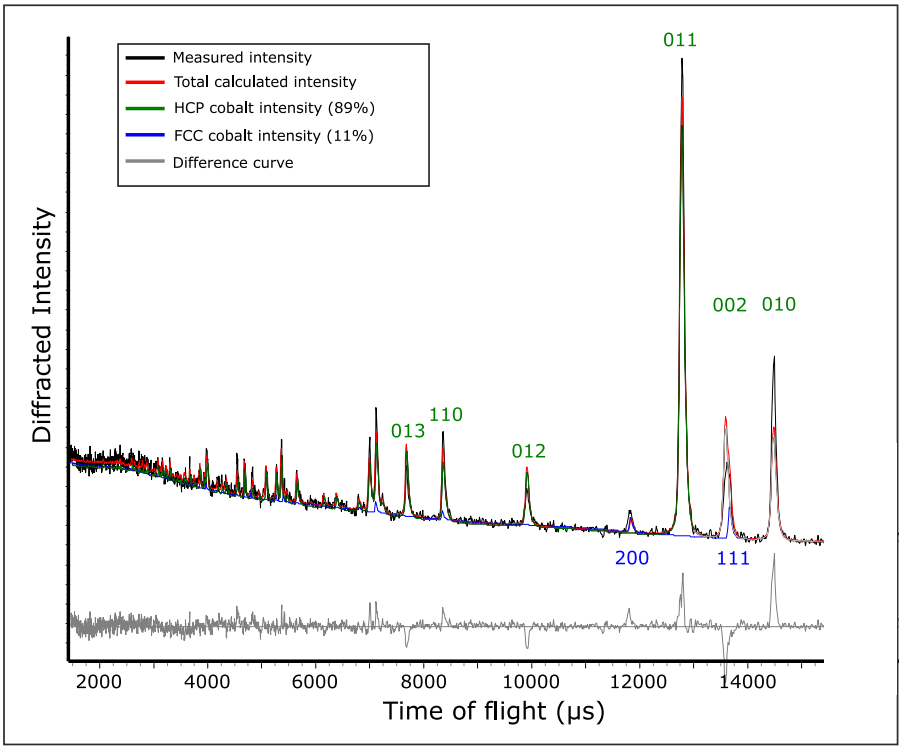

Figure 4.10: Diffractogram from GEM of pure cobalt at room temperature. Mainly HCP cobalt is seen (green, 89 weight percent) but some FCC cobalt (blue, 11 weight percent) is retained.

majority of the sample with a smaller amount of the face centred cubic phase present. Although the phase diagram predicts that HCP-cobalt is the stable phase under ambient conditions, the very low free energy difference between the two phases often results in retention of some FCC-phase[127]. At temperatures of 600°C and above the diffractogram changes to that shown in figure 4.11 due to the phase transition from HCP to FCC-cobalt at 420°C[128]. The cobalt-tungsten alloy, however, appears to exist only in the FCC structure even at room temperature as shown by the room temperature diffractogram in figure 4.12.

The lattice parameters of pure cobalt (at temperatures where it is in the FCC phase) and the FCC cobalt-tungsten alloy are shown as a function of temperature in figure 4.13. The statistical errors in fitting peaks to the cobalt diffraction data was on the order of 0.0003 Å calculated by the refinement software for all cobalt lattice parameters. Figure 4.14 shows a higher magnification view of the allowed cobalt {200} reflection (bank 5, 91°) from the binder phase in PCD which sits between the

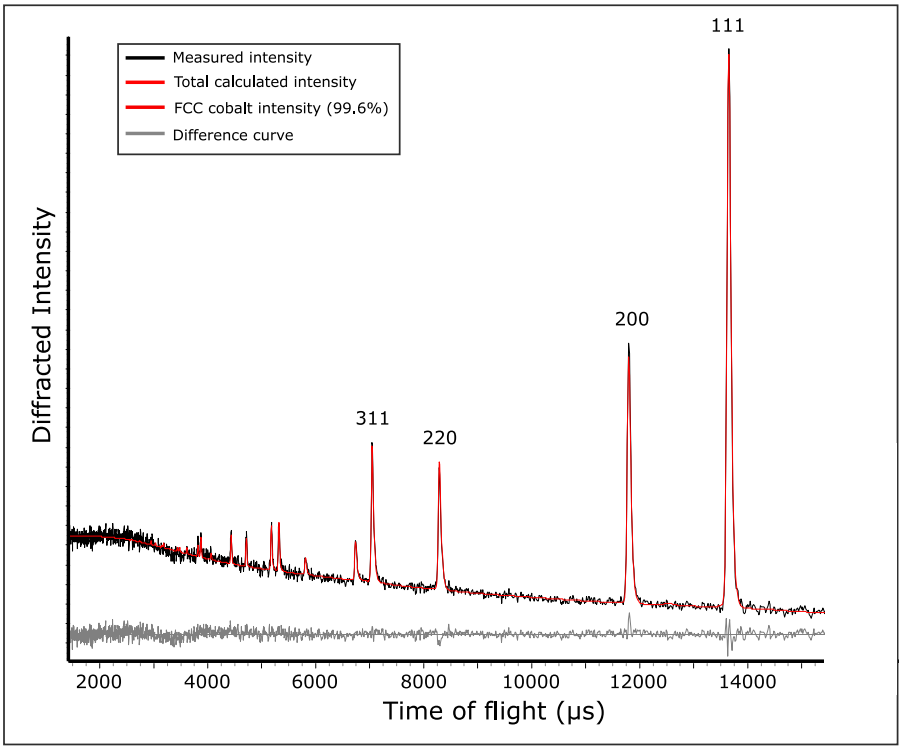

Figure 4.11: Diffractogram from GEM of pure cobalt at 600 °C. Almost all of the low temperature HCP cobalt phase has transformed into the high temperature FCC phase which is calculated at representing 99.6 weight percent of the sample.

{111} and {220} diamond peaks. Single peak analysis was performed on this peak and the same peak from the cobalt-tungsten alloy diffractogram, shown in figure 4.15.

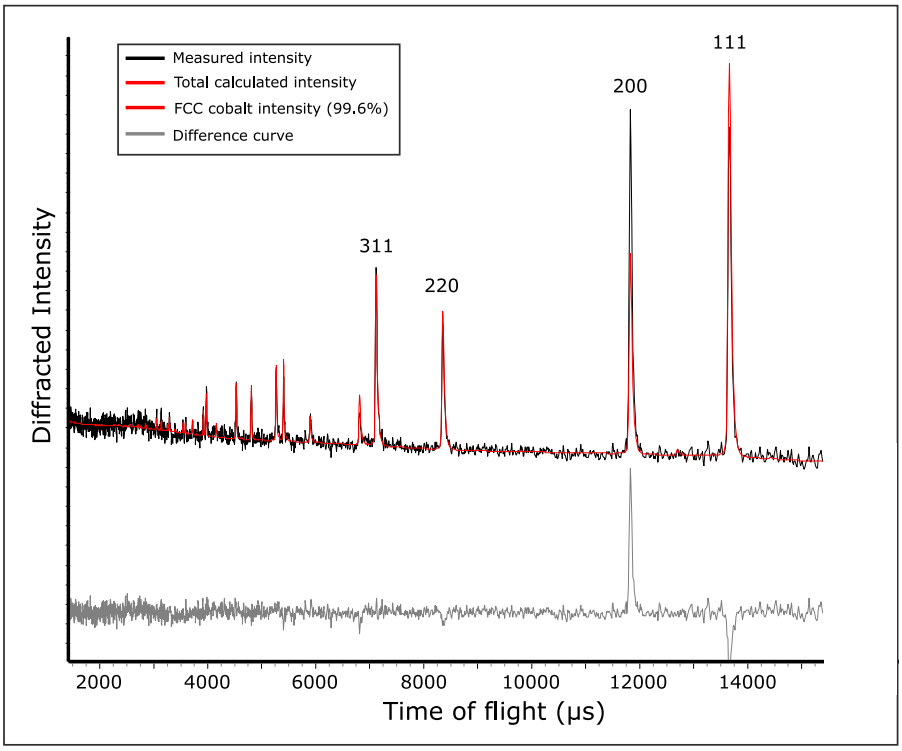

Figure 4.12: Diffractogram from GEM of the bulk cobalt-tungsten alloy at room temperature. The added tungsten can be seen to stabilise the FCC phase (which would normally only be present at high temperatures) at room temperature. The ratio of peak heights of the {111} and {200} peaks have changed relative to that seen in the FCC phase of the pure cobalt (figure 4.11) due to the different scattering factor of the tungsten atoms which now occupy some of the cobalt lattice sites. This is not taken account of in the refinement and can be seen as the large peaks in the grey difference curve.

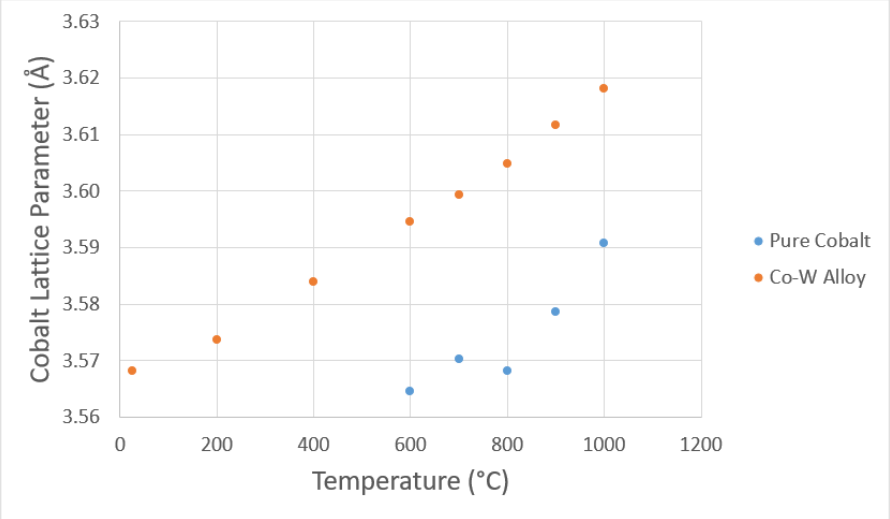

Figure 4.13: Lattice parameters of FCC cobalt (above 400 °C) (blue) and the bulk cobalt-tungsten alloy (orange) as a function of temperature measured on GEM. The statistical peak fitting error was on the order of 0.0003 Å for all cobalt lattice parameters.

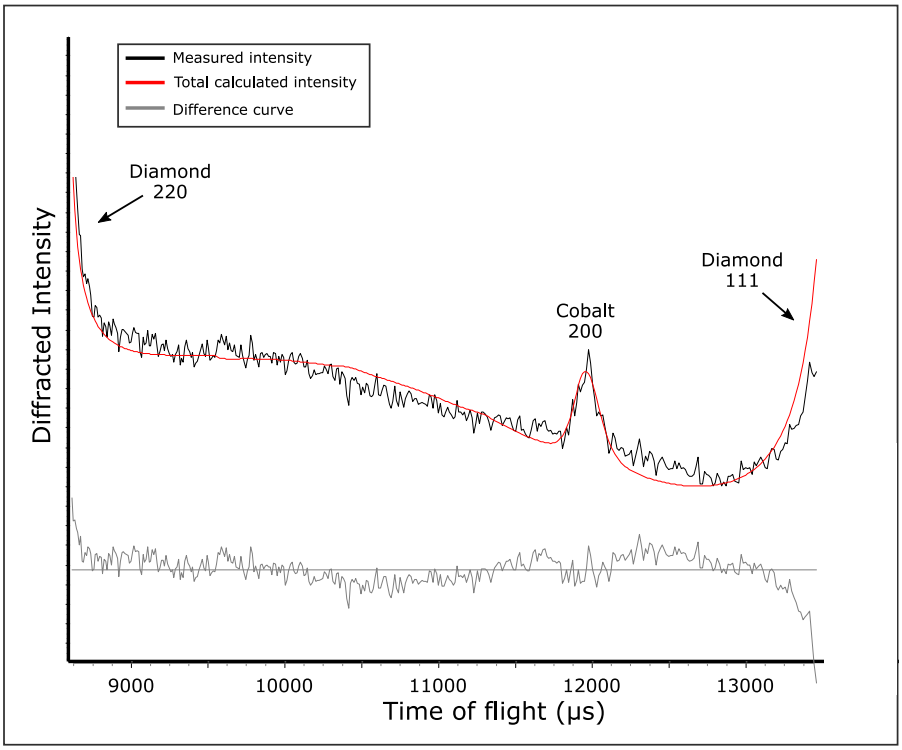

Figure 4.14: Cobalt {200} peak seen in the diffractogram of unleached PCD at room temperature from GEM. This is the only visible cobalt peak that does not overlap with (and hence is completely obscured by) one of the diamond peaks.

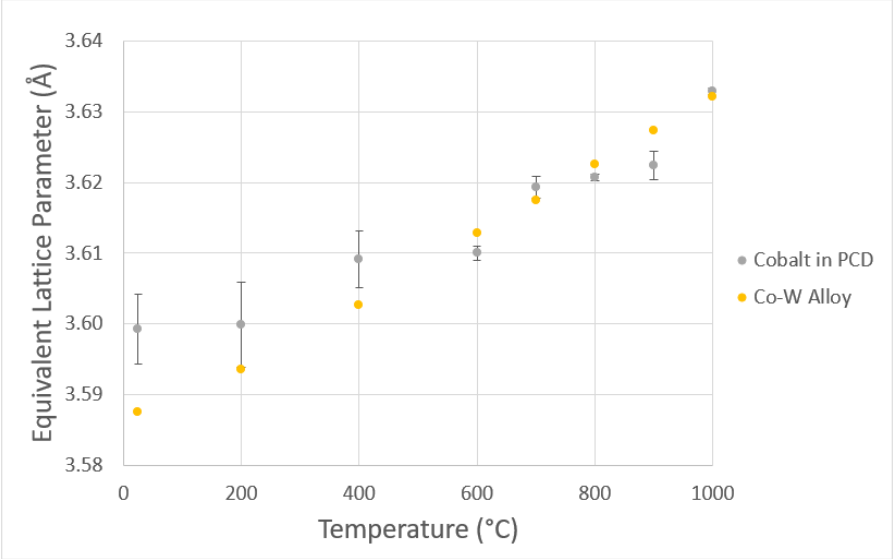

Figure 4.15: Lattice parameter of the bulk cobalt-tungsten alloy (yellow) and the lattice parameter calculated from the position of the cobalt {200} peak that was visible in the diffraction patterns of PCD as a function of temperature. The error bars show the standard error in the single cobalt peak position calculated by the 'lmfit' Python module used to calculate the position of the peak. The statistical error in the Co-W alloy peak position is on the order of 0.0003 Å reported by the refinement software.

4.4.3 High Resolution Powder Diffractometer (HRPD)

4.4.3.1 Diamond Lattice Parameter

Figure 4.16 shows a diffractogram from the unleached material at room temperature. Comparing this to the diffractograms from the GEM instrument, it can be seen that the counting statistics from HRPD are much poorer giving a much noisier result. This is due to HRPD having around half the neutron flux of GEM and also the significantly smaller samples used in this experiment whilst keeping the counting time approximately the same. By magnifying the {111} peak (figure 4.17), reasonably good agreement can be seen between the position of the calculated peak position with that of the measured data. The roughly symmetrical peak in the difference curve shows that the error is in peak height rather than peak position. The room temperature diffractogram for the powder is shown in figure 4.18.

Calculated lattice parameter vs. temperature is plotted for leached, unleached and powder materials in figure 4.19. As with figure 4.9, the unleached lattice parameter begins at a lower value than the leached one at room temperature, exhibiting a cross-over at around 700°C. The diamond powder lattice parameter is significantly lower than both leached and unleached PCD at all temperatures but room temperature.

4.4.3.2 Cobalt Lattice Parameter

At temperatures of 600°C and above, the cobalt {200} peak becomes visible and also the {111} peak moves away from the diamond {111} peak sufficiently to be resolved separately. This allows a lattice parameter to be calculated confidently for the cobalt binder phase in PCD above this temperature. This occurs due to recrystallisation and/or recovery of the cobalt binder pools. The fact that the cobalt {200} peak is visible once the PCD is cooled down below 600 °C again supports this hypothesis. On heating, below 600°C, the {200} peak is not visible above the level of the noise and the {111} peak has to be deconvoluted from that of the diamond making its exact position and hence lattice parameter much less certain. The variation of the cobalt lattice parameter with temperature is shown in figure 4.20.

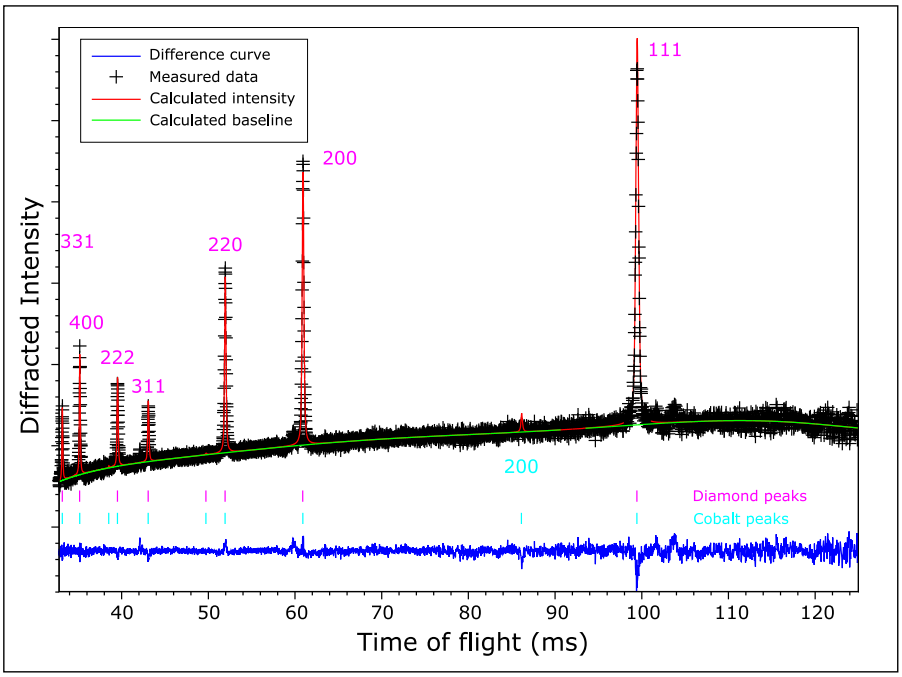

Figure 4.16: Diffractogram from HRPD of unleached PCD at room temperature. The measured diffraction intensity is shown by black crosses and the diffracted intensity calculated by Rietveld refinement is shown by a red line. Diamond peaks are labelled in magenta and the one cobalt peak is labelled in cyan but this peak is not strong enough to be seen above the background noise. The difference between the measured and calculated intensities is shown in blue.

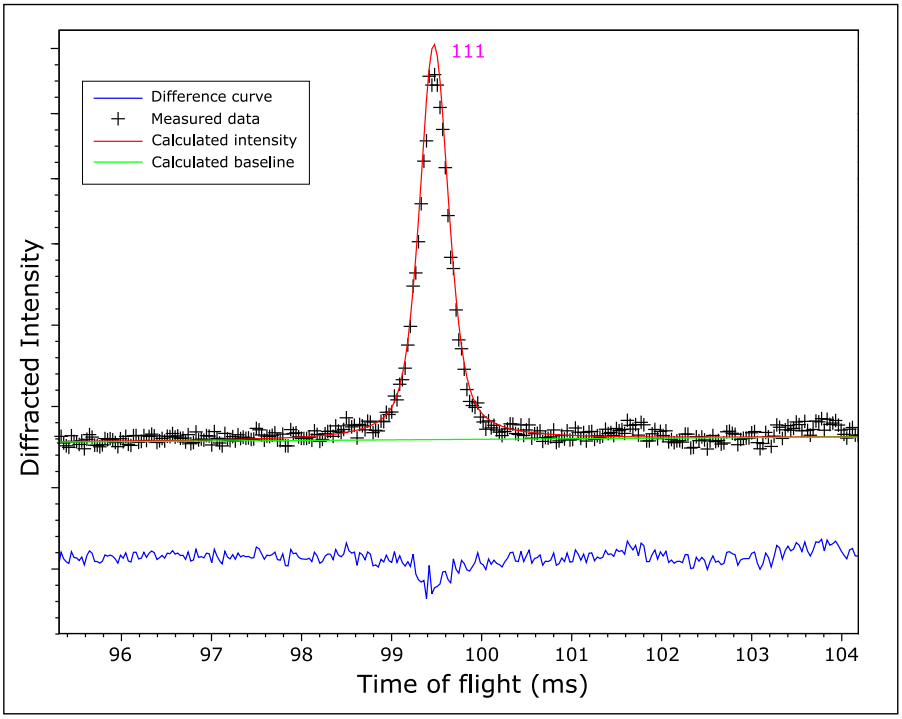

Figure 4.17: Zoomed in view of the {111} diamond peak from figure 4.16. The slight overestimation of the peak height by the refinement can be seen as a dip in the blue difference.

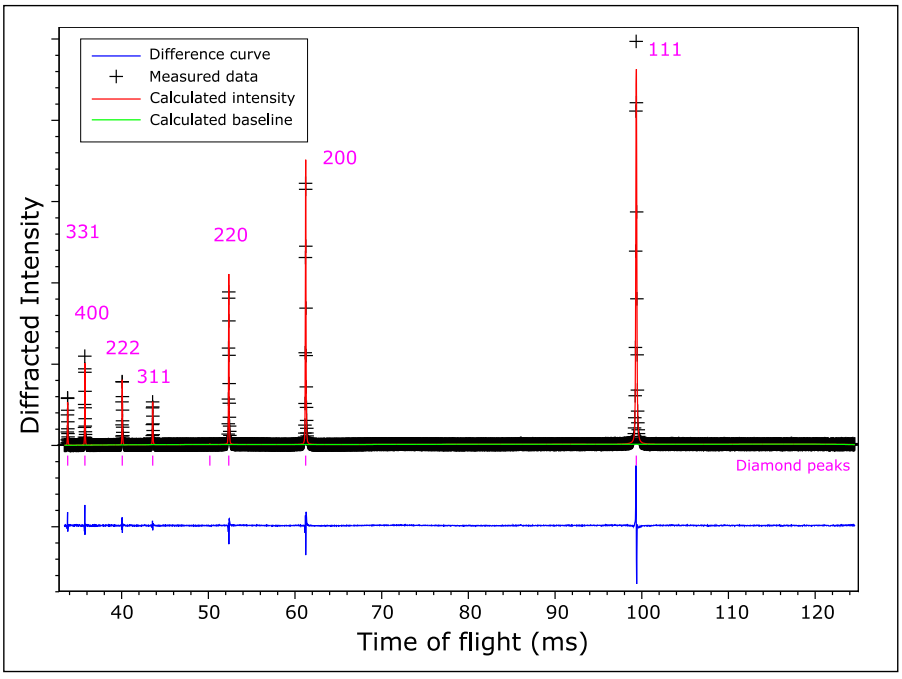

Figure 4.18: Room temperature diffractogram of diamond powder from HRPD. The signal-to-noise ratio was much better for the diamond powder as a large volume of it was used that for the PCD. The refinement has been unable to perfectly fit the peaks as seen by the peaks and troughs around and it is not clear why this was the case.

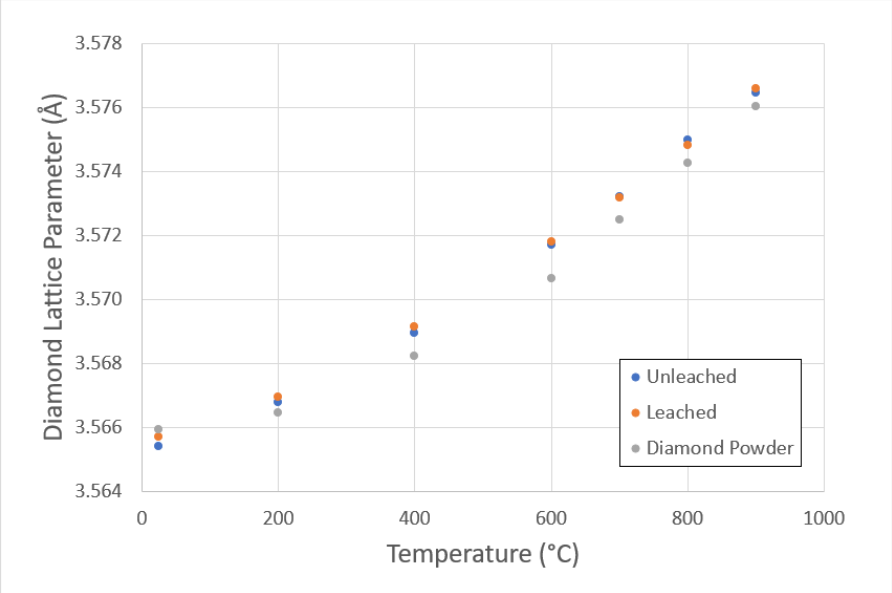

Figure 4.19: Diamond lattice parameter for unleached and leached PCD and diamond powder as a function of temperature for the HRPD experiment, calculated with Rietveld refinement. The uncertainty in the diamond lattice parameter is characterised by the statistical peak fitting error calculated by the refinement software and is on the order of 0.000 03 Å.

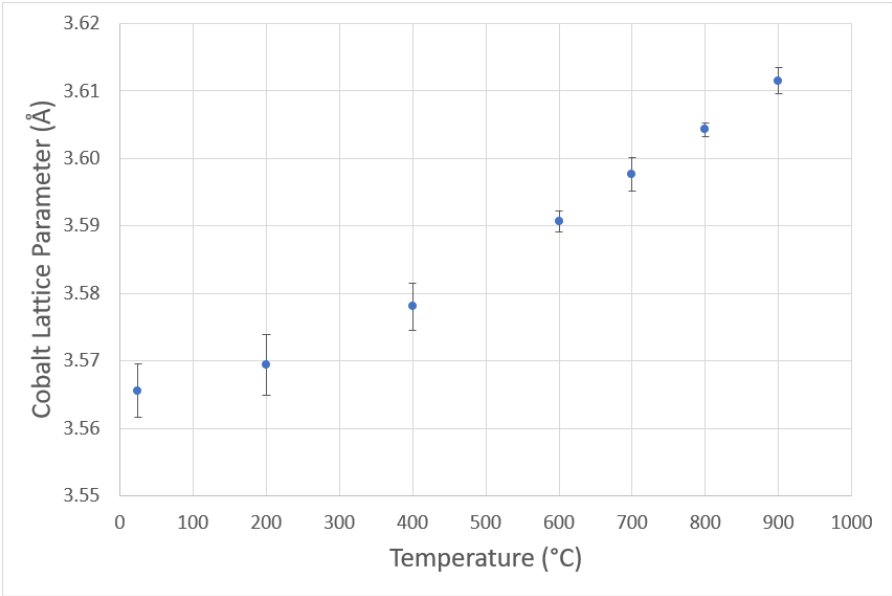

Figure 4.20: Lattice parameter of cobalt calculated from the peak position of the cobalt {200} peak visible in the diffractograms of unleached PCD from GRPD. From 400 °C and below, the intensity of the cobalt peak was very close to the level of the noise and so its calculated lattice parameter has a larger uncertainty. The error bars show the standard error in the peak fit position calculated by the 'lmfit' Python module used to calculate the cobalt peak position.

4.4.4 Laboratory X-ray Diffractometer

Figures 4.21 and 4.22 show the remeasured diamond powder and cobalt alloy lattice parameter values as a function of temperature. The signal-to-noise ratio of the measurements was significantly worse than the neutron diffraction experiments and so some refinements produced clearly incorrect lattice parameter results and have been omitted from the figures as a result.

4.4.5 Defect Analysis

The values obtained from measuring the position of the first order Stokes Raman peak of the sample before and after heating is shown in figure 4.23. Before heating, it had an average value of $1329\,\mathrm{cm}^{-1}$ and after a value of $1334\,\mathrm{cm}^{-1}$. An example EPR spectrum is shown in figure 4.24 and the average concentration of N_s^0 defects before heating was (140 ± 14) ppm and after (120 ± 12) ppm each based on measurements of two separate samples.

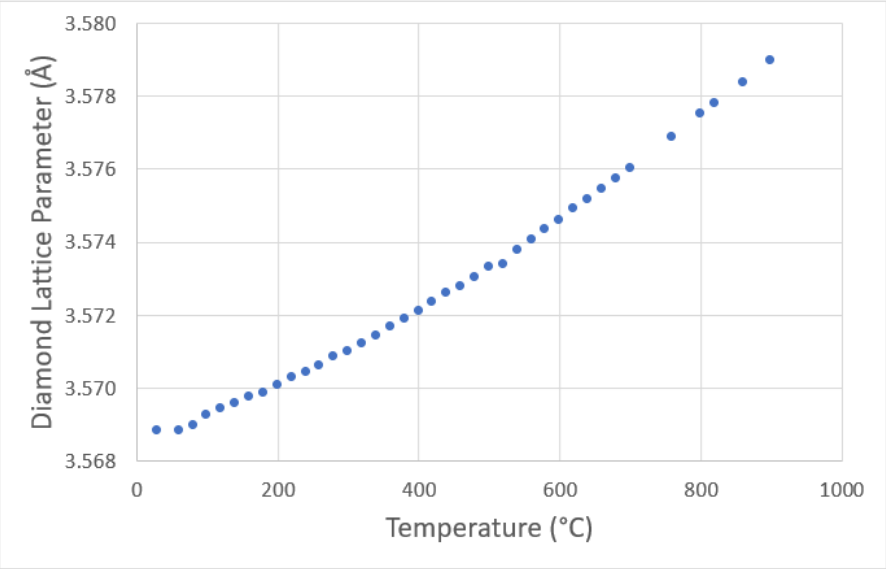

Figure 4.21: Diamond lattice parameter as a function of temperature calculated from Rietveld refinement of laboratory X-ray diffraction data. The uncertainty in the diamond lattice parameter is given by the statistical peak fitting error output by the refinement program and was on the order of 0.000 04 Å for all results.

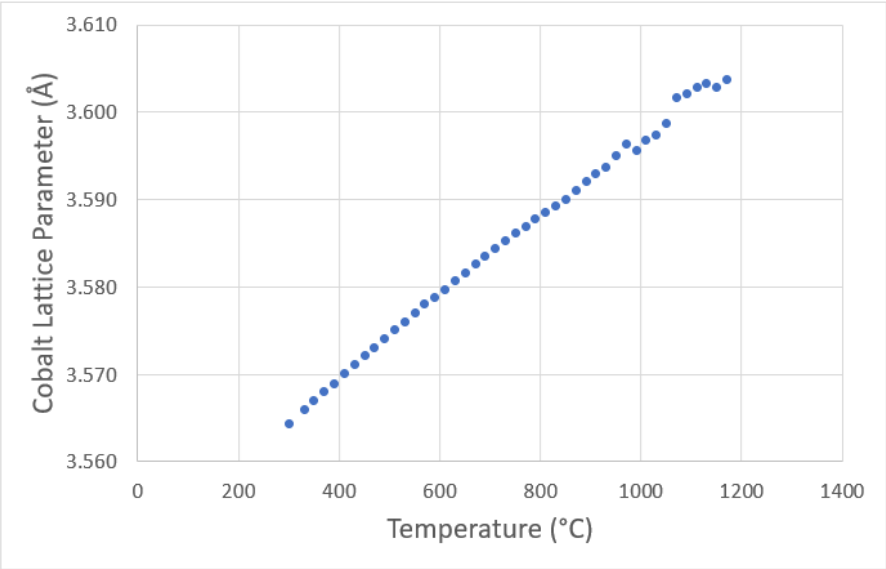

Figure 4.22: Cobalt-tungsten alloy lattice parameter as a function of temperature calculated from Rietveld refinement of laboratory X-ray diffraction data. The uncertainty in the cobalt lattice parameter is given by the statistical peak fitting error output by the refinement program and was on the order of 0.0002 Å for all results.

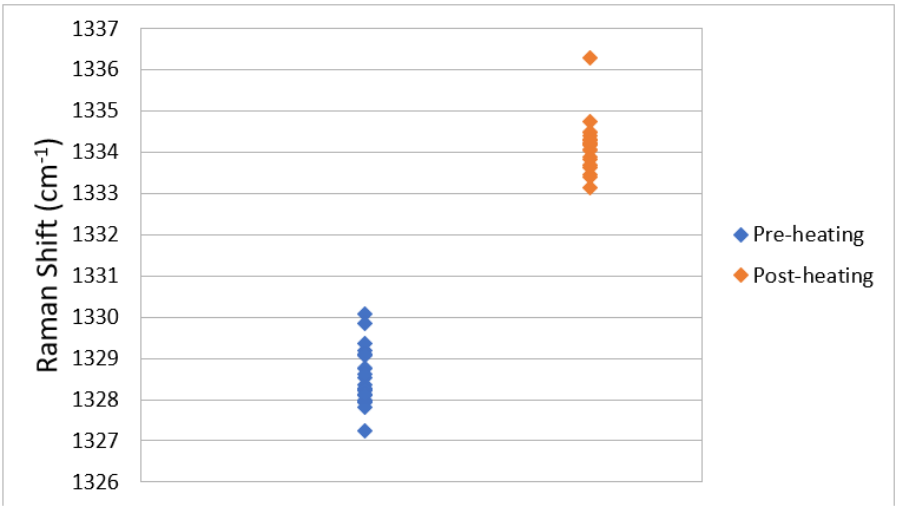

Figure 4.23: Peak position for the first order diamond Raman peak measured before and after heating to 800 °C for 3 h. The average peak position can be seen to increase by approximately 6 cm^{-1} after heating.

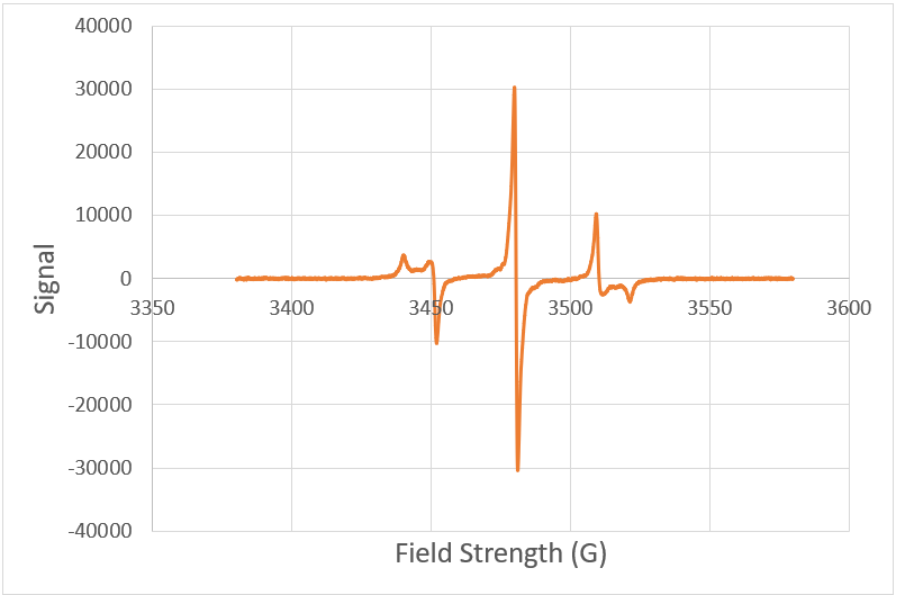

Figure 4.24: Example EPR spectrum of the single substitutional nitrogen defect in diamond. The 'Signal' on the y-axis it the first derivative of the absorbance of the applied radio waves.

4.5 Discussion

4.5.1 Understanding the Sintering Process

To understand the stress state that the components of PCD are in under room conditions, it is first necessary to understand the processes that occur during sintering. To aid this, the sintering process will be broken down and simplified to its important steps and a thought experiment will be performed. The two phases will be conceptually separated from one another and at each stage, the stress-free strain in each phase will be considered. Finally, at room temperature and pressure, the two phases will be rejoined with their interfaces in contact and the total difference in strain between them will be evaluated. The following assumptions will be used to simplify the understanding of the process:

1. The microstructure consists of a series of isolated, spherical pools of cobalt in a diamond matrix.[2].

2. All deformation is elastic, no plasticity occurs in either phase and stresses do not relax[2].

3. The only component of the strain is the mean, hydrostatic component. This assumption is necessary in part because the true strain state is complicated and in part because this was the strain component that was measured. Other components will be considered later.

4. Given the assumptions already made and because volume is a state function, the resultant mismatch strain does not depend on the order in which the pressure and temperature are changed.

In reality, the microstructure of PCD consists of an interconnected network of cobalt pores which will allow some degree of stress relaxation both during solidification by liquid flow and after by plastic flow. Furthermore, the stress state in both components will be more complicated than purely hydrostatic. The

[2]The validity of these quite large assumptions will be discussed in section 4.5.5.1.

simplifications necessary to arrive at an answer to the questions this thesis aims to answer and how they affect the results will be discussed in a further section.

During sintering, both diamond and cobalt are at a temperature of 1500°C and under a hydrostatic pressure of 5.5 GPa with the liquid cobalt completely filling the spaces between diamond grains (figure 4.25).

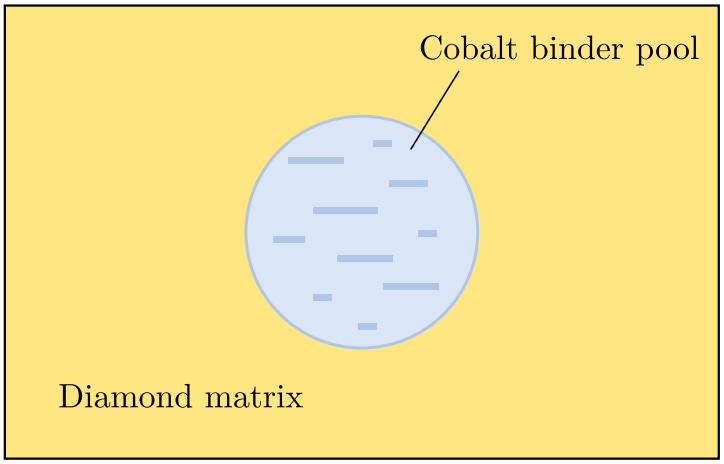

Figure 4.25: Temperature: 1500 °C, pressure: 5.5 GPa. Cobalt is liquid, filling spaces between diamond grains. Sintering of diamond grains is occurring.

Once a sufficient degree of sintering has been achieved, the temperature is dropped below the freezing point of cobalt, causing it to solidify and shrink relative to the diamond shell (figure 4.26). As the sintering temperature is only slightly above the cobalt melt temperature, this temperature drop is small and the thermal contraction in the diamond is neglected.

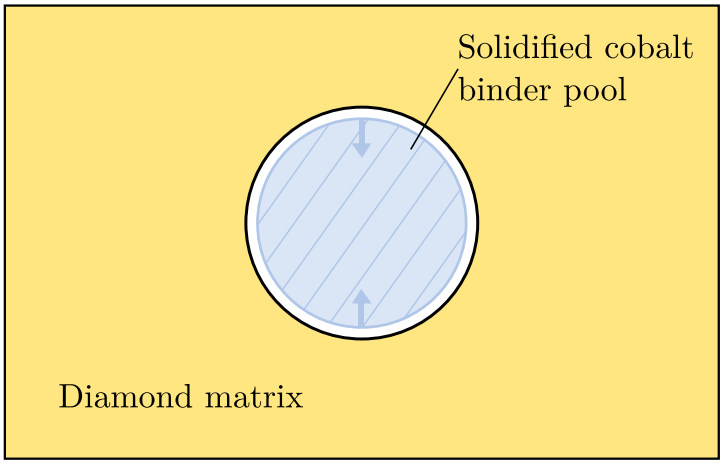

Figure 4.26: Temperature: < cobalt T_m, pressure: 5.5 GPa. Cobalt shrinks on solidification, putting surrounding diamond into compression.

The sintering pressure is removed. Cobalt has a much higher compliance (lower bulk modulus) than diamond and so it expands much more than the surrounding diamond matrix (figure 4.27).

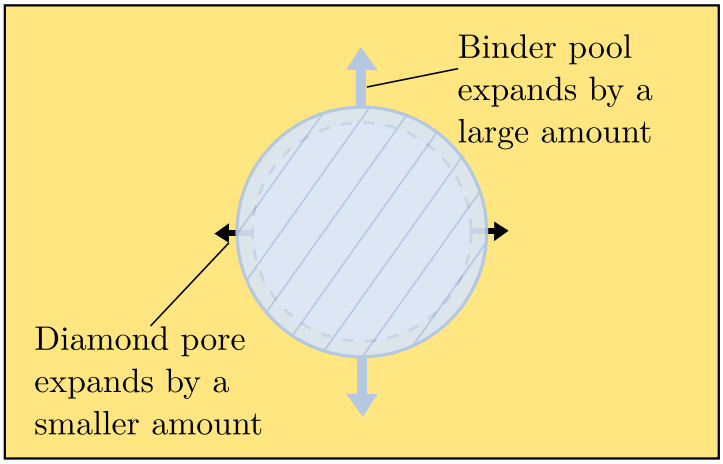

Figure 4.27: Temperature: < cobalt T_m, pressure: 0. The higher compliance of cobalt causes it to expand much more than the surrounding diamond when the sintering pressure is released. This causes a tensile component in the diamond.

Finally, the temperature is reduced. As the thermal expansion coefficient of cobalt, α_{Co}, is greater than that of diamond, α_D, the cobalt contracts more than the diamond on cooling. Assuming that the magnitude of this contraction is greater than the expansion due to pressure release (which will be verified in a following section),

the system will pass through a point where the relative strain and hence stress in both phases is zero, referred to as the stress-free temperature (indicated in figure 4.28).

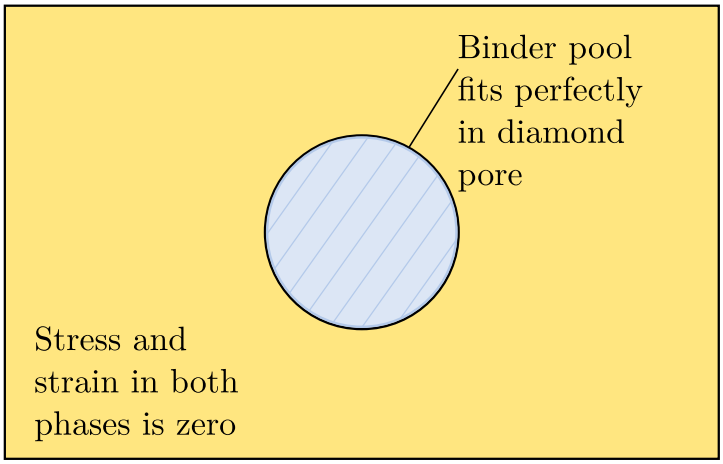

Figure 4.28: Temperature: T_0, pressure: 0. At the stress-free temperature, the compressive and tensile strains are balanced in both phases and the total strain (and hence stress) in both phases is zero.

After passing through this temperature, the system continues to cool to room temperature where once the two phases are conceptually joined back together, the diamond experiences a net compression due to the sum of the previous transformations.

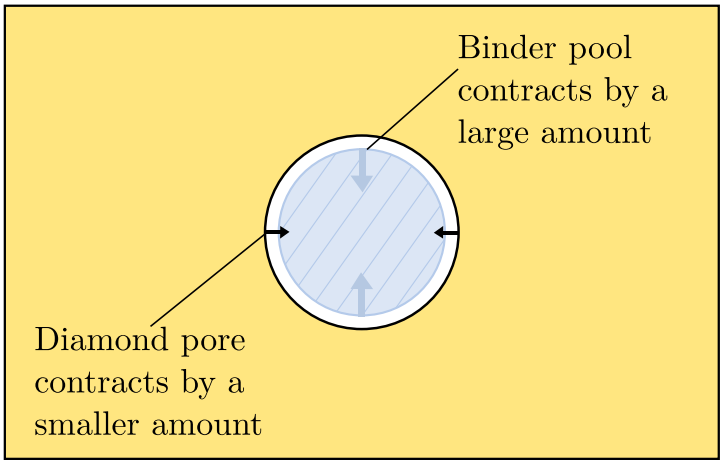

Figure 4.29: Temperature: 25 °C, pressure: 0. On cooling, the greater thermal expansion coefficient of cobalt causes it to contract more than the diamond, imposing a compressive component on the diamond.

The stress-free mismatch in strain between the two phases is therefore given

as the sum of all the effects:

$$\epsilon^{D}_{TOT} = \epsilon_{sol.} + \Delta\epsilon_P + \Delta\alpha\Delta T \tag{4.4}$$

where $\epsilon_{sol.}$ is the solidification strain, $\Delta\epsilon_P$ is the difference in strain between the two phases due to their differential expansion under the pressure release because of their differing bulk moduli and $\Delta\alpha\Delta T$ is the strain due to the differing thermal expansion coefficients of cobalt and diamond through a temperature drop from the stress-free temperature to room temperature. Defining mismatch strains which cause a compressive strain in the diamond phase as negative, $\epsilon_{sol.}$ will result in a negative strain as cobalt contracting on solidification will cause a compressive strain on the diamond, $\Delta\epsilon_P$ positive as the cobalt expands more than the diamond when the pressure is released putting diamond into tension and $\Delta\alpha\Delta T$ also negative as the cobalt contracts more than the diamond under the same temperature drop again putting the diamond. The stress-free temperature is therefore represented by equation 4.4 when $\epsilon^{D}_{TOT} = 0$.

From this description of the sintering process, the expected behaviour of the stress-state with temperature can be predicted qualitatively. At room temperature, the sum of the strains puts the diamond in compression that diminishes up until the stress-free temperature. At this point, the strains and stresses are zero and above it, the diamond moves into tension. The fact that the stress-free temperature is lower than the sintering temperature is due to the opposing direction of the depressurisation strain, $\Delta\epsilon_P$, and the thermal expansion mismatch strain, $\Delta\alpha\Delta T$. Furthermore, as the stress-free temperature does not depend on the volume fractions of the two phases (under the current set of assumptions), the lattice parameters of diamond in two PCD materials with differing volume fractions of cobalt (such as unleached and leached PCD) will be equal at this temperature. As the aim is to quantitatively calculate the stresses present in PCD as a function of temperature, the stress-free temperature must be determined and applied to an appropriate model in order to achieve this.

4.5.2 Direct Observation of the Stress-free Temperature

The stress-free temperature can be measured from both GEM (figure 4.9) and HRPD (figure 4.19) results by noting the point at which the unleached and leached diamond lattice parameter vs temperature graphs cross (table 4.2).

HRPD	$(664 \pm 67)\,^{\circ}\mathrm{C}$
GEM	$(676 \pm 274)\,^{\circ}\mathrm{C}$

Table 4.2: Stress-free temperatures calculated from cross-over temperatures of leached vs. unleached diamond lattice parameter graphs.

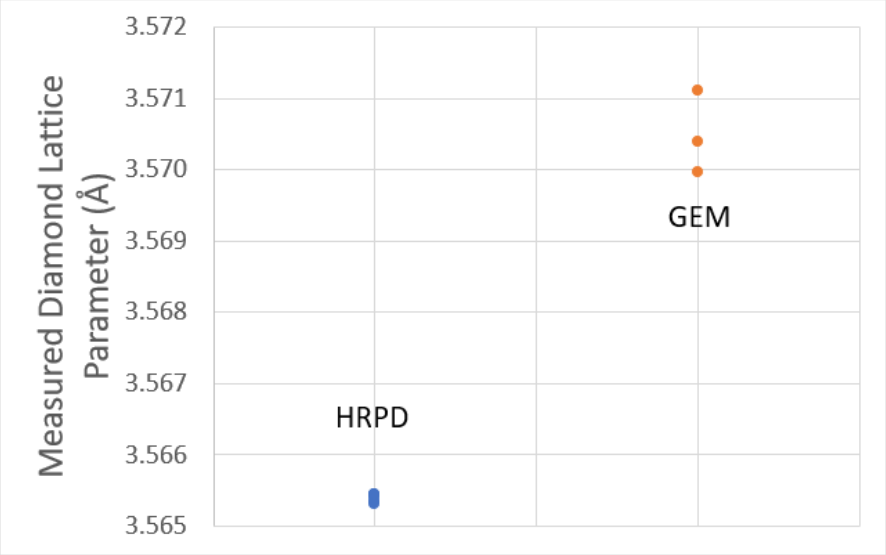

Figure 4.30: Spread in measurement of diamond lattice parameter of nominally identical samples for HRPD (5 measurements) and GEM (3 measurements). Although samples were manufactured in different batches which could cause the difference in lattice parameter observed between the two instruments, the most likely explanation is a combination of significantly different sample geometry and thickness and, a different, unknown systematic error introduced by each diffractometer that is not removed by Rietveld refinement.

However, this method of determining the stress-free temperature suffers from a large amount of error as it is only determined by the two points either side of the cross-over point which theoretically lie on two curves with very similar gradients. Small movements of those points (such as those caused by random errors due to one sample being positioned slightly differently in the beam to another) result in large changes in the measured value of the stress-free temperature. Figure 4.30

shows the spread in measurement of the diamond lattice parameter of nominally identical samples measured with GEM and HRPD. The standard deviation in these measurements was then used to calculate the error bars on the measured stress-free temperature in table 4.2. In light of the over-reliance of this method of determining T_0 on the two data points either side of it, another method that makes full use of all of the data is necessary.

4.5.3 Calculation of the Stress-free Temperature

A simple isotropic model consisting of a spherical particle (cobalt) in a spherical shell of matrix (diamond) can be used to calculate a value for both T_0 and the strain (and hence stress) in both phases. This will be calculated using the pair of unleached and leached diamond lattice parameter measurements at each temperature. The radii of each phase will be set to give the same volume fractions as those measured for leached and unleached PCD experimentally. By first calculating the stress-free temperature, the model can be validated against the value measured in section 4.5.2 and if found to be in agreement, used to quantify the stress in the diamond as a function of temperature. This method has previously been used by Wain *et al.* to analyse neutron diffraction measurements made on distributed inhomogeneities within a ceramic matrix that experience a thermal residual stress[129].

Equation 4.5[130] describes the mean, hydrostatic strain in the matrix:

$$\overline{\epsilon_m^h} = \frac{f E_p (1-2\nu_p) \int_T^{T_0} \alpha_m - \alpha_p \, dT}{(1-f)E_m(1-3\nu_p) + E_p[f(1-2\nu_m) + \frac{1}{2}(1+\nu_m)]} \tag{4.5}$$

where subscript m refers to the matrix and p to the cobalt particles. f is the volume fraction of particles, E the Young's modulus, ν the Poisson's ratio and α the thermal expansion coefficient. T is the measurement temperature and T_0 the stress-free temperature.

At each temperature, the data consists of measured diamond lattice parameter for leached and unleached PCD with two different volume fractions of cobalt. From this, a pair of simultaneous equations can be established to infer the temperature at which the system was free from stress.

The thermal expansion coefficients in equation 4.5 can be derived from the unstressed diamond powder and cobalt alloy lattice parameter with temperature measurements shown in figures 4.19 and 4.13 and equation 4.6:

$$\alpha(T) = \frac{1}{a}\frac{da}{dT} \tag{4.6}$$

Making a substitution, this can be written:

$$\alpha(T) = \frac{d(lna)}{dT} \tag{4.7}$$

and so the thermal expansion coefficient as a function of temperature can be determined by plotting the natural logarithm of the lattice parameter against temperature, fitting a trendline to the data and differentiating its equation to get the gradient. This is performed in figure 4.31, a quadratic trendline gave the best fit and so once differentiated, the thermal expansion coefficient is a linear equation of the form:

$$\alpha_i(T) = A_i T + B_i \tag{4.8}$$

whose coefficients are summarised in table 4.3.

Material	A_i ($10^{-9}\,\mathrm{K}^{-2}$)	B_i ($10^{-6}\,\mathrm{K}^{-1}$)
Diamond Powder ($_D$)	6.1 ± 0.5	-1.2 ± 0.3
Cobalt-Tungsten Alloy ($_{Co}$)	8 ± 1	8 ± 1

Table 4.3: Coefficients for equations of thermal expansion coefficient with temperature for diamond powder and cobalt-tungsten alloy.

Equation 4.5 gives an expression for the mean, hydrostatic strain in the matrix. This strain can also be written as:

$$\overline{\epsilon_m^h} = \frac{a_i - a_0}{a_0} \tag{4.9}$$

where a_i is the measured leached or unleached diamond lattice parameter and a_0 is the stress-free lattice parameter. In the unleached material, the matrix is just diamond and the calculation can proceed with this form of the equation. However, in the leached material, this relation requires modification. As some of the cobalt

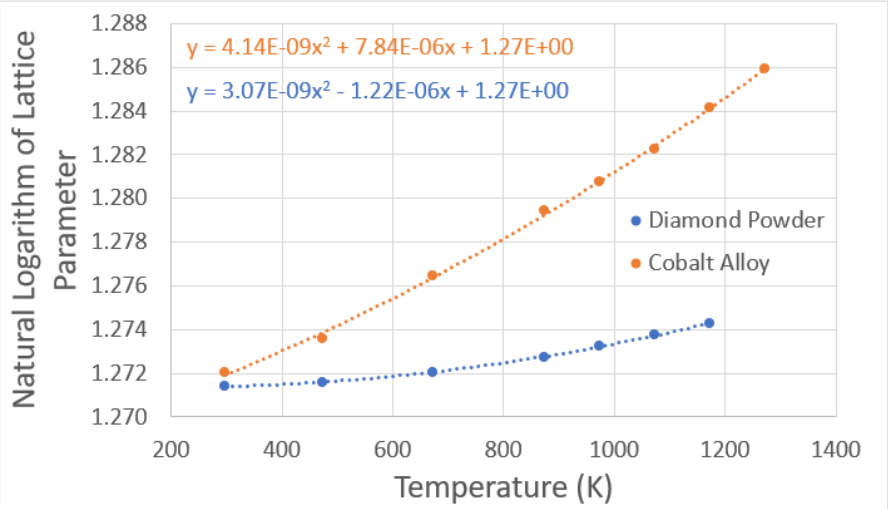

Figure 4.31: Natural logarithm of lattice parameter against temperature for diamond powder and cobalt alloy. To get the thermal expansion coefficient as a function of temperature, the trendline equation can be differentiated to get the gradient as per equation 4.7.

has been removed, the matrix is now a combination of diamond and voids. The strain in the matrix is no longer equal to the strain in the diamond yet it is still the diamond lattice parameter (and hence strain in the diamond) that is being measured. To solve this problem, a force balance is considered between the two phases (diamond, d and voids, v) in the matrix, m:

$$\sigma_m = f_d\sigma_d + f_v\sigma_v \tag{4.10}$$

where σ_i is the stress in each component and f_i is the volume fraction of each phase.

As the voids cannot support a stress, $\sigma_v = 0$, giving:

$$\sigma_m = f_d\sigma_d \tag{4.11}$$

The relationship between a hydrostatic stress and strain (as in the matrix) is:

$$\sigma_m = \frac{\epsilon_m E_m}{1 - 2\nu_m} \tag{4.12}$$

Substituting the result of equation 4.11 into this equation gives:

$$f_d\sigma_d = \frac{\epsilon_m E_m}{1 - 2\nu_m} \tag{4.13}$$

Finally, σ_d is written in terms of the strain in the diamond using the hydrostatic stress-strain relation and the expression is rearranged for ϵ_m so that it can be substituted back into equation 4.5 now with the correct strain, ϵ_d:

$$\epsilon_m = \frac{\epsilon_d E_d}{1-2\nu_d}\frac{1-2\nu_m}{E_m} \tag{4.14}$$

Another consequence of the inclusion of voids in the "matrix" of the leached material is that the elastic constants are affected. Assuming that the voids are spherical holes of a uniform size and homogeneous distribution, the bulk (K)and shear (μ) moduli can be modified as follows[131]:

$$\frac{1}{K} = \frac{1}{K_0\rho} + \frac{3}{4\mu_0}\frac{1-\rho}{\rho} \tag{4.15}$$

$$\mu = \mu_0\left(1 + 5\frac{3K_0+4\mu_0}{9K_0+8\mu_0}(1-\rho)\right) \tag{4.16}$$

where K_0 and μ_0 are the bulk and shear moduli of the pristine material and ρ is $1-f_v$.

Two equations of the form:

$$\frac{a_i - a_0}{a_0} = P_i f_i \int_T^{T_0} \alpha_m - \alpha_p dT \tag{4.17}$$

(where P_i is the prefactor containing the correct elastic constants for the material i) can be established, a_0 eliminated and a quadratic equation set up in terms of T_0 to solve for the stress-free temperature at each measurement temperature. The results of this calculation are shown in table 4.4 and a full treatment of the equations is given in appendix A.

4.5.4 Validation of the Model

Figure 4.32 shows the results of the calculation on a graph of calculated stress-free temperature against measurement temperature (also tabulated in table 4.4). The data are scattered randomly about a mean of of 782 °C with a standard error of 62 °C for measurement temperatures up to 700°C. Above this temperature, the scatter increases dramatically which is due to processes such as graphitisation affecting the diamond lattice parameter from this point onwards as will be shown in chapter 5. The reasonably tight scatter about a constant value is a good indication that the model is

Measurement Temperature °C	Calculated Stress-Free Temperature °C
25	828
200	666
400	936
600	901
700	624
800	236
900	1261

Table 4.4: Calculated stress-free temperature as a function of measurement temperature. Details on how these values were calculated is given in appendix A.

performing well as the pair of measured lattice parameter values at each temperature should predict the same value of T_0. Given the possibility for stress-release in the true microstructure, it would be expected that the calculation should predict a higher stress-free temperature than the direct measurement from the crossover point of the lattice parameters. This is indeed what is seen as the calculation has a mean stress-free temperature of $(782 \pm 62)\,°C$ and the direct measurement gives $(664 \pm 67)\,°C$ showing that only a small amount of stress-relaxation has occurred thereby giving confidence that the assumptions of the present model can be used.

4.5.4.1 Uncertainties

Many of the parameters used in the solution of equation 4.5 have been either measured in this experiment or derived from the literature and so the sources of uncertainty in these quantities will be discussed below:

Diamond lattice parameter This is measured by neutron diffraction and has already been shown in figure 4.30. The relative error in this quantity is 2×10^{-5} which is small compared to the other errors. This error is caused by a discrepancy between the geometry of the sample relative to the detector during calibration and the true relationship during measurement. It is impossible to place the sample in exactly the same place each time which will have an effect on the diffraction geometry and hence the measured lattice parameter. Different

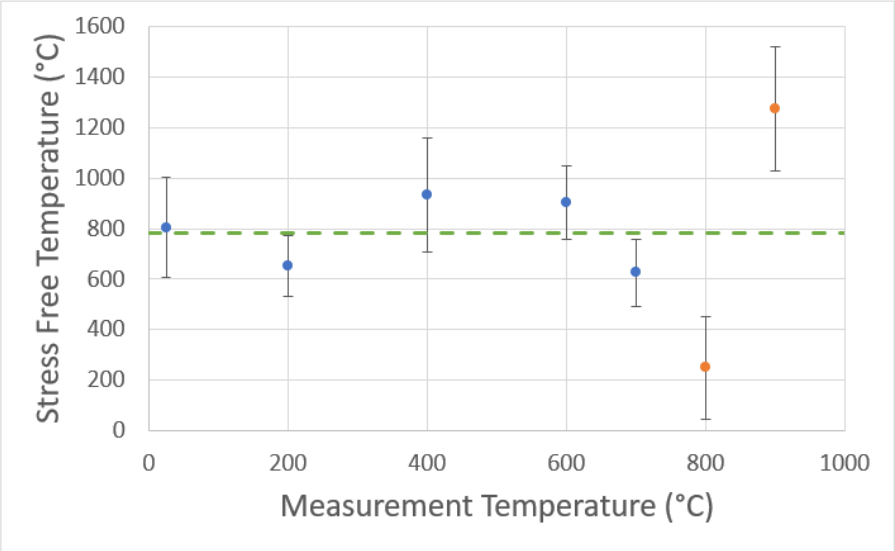

Figure 4.32: Plot of stress-free temperature against measurement temperature. The data (blue points) has a mean temperature of 782 °C indicated by the green line. Orange points denote data not correctly predicted by the present model due to the formation of graphite that affects the lattice parameter measurements in unknown ways at temperatures above 800°C. These orange points are therefore omitted from mean and error values for the stress-free temperature.

measurement techniques have different sensitivities to this positional inaccuracy which explains the slightly different diamond lattice parameter measured by the different techniques. Backscattering detectors were used as this minimises the effect of the introduced error and the results from HRPD were seen to be much less sensitive to this positional error than the results from GEM.

Volume fraction of cobalt This was measured by ICP etching followed by mass spectrometry by Element Six and has a quoted accuracy of within 0.1 %. Unless the cobalt volume fraction varies strongly through the thickness of PCD and the volume measured was not representative of the sample, this represents another small random error and is unlikely to be the cause.

Elastic constants The elastic constants were derived from literature studies as detailed in appendix B. There are no known reasons why the diamond studied in the literature and in this study should have different elastic constants but the composition of the cobalt differs significantly. This could potentially produce a

large systematic error in the results but as the results from two different studies using pure cobalt and cobalt alloys give consistent results, it is suggested that the effect of composition on the elastic properties of cobalt is not that great. A nominal uncertainty of 10 % in elastic constants was used to calculate the uncertainty in the stress-free temperature.

Thermal expansion coefficient This was measured for diamond powder and a cobalt-alloy using neutron diffraction. By propagating errors through equation 4.5 it was found that the random error in these quantities have the most significant effect on the error in the calculated stress-free temperature. Looking at figure 4.31, a large degree of scatter is present about trendlines and hence there is a large uncertainty in the coefficients derived from this in table 4.3. In an attempt to rectify this, a laboratory x-ray diffractometer was used to make further measurements of the variation of the diamond and cobalt-alloy lattice parameter (figures 4.21 and 4.22) and hence thermal expansion coefficient with temperature. However, comparing this with the neutron diffraction measurements, it can be seen that the resultant thermal expansion coefficient measured is different. This is thought to be due to the inferiority of the furnace causing an inability to maintain higher temperatures in this particular laboratory x-ray diffractometer. Although the statistical error is reduced, it would not be beneficial to introduce an additional, unknown systematic error and hence this data will not be used. Ideally, further measurements would be taken using neutron diffraction to reduce this uncertainty. Furthermore, the bulk alloy composition was determined by making EDX measurements of binder pools which is well known to be a semi-quantitative technique at best. The composition of the bulk alloy is therefore likely not the same as in the binder pools but the effect of composition on the thermal expansion coefficient is not known.

The error in the calculated stress-free temperatures (shown in figure 4.32) was calculated by calculating minimum and maximum possible values (using the errors in measured quantities) of T_0 from equation A.10.

4.5.5 Predicting the Stress-free Temperature

Having satisfactorily validated the model, it can now be used to calculate the stress in the PCD as a function of temperature and this will be done in section 4.5.6. However, to complete the understanding of the origin of these stresses, the physical model of sintering put forth in section 4.5.1 will be reconciled with the numerical model.

Using equation 4.4, the stress-free temperature can be predicted from the known sintering conditions and other materials properties of diamond and cobalt.

$$\epsilon_{TOT}^{D} = \epsilon_{sol.} + \Delta\epsilon_P + \Delta\alpha\Delta T \tag{4.4}$$

where $\epsilon_{sol.}$ is the solidification strain, $\Delta\epsilon_P$ is the depressurisation strain and $\Delta\alpha\Delta T$ is the thermal expansion coefficient mismatch.

The thermal expansion term is simply given by the integral in equation 4.5:

$$\Delta\alpha\Delta T = \int_{T_0}^{T_s} \alpha_m - \alpha_p dT \tag{4.18}$$

where T_0 is the stress-free temperature and T_s is the sintering temperature.

The depressurisation strain is given by the difference in hydrostatic strains caused by the difference between the sintering pressure and room pressure, P, of 5.5 GPa and the elastic constants of diamond and cobalt at the sintering temperature:

$$\Delta\epsilon_P = \frac{P\,(1 - 2\nu_{p,T_s})}{E_{p,T_s}} - \frac{P\,(1 - 2\nu_{m,T_s})}{E_{m,T_s}} \tag{4.19}$$

the elastic constants of the diamond and cobalt at the sintering temperature must be used here to properly account for the strain difference that develops on release of the pressure as it was only at this point that both phases were under equal pressure.

This leaves the solidification strain as the last strain to calculate. This strain is dependent on the geometry of the solidifying volume (in which there is a huge variation throughout a single PCD sample) and the degree of continued feeding with molten metal during solidification. Furthermore, the unknown degree of plastic relaxation that occurs during cooling can also be absorbed into this quantity. Given these unknown and difficult to estimate quantities, it is unlikely that an accurate value will be found without significant effort. In light of this, a solidification

strain will be chosen to give a value of the stress-free temperature that agrees with the other two values and then it will be determined if this is a plausible value given the available literature.

Equation 4.4 can now be expanded as follows:

$$\epsilon^{D}_{TOT} = \epsilon_{sol.} + \frac{P\left(1-2\nu_{p,T_s}\right)}{E_{p,T_s}} - \frac{P\left(1-2\nu_{m,T_s}\right)}{E_{m,T_s}} + \int_{T_0}^{T_s} \alpha_m - \alpha_p dT \tag{4.20}$$

and at the stress-free temperature, the strain in the matrix is zero. As the thermal expansion coefficients derived from figure 4.31 are linear in terms of temperature, when the integration is carried out, a quadratic in terms of temperature is produced:

$$T_0^2\left(\frac{A_p - A_m}{2}\right) + T_0\left(B_p - B_m\right) + \left\{\epsilon_{sol.} + \Delta\epsilon_p + T_s^2\left(\frac{A_m - A_p}{2}\right) + T_s\left(B_m - B_p\right)\right\} = 0 \tag{4.21}$$

which is solved in terms of the stress-free temperature, T_0. As the precise value of $\epsilon_{sol.}$ is not known, a variety of values is chosen and the solution obtained is plotted in figure 4.33. For the predicted stress-free temperature to lie in the range 597–854 °C (the upper and lower bounds of the two estimates for the stress-free temperature) a solidification strain of between 0.0189 and 0.0218 is required. Examining the literature on this subject, Wray states that the solidification shrinkage (simply the change in density going from a liquid to solid) of pure cobalt is 5.26 %[132]. No literature could be found on cobalt-tungsten alloys but Earnshaw reported casting shrinkages for cobalt-chrome alloys (approximate composition 65 % Co, 25 % Cr, 5 % Mo, 0.20–0.40 % C with the remainder of the alloy consisting of a mixture of unspecified elements) used in dental prosthetics as being in the range 2.13–2.34 %[133]. It must be noted that these values are for true casting shrinkage so include the pure solidification shrinkage and the effect that geometry and potential plastic deformation have on this during cooling. The author also states that the percentage of carbon in the alloy is thought to have a large effect on casting shrinkage due to its effect on the ductility of the alloy. Given the differences in alloy composition of the cobalt binder pools, the possibility for continued feeding with liquid metal during solidification and the values of other cobalt alloys in the literature, the range of solidification shrinkages predicted in figure 4.33 are quite feasible.

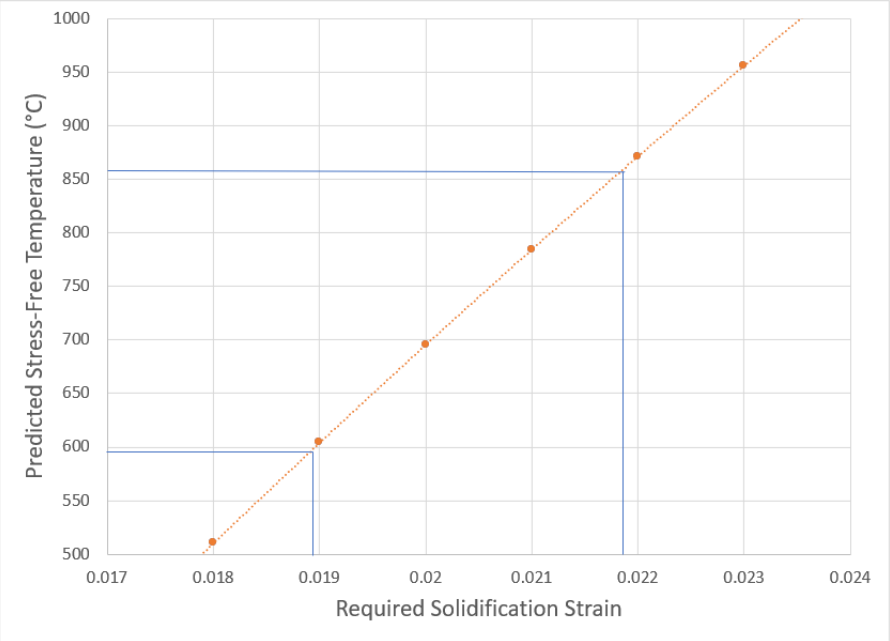

Figure 4.33: Plot of stress-free temperature predicted by equation 4.21 against the solidification required to achieve this temperature. The blue horizontal lines represent the upper and lower bounds of the estimates of stress-free temperatures measured from the results and calculated using equation 4.5.

To put the results of the prediction into perspective, all values of stress-free temperature (measured from raw results, calculated with a quantitative model and predicted from first principles) are presented in table 4.5 and the contributions of the three strains in equation 4.4, $\epsilon_{sol.}$, $\Delta\epsilon_P$ (for the particle and matrix) and $\Delta\alpha\Delta T$, at the predicted stress-free temperature are given in table 4.6.

HRPD Measurement	$(664 \pm 67)\,^{\circ}\mathrm{C}$
GEM Measurement	$(676 \pm 274)\,^{\circ}\mathrm{C}$
Model Calculation	$(782 \pm 62)\,^{\circ}\mathrm{C}$
Prediction	$811\,^{\circ}\mathrm{C}$

Table 4.5: Table of all results for the stress-free temperature. The 'Prediction' value is calculated using a solidification strain of 0.021 65 (the bottom of the range reported for cobalt-chrome alloys from Earnshaw[133]).

Clearly from these values, the two most significant contributions to the strain at the stress-free temperature are the solidification strain and the depressurisation strain in the particle.

$\epsilon_{sol.}$	-0.022
$\Delta\epsilon_P^p$	0.034
$\Delta\epsilon_P^m$	-0.0043
$\Delta\alpha\Delta T$	-0.0081

Table 4.6: Table of all components of strain from equation 4.4 at the stress free-temperature. $\Delta\epsilon_P$ in the equation is made up of the values for the particle and the matrix given above.

4.5.5.1 Model Simplifications

The largest simplification used in the present model is the assumption that the microstructure of PCD consists of isolated pools of cobalt, completely separated from one another, in a diamond matrix. From the small degree of retained cobalt even after intensive leaching, it is clear that some of the pools must be like this but the vast majority are not as most of the cobalt can be leached. The implication of this is that some of the locked in stress can be relieved during solidification by more liquid flowing into the pores. This will be reduced by cobalt first solidifying at the edges of the PCD but plastic flow of the cobalt just below the melting point will continue to allow this to occur. Evidence of this taking place can be seen by cobalt extruding from the pores on the surface during heating[134]. The logical extreme of this, if the cobalt flows without resistance, is that the stress-free temperature will be at room temperature as the cobalt will deform without resistance allowing the stresses in the diamond to also relax. As this is not the case, the reality is likely somewhere between the assumption of the model and this logical extreme. The plastic flow stress of cobalt will increase as it cools and eventually, stress-release will stop when the flow stress equals the frictional resistance imparted by the pores. As these pores are typically in the range 0.1–5 µm, this resistance is likely considerable. As discussed in section 4.5.4, the stress-free temperature calculated by the model is only slightly higher than that measured from the raw results which suggests that the amount of relaxation that occurs is minimal and that this is an acceptable assumption to use.

The model assumes that the pressure is released at high temperature when the cobalt is still liquid and so should use the bulk modulus of liquid cobalt to calculate

the depressurisation strain. The literature values for the bulk modulus of pure liquid cobalt near the melting point have quite a degree of spread (values given in appendix B) and are all higher than that extrapolated for the solid cobalt near the melting point. This is likely due to the literature values being for pure cobalt rather than the alloy it exists in in the present work. However, the bulk modulus for cobalt used in this thesis has been extrapolated from data for a cobalt alloy measured up to 1121 °C and hence is a relatively reliable extrapolation. Work on aluminium, another fcc metal, shows that its bulk modulus changes very little during melting[135]. As such, the bulk modulus values for solid cobalt have been used.

Although a number of quite large assumptions have been used in this model, comparison with the raw results show good agreement. Possible refinements to the model are suggested in the forthcoming Further Work section.

4.5.6 Calculated Residual Stresses

The value of the stress-free temperature calculated in section 4.5.3 ((782 ± 62) °C) can be put back into equation 4.17 to calculate values for the theoretical stress-free lattice parameter for each measurement temperature. By comparison of this value with the measured lattice parameter, the strain in the diamond for unleached and leached materials can be calculated. Following the previous assumptions of hydrostatic strain, the stress can be calculated with equation 4.12:

$$\sigma = \frac{\epsilon E}{1 - 2\nu} \tag{4.12}$$

The results of this calculation are shown in tables 4.7 and 4.8.

The variation of residual stress with temperature is shown in figure 4.34. It can be seen that diamond is in compression at room temperature until around 700°C where it crosses into tension. The precise cross-over temperature between compression and tension of 713 °C is slightly different to the calculated stress-free temperature of (782 ± 62) °C. This is due to the calculated temperature being an average of the stress-free temperature calculated at each measurement temperature and the exact cross-over temperature depending only on the stresses at 700 °C and

Temperature (°C)	Unleached Lattice Parameter (Å)	Leached Lattice Parameter (Å)	Stress-free Lattice Parameter (Å)
25	3.56541	3.56571	3.56580
200	3.56679	3.56696	3.56705
400	3.56896	3.56915	3.56916
600	3.57169	3.57178	3.57179
700	3.57319	3.57317	3.57320
800	3.57497	3.57482	3.57489
900	3.57646	3.57657	3.57649

Table 4.7: Summary of unleached and leached lattice parameters measured by neutron diffraction and the stress-free lattice parameter calculated with equation 4.17. The standard error in lattice parameter measurements determined by repeat measurement of a single sample is 0.000 02 Å.

Temperature (°C)	Unleached Diamond Strain (10^{-5})	Leached Diamond Strain (10^{-5})	Unleached Residual Stress (MPa)	Leached Residual Stress (MPa)
25	-11 ± 3	-2.4 ± 0.6	-146 ± 49	-30 ± 11
200	-7 ± 1	-2.6 ± 0.5	-97 ± 28	-33 ± 10
400	-6 ± 1	-0.5 ± 0.1	-77 ± 25	-6 ± 2
600	-2.8 ± 0.4	0.0 ± 0.1	-37 ± 10	0 ± 1
700	-0.3 ± 0.1	-1.0 ± 0.2	-4 ± 1	-12 ± 4
800	2 ± 2	-2 ± 2	29 ± 25	-26 ± 21
900	-0.8 ± 0.2	2.3 ± 0.4	-11 ± 3	28 ± 8

Table 4.8: Strains calculated using equation 4.9 and stresses calculated using equation 4.12 in the diamond for unleached and leached PCD.

800 °C, the latter of which is less than reliable due to the onset of graphitisation and its additional effect on the diamond lattice parameter.

As it is the mean hydrostatic stress that is under consideration, the results shown in table 4.8 can be used to calculate the residual stress in the cobalt phase with a force balance as the total stress in the composite must sum to zero:

$$f_m \sigma_m + f_p \sigma_p = 0 \tag{4.22}$$

Another means of calculating this stress is by comparing the lattice parameter inferred from the {200} cobalt peak in the unleached diffractogram to that of the

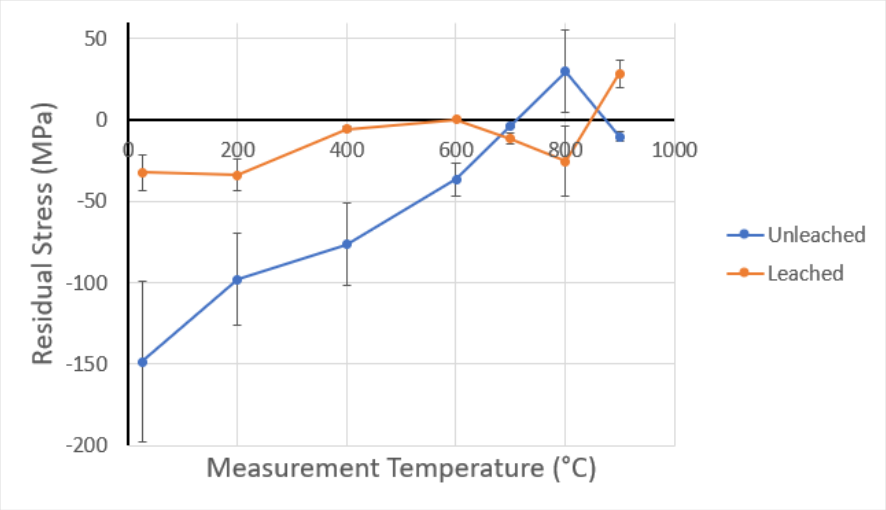

Figure 4.34: Plot of residual stress in the leached and unleached phases as a function of temperature. The error bars show the uncertainty in the residual stress calculated by propagating the errors in lattice parameter, stress-free temperature and elastic constants discussed in section 4.5.4.

cobalt- tungsten alloy, assuming the latter to be its stress-free equivalent (figure 4.15). The results of these two calculations are shown in figure 4.35.

It can be seen that the calculation using the alloy sample as a stress-free reference shows roughly the same trend as the force-balance calculation but generally predicts a lower stress and has a much larger scatter. The size of the error bars are also much greater as the cobalt peak position was calculated from a single, noisy peak. The likely reasons behind this are as follows: the lattice parameter of the bulk alloy sample was measured using GEM which has a much greater sensitivity in the measured lattice parameter to positional errors than HRPD and the bulk alloy is likely of a different composition to the cobalt binder pools increasing an offset in lattice parameter compared to the "true" value. Finally, and most significantly, the cobalt {200} peak is very small and noisy in the HRPD diffractogram and so calculating the lattice parameter from this single peak is likely to result in a large, random error. Therefore, the force-balance calculation is used to calculate stresses for the cobalt phase showing that they are approximately an order of magnitude greater than those in the diamond.

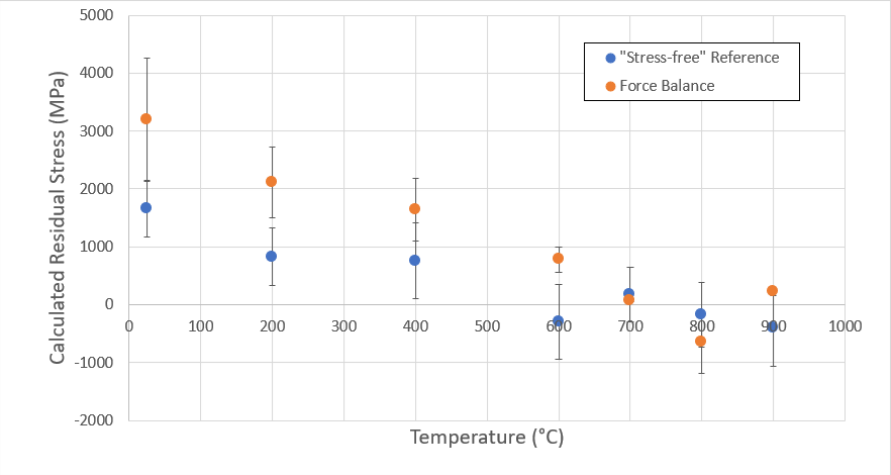

Figure 4.35: Comparison of the residual stress in the cobalt calculated by two methods. Blue points show the stress calculated by comparison of the cobalt {200}-peak-calculated lattice parameter from the neutron diffraction of PCD results with the lattice parameter of the bulk cobalt alloy. Orange points show the results of the force balance (equation 4.22). The error bars show the uncertainties in the residual stresses calculated by propagating the errors in lattice parameter, stress-free temperature and elastic constants discussed in section 4.5.4. The Force Balance data uses the spread in values obtained from repeat measurements of the lattice parameter whereas the Stress-free Reference data uses the standard error in the peak position calculated by the 'lmfit' Python package used to calculate the single cobalt peak position.

4.5.6.1 Comparison with WC-Co

Tungsten carbide-cobalt is a somewhat similar material to PCD in that it consists of metallic cobalt particles in a stiff matrix of tungsten carbide. Similar experiments were performed on this system by Mari *et al.*[136] and so their results will be compared with those for PCD from the present section. Figure 4.37 shows an adapted plot from the work of Mari *et al.* of the residual stress in the WC phase as a function of temperature for two heating and cooling cycles. Similarly to that shown for diamond in the present work (figure 4.34), the residual stress starts off compressive at room temperature and decreases in magnitude until the point where it is close to zero. With tungsten carbide, additional increases in temperature past this point cause the stress to again increase in compressive magnitude. The residual stress of diamond also appears to follow a similar trend, however, the magnitude of the change is below the level of the error. Mari *et al.* explain this increase in compressive residual stress in the "high temperature regime" as being due to large

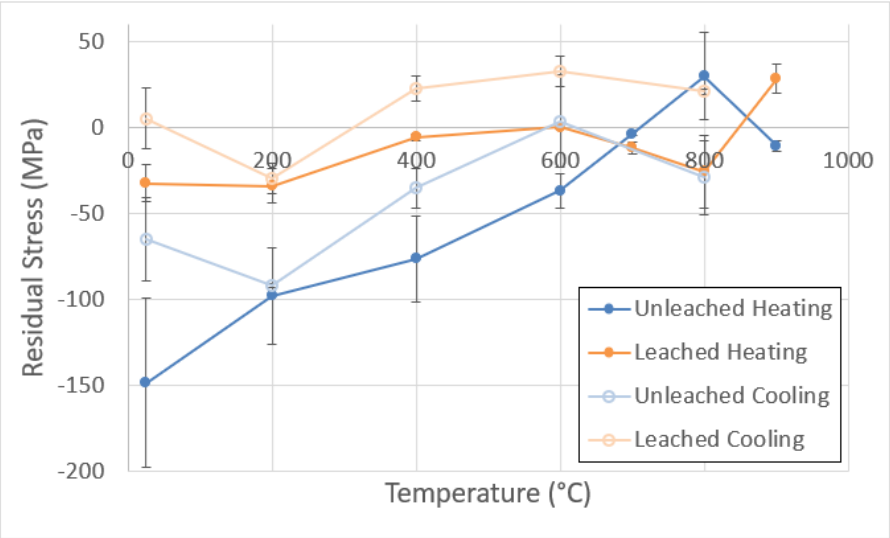

Figure 4.36: Plot of residual stress vs. temperature for PCD in heating and subsequent cooling. It can bee seen that, within the bounds of the error, the stresses follow very similar patterns in both heating and cooling and so it is concluded that the effect of dissolving solutes in the cobalt binder is minimal.

amounts of tungsten dissolving into the cobalt binder. Its lattice parameter expands but the shrinking size of the WC matrix puts it into compression. In PCD, the available supply of tungsten is orders of magnitude smaller due to the far lesser prevalence of tungsten carbide (up to 4 wt%) and so its effect on the residual stress will be much smaller. The analogous effect in PCD would be carbon from the diamond dissolving into the cobalt binder. However, the maximum solubility of carbon in cobalt is only around 0.2wt%[137] and so this is likely to have a much smaller effect. This effect is examined in the model of a cobalt particle surrounded by diamond with a graphite nucleus forming in it developed in chapter 5. Mari *et al.* suggest that the hysteresis in the residual stress on heating and cooling shown in figure 4.37 is indicative of dissolution induced stresses. Comparing this to heating and subsequent cooling measurements of residual stress in PCD, shown in figure 4.36, very little hysteresis can be seen within the bounds of the error and so it is concluded that dissolution of solutes into the binder plays a small part in the development of residual stresses.

Furthermore, there is very compelling evidence (discussed in detail in chapter 5) that at these temperatures, graphitisation and both microscopic and macroscopic

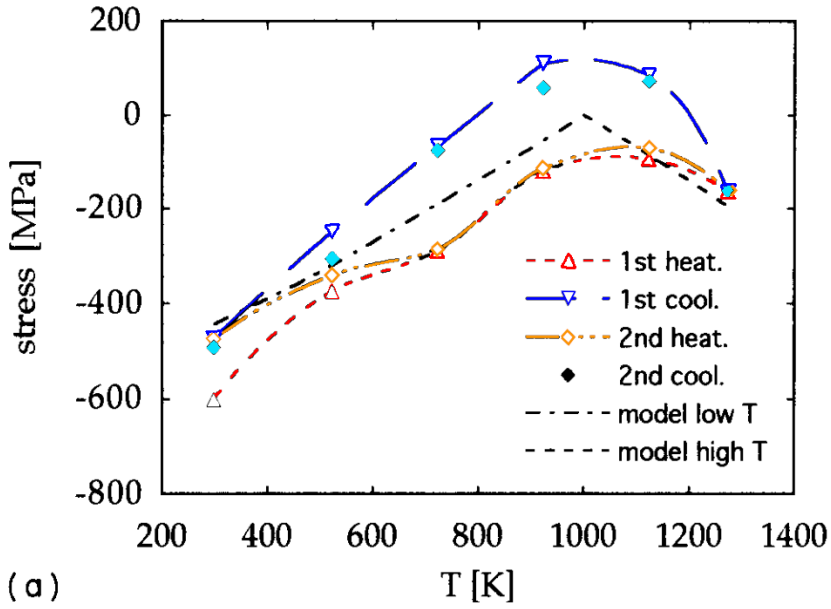

Figure 4.37: Plot of residual stress as a function of temperature in tungsten carbide in a WC-11wt%Co system. The graph has been coloured to aid in distinguishing the different heating and cooling cycles.

cracking occur at these temperatures which will have a large effect on the residual stresses present. It is concluded that although the process seen in the work of Mari *et al.* cannot be ruled out from occurring in PCD, its effect is likely to be small and overshadowed by the large-scale, graphitisation mediated cracking that occurs in PCD at these temperatures.

4.5.7 Effect on Mechanical Properties

4.5.7.1 Spontaneous Thermo-Physical Breakdown of PCD

Compared to the strength of polycrystalline diamond of between 1.2 and 2.2 GPa in tension found in section 3.4.1 and between 1.9–6.9 GPa in compression[67]) the maximum compressive stress of 146 MPa and tensile stress of 29 MPa experienced by the diamond during heating are insignificantly small. The intuitive argument that much of the literature follows is that as cobalt has a greater thermal expansion coefficient than diamond, heating causes the binder pools to expand more than the surrounding diamond putting stress on the diamond-diamond bonds and eventually causing fracture of the PCD. However, this simplistic explanation neglects to take

account of the fact that the diamond and cobalt are joined together at 1500 °C and under 6 GPa of pressure. By taking account of how PCD is made, it has been possible to model all of the factors affecting the residual stresses in PCD, successfully corroborate this model with experimental measurements and show that the true behaviour is quite the opposite to the intuitive explanation. At exactly the point where Sneddon and Hall suggested that the onset of spontaneous thermo-physical breakdown occurs (730 °C[80]), the thermal residual stresses are close to zero. This work therefore conclusively shows that any increased mechanical breakdown that occurs at these temperatures must occur by a different mechanism.

4.5.7.2 Toughness Degradation

At room temperature, the cobalt binder pools cause a compressive residual stress in the diamond. This will represent an additional energy barrier to cracks trying to propagate through PCD and hence a toughening effect. Taya *et al.* provide a simple equation to calculate the toughening effect of a distributed network of particles given that the average compressive stress they cause in the matrix is known[138]:

$$\Delta K = 2\sigma\sqrt{\frac{2\,(\lambda - d)}{\pi}} \tag{4.23}$$

where ΔK is the increase in the critical mode I stress intensity factor needed to cause fracture, λ is the particle spacing and d is the particle diameter. For this calculation, average values of λ and d must therefore be found.

The model behind equation 4.23 assumes that cracks advance from one tensile region (cobalt particle) to the next and are impeded from doing so by the uniform compressive stress field in the matrix (diamond). Looking at a 2-dimensional cross section of the microstructure of PCD in figure 4.38, regions of highly intermixed cobalt (grey) and diamond (black) can be seen to be separated by much larger expanses of diamond, a few of which are highlighted in red. In three dimensions, these regions are in fact contiguous regions of cobalt and hence represent single tensile regions through which a crack would easily pass. As such, these regions will be considered as single particles (of width d) and the particle spacing will

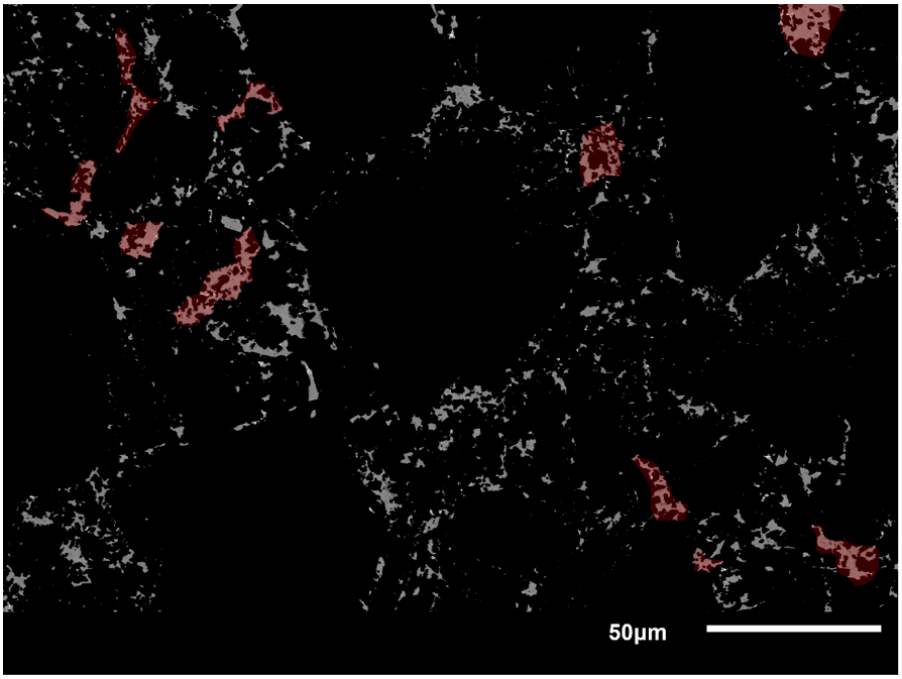

Figure 4.38: SEM backscattered electron micrograph of PCD with areas of approximately 50:50 mixing of diamond (black) and binder (grey) highlighted in red. These highlighted areas are taken to be contiguous regions of cobalt in 3D and the particle spacing between these regions is calculated.

be the separation of these regions. Note that particle spacing is different to the average grain size as in the current model, grain boundaries are not considered to have a toughening effect unless a particle exists on them. To determine the mean particle spacing, a set of random lines were drawn across micrographs of PCD and the number of particles intersected were counted. The mean spacing was taken to be the average of the line lengths divided by their respective intersection counts. The mean particle spacing was calculated as 16.1 µm for this grade of PCD. Measuring the equivalent circular diameter of binder pool regions results in an average diameter of 3.1 µm. Using equation 4.23 with these values and the maximum compressive residual stress of -146 MPa yields an increase in toughness of $\Delta K_{IC} = 0.84\,\text{MPa}\sqrt{\text{m}}$ compared to a completely stress-free sample.

Within industry, the leaching process is believed to cause a "30% drop in strength and toughness"[139], however, the only available literature values of toughness before and after leaching are provided by McNamara *et al.*[44]. They measured the toughness of PCD with a nominal grain size of 30 µm with varying degrees of

cobalt. Toughness was evaluated by performing 3-point bending tests on single edged V-notch beams with blunt notches (between 170 and 300 µm notch root radius) and the results analysed with the *Theory of Critical Distances* described by Taylor[45]. However, the poor fit of the data to the model suggests that this theory is not appropriate for describing the fracture behaviour of PCD and as such the absolute fracture toughness values calculated with it should be used cautiously. Table 4.9 shows a summary of their results and suggests that there is a 2.04–2.22 MPa $\sqrt{\text{m}}$ drop in toughness after leaching depending on the starting amount of cobalt (representing a 24 % and 23 % decrease respectively). Despite criticism of the method used to measure toughness, the values obtained are in the same area as those measured by other authors for fracture toughness of unleached PCD. Assuming that the method is self-consistent, it is reasonable to accept the difference between the unleached and leached measurement as an estimate for the toughness loss on leaching. As industry anecdotal testimony appears to be supported by these results, the predicted drop in toughness due to the removal of the protective compressive residual stress (0.84 MPa $\sqrt{\text{m}}$ predicted by equation 4.23) forms only part of the explanation of the drop in toughness that occurs after leaching.

Designation	Pre-leach Cobalt Content (%)	Pre-leach Toughness (MPa $\sqrt{\text{m}}$)	Post-leach Toughness (MPa $\sqrt{\text{m}}$)
PCD30B	7.5	9.53	7.31
PCD30C	6.5	8.52	6.48

Table 4.9: Summary of the toughnesses of two grades of PCD before and after leaching from McNamara *et al.*[44].

The other component that reduces the fracture toughness of PCD after leaching can be seen by looking at the Griffith criterion for fracture[140]:

$$\sigma_f = \sqrt{\frac{G_c E}{\pi c}} \tag{4.24}$$

(where σ_f is the failure stress, G_c is the critical energy release rate, E is the Young's modulus and c is the flaw size). When the material is leached, both G_c and E

are reduced. G_c is the amount of energy required to advance a crack by unit area. Leaching removes a large proportion of cobalt binder pools, replacing them with air and it is fairly self evident that less energy will be required to propagate a crack through a void than through a cobalt binder pool thereby reducing G_c. Secondly, it has already been shown in equations 4.15 and 4.16 that the elastic moduli of a matrix are reduced by the inclusion of voids and so E will also be reduced. A third possible factor is the increase of the flaw size, c. By leaching the cobalt, it is possible that the resultant voids will be larger than the original binder pool size due to the leachant attacking the surrounding grain boundaries and also removing small pieces of diamond.

Finally, binder pools are significantly more ductile than the extremely brittle diamond as seen in section 3.5.4. During fracture, the ductility of the cobalt acts to dissipate energy through plasticity that is then unavailable to propagate the crack and hence its presence will increase G_c. Removing the binder pools through leaching clearly removes this effect and must lower G_c.

4.5.8 Lattice Parameter of Diamond Powder

In the GEM and HRPD experiments, the average discrepancies between the lattice parameter of the leached material and the diamond powder over the whole measurement temperature range are 0.0012 Å and 0.0007 Å which represent stresses of −271 MPa and −454 MPa (the experiments used 75 µm and 4 µm diamond powder respectively). These differences are much bigger than the difference between the leached and unleached materials and are much bigger than that which the small amount of retained cobalt in the leached material would be able to cause due to residual stress. As the powder particles should not be able to support internal stresses, other factors that can affect the lattice parameter, such as the defect concentration, were investigated. As the presence of the small amount of unleachable cobalt in the leached material makes techniques such as Raman microscopy (due to a large fluorescent background) and EPR difficult to perform, direct comparison between leached material and diamond powder was eschewed in favour of measuring

the effect of heating on diamond powder. Diamond powder and PCD are made by broadly similar techniques (heating under high pressure in the presence of a metal catalyst) but as PCD is made from diamond powder, it was hypothesised that the additional heating step may have affected the defect concentration resulting in the change in lattice parameter.

The single substitutional nitrogen (N_s^0) concentration has been shown to affect the lattice parameter of diamond in the following way[141]:

$$\frac{\Delta a_0}{a_0} = (0.14 \pm 0.02)\, c_N \tag{4.25}$$

where a_0 is the nitrogen-free diamond lattice parameter and c_N is the concentration of N_s^0 defects. Using this equation, an increase of N_s^0 concentration of 2400 ppm would be required to cause the change in lattice parameter difference seen between the 75 µm powder and the leached material. In section 4.4.5, the defect analysis indicated that there was a decrease of 20 ppm after heating. It is therefore concluded that heating alone does not cause an increase in the N_s^0 concentration that can account for the lattice parameter change observed. Furthermore, as the substitutional nitrogen atom is suggested to take up 1.41 times as much space as the carbon atom it replaces[141] it is unlikely that there is a driving force for increasing the concentration of these defects when the additional high pressure of sintering is taken into account. It is also seen that the position of first order diamond Raman peak increases by around 5.5 cm^{-1} after heating. However, as the interaction between lattice vibrations, lattice parameter and defect concentration is complex, this result is interesting but its interpretation is beyond the scope of this thesis.

4.6 Conclusions

The residual stresses in diamond as a function of temperature have been measured using neutron diffraction. The results showed that the stress in the diamond is small and compressive at room temperature and slowly diminishes as the temperature approaches the stress-free temperature that was shown to be in the region of 700–800 °C. A model is presented that takes into account the sintering conditions

of PCD to explain the measured stresses. The claims found in the literature that PCD experiences mechanical breakdown at 700–800 °C due to differential thermal expansion of the diamond and cobalt have been shown to be incorrect as the stress in the diamond is measured to be close to zero in this temperature range. The small compressive stress in the diamond at room temperature has been shown to produce a slight toughening effect but is not of a great enough magnitude to explain the loss of strength and/or toughness that is seen when the cobalt pools are leached out. Finally, the discrepancy between the diamond powder lattice parameter and leached lattice parameter was investigated in terms of the defect concentration of the material. It was shown not to be solely due to single substitutional nitrogen defects and so further work is suggested.

4.7 Further Work

Neutron diffraction was chosen as an experimental technique as it was thought that the greater neutron scattering cross-section of carbon compared to cobalt (as opposed to the comparative X-ray scattering cross sections) would produce more accurate results when measuring the lattice parameter of the diamond at the expense of measuring the cobalt lattice parameter. However, experiments described in the next chapter showed that highly satisfactory diamond diffraction peaks could be obtained with synchrotron X-ray diffraction as well as being able to measure sufficient cobalt peaks to calculate its lattice parameter accurately. It is therefore suggested that the same experiment be performed using synchrotron X-ray diffraction so that the cobalt lattice parameter may be measured at the same time and the residual stresses be calculated confidently in both phases. It would also be beneficial to crush a leached PCD sample to expose any residual cobalt and re-leach it to produce a truly stress-free reference sample whose diamond is identical to that of the leached material. Furthermore, how these residual stresses change as a function of microstructure would be of interest and so testing samples with different grain sizes would be desirable.

To verify the effect on the mechanical properties of the diamond residual stresses up to the stress-free temperature, a series of experiments to test the fracture toughness as a function of temperature should be performed. If the theory proposed here is correct, the fracture toughness should diminish slightly as the temperature is increased as the residual stress in the diamond is reduced to zero. An ideal technique to perform this experiment would be that of stable crack growth by the double torsion technique that has been used for PCD by Petrov and Tait[142] as equipment to use this technique inside a furnace has been developed (an overview of the technique is given in ref [143]). Also, the fracture toughness could be measured for a variety of temperatures for the same sample due to the crack-length independent nature of the stress intensity factor in this geometry.

Lastly, the origins of the discrepancy in lattice parameters between diamond powder and leached material should be investigated further. Single substitutional nitrogen defects have been shown not to cause the level of difference observed but there are many other common defects that have not been tested.

5

Graphitisation Kinetics

Contents

5.1 Introduction and Aims 146
5.2 Materials and Sample Preparation 146
5.2.1 PCD Materials 146
5.2.2 Neutron Diffraction Samples 147
5.2.3 Synchrotron X-ray Diffraction Samples 147
5.2.4 Microstructural Analysis 148
5.3 Experimental Techniques 152
5.3.1 Neutron Diffraction 152
5.3.2 Synchrotron X-ray Diffraction 152
5.3.3 Laboratory X-ray Diffraction 157
5.3.4 In-situ Heating TEM Experiment 157
5.3.5 Graphitisation of Mechanical Test Specimens 159
5.4 Results and Discussion 159
5.4.1 GEM Neutron Diffractometer 159
5.4.2 Synchrotron X-ray Diffractometer 169
5.4.3 In-situ Heating TEM Experiment 191
5.4.4 Explanation of Observed Phenomena 198
5.4.5 The Effect of Graphitisation on Mechanical Properties . 222
5.5 Conclusions 225
5.6 Further Work 227

5.1 Introduction and Aims

Section 2.3 of the literature review detailed mechanisms of graphitisation that have been observed from diamond and non-diamond carbon. The present chapter will be concerned with exploring which, if any, of these mechanisms operate in PCD at high temperature. Neutron and synchrotron X-ray diffraction experiments will be performed to investigate whether the new phases that form during graphitisation and the behaviour of the lattice parameters of diamond and cobalt are indicative of the nature of the reaction. Microscopy techniques such as SEM, TEM and Raman will be used to look at the microstructure of the PCD at various stages of graphitisation and an in-situ heating TEM experiment will be performed to observe the graphitisation process in real-time. Finally, the effect of partial and catastrophic graphitisation on the mechanical properties of PCD will be tested.

5.2 Materials and Sample Preparation

5.2.1 PCD Materials

5.2.1.1 Standard Cobalt Binder

The majority of the material used in this chapter has a standard cobalt binder chemistry. Although a significant amount of tungsten and carbon will be dissolved in the cobalt due to contact with tungsten carbide (from the substrate) and diamond grains, no additional elements have been added. All of the materials were sintered between 1450 and 1480 °C. A summary of each material used is given below:

G75-A Mono-modal 75 µm feed, sintering pressure 5.5 GPa, sintering time 20 min.

G75-B Mono-modal 75 µm feed, sintering pressure 5.5 GPa and sintering time 10 min.

G75-A-L Identical to G75-A but with as much as possible of its cobalt binder phase leached out by boiling in hydrochloric acid at 109 °C for several hundred hours.

5.2.1.2 Altered Binder Chemistry

A group VII transition metal was thought to increase the melting temperature of the cobalt binder in tungsten carbide-cobalt cermets and hence its effect on the graphitisation reaction was of interest. Due to commercial secrecy, the precise element in question cannot be named. The weight percentages given below correspond to the amount of that element dissolved in the cobalt binder of the WC-Co substrate on which the PCD was manufactured. The amount of this element that ended up in the binder phase of the finished PCD was not measured. All altered binder chemistry material was made from a tri-modal feed with an arithmetic average particle size of 22 µm. The sintering pressure was 7.7 GPa with a sintering time of 10 min.

G22-40X 40 weight percent group VII transition metal.

G22-20X 20 weight percent group VII transition metal.

G22-05X 5 weight percent group VII transition metal.

G22-00X 0 weight percent group VII transition metal, this material served as the control as the binder phase is 100 % cobalt.

5.2.2 Neutron Diffraction Samples

Samples used in neutron diffraction experiments on the GEM beamline discussed in the present section are identical to those described in section 4.2.1.1. Unleached samples were made from G75-A and leached materials from G75-A-L.

5.2.3 Synchrotron X-ray Diffraction Samples

Bar-shaped PCD samples were first manufactured by the method detailed in section 4.2.1.2. Following this, a 1 mm hole was drilled using a laser into the square end face to a depth of approximately 5 mm so that a thermocouple could be inserted into the beam to monitor its temperature during the experiment.

Materials G75-A, G75-B from the standard binder chemistry and materials G22-40X, G22-20X, G22-05X and G22-00X from the altered binder chemistry were used in this experiment.

5.2.4 Microstructural Analysis

As sectioning and polishing of PCD samples is a very aggressive technique that often results in preferential removal of surface cobalt binder pools, a lot of the micron-scale microstructural information is lost when preparing samples in this manner. Therefore, a number of alternative techniques were adopted to prepare samples for microstructural analysis.

5.2.4.1 FIB Cross-sections

Polished surfaces from the interior of the PCD sample were required for microstructural analysis and were produced by the following method. Bar samples as described in section 5.2.3 were attached to aluminium pin stubs for use in scanning electron microscopes using conductive silver paint. Samples were then loaded into either a Zeiss Auriga or Zeiss NVision focussed ion beam microscope and tilted to 9° so that the ion beam would intersect with the surface of the sample at 45°. The edge of the sample was then located and a region approximately 50–100 µm wide by 20 µm high milled from it at high beam currents (16–20 nA) to create a new flat surface at 45° to the existing faces of the beam. This process took between 8 and 12 h and was followed by cleaning steps at progressively lower beam currents down to 150 pA. The geometry of these polished surfaces with respect to the original beam is shown in figure 5.1. These samples were then used for scanning electron microscopy, EDX spectroscopy and Raman microscopy.

5.2.4.2 Transmission Electron Microscopy Samples

Samples of G75-A were prepared for transmission electron microscopy (TEM) by focussed ion beam (FIB) liftout using Zeiss Auriga and Zeiss NVision FIB microscopes. The first stage was to deposit a 1–2 µm thick layer of platinum on top of the feature of interest to protect against damage from the beam of gallium

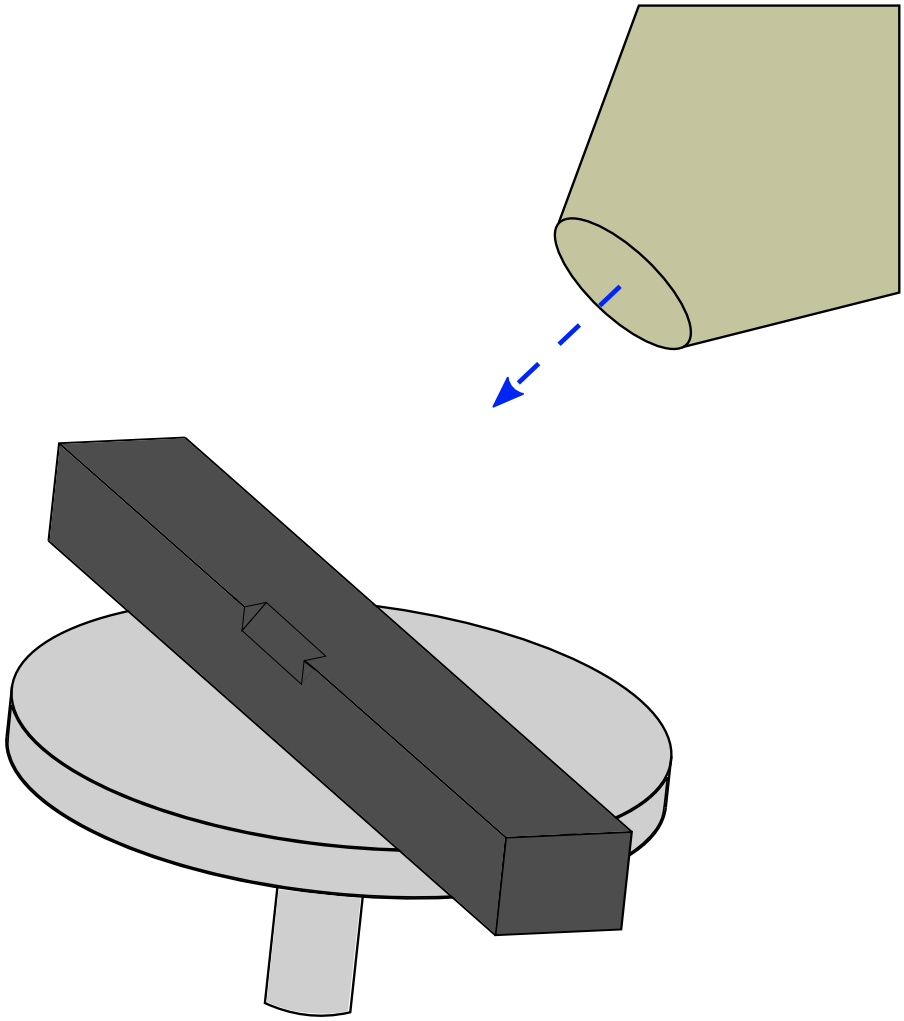

Figure 5.1: Schematic representation of how FIB cross-sections are made in PCD bars. The FIB column is shown in the top right hand corner of the image. The ion beam is incident on the sample (mounted on an aluminium pin stb) at 45° so that a cross-section through the microstructure is made.

ions used in milling. Either side of this, two square trenches with side length 20 µm were milled to a depth of approximately 10 µm using a beam current of 4 nA. The lamella between the two trenches was then thinned to approximately 1 µm with successively lower beam currents. Once the bulk of the thinning was completed, cuts were made to the bottom and side of the lamella as shown in figure 5.2.

The micro-manipulator (a sharpened tungsten needle) was then introduced until it touched the lamella and attached to it by depositing a carbon patch over the point where the two met (figure 5.3). Finally, the remaining attachment points were milled through and the lamella was lifted free from the sample.

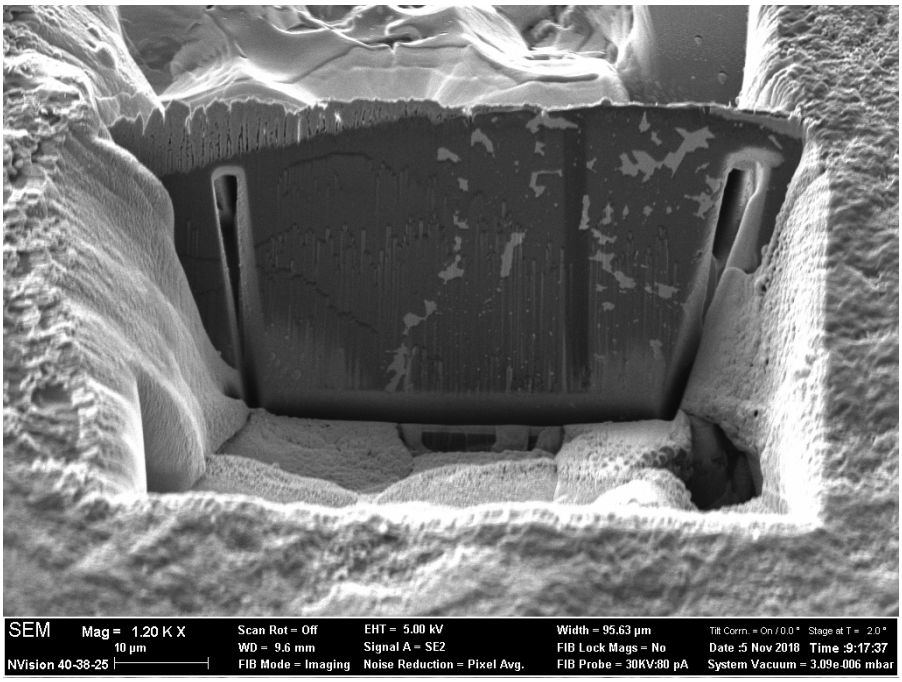

Figure 5.2: TEM sample part way through manufacture. Undercuts have been made in preparation for attachment to the micro-manipulator to fully remove the lamella from the sample. The effects of insufficient protection with a platinum layer can be seen as unwanted texture in the sides of the lamella, so called 'curtaining'.



Figure 5.3: The micro-manipulator (right of image) is introduced and attached to the lamella by depositing a carbon patch over the point where the two meet.

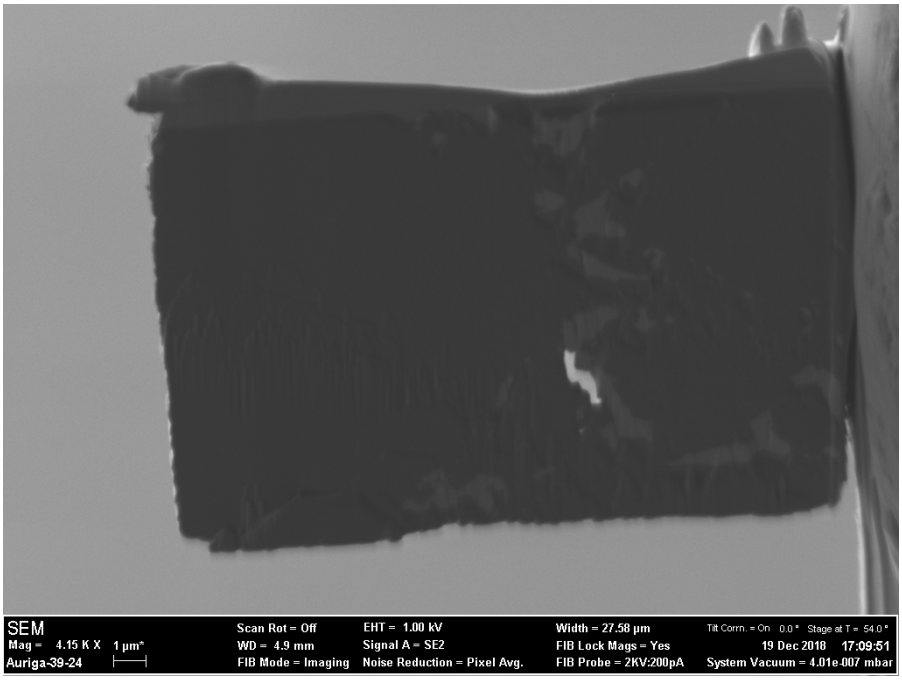

Figure 5.4: This sample was thinned before being deposited on the DENS heating chip to allow better access and prevent damage to the heating chip. Thinning and liftout of this sample was performed by postdoctoral researcher Dr Jack Haley.

The lamella was then attached to a copper TEM grid for further thinning. The beam voltage was steadily dropped from 20 kV to 2 kV as the thickness of the lamella was reduced to ensure the highest quality surface finish possible. The liftout and subsequent thinning stages were performed by Dr Jack Haley, a postdoctoral researcher with a large amount of FIB liftout experience. Figure 5.4 shows an SEM image of the finished lamella using an accelerating voltage of 1 kV. Due to cobalt milling much faster than diamond, a hole can be seen in the centre of the lamella. As only a small region was imaged in TEM microscopy, this did not affect the results of the experiment and due to the tapering effect near the hole, it ensured that at least some part of the lamella was thin enough for successful imaging.

After a thickness of less than 50 nm had been achieved, the lamella was reattached to the micro-manipulator and deposited on a sample holder for TEM imaging.

5.3 Experimental Techniques

5.3.1 Neutron Diffraction

The technique of analysis by neutron diffraction using the General Materials (GEM) diffractometer at ISIS Neutron and Muon Source is as described in section 4.3.1, the only difference is the heating regime applied to the samples and the time resolution of the measurements. Samples were heated from room temperature to the target temperature (800 °C or 850 °C) in less than a minute and held there for 2 to 3 h. Diffracted intensity was collected and integrated over six minute intervals. Although a shorter integration time worsened the quality of the diffractogram, this was deemed an acceptable compromise given the greater time resolution. Lattice parameter and graphite weight percentage was assessed through Rietveld refinement of each six minute diffractogram. One unleached sample was tested at 800 °C and 850 °C and a leached sample was tested at 850 °C only.

5.3.2 Synchrotron X-ray Diffraction

An experiment, EE14316, was undertaken to examine the behaviour of PCD at high temperature with a greater focus on the metallic components using the I15 beamline of the Diamond Light Source synchrotron in Harwell, UK. A vacuum furnace (like that used in the neutron diffraction experiments) was unavailable and so a custom-made furnace using a focussed spot of infra-red radiation surrounding a sample in a quartz capillary tube through which argon was flowing was used (figure 5.5). The beam energy was 72 keV (wavelength 0.1722 Å) in an unfocussed configuration giving a beam width and height of 0.5 mm. A Perkin Elmer 1621 EN flat-panel detector with an image size of 2048 x 2048 pixel (each of size 200 µm^2) was used. A calibration of the source-detector distance and detector tilt was performed using a LaB_6 standard and this calibration was used to correct each diffractogram. A 1 s exposure time was used with a 29 s dead-time between each exposure to prevent cumulative saturation of the detector giving a time resolution of 30 seconds. Samples were in the form of 1.5 x 1.5 mm cross-section, 15 mm

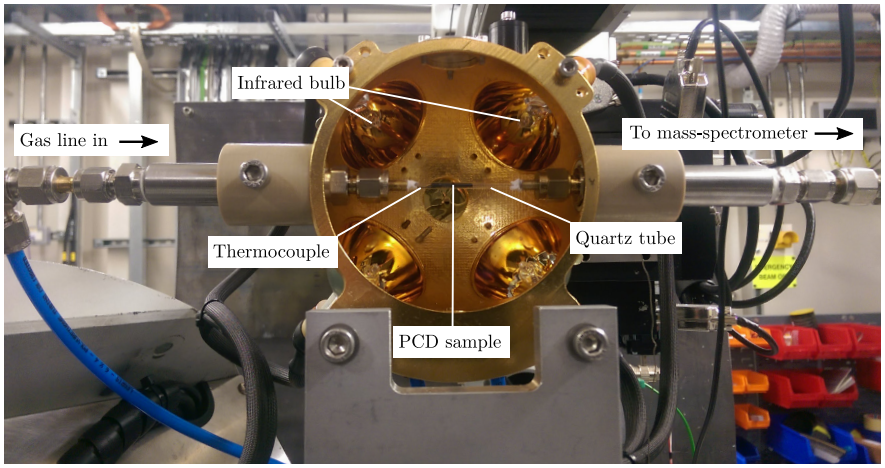

Figure 5.5: Infrared furnace used in Diamond Light Source synchrotron experiments. Four infrared bulbs are focussed onto a quartz capillary tube at the centre of the furnace which is sealed into a gas line with refractory cement. Argon gas is passed through the quartz tube at a flow rate of approximately $4\,\mathrm{L\,min^{-1}}$. The exhaust line is connected to a mass-spectrometer to monitor for the presence of gasses such as oxygen, carbon monoxide or carbon dioxide that would indicate a leak in the line allowing oxidation of the diamond to occur.

length beams with a 1 mm hole drilled into their base (along the axis of the beam) into which a 1 mm diameter, 310-stainless steel k-type thermocouple was inserted to measure sample temperature. All samples were aligned with the cutter top face perpendicular to the beam direction, pointing away from the source. The temperature was controlled by adjusting the infrared power of the furnace bulbs. A mass-spectrometer was attached to the exhaust line to monitor the levels of oxygen, CO and CO_2 which would be indicative of air leaking into the furnace and potentially causing oxidation of the diamond.

The front and back faces of the furnace had cut-outs approximately 1.5 cm in diameter so that the x-ray beam could pass through without interacting with the furnace walls. These openings were further covered with a layer of reflective capton tape with an approximately 2 x 2 mm square hole cut in it to reduce the escape of infrared heating rays from the furnace assembly. These small cut-outs offered a limited range of movement of the whole assembly to position the sample properly in the x-ray beam. To ensure that the thermocouple was as close to the gauge volume as possible, the sample was moved perpendicular to the beam until the

diffraction pattern of the thermocouple could be seen. It was then moved in the opposite direction until the peaks just disappeared.

5.3.2.1 Calibration

Calibration of the diffractometer was performed immediately before the first experiment with a powdered lanthanum hexaboride standard (whose lattice parameter is known very accurately) contained in a glass capillary tube. The standard was loaded into the diffractometer and a diffraction pattern taken. The 'Dawn' software package was used for calibration and approximate values of beam energy and detector distance were input. The software displays the raw output of the flat-plate detector and overlays the predicted diffraction pattern for LaB_6 given the initial guessed parameters. The parameters are first refined manually to give a good fit to the recorded data, the beam energy as fixed as this was known accurately, and then the software performed a least squares refinement to find the distance from the beam to the detector and the tilt of the detector. These settings were then used for the rest of the experiment. As accurate lattice parameter measurements were not particularly important in the following experiments (rather relative changes within a single experiment), errors in this calibration will not be discussed in the forthcoming sections. This is only true for the synchrotron diffraction experiments as accurate lattice parameter measurements were very important in the case of the neutron diffraction.

5.3.2.2 Repeat Measurements

To assess the repeatability of lattice parameter measurements using synchrotron x-ray diffraction, two nominally identical samples were each measured multiple times. The entire furnace assembly was dismantled, the sample removed, placed in a new capillary tube and the furnace reassembled for each measurement to simulate a typical sample change. Two physically different G75-B samples were measured three times each to ascertain the standard error between measurements and the typical variation between nominally identical samples.

5.3.2.3 Heating Schedules

Detailed below is the infrared furnace power for each sample as a function of time.

Behaviour During Graphitisation Figure 5.6. Sample: G75-A. Main temperature hold time: 1 hour.

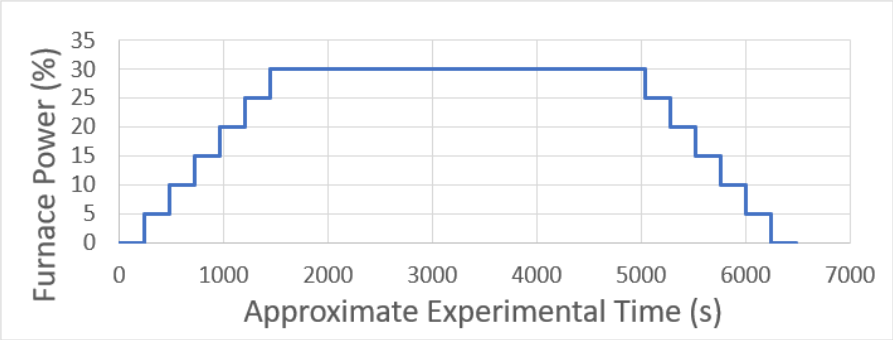

Figure 5.6: "Behaviour during graphitisation" furnace power experimental schedule.

The Period Leading up to Graphitisation Figure 5.7. Sample: G22-00X. Temperature hold times: 30 minutes. It should be noted that the x-ray beam suffered an outage at 25 % furnace power on cooling and so no diffraction data was captured between this point and room temperature. This did not adversely affect the desired results of the experiment.

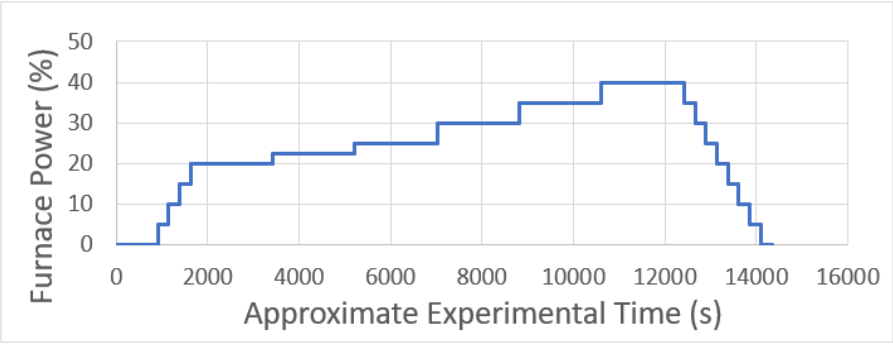

Figure 5.7: "Period leading up to graphitisation" furnace power experimental schedule.

Heating Below Graphitisation Temperature - Sample A Figure 5.8. Sample: G75-B. Temperature hold time: no hold. Note: furnace power was held at 5% for 15 minutes to allow better curing of ceramic cement holding the capillary tube.

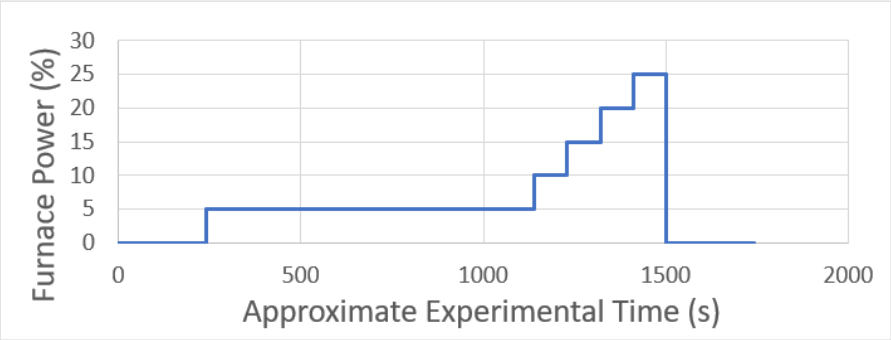

Figure 5.8: "Heating below graphitisation temperature - sample A" furnace power experimental schedule.

Heating Below Graphitisation Temperature - Sample B Figure 5.9. Sample: G75-B. Temperature hold time: 20 minutes. Note: furnace power was held at 5% for 15 minutes to allow better curing of ceramic cement holding the capillary tube.

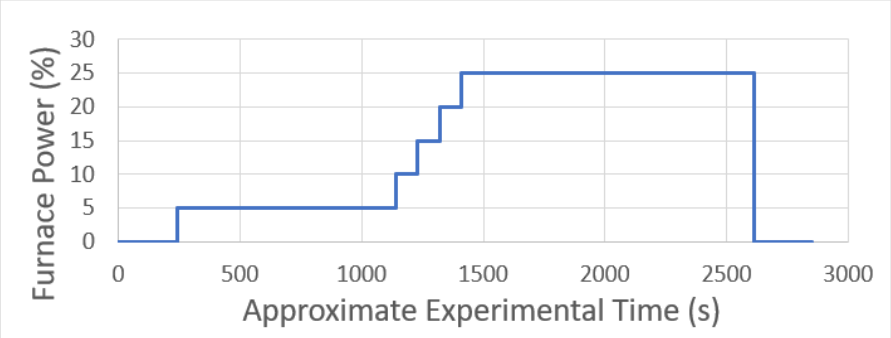

Figure 5.9: "Heating below graphitisation temperature - sample B" furnace power experimental schedule.

Graphitisation of Altered Binder Chemistry Figure 5.10. Samples: G22-00X, G22-05X, G22-20X, G22-40X. Temperature hold time: 1 hour.

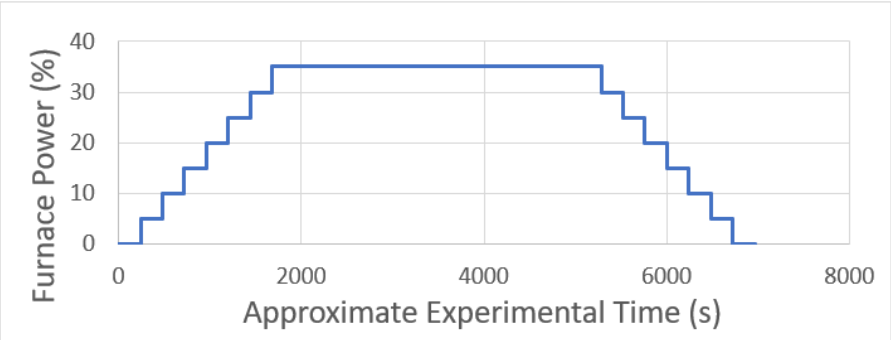

Figure 5.10: "Graphitisation of altered binder chemistry" furnace power experimental schedule.

5.3.3 Laboratory X-ray Diffraction

Laboratory x-ray diffraction was performed on off-cuts of material from bar-shaped specimens manufactured for use in the synchrotron experiment. The main aim of this experiment was to determine whether the alteration of the binder chemistry as described in section 5.2.1.2 had an effect on the graphitisation of diamond at high temperature. G22-40X, G22-20X, G22-05X and G22-00X samples were tested in this experiment.

XRD measurements were taken on a PANalytical X'Pert Pro diffractometer with an Anton Paar HTK-1200N vacuum furnace sample stage. Samples were heated rapidly from room temperature, in vacuum, to 850 °C where they were held for 6 hours. Diffracted intensity was collected over 10 minute intervals and the graphite weight percentage was assessed using Rietveld refinement as a function of time.

5.3.4 In-situ Heating TEM Experiment

In addition to standard transmission electron microscopy, two experiments were performed using an in-situ heating holder in a Jeol ARM200F STEM microscope. After thinning the sample, it was deposited on and attached to a DENS Solutions Wildfire heating chip (figure 5.11). The silicon chip had a thin, spiral track of platinum deposited onto its surface that was used for resistively heating the sample. In between each loop of the spiral was a series of thin windows that could be easily machined away to produce an electron-transparent portion of the chip over

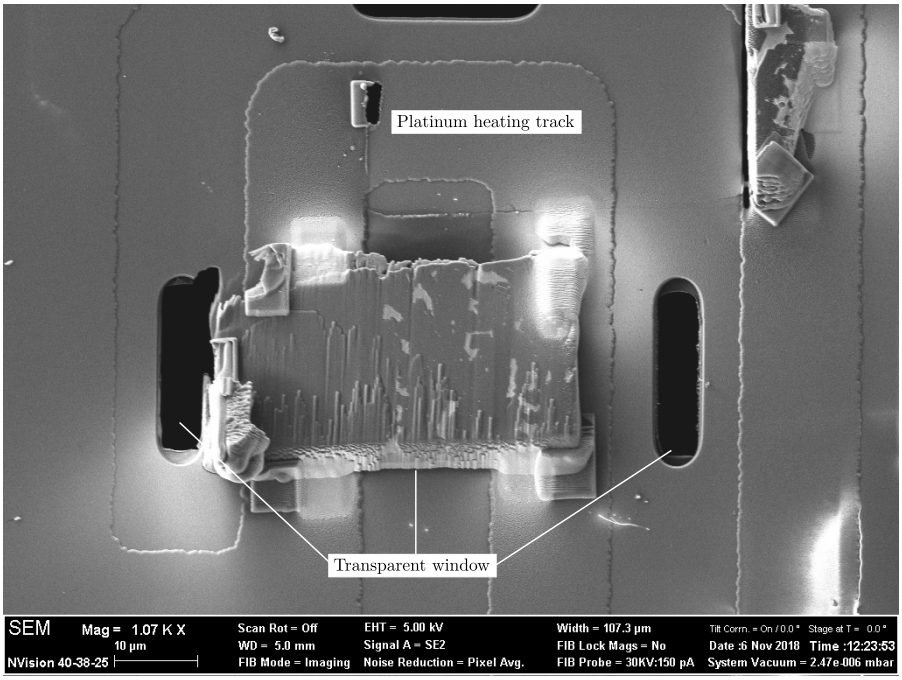

Figure 5.11: TEM sample attached to DENS heating chip. The chip bridges two resistive heating tracks and the region of interest is positioned over a transparent window in the silicon chip. Final thinning of this sample was performed on the chip. Thinning and liftout of this sample was performed by Dr. Ian Griffiths (EM support staff, Department of Materials).

which to position the liftout sample. The first sample had its final thinning stage after being deposited on the DENS chip. This proved to be sub-optimal as the sample did not benefit from the protective effect of the platinum capping layer as once on the chip, it has to be thinned from quite a steep angle. This resulted in a large amount of curtaining and gallium implantation to the sample which created very unclear TEM images. A second sample was therefore prepared that was thinned on a copper TEM grid before being deposited on the DENS chip which proved to be a much more successful technique.

After deposition on the chip, the samples were heated in 100 °C steps from room temperature to 700 °C and then to 800 °C in 50 °C steps with a hold time of 5 min at each temperature whilst being imaged in the TEM. The live feed of the microscope (approximately 2 s refresh time) was recorded with screen capture software and a micrograph was captured before each temperature increase. At 800 °C, the sample graphitised and this process was recorded using the live capture

software. After the reaction slowed significantly, the sample was cooled rapidly to room temperature and another micrograph taken. The sample was reheated to 800 °C, 850 °C then finally 900 °C to ascertain whether the reaction would progress any further at a higher temperature. Electron energy loss spectroscopy (EELS) and energy dispersive x-ray (EDX) spectroscopy were also performed before and after heating to confirm the presence of graphite and observe the changes in spatial distribution of the various elements in the PCD.

5.3.5 Graphitisation of Mechanical Test Specimens

To test the effect of varying degrees of graphitisation on the macroscopic strength, three grades of PCD (G12-M-HP, G17-M-HP and G27-M-HP that are described in section 3.2.1) were heated to 800 °C for 0 h, 1.5 h and 3 h in vacuum whilst x-ray diffraction was performed on them to assess the degree of graphitisation. The heating times were chosen so that the first sample set was completely ungraphitised (control sample), the second had a limited amount of graphitisation (1.5 h of heating) and the last experienced "catastrophic graphitisation" (3 h of heating). After heating, the samples were tested in 4-point bending as described in section 3.3.1. Due to limited samples of the G12-M-HP material, it was not subjected to the 3 h heating treatment as this was deemed to be least important.

5.4 Results and Discussion

5.4.1 GEM Neutron Diffractometer

Figure 5.12 shows the graphite weight percentage as a function of time for samples held at a constant temperature in the GEM neutron diffraction experiment. Unleached PCD graphitised immediately when held at 850 °C with the graphite weight percentage increasing rapidly at first and then slowing down. Similar behaviour was observed at 800 °C but a delay of approximately 3000 s was seen in the onset of graphitisation and the graphite weight percentage was lower at all times. Leached PCD heated to 850 °C did not graphitise even after 3 h at temperature. The relatively large scatter in the data, especially at low graphite percentages, was due

to the difficulty experienced by the Rietveld refinement software in trying to fit the broad {0002} graphite peak on top of the relatively noisy baseline.

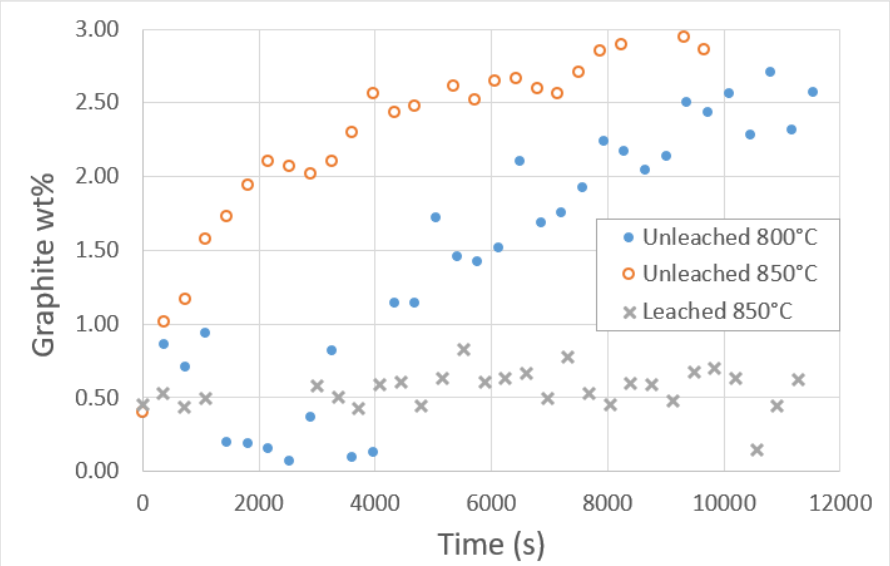

Figure 5.12: Weight percentage of graphite calculated by Rietveld refinement against time. No graphite is seen forming in the leached material. The unleached material begins graphitising straight away at 850 °C and only beings after an incubation period of approximately 3000 s at 800 °C. The statistical uncertainty given by the Rietveld refinement in the weight percentages of graphite in the unleached PCD is 0.25 wt% and the leached PCD is 0.7 wt%.

Figures 5.13 and 5.14 show the diamond and cobalt lattice parameters as a function of time over the same period. The diamond lattice parameter was calculated by Rietveld refinement and the cobalt lattice parameter was calculated by single peak fitting of the {200} peak. The larger scatter in the cobalt lattice parameter values is due to its calculation from only a single, low signal-to-noise peak rather than an entire diffraction pattern. The trend in diamond lattice parameter shows a negligibly small change over the 2–3 h of heating and the cobalt lattice parameter is potentially decreasing over this period but it is difficult to say this with certainty due to the large scatter in the results. Figure 5.15 shows the broad graphite {0002} peak and its relatively poor fit by Rietveld refinement. The likely cause of the broadness of the graphite peak is varying strain in different bits of graphite across the sample.

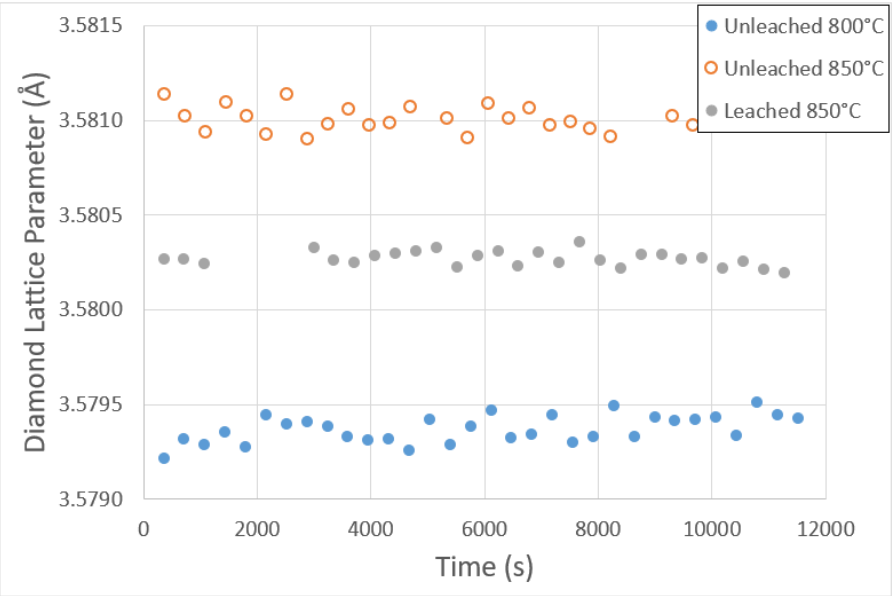

Figure 5.13: Plot of diamond lattice parameter against time for unleached (800 °C), unleached (850 °C) and leached (850 °C) PCD calculated by Rietveld refinement. Over the course of the approximately 3 h heating period, the change in diamond lattice parameter is negligible. The statistical uncertainty in the lattice parameter of diamond given by the Rietveld refinement is on the order of 0.000 05 Å.

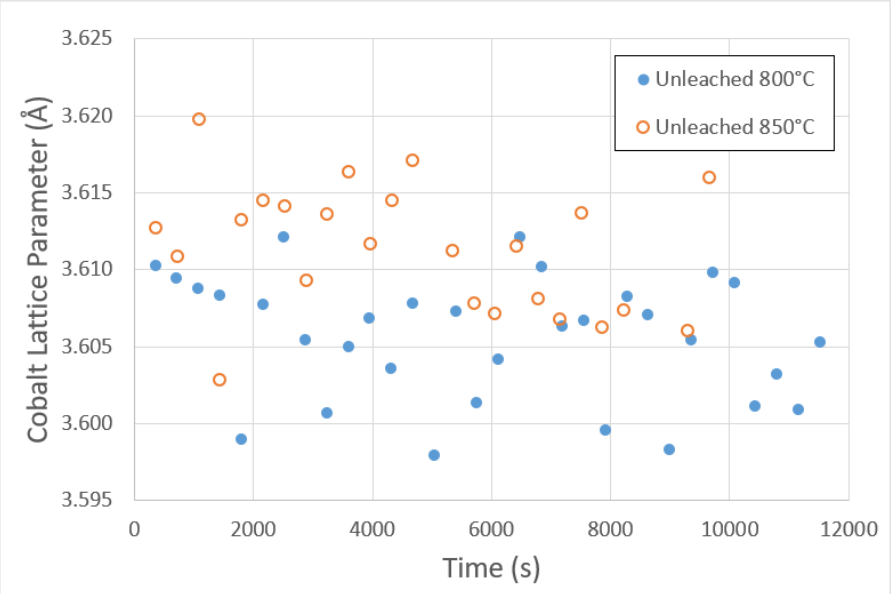

Figure 5.14: Plot of cobalt lattice parameter against time for unleached PCD heated to 800 °C and 850 °C inferred from the position of the {200} cobalt peak. At both temperatures the lattice parameter decreases at approximately the same rate. The statistical uncertainty in the lattice parameter of cobalt given by the Rietveld refinement is on the order of 0.003 Å.

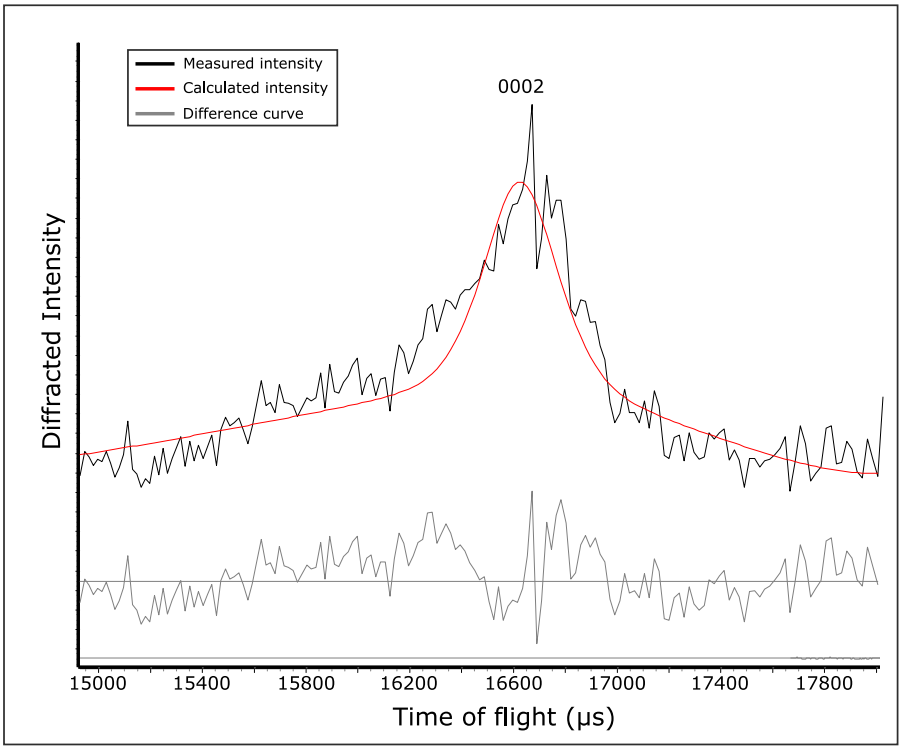

Figure 5.15: Broad {0002} graphite peak with its calculated fit shown in red that was used to calculate the weight percentage of graphite present. The poor fit is thought to be due to varying stress on the graphite throughout the microstructure causing an asymmetrical shape. Another possible explanation is that this graphite is actually turbostratic carbon which has a broader diffraction peak due to its inherently less ordered nature.

5.4.1.1 Microstructural Analysis

Raman microscopy was performed on samples heated to 850 °C for 3 h and the graphite signal was mapped spatially. This was first attempted on a FIB-machined cross-section to give a clear relationship between graphite distribution and microstructure, however, the process of milling the sample in the FIB was found to almost completely destroy both diamond and graphite Raman signals and hence a fracture surface was imaged instead. Figure 5.16 shows maps of diamond and graphite Raman signals and the white light optical image of the region. Graphite is seen to exist primarily around the periphery of large diamond grains.

Samples from this experiment were also investigated using SEM and EDX to examine the microstructure of the graphite that formed during their heating. Figure 5.17 shows a low magnification SEM image of the unleached sample that was heated

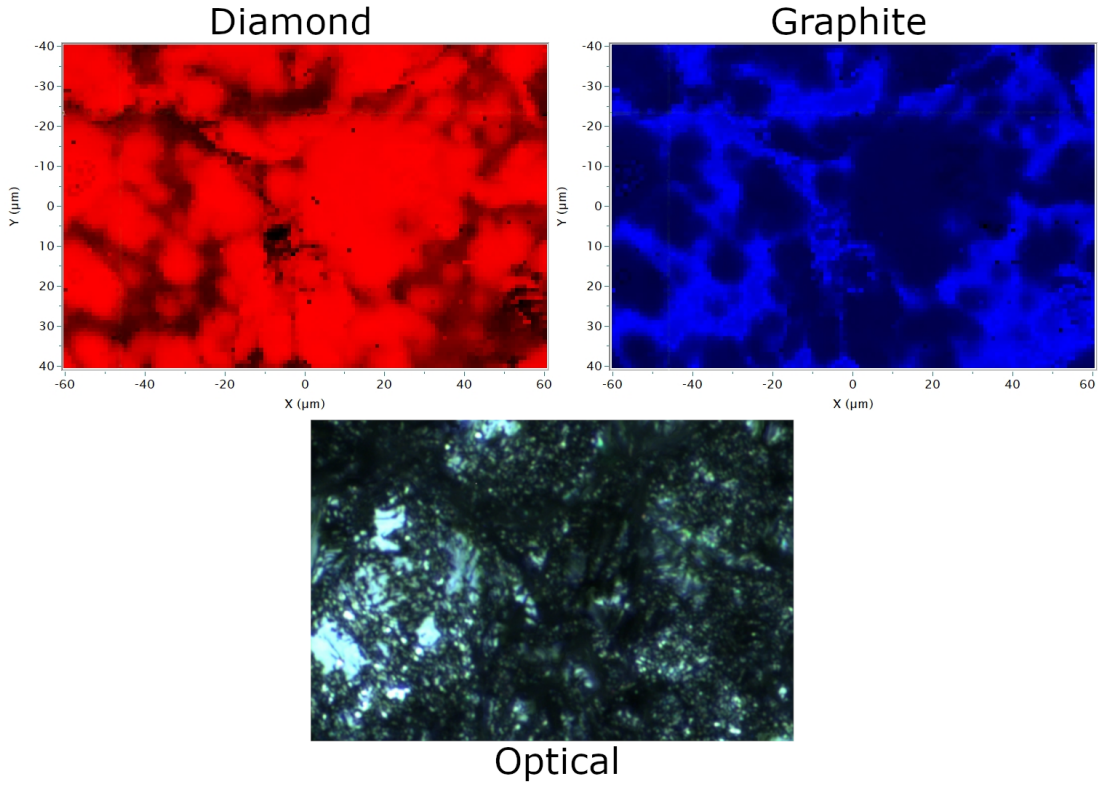

Figure 5.16: Maps of the diamond (red, left) and graphite (blue, right) Raman signals from a fracture surface of graphitised PCD (optical image, bottom) showing graphite that has formed mainly around the edges of large diamond grains.

to 850 °C. The two layers that can be seen in the cross-section are due to a leached layer approximately 200 µm thick on the right-hand face of the cutter. Extensive cracking can be seen in the leached layer with a single crack being transmitted into the unleached layer. Closer examination of the scaife-polished microstructure of the unleached material (figure 5.18) shows heavily degraded grain boundaries that EDX analysis revealed had been excavated and back-filled with a silicon-rich material (likely from the polishing medium or wheel). As this polishing technique proved too damaging to the very soft graphite, FIB cross-sections (detailed in section 5.2.4.1) were produced to analyse the microstructure instead. Figure 5.19 shows a FIB cross-section of a graphitised sample with several large binder pools connected by a crack with a large crack-opening displacement. Regions that are of similar contrast to the diamond but separated from it by a thin boundary can be seen surrounding the binder pools and crack faces (highlighted by black arrows). Figure

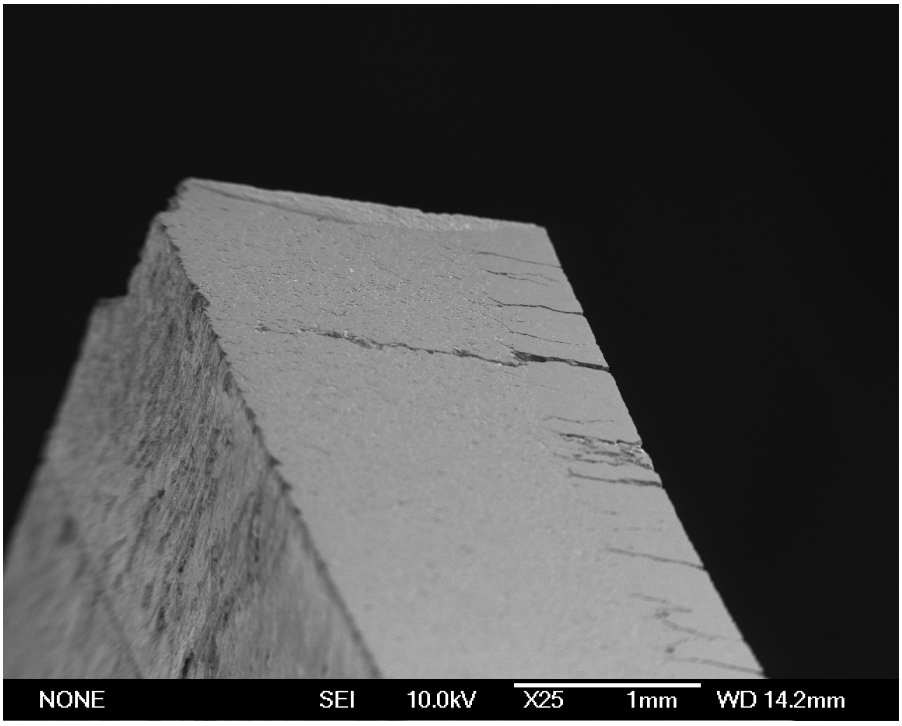

Figure 5.17: Low magnification secondary electron image of the unleached GEM sample that was graphitised at 850 °C for 3 h. This sample contained a leached layer (right hand side of the image) that contains numerous cracks. A single, large crack can be seen traversing the unleached layer (lef thand side of image).

5.20 shows a similar area with the boundary highlighted by black arrows. The top right panel shows a weaker carbon EDX signal in the region between this boundary and the cobalt pool. Graphite has a lower density of carbon atoms than diamond and so this strongly suggests that this region is graphite. As there is a 55 % volume expansion when diamond transforms to graphite, the extensive cracking in the microstructure has likely been caused by the formation of this graphite. This large-scale graphitisation that leads to the destruction of the PCD on a microstructural scale will henceforth be referred to as "catastrophic graphitisation". Within the graphitised region there appear to be accumulations of tungsten and cobalt along with a generally quite high level of both dissolved in the graphite.

SEM analysis of a FIB cross-section of the leached material that was heated to 850 °C for 3 h shows that although there are many small, residual cobalt pools that could not be removed by leaching, the diamond surrounding them did not undergo any detectable graphitisation (figure 5.21). Figure 5.22 shows an EDX

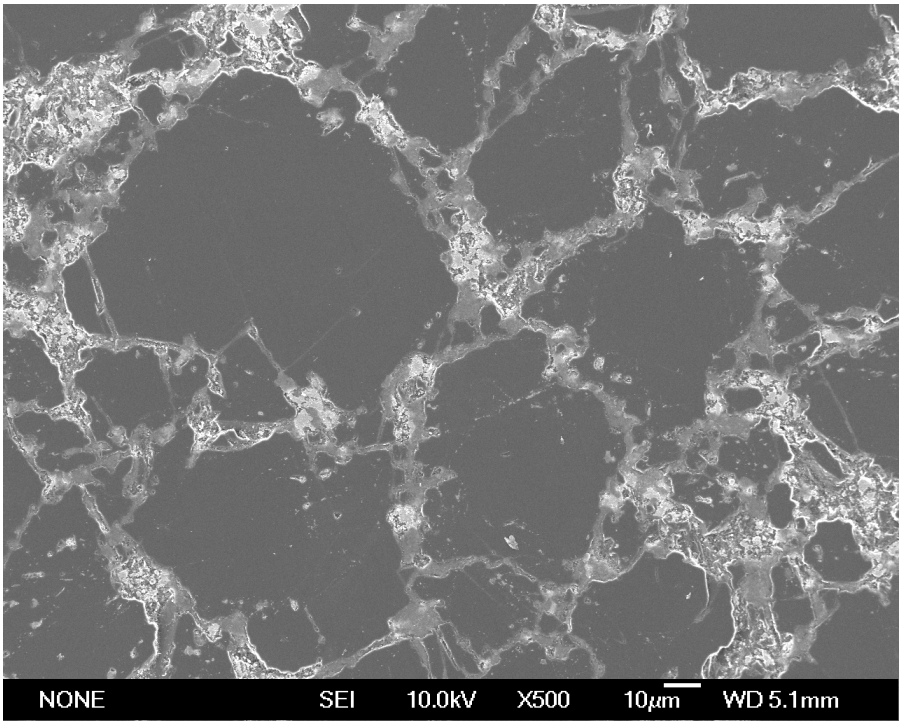

Figure 5.18: Secondary electron image of the heavily degraded grain boundaries of a graphitised sample. This sample was subsequently EDM cross-sectioned and polished which has likely resulted in additional damage to the graphitised boundaries.

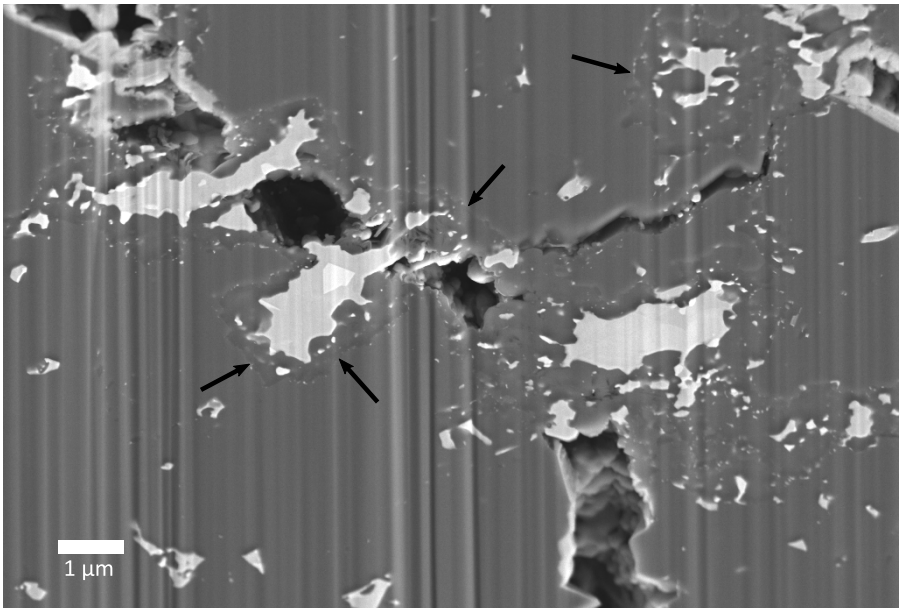

Figure 5.19: FIB cross-section of a graphitised sample. A crack with a large opening displacement can be seen connecting several binder pools. Black arrows highlight the boundary of the region surrounding the binder pools and crack faces which is suspected to be graphite.

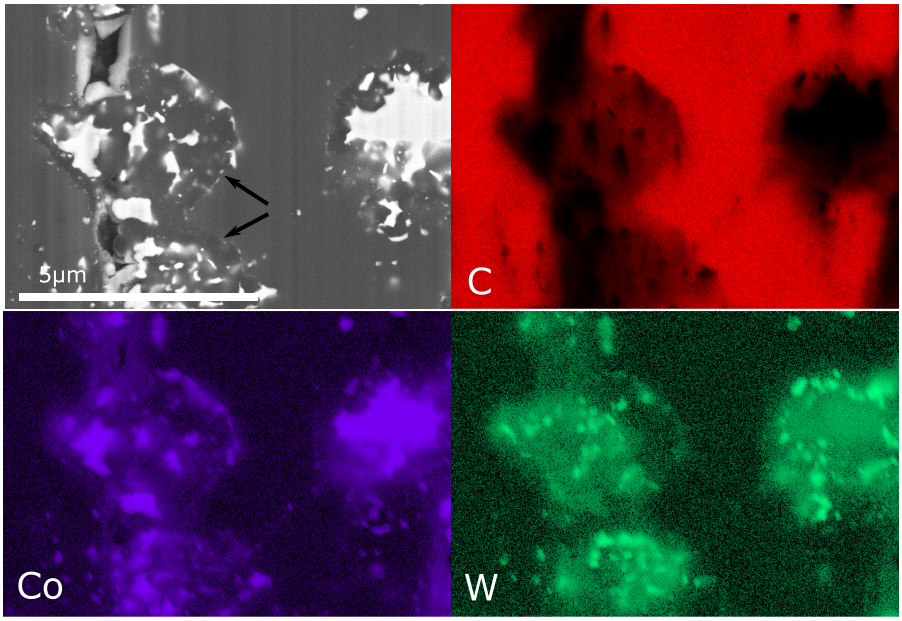

Figure 5.20: EDX maps of the carbon (red, top right), cobalt (purple, bottom left) and tungsten (green, bottom right) signals from a region surrounding a binder pool in a graphitised sample. The black arrows indicate the boundary of the suspected graphitised region which can be seen to have a lower carbon concentration than the surrounding diamond.

map of one the largest binder pools from figure 5.21 with no area of lower carbon content surrounding the cobalt pool indicating the absence of graphite.

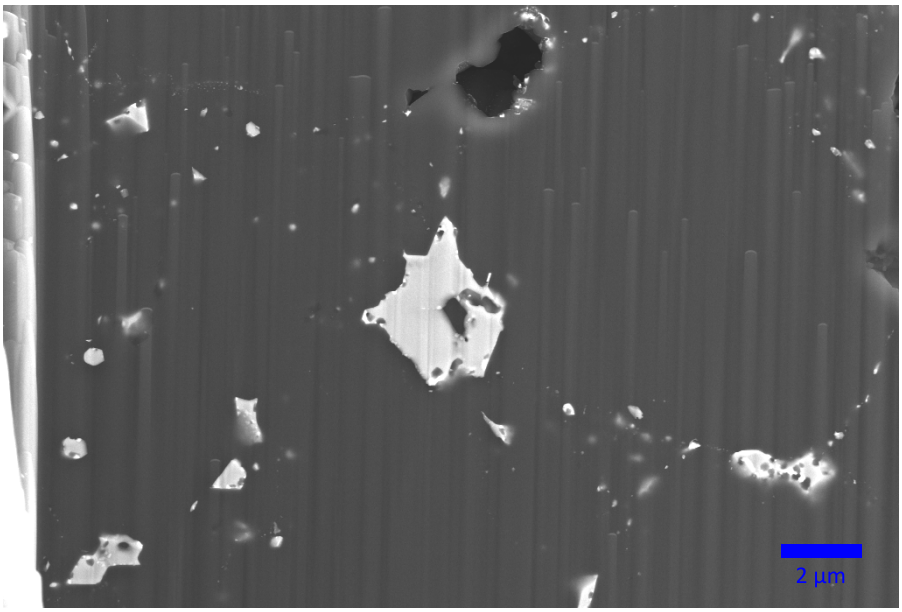

Figure 5.21: FIB cross-section of a leached sample that was heated to 850 °C for 3 h. Several cobalt pools can be seen that were not removed by leaching and there is no evidence of graphitisation surrounding them.

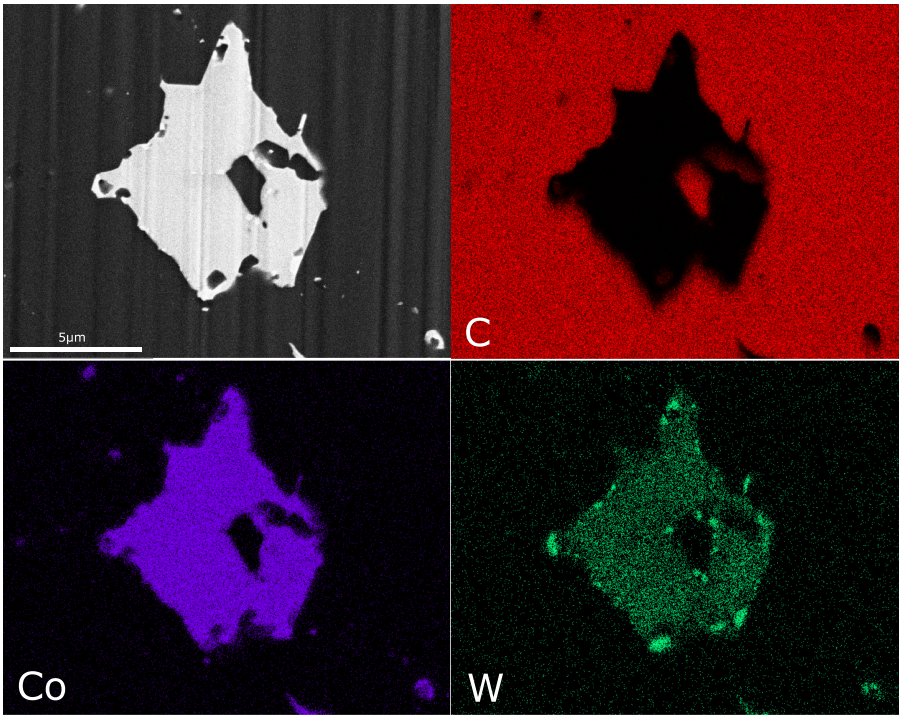

Figure 5.22: EDX map of the carbon (red, top right), cobalt (purple, bottom left) and tungsten (green, bottom right) signals of the largest residual binder pool from figure 5.21. No low carbon concentration region can be seen around the binder pool suggesting that it has not graphitised.

To investigate the microstructural features of the graphitised region surrounding the cobalt pool, a TEM lamella was made from the graphitised material. Figure 5.23 shows a high-angle annular dark field (HAADF) contrast scanning transmission electron image of the graphitised region surrounding a cobalt pool. As the contrast in this imaging technique is derived from very high angle incoherently scattered electrons which come from the nucleus of the atom, the contrast is strongly dependent on the atomic number. Lighter shades are therefore from higher atomic number species such as tungsten and cobalt. On the left of the image is a cobalt binder pool and on the right is a diamond grain (with additional contrast within it due to FIB damage). The darker region between the two is graphite; figure 5.24 shows a high resolution dark field (DF) contrast image of this region where individual planes of atoms can be seen. Measuring the spacing of these planes by measuring the distance between brightness peaks yields a value of 3.7 Å which is close to the graphite {0002} plane spacing (3.35 Å). EDX was used to investigate the

distribution of elements within the microstructure. Figure 5.25 shows the cobalt (magenta) and tungsten (green) EDX signals superimposed on a DF image of a region from figure 5.23 (the carbon signal has been omitted for clarity). Attached to the cobalt pool and also within the graphite region, there are particles that appear darker than the binder pool in the dark field image (indicating differing diffraction contrast) and contain tungsten, cobalt and carbon according to the EDX map. As the solubility of cobalt in tungsten carbide is so low as to be negligible[144], these are likely precipitates of one of the η-carbide phase of tungsten and cobalt (Co_3W_3C or Co_6W_6C)[145], this phase was also identified in graphitised samples at the boundary of the cobalt pool by Westraadt *et al.*[62]. The particles that exist along the diamond-graphite boundary have a more angular morphology than the η-carbide particles and seem to only contain cobalt according to EDX. These particles could be important to the formation of graphite if the reaction requires the constant presence of the cobalt catalyst to continue, however, they could merely be swept along with the graphite front (if the reaction moves through the diamond) or left behind by it (if the reaction moves into the cobalt pool) but from a static TEM image it is difficult to ascertain which of these possibilities is correct.

5.4.1.2 Summary of Key Points

- There is a temperature sensitive incubation period that precedes graphitisation.
- Once graphitised, samples are heavily degraded with the material cracking on a microstructural scale.
- Graphite completely surrounds larger binder pools and cracks connect these regions.
- Leached material does not graphitise at all even if heated to 850 °C for 3 h even though there are residual cobalt pools that remain post-leaching.
- η-carbide particles become isolated in the graphitised regions and cobalt particles are present at the diamond-graphite interface.

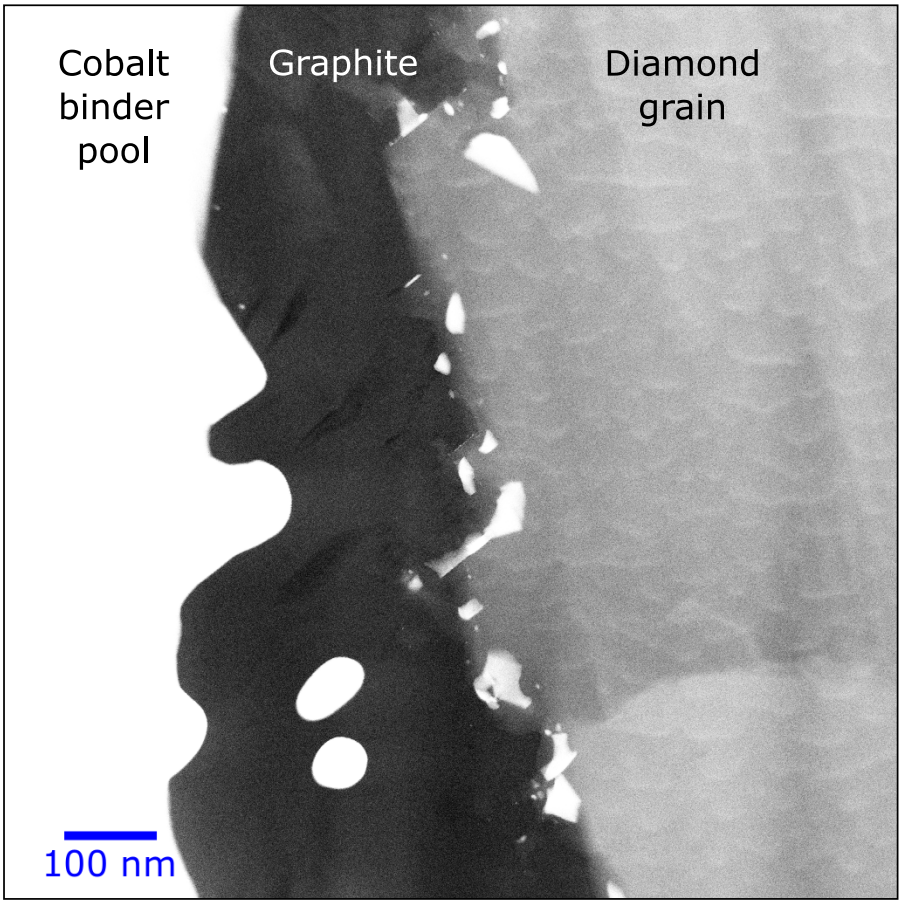

Figure 5.23: High angle annular dark field image of the graphitised region surrounding a cobalt binder pool. This sample was heated and graphitised ex-site and then a TEM sample was made from it.

5.4.2 Synchrotron X-ray Diffractometer

5.4.2.1 Repeat Measurements and Uncertainty

The results of measuring two nominally identical G75-B samples in table 5.1 shows that the standard error between separate measurements is 0.0003 Å ($\frac{\Delta a}{a} = 8 \times 10^{-5}$) and therefore that the two samples have the same lattice parameter within the bounds of the measurement error. The statistical error in the lattice parameters of diamond and cobalt given by the Rietveld refinement are on the orders of 0.000 05 and 0.000 08 respectively and so the larger uncertainty measured by repeat measurement will be taken to represent error for all lattice parameter measurements in this section.

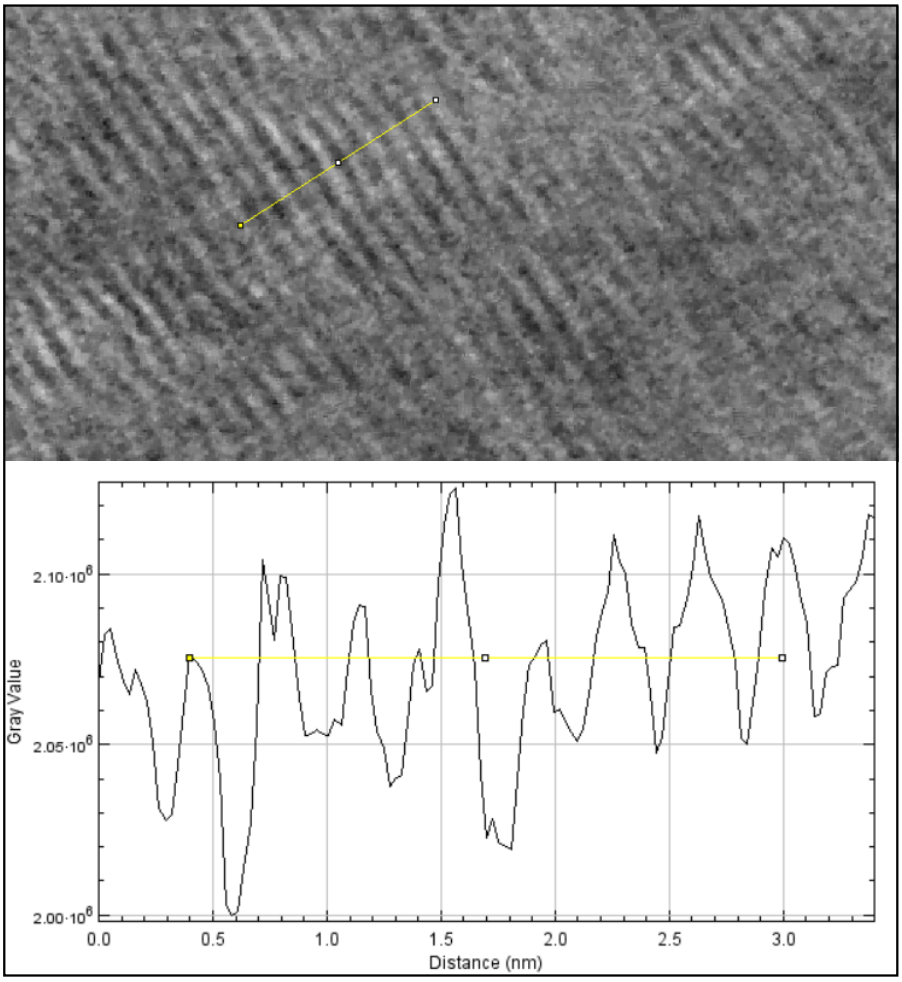

Figure 5.24: STEM image of planes of atoms within a graphite region. A line has been drawn perpendicular to the planes to allow the spacing of the contrast variation to be measured to calculate the plane spacing.

Sample	Average Lattice Parameter
G75-B-A	3.5690 ± 0.0001 Å
G75-B-B	3.5688 ± 0.0003 Å

Table 5.1: Values of diamond lattice parameter measured for two nominally identical samples of G75-B. Each sample was measured three times and the error given is the standard error in these measurements.

5.4.2.2 Calibration of Temperature

Some samples did not have holes drilled in them for thermocouple insertion as this process relied on access to a laser used by industry which could not always be guaranteed when it was needed. These samples instead had to have a thermocouple

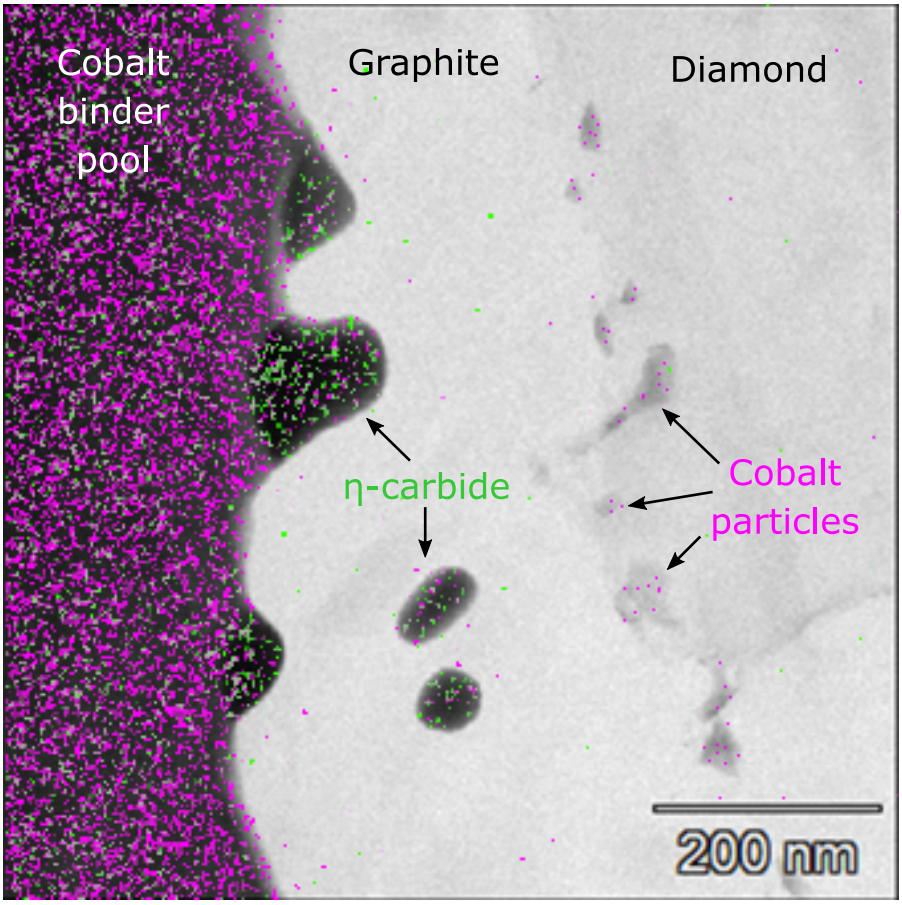

Figure 5.25: TEM EDX map of a region from figure 5.23. The Cobalt signal is coloured in magenta and the tungsten signal, green. The carbon signal has been omitted for clarity. Particles containing tungsten and cobalt with a rounded morphology can be seen attached to the cobalt and isolated within the graphite which are suspected to be η-carbide. Particles of cobalt can be seen at the boundary between the graphite and the diamond.

put in contact with their surfaces which resulted in their recorded temperature being significantly lower than their estimated true internal temperature. This was corrected for by using previously collected data on lattice parameter as a function of temperature for G75-A material determined in the experiment on HRPD. The temperature could then be inferred from the measured diamond lattice parameter as long as no other factors (such as graphitisation or precipitation) significantly affected it. Firstly, the room temperature measurements for the G75-A diamond lattice parameter are compared between synchrotron and neutron diffraction experiments (figure 5.26) as there always seemed to be a small offset between lattice parameters of the same material measured on different instruments (presumably

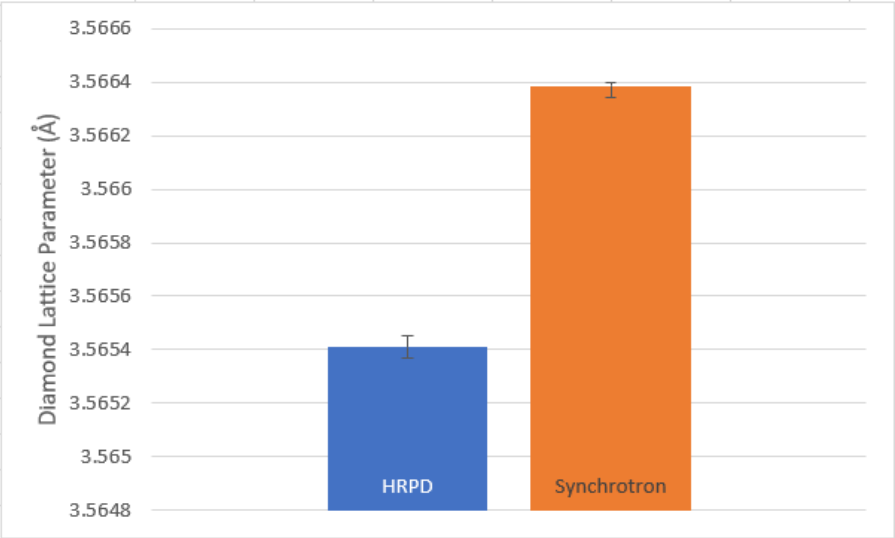

Figure 5.26: Average of measured room temperature diamond lattice parameters from HRPD neutron and Synchrotron x-ray diffraction experiments. The averages are made from different samples of the same G75-A material (HRPD: 4 samples, synchrotron: 2 samples). The error bars show the simple range in the measured values.

due to imperfect calibration). This difference in lattice parameter was subtracted from the synchrotron results as an offset (assuming that it remained constant with temperature). A quadratic trendline was fitted to the unleached diamond lattice parameter from figure 5.27 giving a relationship with temperature from which the true temperature of the sample in the synchrotron experiment was calculated.

5.4.2.3 Behaviour During Graphitisation

A sample of G75-A was heated in steps to a temperature expected to cause graphitisation and then held at this temperature. This sample did not have a hole drilled for a thermocouple and so its measured and calibrated temperatures are shown in figure 5.28. Although the maximum temperature measured by the thermocouple is only around 600 °C, the corrected temperature is above that shown to cause graphitisation in figure 5.12 as it reaches a maximum of 916 °C. As the furnace power is reduced, the calibrated temperature can be seen dropping to negative temperatures. At this point, another factor has affected the diamond lattice parameter and it can no longer be used to measure temperature.

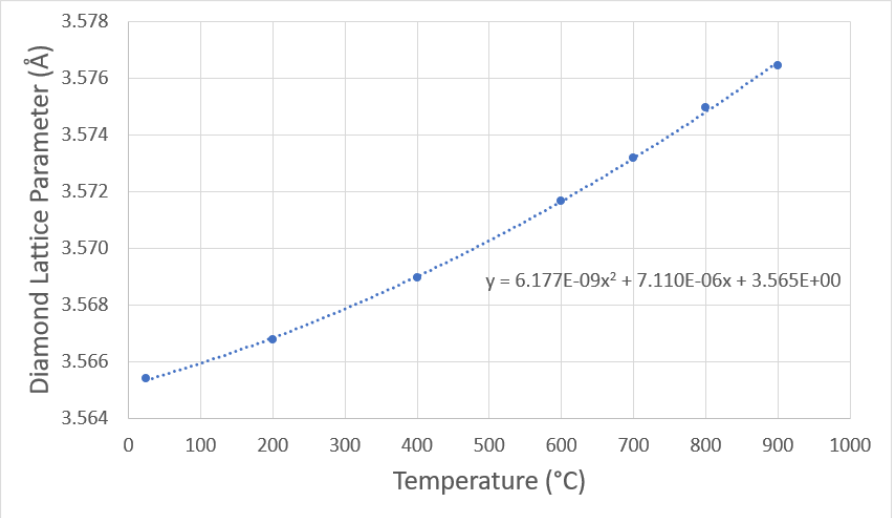

Figure 5.27: Diamond lattice parameter as a function of temperature measured for 75 µm diamond powder using Rietveld refinement from data from GEM. This is used to calculate the temperature of samples in the synchrotron experiments from the measured diamond lattice parameter.

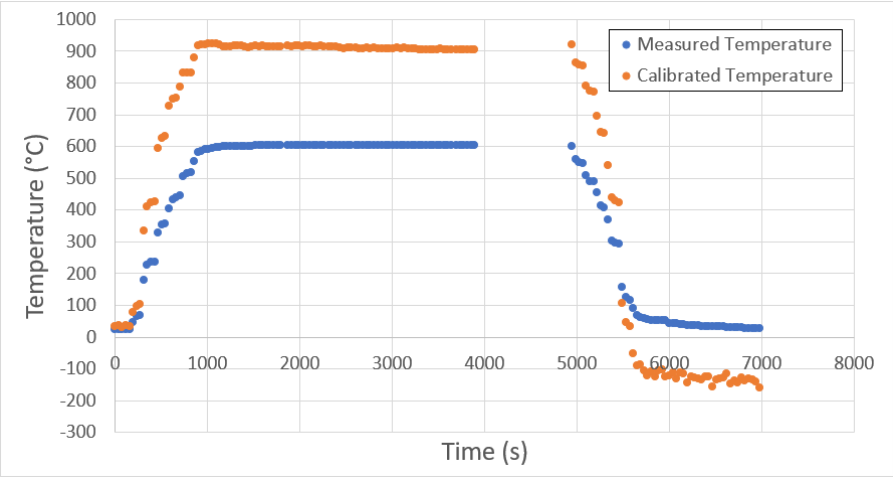

Figure 5.28: Temperature recorded by the thermocouple that was in contact with the outside of the sample (blue points) and the estimated true temperature calculated from the lattice parameter (orange points).

Figure 5.29 shows the diamond and cobalt lattice parameters as a function of time. Both increase step-wise as the furnace power (and therefore temperature) is increased in the region 0–1000 s. Before the lattice parameters level out when the hold temperature is reached, an unexpected dip occurs in the cobalt lattice parameter beginning at around 850 s (highlighted by a black arrow). Figure 5.30 shows the diamond and cobalt lattice parameters (with the cobalt lattice parameter being

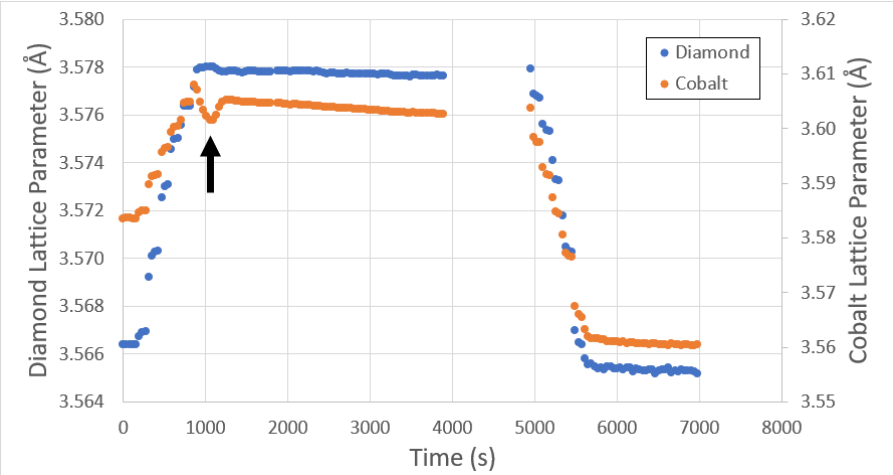

Figure 5.29: Diamond and cobalt lattice parameters as a function of time. The diamond lattice parameter is shown on the left axis and the cobalt lattice parameter on the right. Immediately before the hold temperature is reached, an unexpected dip in the cobalt lattice parameter is seen (highlighted by a black arrow).

scaled to be similar in position to the diamond lattice parameter) superimposed on the graphite weight percentage. The diamond lattice parameter has been corrected to remove the effect of the target temperature not being reached instantly immediately after an increase in furnace power by fitting a curve to the recorded thermocouple temperature, converting this to lattice parameter using the relationship in figure 5.27 and applying a correction so that the target temperature is reached instantaneously. On closer inspection, the diamond lattice parameter can be seen to increase and the cobalt lattice parameter decrease concurrently after the final furnace power increase was applied (highlighted by a black ring). The diamond lattice parameter decreases and the cobalt lattice parameter increases sharply followed by a large amount of graphite suddenly forming.

5.4.2.4 The Period Leading up to Graphitisation

To investigate the origin of the unexpected behaviour seen in the diamond and cobalt lattice parameters in the period before graphitisation, a sample of G22-00X was heated gradually in small steps of furnace power and held at each temperature for 30 min. A thermocouple was inserted into this sample and its temperature as a function of time is shown in figure 5.31. Figure 5.32 shows the diamond and

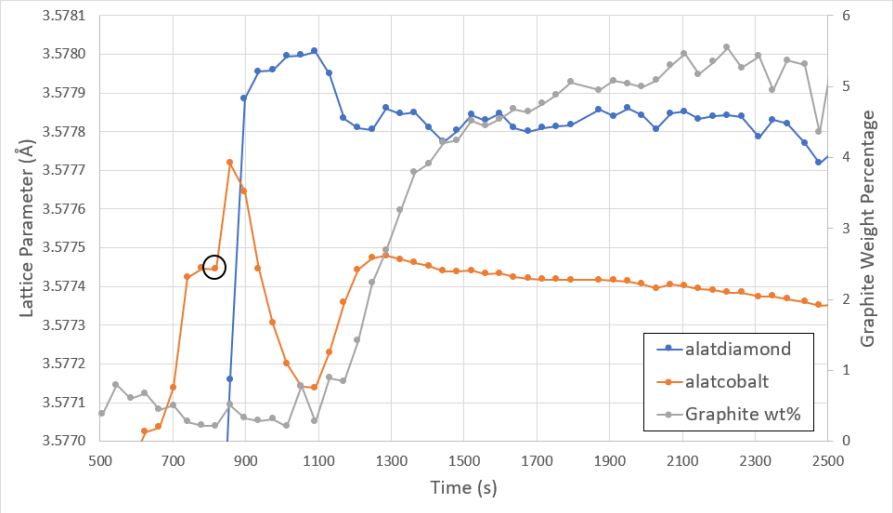

Figure 5.30: Plot of the diamond and cobalt lattice parameters and the graphite weight percentage as a function of time in the region slightly before and after graphitisation. The cobalt lattice parameter has been scaled to appear on the same axis as the diamond lattice parameter and the diamond lattice parameter has been corrected to remove the effect of non-instantaneous heating. The black circle indicates the point at which the last furnace power increase occurred. 'alatdiamond' and 'alatcobalt' refer to the diamond and cobalt lattice parameters respectively.

cobalt lattice parameters and, graphite weight percentage as a function of time. In this experiment, the cobalt lattice parameter began to decrease at the start of the second 30 min heating period (22.5 % furnace power, 650 °C, red arrow, figure 5.32) and then continued decreasing at a greater rate each time the temperature was increased. This occured until the point where the sample rapidly graphitised at around 9500 s (35 % furnace power, 820 °C, black arrow, figure 5.32) at which point the cobalt lattice parameter rapidly increased by approximately 0.008 Å over a very short time period (similarly to the previous experiment).

Figure 5.33 shows a short time-scale either side of the onset of graphitisation in more detail. The cobalt lattice parameter has been scaled to fit better on a single axis with the diamond lattice parameter and the last furnace power increase has been indicated with a black circle. Immediately before graphitisation, the diamond lattice parameter can be seen increasing and then decreasing, shortly after which rapid graphitisation occurs. Summing the total drop in cobalt lattice parameter up over the five 30 min heating stages prior to and including graphitisation gives a value of 0.0061 Å and the drop in cobalt lattice parameter that occurred prior

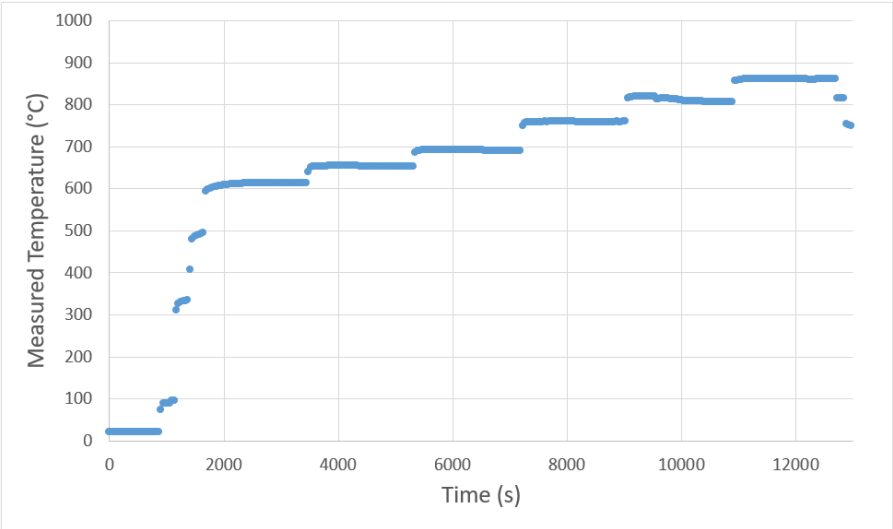

Figure 5.31: Plot of the temperature of the G22-00X sample as a function of time measured by an internal thermocouple and so the temperature reading should be accurate.

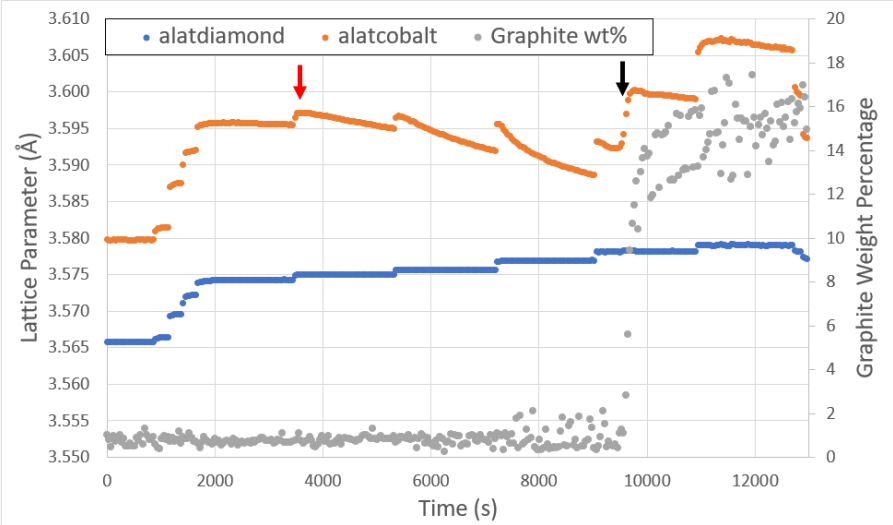

Figure 5.32: Plot of the diamond and cobalt lattice parameter (true, non-scaled values) and the graphite weight percentage as a function of time. The red arrow indicates where the cobalt lattice parameter begins to decrease over time and the black arrow indicates where large-scale graphitisation begins to occur. 'alatdiamond' and 'alatcobalt' refer to the diamond and cobalt lattice parameters respectively.

to the graphitisation of the G75-A sample in figure 5.30 was 0.0064 Å. This is shown graphically in figure 5.34 where the G75-A cobalt lattice parameter has been shifted up by 0.0117 Å (but not scaled) to be coincident with the G22-00X cobalt lattice parameter at time $t = 0$. Figures 5.29 and 5.32 show that the rate at which the cobalt lattice parameter drops is dependent on the temperature and

the similarity in the magnitude of the drop shown in figure 5.34 suggests that it is the same process occurring in both cases. This experiment shows that the temperature sensitive incubation period seen in the neutron diffraction experiment (section 5.4.1, figure 5.12) is likely connected to the behaviour of the cobalt lattice parameter. Although the time-scale of the drop in cobalt lattice parameter is temperature dependent, the fluctuation in diamond lattice parameter appears to occur immediately before graphitisation independent of how quickly the sample was heated and therefore it can be concluded that this phenomenon is connected to the onset of large-scale graphitisation.

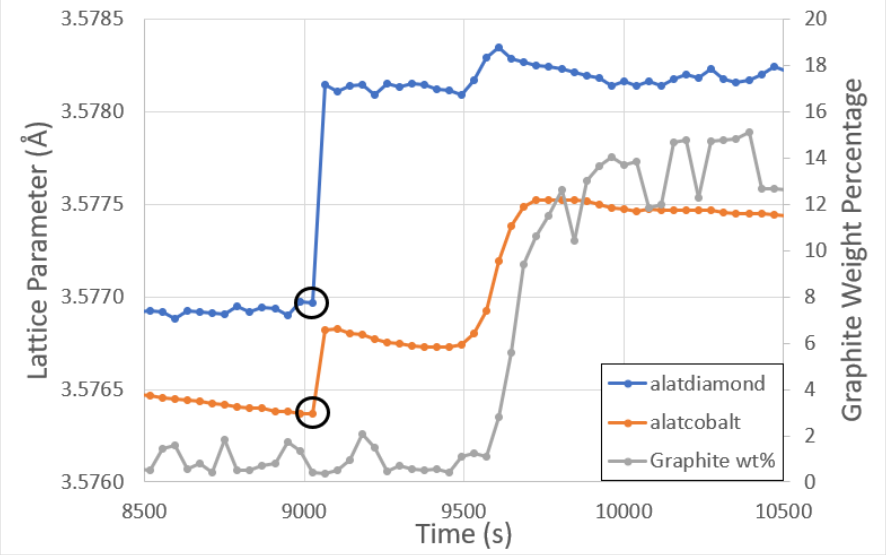

Figure 5.33: A short timescale either side of graphitisation from figure 5.32 showing the diamond and cobalt lattice parameters (cobalt scaled to appear on the same axis as the diamond) and graphite weight percentage. The cobalt lattice parameter can be seen increasing rapidly and the diamond lattice parameter increasing and then decreasing as graphitisation occurs. The black circles represent when the furnace power increased from 30 % to 35 %. 'alatdiamond' and 'alatcobalt' refer to the diamond and cobalt lattice parameters respectively.

5.4.2.5 Heating Below Graphitisation Temperature

In order to understand what was occurring during the incubation period, two nominally identical samples of G75-B were heated to a temperature that would cause graphitisation (given enough time) but cooled before it could actually occur.

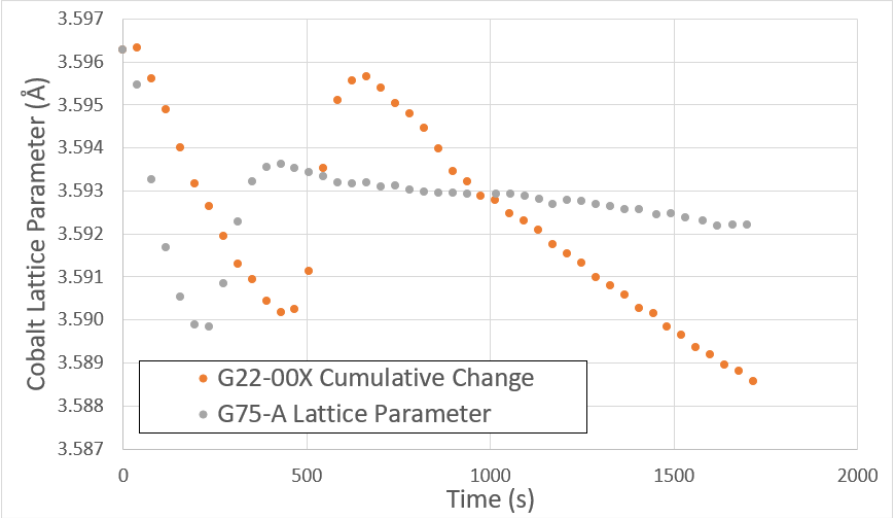

Figure 5.34: Plot showing the cumulative cobalt lattice parameter drop over the 20 %, 22.5 %, 25 %, 30 % and 35 % heating periods (orange points) compared to the behaviour of the cobalt lattice parameter during the heating of a G75-A sample (grey points, originally shown in figure 5.30. The grey points have been shifted so that the lattice parameters are equal at $t = 0$ but they have not been scaled.

The microstructures of the two samples were then examined. The thermocouple-measured temperature of the G75-B samples was also corrected using the method in 5.4.2.2 (as it did not have one inserted internally) however, its reduced sintering time compared to the G75-A material may have had an effect on its thermal expansion coefficient thus introducing an error into this calculation. Data from both samples is generally shown on the same graph so where the labels 'Sample A' and 'Sample B' are seen, the data represents two physically different samples.

Sample 'A' was heated to approximately 800 °C and immediately cooled and 'Sample B' was held at the same target temperature for 20 min (shown in figure 5.35). Figure 5.36 of the diamond and cobalt lattice parameters as a function of time shows that there is little difference in the cobalt lattice parameter before and after the heating of 'Sample A' and that the cobalt lattice parameter decreases sharply during the course of the longer heating of 'Sample B'. Figure 5.37 shows the weight percentages of graphite, tungsten carbide (WC) and η-carbide (Co_3W_3C/Co_6W_6C) as a function of time. The dotted line indicates where data for 'Sample A' stops and 'Sample B' begins and so it is expected for there to be a discontinuity at this point. The graphite graph mostly shows a highly scattered amount between

0.5 and 1.5 wt% which is caused by the Rietveld refinement software trying to fit a very broad peak to an essentially flat line. Around halfway through the heating of 'Sample B' (at around 2000 s), the behaviour appears to change (indicated by a black arrow). Looking at individual diffractograms, it is possible that a small amount of graphite began forming here but as graphite is only represented by a single very small, very broad peak, it is difficult to confidently say whether this is the case or not. Compared to other samples that graphitised heavily, no significant amount of graphite was detected by Rietveld refinement. The other graphs show that although tungsten carbide increases as the sample is heated, it drops back to a similar level after the sample is cooled and that a small amount of η-carbide began forming during the heating of 'Sample B' just before 2000 s.

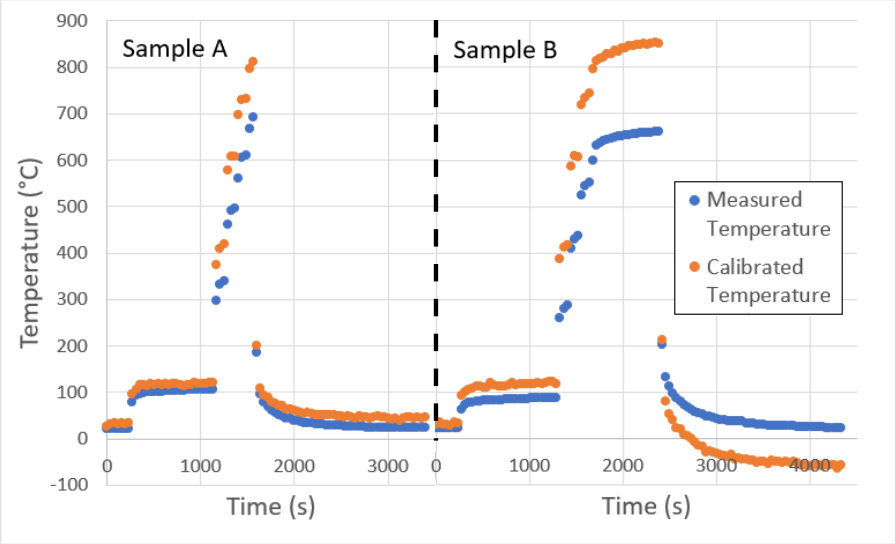

Figure 5.35: Measured temperature recorded by the thermocouple touching the sample and the corrected, calibrated temperature calculated from the lattice parameter of 'Sample A' and 'Sample B', G75-B material. 'Sample A' was heated to just over 800 °C briefly before being quenched to room temperature and 'Sample B' was held at the target temperature (closer to 850 °C for 20 min.

Figure 5.38 shows a secondary electron image of a FIB cross-section of a typical binder pool from 'Sample A'. Some very small dark particles can be seen at the edges of the binder pool but it is mostly clear. Figure 5.39 shows a larger region of the same cross-section with EDX data. Several binder pools can be seen with high cobalt concentrations, dilute tungsten concentrations and generally very little carbon

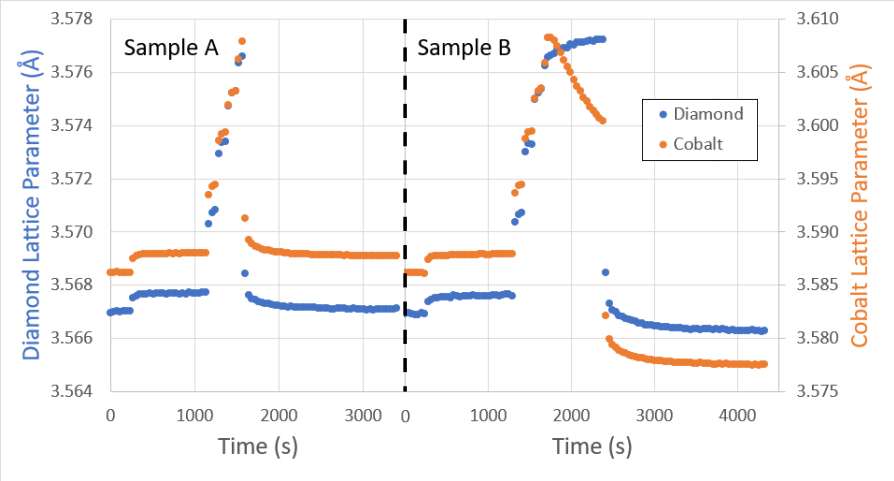

Figure 5.36: Diamond and cobalt lattice parameters for 'Sample A' and 'Sample B', G75-B material during heating. The diamond lattice parameter is shown on the left axis and the cobalt on the right.

except where the occasional diamond particle has been surrounded by binder. Some small regions of concentrated tungsten are seen which are thought to be tungsten carbide particles. Figure 5.40 shows a typical binder pool from 'Sample B'. Several precipitates can be seen within the binder pool (highlighted with arrows). The precipitates are nodular in appearance and have formed close to but not exactly on the diamond-cobalt boundary. Figure 5.41 of the EDX data from this binder pool shows that the precipitates are mainly carbon and deficient in both cobalt and tungsten. The particles in figure 5.40 look very similar to particles observed in TEM micrographs of a PCD sample that was thermally soaked in argon at 800 °C for 30 min by Westraadt *et al.*[62] (figure 5.42). These particles were identified as graphite by EELS and from their similar morphology and location it is likely that the particles formed in 'Sample B' are also graphite.

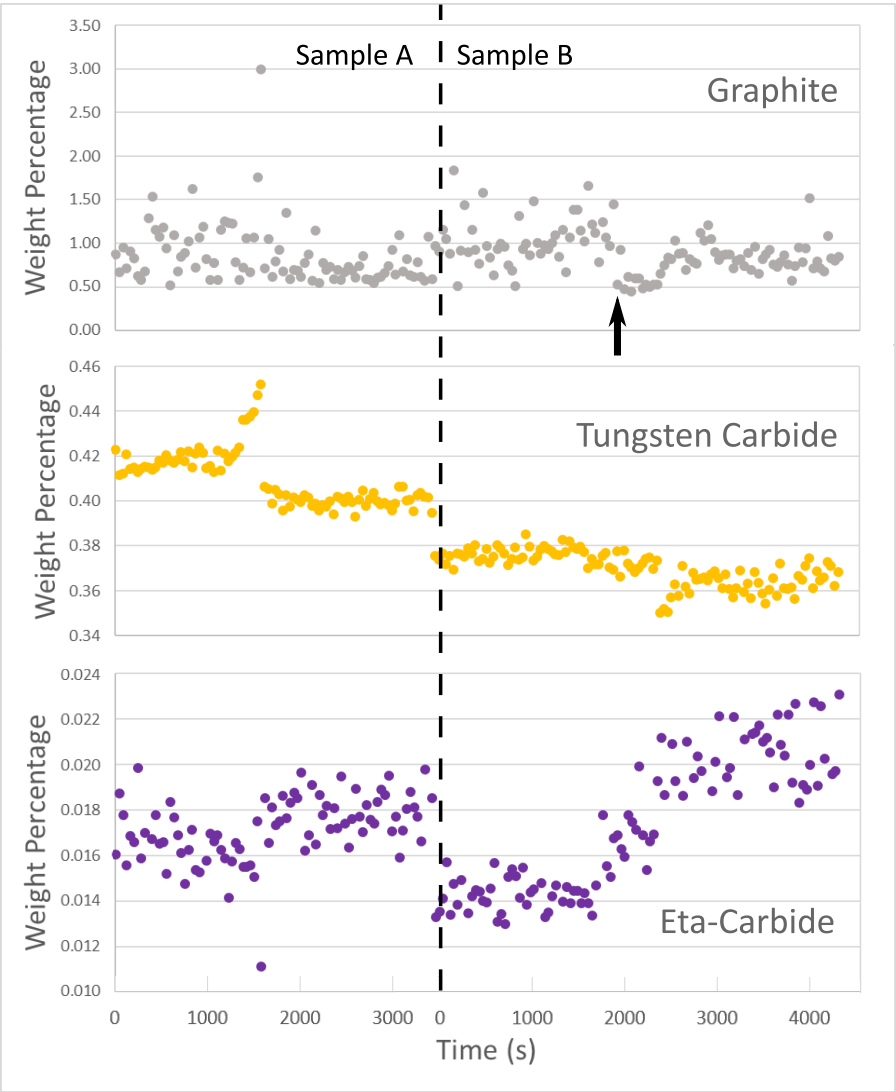

Figure 5.37: Weight percentages of graphite (top, grey), tungsten carbide (yellow, middle) and η-carbide (bottom, purple) for 'Sample A' and 'Sample B', G75-B material as a function of time during heating. The black arrow indicates where a possible change in behaviour in the graphite weight percentage data is seen.

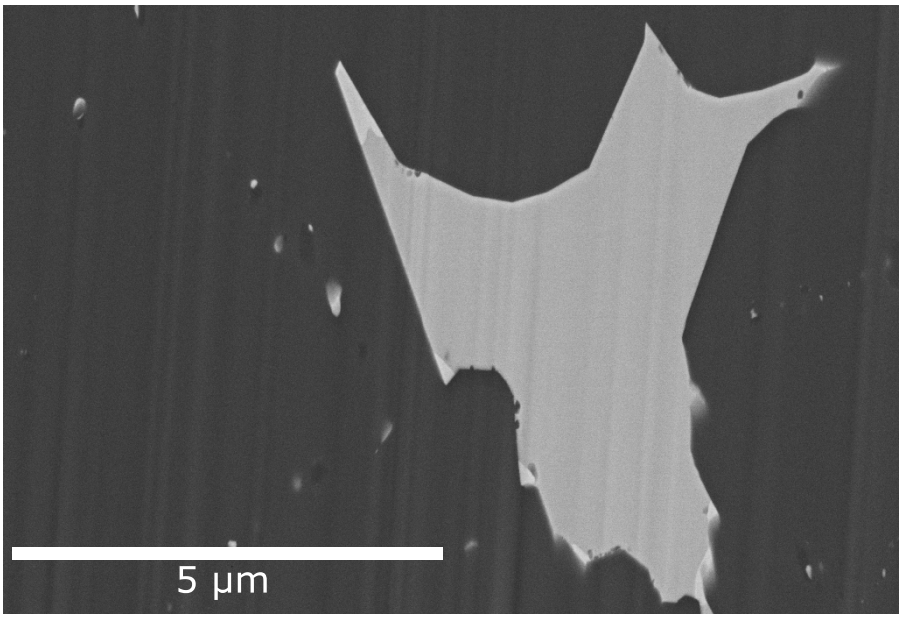

Figure 5.38: FIB cross section of a typical binder pool from 'Sample A' showing little evidence that any graphite particles have formed within it.

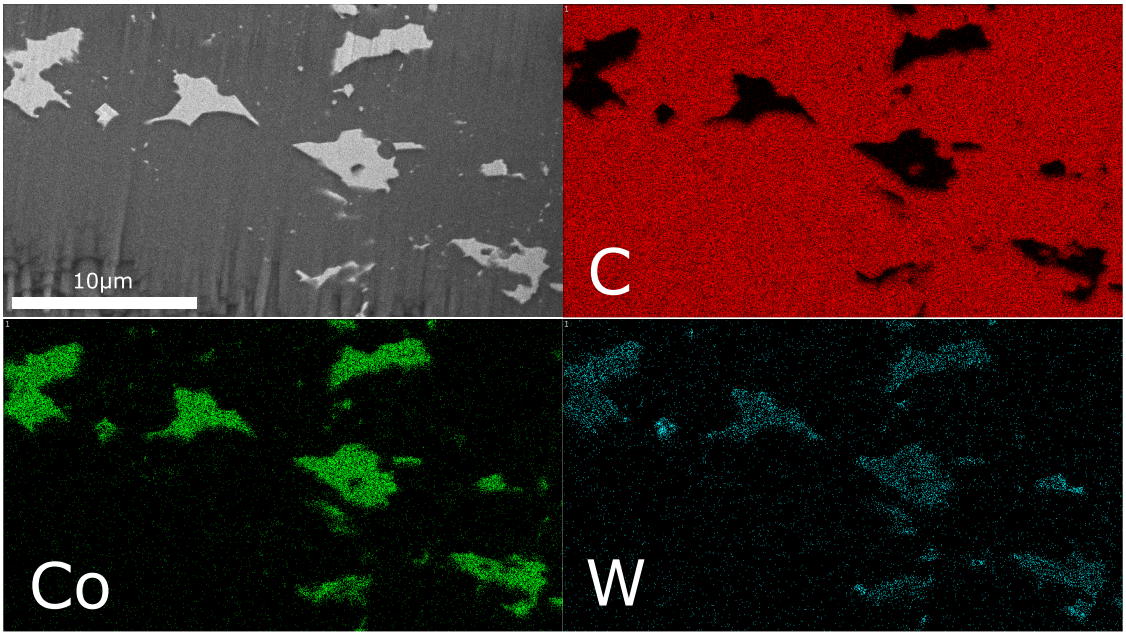

Figure 5.39: FIB cross-section of a wider area from 'Sample A' showing the carbon, cobalt and tungsten signals.

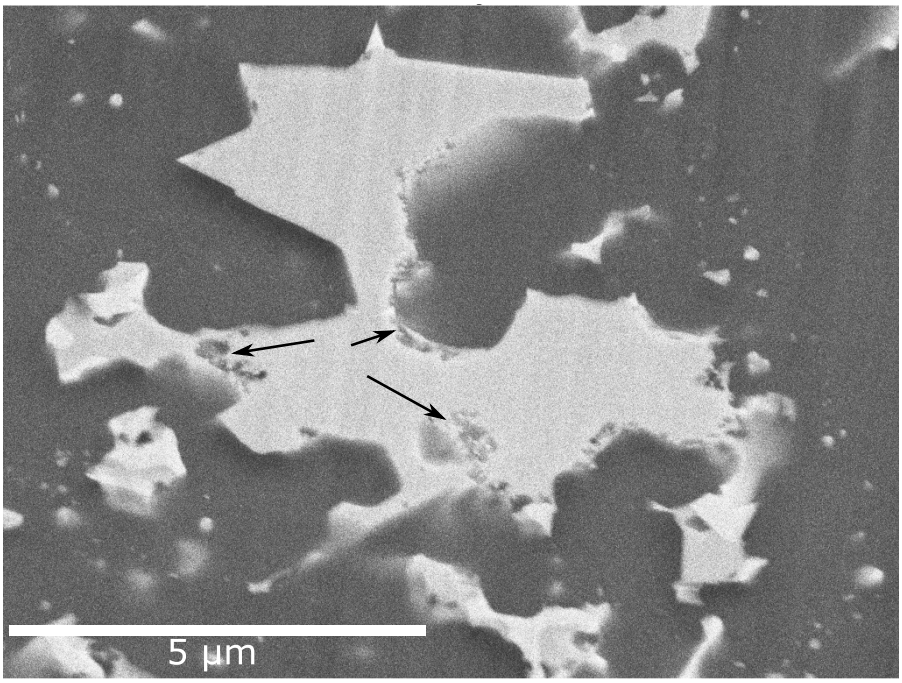

Figure 5.40: FIB cross-section of a typical cobalt binder pool from 'Sample B' after heating showing several suspected graphite particles within it (highlighted with black arrows).

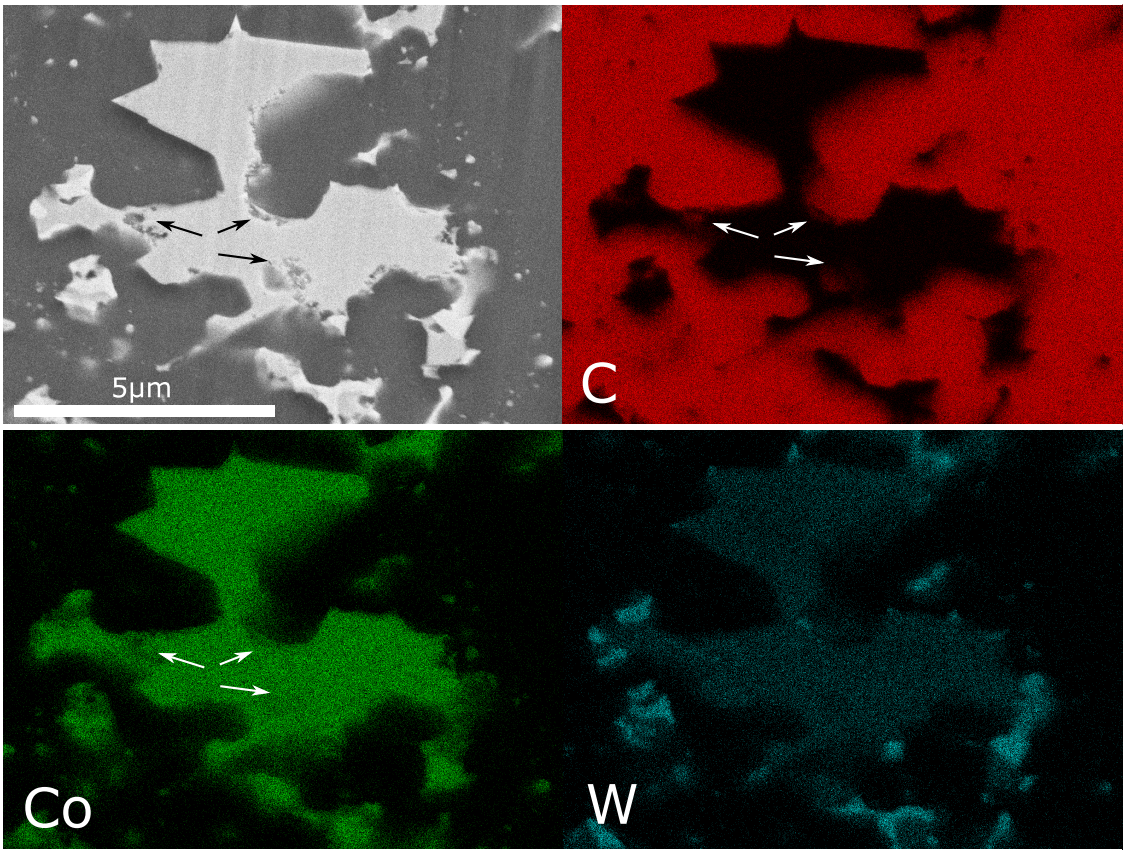

Figure 5.41: EDX map showing carbon, cobalt and tungsten signals of the binder pool from 'Sample B' with suspected graphite particles. These particles appear to have a weak carbon signal (black arrows) and are deficient in cobalt (white arrows). They do not appear to have a significant concentration of tungsten within them.

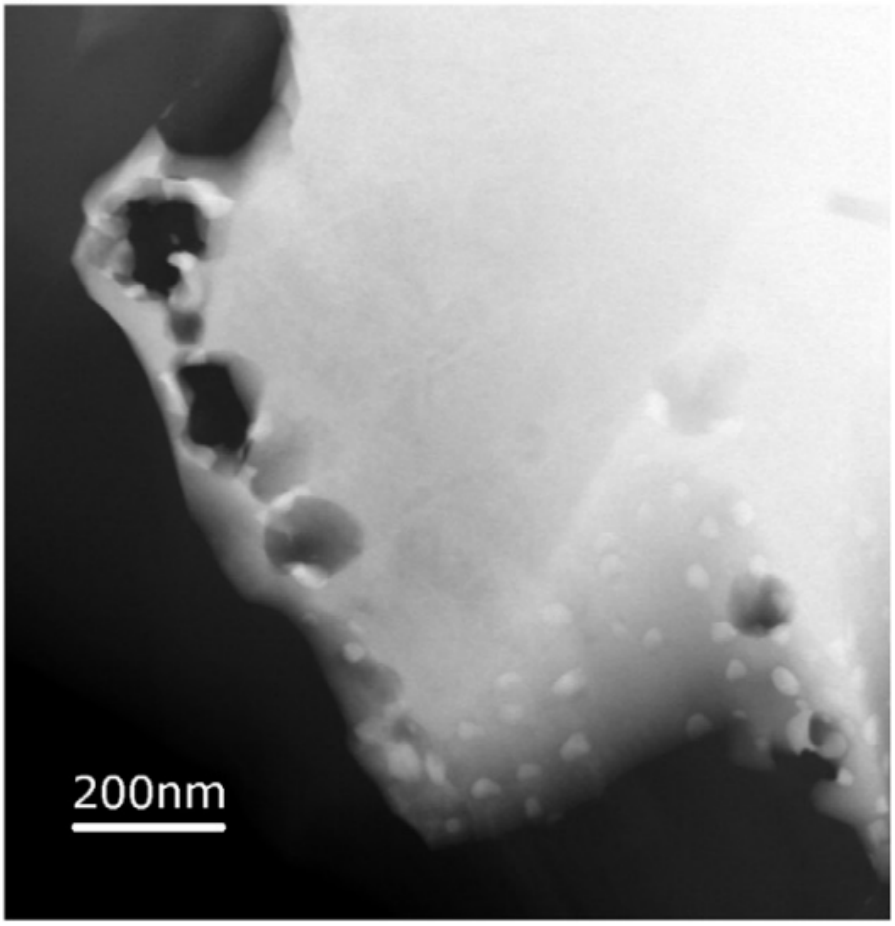

Figure 5.42: TEM image of a binder pool from a sample heated to 800 °C for 30 min from Westraadt *et al.*[62]. These particles appear to have a similar morphology and location to the suspected graphite particles in figure 5.40.

5.4.2.6 Graphitisation of Altered Binder Chemistry PCD

Laboratory X-ray Diffractometer To ascertain whether the binder chemistry affected the graphitisation of the diamond, samples with four different concentrations (G22-00X: 0 %, G22-05X: 5 %, G22-20X: 20 % and G22-40X: 40 %) of a group VII transition metal element (the precise element is omitted to maintain commercial secrecy and will be referred to as the 'Additive' henceforth) were made. Each sample was heated to 850 °C for 6 h and the amount of graphite formed as a function of time for the four samples is plotted in figure 5.43. The onset time (incubation time) of graphitisation was found by fitting a straight line to the initial slope of each graph and finding where it intersected with the x-axis. This is plotted as the inverse of the incubation time against Additive concentration. Increasing the concentration of the Additive increases the length of the incubation period (decreases $\frac{1}{t_{inc}}$) until at 40 % Additive, the sample no longer graphitises at 850 °C even after 6 h at this temperature. This shows that the Additive has a preventative effect on graphitisation.

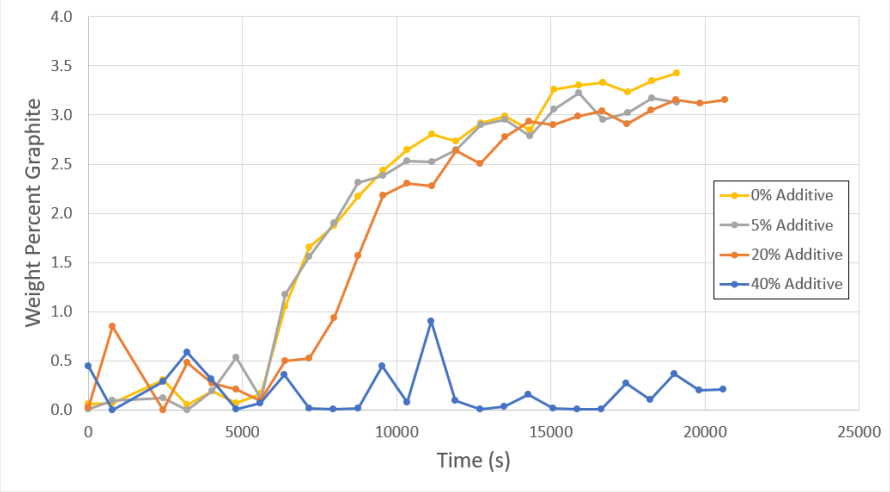

Figure 5.43: Weight percentage of graphite as a function of time calculated by Rietveld refinement for samples heated to 850 °C with 0 % (yellow), 5 % (grey), 20 % (orange) and 40 % (blue) of a group VII transition metal added to the substrate cobalt.

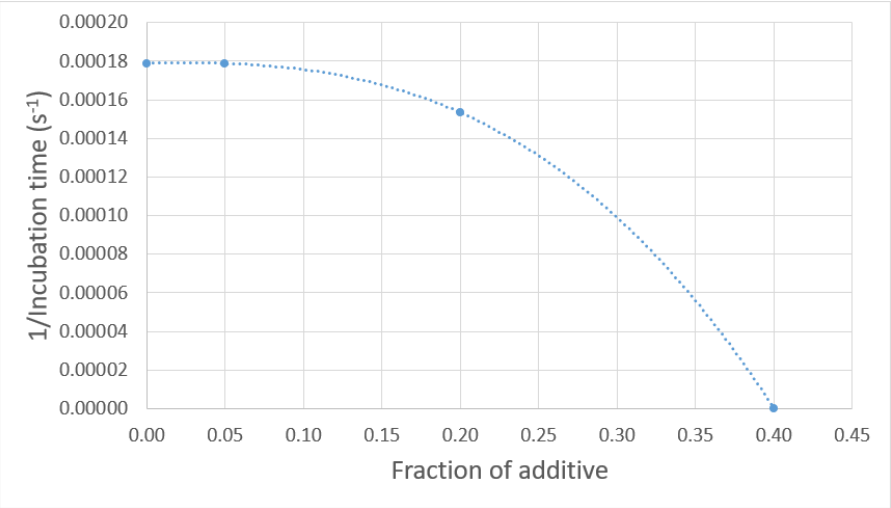

Figure 5.44: The inverse of the incubation time before graphite formed against the fraction of additive (group VII transition metal) added to the substrate cobalt. A cubic trendline is added to draw attention to the trend observed.

Synchrotron X-ray Diffractometer Due to the inability to have fine, accurate control of the temperature that the furnace heated the sample to, the original quantitative analysis of the effect of adding the group VII transition metal element to the binder as a follow up to the laboratory X-ray diffraction in section 5.2.1.2 was not possible. All samples were heated to the same furnace power but due to a variety of factors, they all reached different maximum temperatures. Because of this, meaningful comparison between samples is not possible and so the focus will be on the qualitative information present in the data. The samples were heated to a temperature in the range 800–900 °C and held there for an hour. All of the samples behaved in similar ways (with slight variations due to the maximum temperature reached) and so only the results from the G22-40X sample will be shown here. In all of the figures in this section, a red arrow indicates where the heating of the sample began and a black circle indicates the point at which the furnace reached maximum power. Figure 5.45 shows the diamond and cobalt lattice parameters (scaled and shifted to appear on the same axis) and graphite weight percentage of a G22-40X sample as a function of time. The same fluctuations in the lattice parameters before large-scale graphitisation as seen previously are evident. Figures 5.46 and 5.47 show the tungsten carbide and η-carbide weight percentages as a function of time with

the diamond and cobalt lattice parameters included for reference. Tungsten carbide begins forming as soon as the heating begins, appearing to simply precipitate in response to heating, and η-carbide shows a jump in weight percentage midway through the decrease in cobalt lattice parameter prior to graphitisation. Both carbide percentages then show a jump concurrent with the onset of graphitisation.

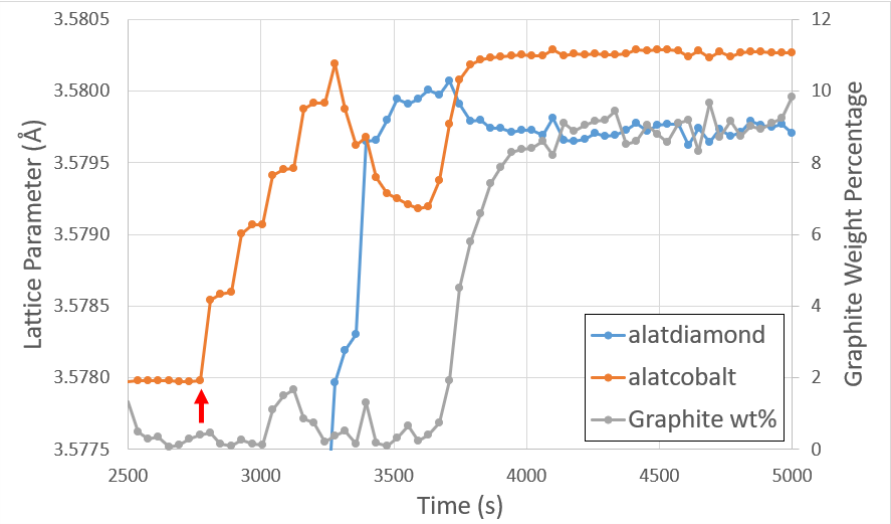

Figure 5.45: Plot of diamond and cobalt (scaled to appear on the same axis) lattice parameters and graphite weight percentage as a function of time for a G22-40X sample heated to approximately 900 °C. The point at which heating began is highlighted with a red arrow. 'alatdiamond' and 'alatcobalt' refer to the diamond and cobalt lattice parameters respectively.

Figure 5.48 shows the graphite weight percentage with the temperature measured by the internal thermocouple as a function of time. A sharp drop of approximately 10 °C can be seen coinciding with the graphitisation event. Although it is expected for there to be a change in heat when a new species forms, the diamond to graphite reaction is reported to have a small, negative reaction enthalpy[146][147] and so an expression of heat would be expected resulting in a temperature rise rather than the drop observed.

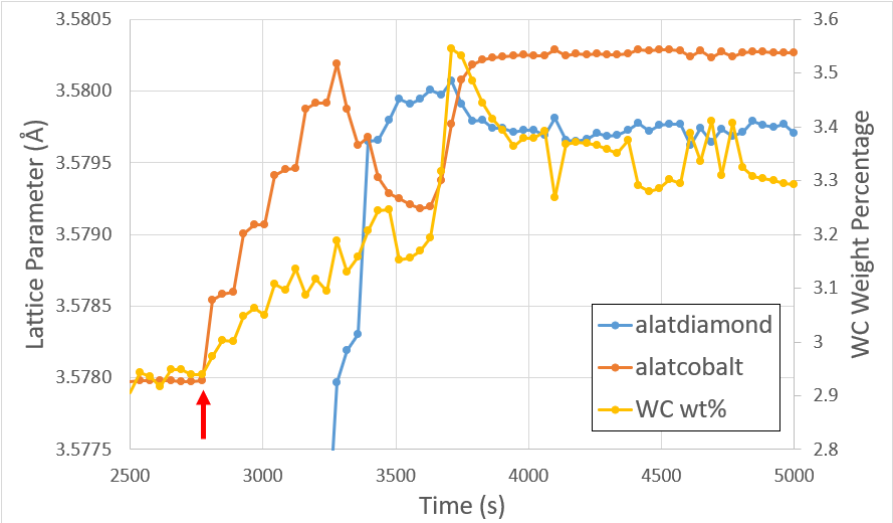

Figure 5.46: Plot of diamond and cobalt (scaled to appear on the same axis) lattice parameters and tungsten carbide weight percentage as a function of time for a G22-40X sample heated to approximately 900 °C. The point at which heating began is highlighted with a red arrow to show that the start of the formation of additional tungsten carbide coincided with this point. 'alatdiamond' and 'alatcobalt' refer to the diamond and cobalt lattice parameters respectively.

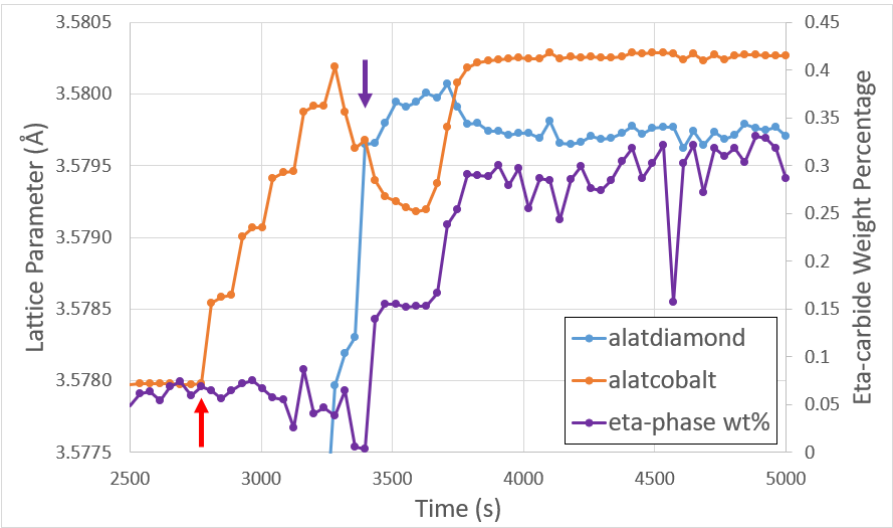

Figure 5.47: Plot of diamond and cobalt (scaled to appear on the same axis) lattice parameters and η-carbide weight percentage as a function of time for a G22-40X sample heated to approximately 900 °C. The point at which heating began is highlighted with a red arrow to show that the η-carbide formation did not coincide with the start of heating and the start of η-carbide formation is highlighted with a purple arrow to show that this did not coincide with the start of the decrease in the cobalt lattice parameter. 'alatdiamond' and 'alatcobalt' refer to the diamond and cobalt lattice parameters respectively.

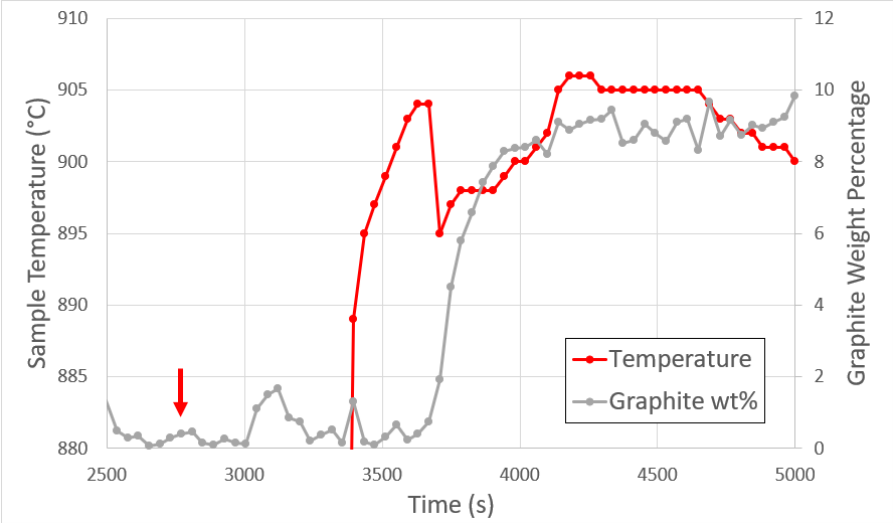

Figure 5.48: Plot of graphite weight percentage and the temperature measured by a thermocouple that was inserted into a hole drilled in the base of the sample. The start of the heating is indicated with a red arrow. A roughly 10 °C drop can be seen occurring as the graphite weight percentage increases rapidly.

5.4.2.7 Summary of Key Points

- Prior to graphitisation, a previously unreported deviation in the cobalt and diamond lattice parameters is observed that is not due to the heating of the sample.
- The decrease in the cobalt lattice parameter occurs over a variable time-scale dependent on the temperature and it is suggested that this is linked to the incubation period observed in the neutron diffraction results.
- The increase in diamond lattice parameter appears to occur immediately before the onset of graphitisation no matter the heating rate.
- The changes in weight percentage of tungsten carbide and η-carbide are not particularly well correlated with the decrease in cobalt lattice parameter.
- The changes in cobalt and diamond lattice parameter reverse when graphitisation occurs and a jump in tungsten carbide and η-carbide amount is also seen at this point.
- A temperature drop of 10 °C is observed by the sample-internal thermocouple as graphitisation occurs.

5.4.3 In-situ Heating TEM Experiment

In order to understand the process of graphitisation, two experiments were performed to try to observe it occurring in real time by heating samples and causing them to graphitise whilst imaging them in a high resolution scanning transmission electron microscope.

In the first experiment, the sample was heated beyond 800 °C as graphitisation was not detected during heating. Later electron energy loss spectroscopy (EELS) showed that the sample had graphitised extensively but the onset was likely missed during heating due to suboptimal contrast settings. Figure 5.49 shows a series of screenshots of the live video from the high-angle annular dark-field (HAADF) display at 960 °C. The field of view is of an area adjacent to a cobalt binder pool that

has already graphitised. Brighter contrast in these images is attributed to higher atomic number species. Panel 'a)' shows areas of higher tungsten content within the cobalt binder. In panels 'b)' and 'c)', the tungsten containing areas appear to have gotten smaller, suggesting that some of the tungsten is dissolving into the cobalt binder. As the solubility of carbon is likely already at its limit in the binder, the carbon from the η-carbide phase ($(Co,W)_6C$) has to precipitate as graphite. Finally, in panel 'd)', these areas of high tungsten concentration become completely separated from the binder pool by the graphite and they can no longer dissolve into it. As this process has only been seen as a video, it is difficult to definitively conclude the exact mechanism that is occurring. A significant amount of further work would be required to determine the phase compositions and hence derive useful information from a phase diagram. However, by comparing the morphology and contrast of these isolated particles with the similar looking particles in the ex-situ heated TEM sample (figures 5.23 and 5.25), it can be concluded that they are η-carbide. Furthermore, the presence of particles of η-carbide that are isolated within the graphite in the ex-situ heated sample (which was in the form of a bulk sample rather than a thin TEM lamella when it was heated) shows that the high mobility of the cobalt phase as it retreats away from the η-carbide particles also occurs in bulk samples rather than just being due to the proximity to a free surface in the case of a TEM lamella. The behaviour seen in this experiment is very similar to that reported by Ramirez *et al.* in their experiment with a cobalt layer deposited between two layers of amorphous carbon. The cobalt layer migrated through the microstructure and spherodised leaving graphite behind it (figure 2.26). The dissolution-reprecipitation mechanism (proposed by Oya[96]) seems the most likely explanation for this behaviour. However, this process occurred at very high temperature, a long time after graphite had initially nucleated and begun to grow and so does not necessarily explain how this graphite initially formed.

In the second experiment, a graphite nucleation event was captured in a video. Figure 5.50 shows a HAADF image of the boundary between a cobalt binder pool and the diamond matrix at room temperature. A number of lighter particles

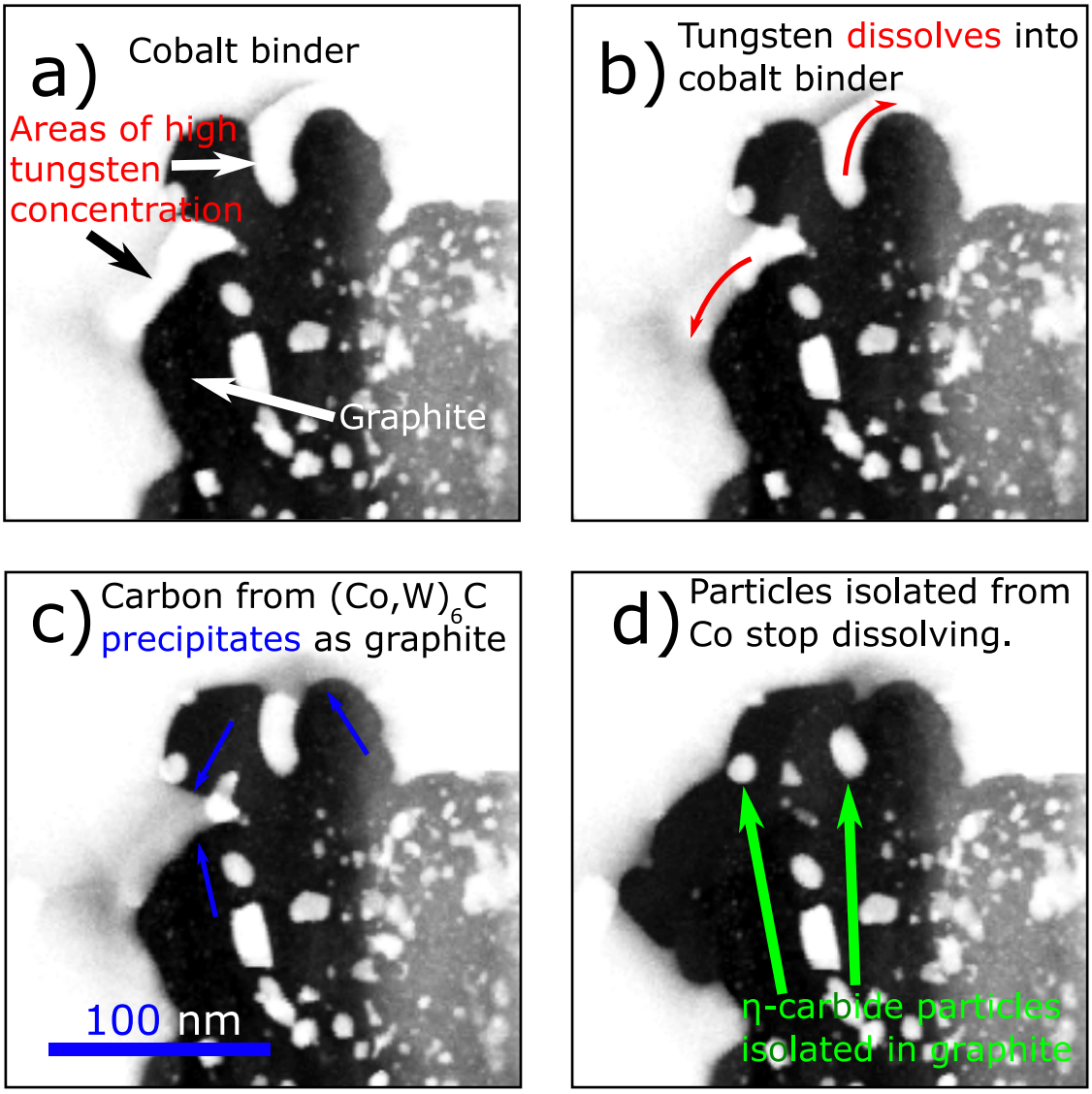

Figure 5.49: Series of snapshots of the HAADF display from the in-situ heating STEM experiment at 960 °C. In panels 'a)' to 'c)' regions of high tungsten concentration (brighter areas) can be seen diminishing in size. It is suggested that the tungsten from these η-carbide particles is dissolving into the binder and precipitating graphite. The graphite eventually isolates the particles from the binder and so they can no longer dissolve in panel 'd)'.

can be seen at the boundary (indicated by red arrows) and as HAADF contrast is strongly sensitive to atomic number contrast, these particles are likely to be tungsten-containing η-carbide. Figure 5.51 shows a series of screenshots from a video of the live display of the microscope showing a HAADF image on the left and a dark field (DF) image on the right. The first panel was taken 4 min after the sample was heated to 800 °C and the other two panels were taken after increments

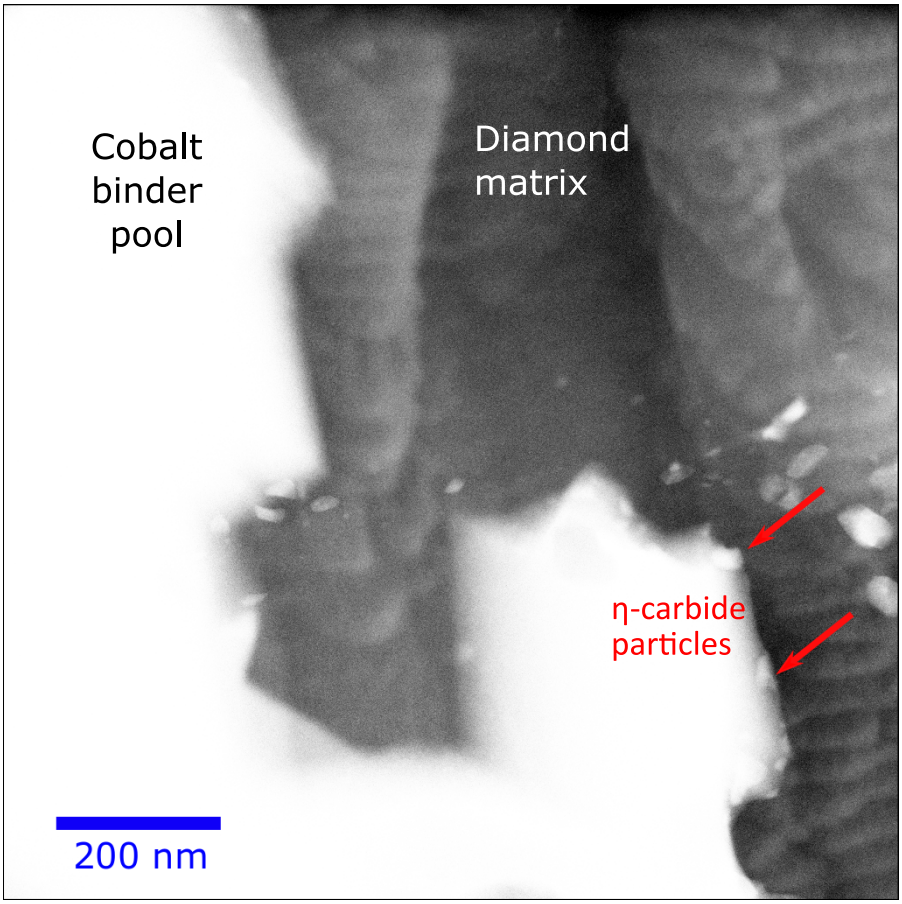

Figure 5.50: HAADF STEM image of a boundary between a cobalt binder pool (left of image) and the diamond matrix (right of image) taken at room temperature. Several bright spots can be seen at the edge of the cobalt pool which are suggested to be η-carbide particles (indicated with red arrows).

of 40 s. Panel 'a)' shows one of the η-carbide particles (indicated by a red arrow) that was highlighted in the room temperature HAADF image (figure 5.50). It can only be seen in the dark field image as the cobalt has begun to expand from the original bounds of the binder pool. It is thought that the expansion of the cobalt pool is due to it forming a mobile film on the surface of the TEM lamella due to the high temperature rather than it dissolving a large amount of the surrounding diamond as features associated with the diamond can be seen through it. After 40 s in panel 'b)', graphite is seen nucleating from the η-carbide particle and growing very quickly in the direction of the blue arrow until its growth is arrested by another (dark) carbide particle. It can be seen via diffraction contrast in the dark field image and appears darker than the cobalt in the HAADF image due to its lower

atomic number. In panel 'c)', the graphite has thickened slightly in a perpendicular direction indicated by the green arrows but at a much slower rate than its original growth. Additional graphitisation can now be seen encroaching into the bottom of the frame from an unseen nucleation site. Figure 5.52 shows that approximately 9 min after the temperature reached 800 °C, the graphite has extended a long way into the diamond region and has nearly encompassed the entire binder pool. The position of the graphite front is shown as a blue dotted line on HAADF and DF images. The η-carbide particle from which graphite was observed to nucleate is highlighted by a green arrow and has grown significantly in size and has spherodised.

The way the graphite grows very quickly in one direction and then thickens slowly in the perpendicular direction in figure 5.51 suggests it occurs by Howes' proposed mechanism for direct transformation from diamond to graphite[87]. It was suggested that graphite grows quickly along {112} planes due to their similarity to hexagonal graphene sheets but growth of additional sheets is restricted by the much smaller spacing between the planes than the graphite {0002} spacing and hence development of large stresses (figure 2.22). However, it is difficult to tell whether graphite is forming within the binder pool, at the boundary or directly in the diamond. If stress is the limiting factor in graphite growth (as with this mechanism), this also explains why there appears to be very little incubation period in the TEM sample compared to the bulk neutron diffraction sample at the same temperature. Every point in the thin lamella is very close to a free surface and so stresses due to expansion of graphite are easily relaxed whereas the three-dimensional constraint of a bulk sample means that even a small amount of graphite forming will result in a large stress.

The series of STEM images taken at 800 °C (figure 5.51) show that an η-carbide particle acted as a nucleation site for graphite. This η-carbide particle was observed at room temperature (figure 5.50) and remained largely unchanged until after graphite had nucleated from it. This suggests that it is not the time required for the formation and growth of η-carbide that is responsible for the incubation period. According to a review of cemented carbide microstructures by Garcia *et*

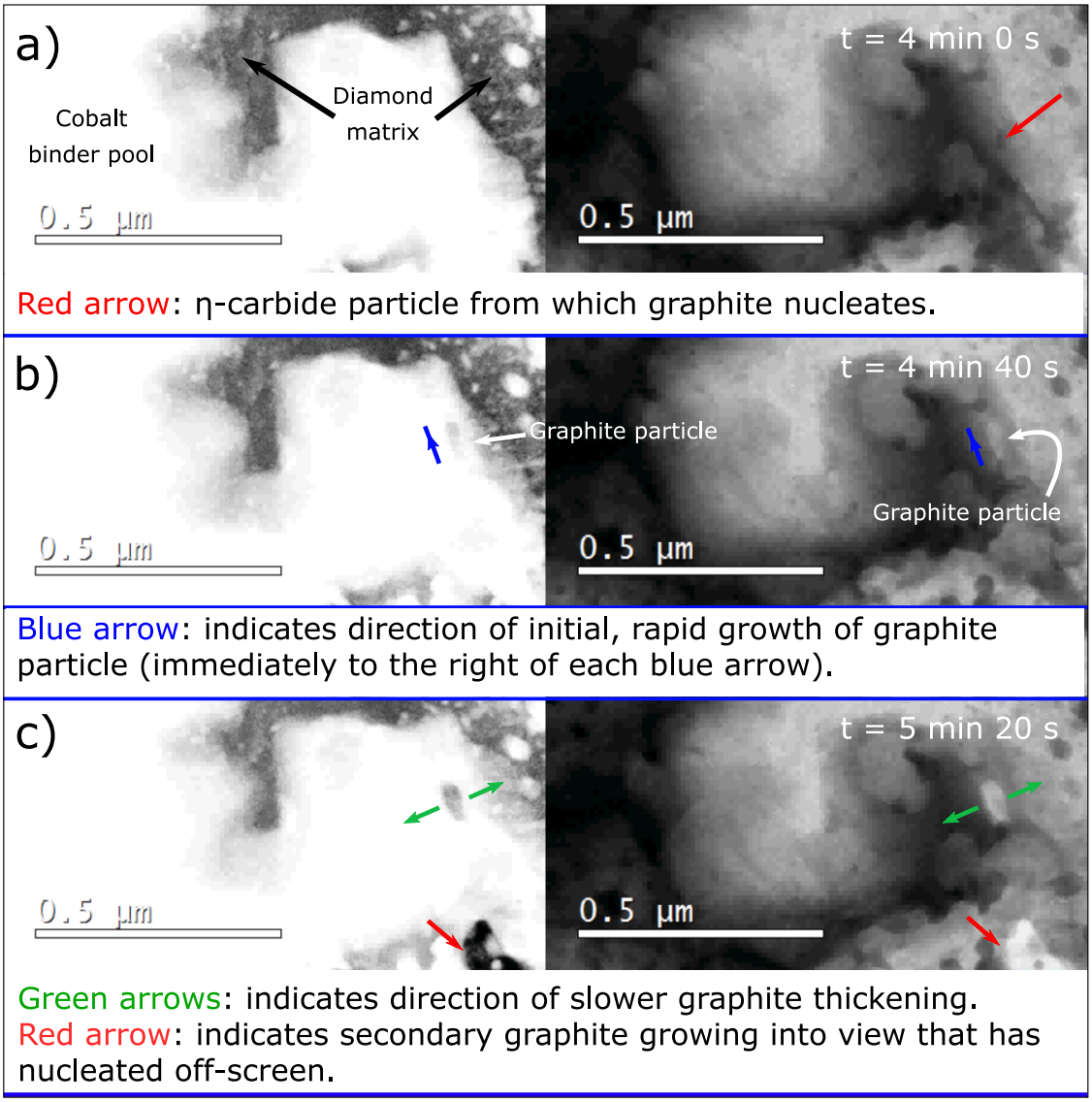

Figure 5.51: A series of 3 snapshots of the HAADF and DF output of the in-situ heating of the sample displayed in figure 5.50. Panel 'a)' is 4 min after the sample was heated to 800 °C and panels 'b)' and 'c)' are each after increments of 40 s. The main phenomenon that is being observed in this series of images is the nucleation of a graphite particle which first appears in panel 'b)'. The η-carbide particle that the graphite nucleates from is highlighted in panel 'a)' with a red arrow. The graphite then rapidly grows in the direction of the blue arrow in panel 'b)' (the elongated graphite particle is on the right of the blue arrow and is highlighted). Finally, in panel 'c)' the graphite has thickened slightly in the direction of the green arrows but a t a much slower rate than its initial growth. More graphite can also be seen encroaching into the frame that has nucleated elsewhere.

al.[148], the Co_3W_3C form of the η-carbide is stable at low temperatures and can be retained in cases of fast cooling but only where the binder is carbon deficient (whereas the Co_6W_6C form is only stable above 1000 °C). At first, this requirement

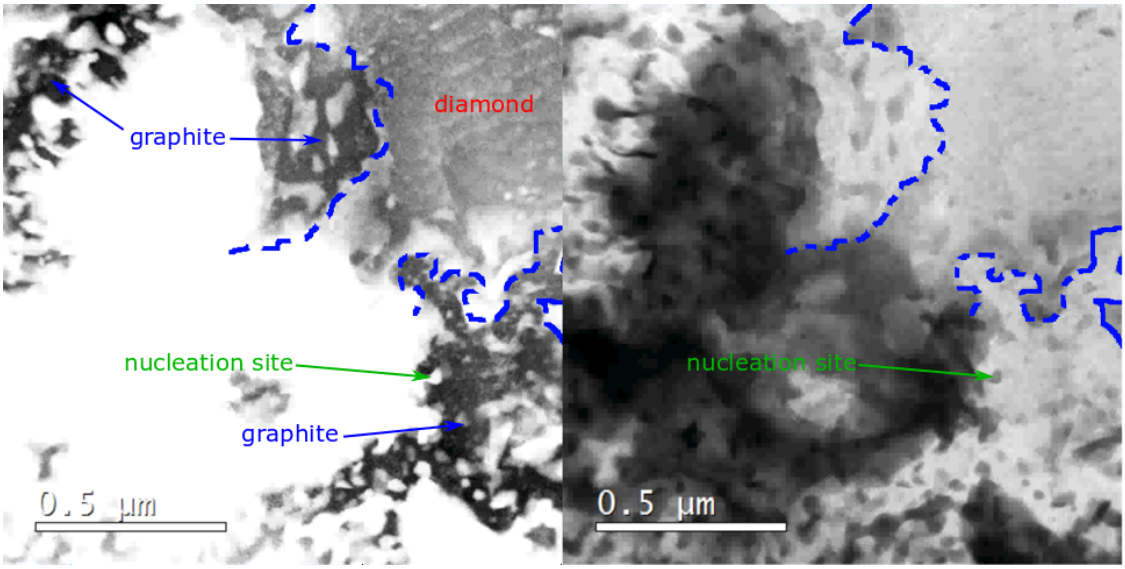

Figure 5.52: This image shows the extent of graphitisation after 9 min at 800 °C. The "nucleation site" highlighted with a green arrow is the η-carbide particle that was shown in the room temperature STEM image in figure 5.50. The boundary between graphite and diamond has been illustrated with a dashed blue line.

seems incompatible with PCD where the liquid cobalt is surrounded by a large amount of diamond. However, Garcia *et al.* also note that the level of carbon in the cobalt binder in WC-Co cemented carbides (the sole source of the cobalt binder in PCD) is determined by the tungsten-carbon stoichiometry of the tungsten carbide grains. Excessive milling, through the incorporation of oxygen, can cause a sub-stoichiometric amount of carbon in the tungsten carbide and hence a carbon deficient binder phase. As the carbon and tungsten activities in cobalt are inversely proportional to one another[148], the carbon deficiency allows a large amount of tungsten to dissolve which then further prevents carbon from dissolving until the tungsten is removed. During the sintering of the PCD, cobalt melts and infiltrates the diamond powder whilst under a high, hydrostatic pressure to ensure diamond is the stable phase which also reduces the tendency for diamond to dissolve into the cobalt. After sintering is completed, the temperature is rapidly dropped before the pressure is removed, potentially allowing η-carbide to form in the still carbon-deficient cobalt binder and be present at room temperature. Further evidence that η-carbide particles are not the only requirement for graphitisation to occur

is their presence in the leached sample that was heated to 850 °C for 3 h (figure 5.22) and the absence of any graphite.

5.4.3.1 Summary of Key Points

- At 960 °C, the dissolution-reprecipitation mechanism appears to allow graphite to form directly from the cobalt binder pool.
- This mechanism also creates the η-carbide particles isolated within graphite that were observed in the ex-situ heated samples.
- At 800 °C, graphite nucleates from η-carbide particles.
- These particles are present at room temperature and appear unchanged up to the point of graphitisation and so it can be concluded that the incubation period is not related to the growth of these particles.
- The growth of this early-stage graphite looks like it occurs by the direct transformation mechanism suggested by Howes[87].
- The incubation period was not seen during the in-situ heating TEM experiment. A possible reason for this is that nucleation and early growth of graphite is held in check by the stress due to expansion of the graphite and the constraint of the surrounding material which is severely limited in a TEM lamella.

5.4.4 Explanation of Observed Phenomena

The experiments presented so far have shown a number of previously unreported phenomena involving the diamond and cobalt lattice parameters and, weight fractions of other phases that were observed during heating. The present section will discuss a number of physical models that can be used to explain these phenomena in the light of the direct observation of the graphitisation process that was discussed in section 5.4.3.

5.4.4.1 Origin of the Decrease in Cobalt Lattice Parameter

Changes in solute concentration As the molten cobalt binder has been in contact with tungsten carbide it will have a high concentration of dissolved tungsten and possibly carbon. The solubility of tungsten in cobalt is reportedly as high as 15 wt% at 1250 °C and 3.5 wt% at ambient temperatures[149]. The presence of some tungsten-containing particles in figures 5.39 and 5.50 (samples that were briefly heated and not heated respectively) suggest that some tungsten has precipitated as either tungsten carbide or η-carbide when the PCD was cooled from its sintering temperature to room temperature but the binder may still exist in a state of super-saturation due to the extremely non-equilibrium conditions during sintering and cooling. If carbon and tungsten come out of solution when samples are heated in graphitisation experiments, this could cause a decrease in the lattice parameter. However, there are several pieces of evidence to suggest that this isn't the main cause of the cobalt lattice parameter drop prior to graphitisation. An equation is provided by Wheeler[150] based on work by Roebuck *et al.*[115] that gives the lattice parameter change (in nanometres) of FCC cobalt based on the concentration of dissolved tungsten and carbon:

$$a^{fcc} - a_0^{fcc} = 0.00036[W] + 0.0012[C] \tag{5.1}$$

where $a^{fcc} - a_0^{fcc}$ is the difference in lattice parameter between pure FCC cobalt and the cobalt alloy in nanometres and $[W]$ and $[C]$ are the atomic percentages of tungsten and carbon in solution. Using this equation and the cobalt lattice parameter drop of the graphitised G75-A sample of 0.000 64 nm (shown in figure 5.30) the two extreme examples are:

1. Tungsten content stays the same and only carbon comes out of solution. This would require a change in the atomic percentage of carbon dissolved in the cobalt of 0.53 %. Based on the binder containing 2 wt% tungsten and 0.2 wt% carbon (from ref [137]) this gives a maximum carbon atomic percentage of just under 1 % and so this is possible. However, these values of maximum

carbon solubility were at 1250 °C and at the lowest possible tungsten contents and the presence of η-carbide suggests that the binder may be significantly higher in tungsten than this and hence deficient in carbon than this.

2. Carbon content stays the same and only tungsten comes out of solution. Using the same figures, this would necessitate a change in atomic percent of tungsten of 1.8 % which is possible as the range of possible atomic percentages of tungsten in cobalt according to Fernandes *et al.*[137] is 0.6–5.4 %.

To test the second hypothesis EDX was performed on binder pools (ensuring to avoid any areas of high tungsten concentration indicating either tungsten carbide or η-carbide precipitates) of 'Sample A' (heated briefly, no cobalt lattice parameter drop) and 'Sample B' (heated for 20 min, large cobalt lattice parameter drop observed) to see if heating changed the bulk binder tungsten concentration. Figure 5.53 shows how a typical binder pool was measured and table 5.2 shows that there was only a very slight change in the tungsten content between the two samples suggesting that the second hypothesis is not the cause of the lattice parameter change. It should be noted that the absolute values of atomic percentage

Sample	Average Binder Tungsten Content (at %)
A	2.63 ± 0.08
B	2.81 ± 0.09

Table 5.2: Average tungsten content of the binder pools of G75-B 'Sample A' and 'Sample B' measured by EDX.

tungsten are underestimated here due to the large (typically around 50 %) measured carbon content due to overspill of the electron beam interaction volume into the surrounding diamond grains. Furthermore, the increase in the weight percentages of the two available tungsten sinks (tungsten carbide and η-carbide) do not correlate particularly well with the decrease in lattice parameter further suggesting that tungsten coming out of solution is not the cause of the lattice parameter drop. The final and most compelling piece of evidence that solution concentration changes are

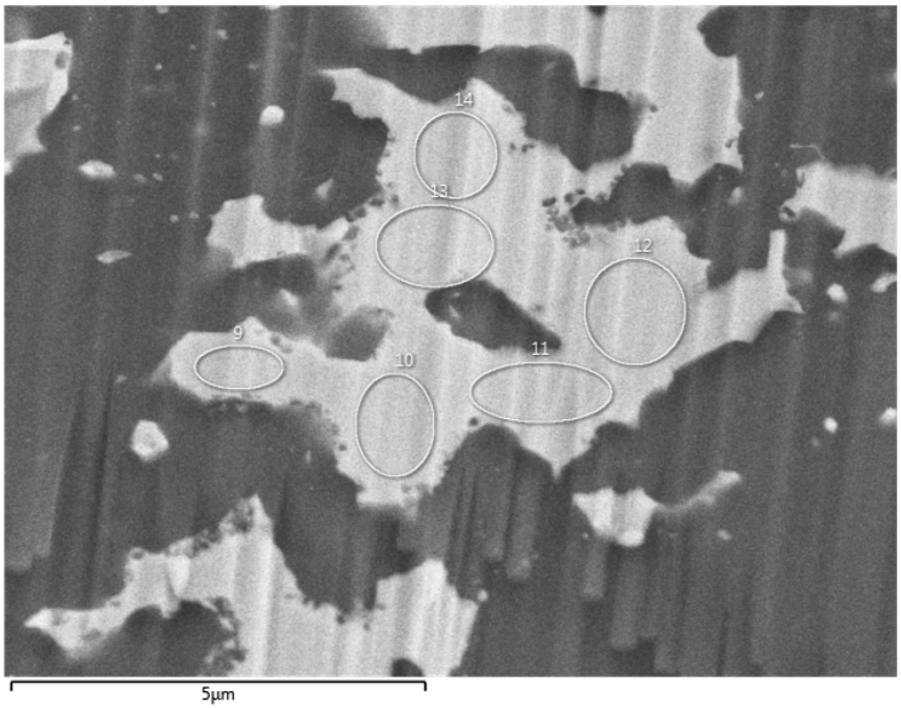

Figure 5.53: An example of a binder pool from G75-B 'Sample B' showing the regions that were used to measure the bulk tungsten content.

not the main cause of the change in cobalt lattice parameter is that in all cases where graphitisation occurs, the lattice parameter recovers to near its original level very quickly as the sample is graphitising regardless of the rate at which the original decline took place. As solution concentration changes are limited by the rate at which diffusion can occur, the very quick recovery of the lattice parameter suggests that another mechanism, such as stress, is the cause.

Stress due to new phases forming It is clear that high stresses must develop in the PCD at some point as SEM images of post-graphitised samples show extensive fracturing of the diamond. Furthermore, as previously mentioned, the decrease in the cobalt lattice parameter is always followed by an increase to roughly the same level as before suggesting that it is caused by stress and its subsequent release. Both tungsten carbide and η-carbide are very dense phases ($15.5\,\mathrm{g\,cm^{-3}}$ [151] and 14–$15\,\mathrm{g\,cm^{-3}}$[145]) and have been shown to correlate poorly with the change in lattice parameter indicating that the formation of these phases is not the source of such a stress. It has been shown in the literature (Westraadt *et al.*[62]) and

in the present work that graphite particles form in the cobalt binder pools when PCD is heated. As the formation of graphite from diamond is associated with a 55 % volume expansion, it is suggested that these particles are the source of the hydrostatic stress in the cobalt that decreases its lattice parameter.

Using data from the G75-A sample whose lattice parameters are shown in figure 5.30, the drop in cobalt lattice parameter from peak to trough of 0.0065 Å represents an elastic strain of 0.0018 and a corresponding hydrostatic stress of 576 MPa (elastic constants as a function of temperature are provided in appendix B). To investigate whether this stress is realistic, a simple elastic model with spherical symmetry is proposed. Figure 5.54 shows a graphite nucleus, of radius r_{g1}, inside a cobalt pool of radius r_{Co}, surrounded by a diamond shell of outer radius r_d. The graphite particle is conceptually removed from the cobalt-diamond shell, allowed to expand (due to the formation of additional graphite) stress-free and then reinserted into the now too small hole from which it originated and then all phases elastically deformed to allow it to fit such that the stresses are in equilibrium. The expansion of the graphite particle is written as the ratio $\alpha = \frac{r_{g2}}{r_{g1}}$.
The linear elastic solution gives radial displacement, U_r as a function of distance, r, from the centre:

$$U_r = Ar + \frac{B}{r^2} \tag{5.2}$$

where A and B are constants to be found by solving a series of six simultaneous equations (which are shown fully in appendix C) in six unknowns (A and B for all three phases) based on six boundary conditions using the software package Maxima[152]. These can then be used to calculated the radial, hoop and hydrostatic stresses in each phase:

$$\sigma_{rr} = A_i \left(2\mu + 3\lambda\right) - \frac{4\mu B_i}{r^3} \tag{5.3}$$

$$\sigma_{\theta\theta} = \sigma_{\phi\phi} = A_i \left(2\mu + 3\lambda\right) + \frac{2\mu B_i}{r^3} \tag{5.4}$$

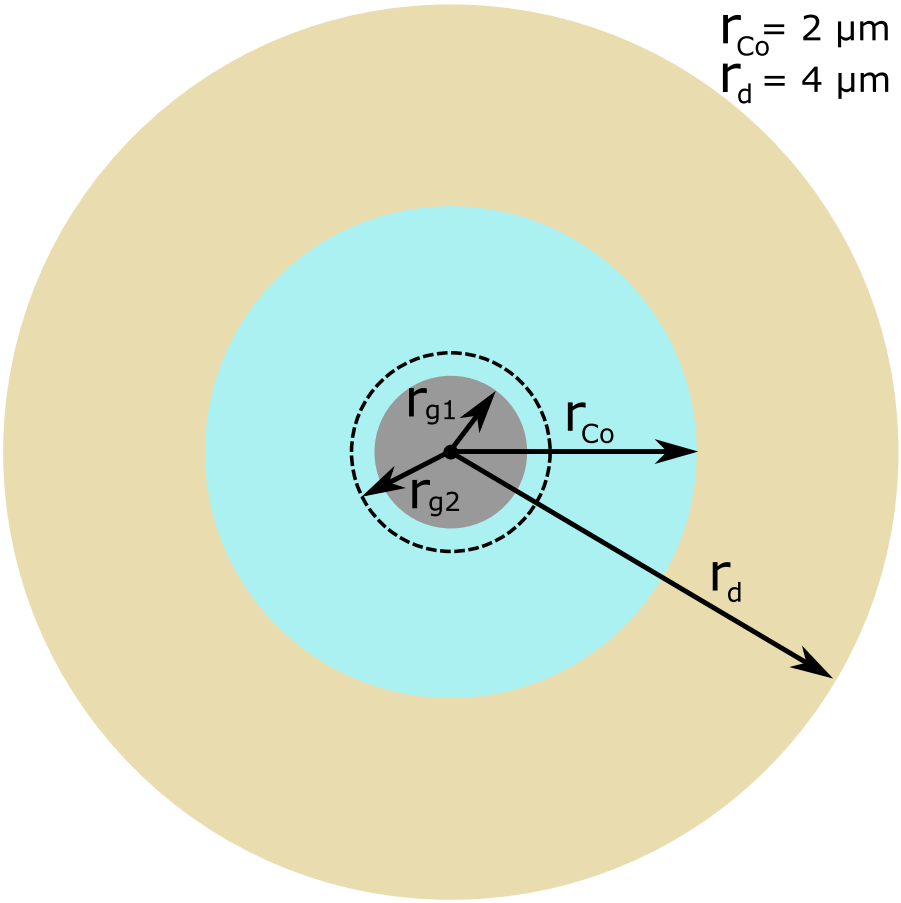

Figure 5.54: Schematic representation of the "Fully Elastic Regime" solution. r_d is the outer diamond shell radius and was 4 µm. r_{Co} is the outer cobalt particle radius and was 2 µm. r_{g1} is the initial graphite particle radius which was 5 nm and r_{g2} is the radius of the graphite particle after it has expanded.

$$\sigma_h = \frac{1}{3}\left(\sigma_{\theta\theta} + \sigma_{\phi\phi} + \sigma_{rr}\right) = A_i\left(2\mu + 3\lambda\right) \tag{5.5}$$

where λ and μ are the Lamé constants for each phase at 800 °C. The initial graphite will be assumed to have formed by a local diffusion of carbon and rearrangement of cobalt atoms and it will be assumed to be stress-free. It is assumed to have a radius of 5 nm as this has been shown to be the lower size limit for stable graphite nuclei[153]. After solving for all six of the A_i and B_i terms, the hydrostatic stresses in the cobalt and graphite phases and the Von Mises stress in the cobalt at the edge of the graphite particle are plotted as a function of the graphite expansion ratio, α, in figure 5.56. The diamond hydrostatic and hoop stresses are omitted from this graph for clarity but remain as negligibly small as the cobalt hydrostatic

stress. The expression for the Von Mises stress is:

$$\sigma_{VM} = \sqrt{\frac{1}{2}\{(\sigma_1 - \sigma_2)^2 + (\sigma_2 - \sigma_3)^2 + (\sigma_3 - \sigma_1)^2\}} \tag{5.6}$$

and given that two of the principal stresses are identical (the hoop stresses), this reduces to:

$$\sigma_{VM} = \sigma_{\phi\phi} - \sigma_{rr} = \frac{6\mu B_{Co}}{r^3} \tag{5.7}$$

As the graphite particle grows, it experiences a rapidly increasing compressive hydrostatic stress which, after it reaches an expansion of around 8 %, exceeds the limit of stability of graphite which is −3.94 GPa at 800 °C according to the carbon phase diagram determined by Bundy[147] (shown in figure 5.55). Clearly then, graphite particles cannot grow if the cobalt behaves purely elastically and the discrepancy between the mean cobalt lattice parameter decrease measured in figure 5.30 and the very low level of hydrostatic stress predicted in the cobalt by this model shows that it is not reflective of reality. However, values of yield stress for a highly constrained cobalt binder phase were calculated to be between 2.2 and 3.7 GPa by Sigl *et al.*[154]. These upper and lower bounds of the cobalt yield stress are shown on figure 5.56 as red dotted lines; tracking down to the hydrostatic stress in the graphite, it can be seen that even the higher estimate of yield stress results in the Von Mises stress in the cobalt at the edge of the graphite particle reaching the yield stress of cobalt before the graphite becomes unstable, suggesting that the cobalt here will plastically deform.

Although the current model cannot directly take plastic strains into account (and using one that can is beyond the scope of this thesis), an adjustment can be made to approximate the effect of plastic deformation. Instead of considering the graphite particle on its own as the misfitting element, the graphite and cobalt are both removed together from the diamond shell, the graphite is allowed to expand and a shell of cobalt removed from the centre to allow the graphite to fit back in. This cobalt is then re-plated onto the outside of the cobalt particle, increasing the total radius. The graphite-cobalt particle is now re-inserted into the too-small

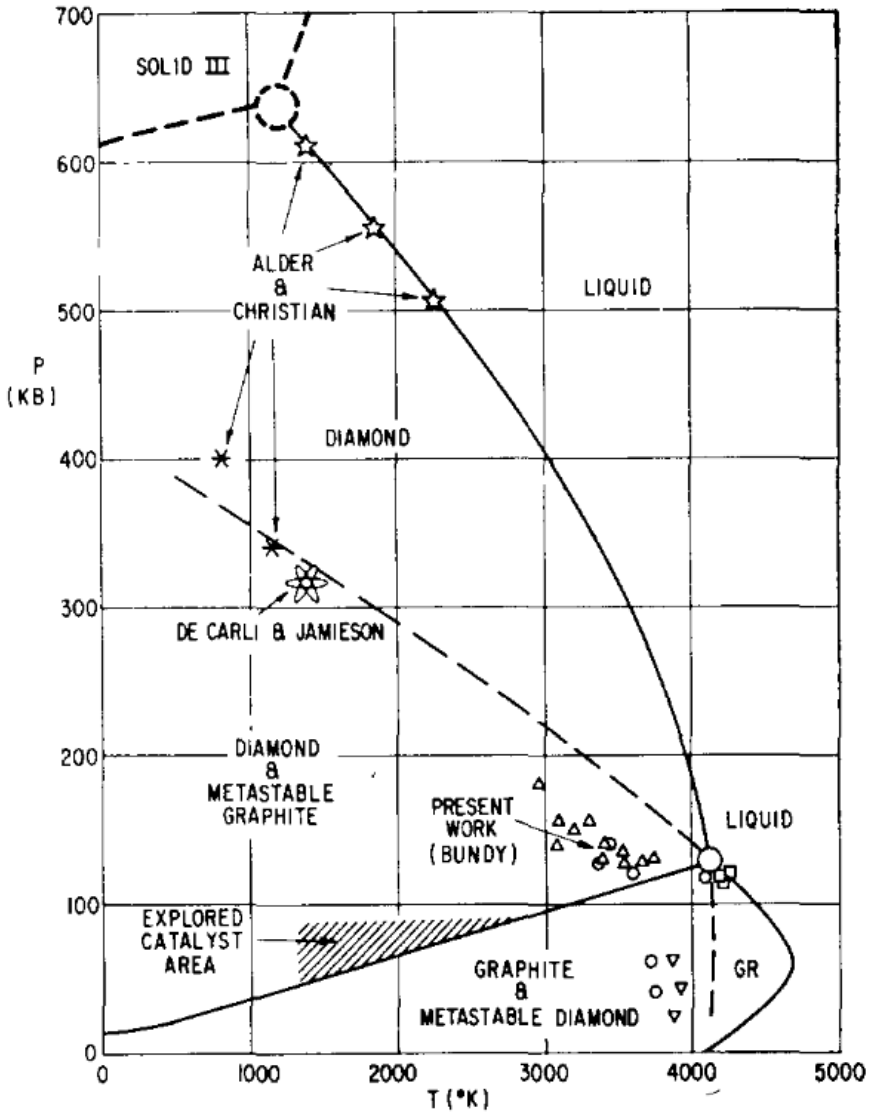

Figure 5.55: Carbon pressure-temperature phase diagram from Bundy[147] from which the pressure stability limit of graphite was calculated at 800 °C.

diamond shell and the strains accommodated elastically. This approximates the effect of plastic deformation as it relieves some of the high hoop stresses at the graphite-cobalt interface (as would occur if the cobalt here yielded) and distributes them hydrostatically into the whole cobalt shell. This is shown schematically in figure 5.57, again, where the expansion ratio of the graphite is given by $\alpha = \frac{r_{g2}}{r_{g1}}$ and the expanded cobalt radius is given by:

$$r_{Co,2} = \sqrt[3]{{r_{Co,1}}^3 + {r_{g2}}^3 - {r_{g1}}^3} \tag{5.8}$$

The stresses calculated from solving this elastic solution are shown in figure

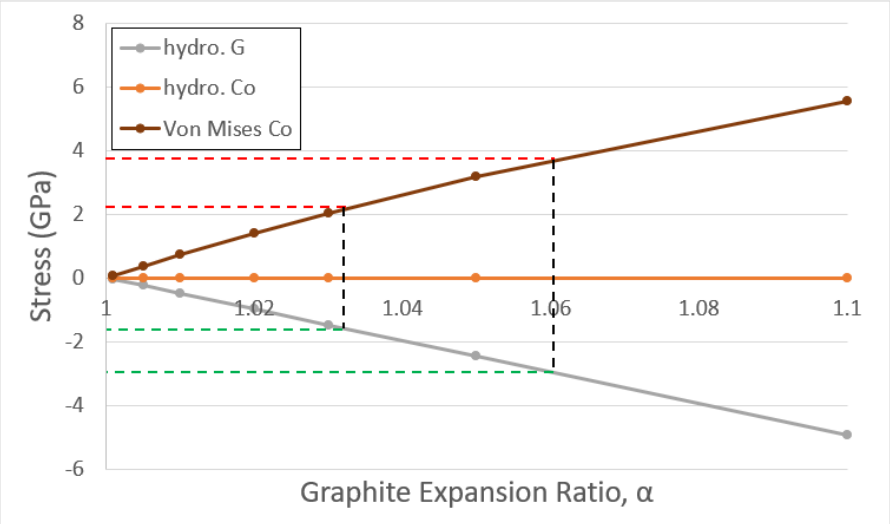

Figure 5.56: Graphite (grey) and cobalt (orange) hydrostatic stresses and the cobalt Von Mises stress at the boundary between the graphite and cobalt particle as a function of the graphite particle expansion ratio. The upper (3.7 GPa) and lower (2.2 GPa) bounds for the yield stress of cobalt are shown by dashed red lines. Even taking the higher value of the yield stress, the hydrostatic stress in the graphite is just over −3 GPa when the cobalt Von Mises stress exceeds this upper bound indicating that the graphite is still stable (limit of stability being −3.94 GPa) and able to continue growing and that the cobalt will therefore yield at the boundary.

5.58. In this case, data is shown up to a graphite particle radius of 0.4 µm. Even at this size, the hydrostatic stress in the graphite phase has only reached a maximum of −280 MPa and so it remains well within its region of stability on the phase diagram. This shows that it is plastic deformation in the cobalt that allows the graphite particles to form. The cobalt and diamond hydrostatic stresses also exhibit behaviours much closer to those seen in the synchrotron diffraction derived lattice parameter measurements. Figure 5.59 shows a comparison between an average from all samples of the hydrostatic stress measured by synchrotron x-ray diffraction and the values calculated from the plastic-approximating elastic model with a graphite radius of 400 nm. The graphite particle size assumed is slightly bigger than the maximum size of graphite particles seen in figure 5.40 which appears to be around 200 nm but there are many more of these smaller particles in the real binder pool which will likely increase the total hydrostatic stress in the cobalt. The close agreement between these stress figures increases the confidence that this model can be used to explain the lattice parameter changes seen in the synchrotron results.

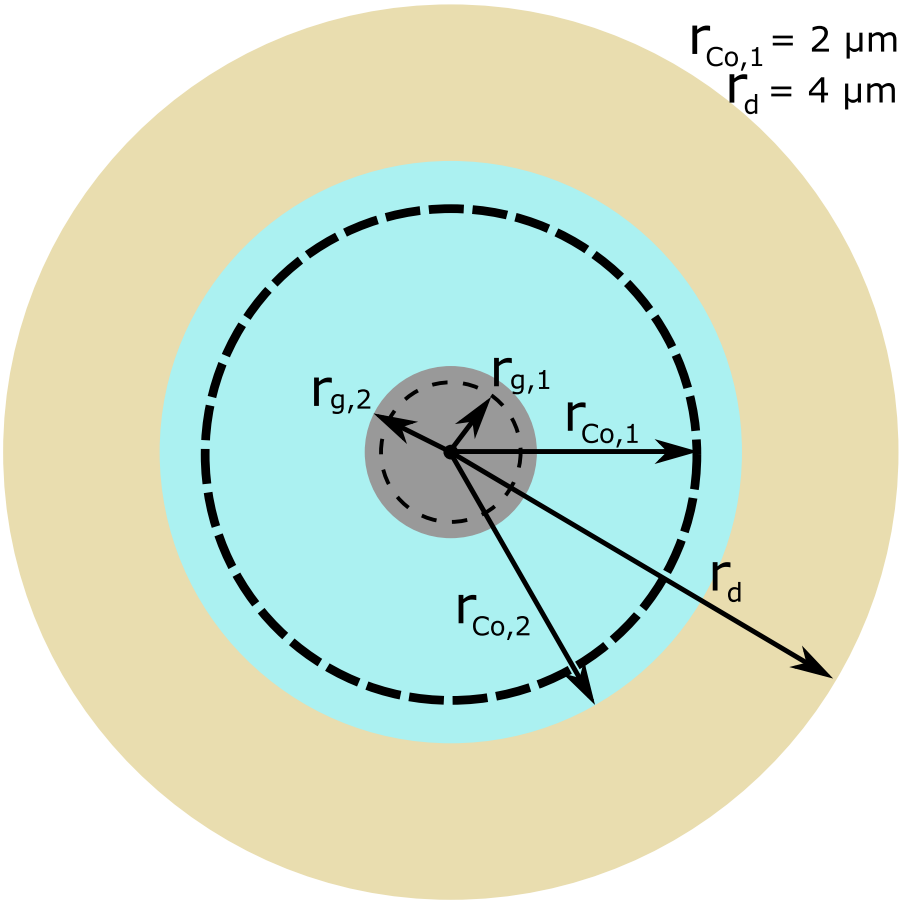

Figure 5.57: Schematic representation of the "Fully Plastic Regime" solution. r_d is the outer radius of the diamond shell and is equal to 4 µm as before. $r_{Co,1}$ is the initial radius of the cobalt particle (and the radius of the hole left in the diamond shell) and is equal to 2 µm as before. r_{g1} is the radius of the initial graphite particle (5 nm) and r_{g2} is the expanded graphite radius. $r_{Co,2}$ is the radius of the cobalt-graphite particle after the cobalt has been re-plated onto the expanded graphite particle and will be greater than $r_{Co,1}$.

Figure 5.58 also shows the hoop stress in the diamond at the edge of the cobalt pool which reaches 493 MPa at a graphite particle radius of 0.4 µm whereas in the "Elastic Regime" this stress was still insignificantly small at the point that the graphite became unstable. This suggests a mechanism for the transition from graphite formation within cobalt pools to the catastrophic graphitisation that results in the complete degradation of the mechanical properties of PCD. Although this level of stress won't be sufficient to cause fracture of a perfect spherical shell of diamond, micrographs show that the binder pools are very far from perfect spheres. Irregularities in the diamond surrounding the pool could act like notches or flaws to

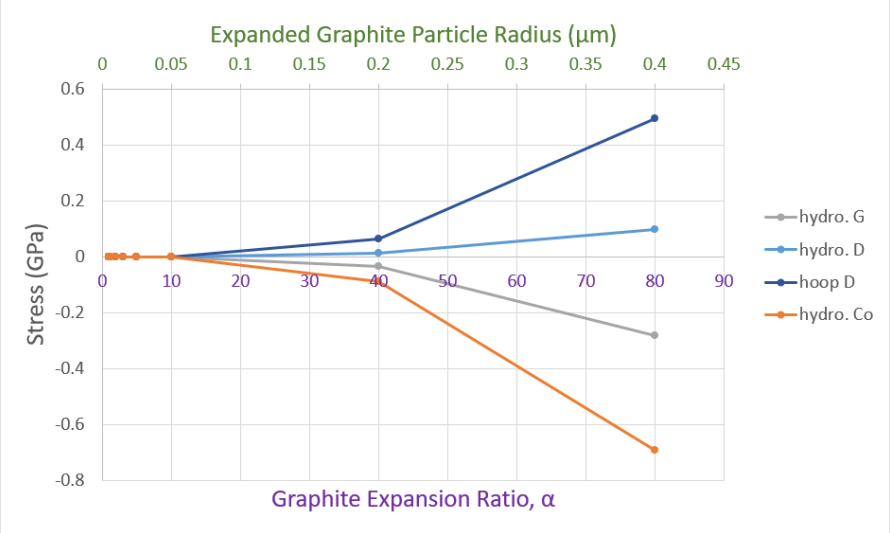

Figure 5.58: Graphite (grey), diamond (light blue) and cobalt (orange) hydrostatic stress and diamond hoop stresses (dark blue) are shown as a function of graphite expansion ratio (purple axis) and the equivalent expanded graphite particle size (green axis). It can be seen that the graphite particle can grow to much larger sizes before the graphite is put under enough pressure to prevent its further formation or the diamond is put under enough stress to crack.

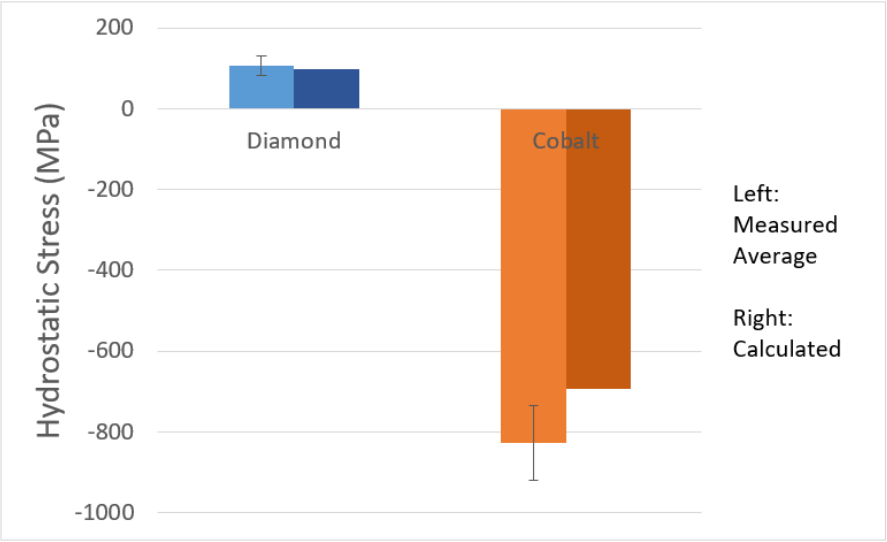

Figure 5.59: Comparison of the stresses measured from the lattice parameter changes of diamond (blue) and cobalt (orange) from the synchrotron diffraction results (left hand column of each pair) with that predicted by the "Fully Plastic Regime" model for an expanded graphite particle radius of 400 nm.

cause a concentration of this hoop stress resulting in local fracture of the diamond. Fracture would allow the compressive stresses in the cobalt and more importantly graphite to be locally relieved which would greatly lower the thermodynamic barrier

to graphite formation (essentially dropping vertically from just below the diamond-graphite equilibrium line in figure 5.55 to being well within the graphite phase field) and allow it to form in larger quantities. The large, sudden expansion of this transformation from diamond to graphite would further force the crack faces apart and the crack would be attracted to the tensile stresses surrounding other binder pools allowing them to go through the same process. This runaway procedure explains why graphite weight percentage increases very rapidly in all cases and is also associated with the rapid release of the stresses (rapid rise in cobalt lattice parameter) of the cobalt and diamond phases.

5.4.4.2 Origin of the Incubation Period

The transition from purely elastic strains to plasticity in the cobalt has been shown to transfer stress onto the diamond, potentially causing it to fracture and leading to the catastrophic graphitisation that is observed in the synchrotron and neutron diffraction results. However, the results show an incubation period exists before large-scale graphitisation occurs that is sensitive to both temperature and binder composition. Instead of assuming that the entirety of the binder pool has yielded all at once, a shell of plastically deformed material can be considered surrounding the graphite nucleus whose radius is determined by the distance at which the Von Mises yield criterion is exceeded. Figure 5.60 shows a diagram of the four-phase elastic problem that must be solved by the same method as described previously (this time with eight boundary conditions). The displacements of the cobalt and diamond at the outer boundary (r_{Co}) are locked together as the cobalt is treated as deforming elastically here. The model for purely elastic deformation shown in figure 5.54 is used to calculate the radius at which the Von Mises yield criterion is exceeded for a given expansion of the graphite particle ($\alpha = \frac{r_{g,2}}{r_{g,1}}$) and this sized graphite-cobalt particle is conceptually removed. It is then allowed to expand stress-free to a size $r_{Co,Plastic}$ and treated as if it has plastically relaxed as in the 'plastic regime' model of figure 5.57. This particle is then reinserted into the hole in the remaining cobalt (of size $r_{Co,Elastic}$) which is now too small for it and the

strains are accommodated elastically. When this graphite-'Plastic' cobalt particle is reinserted, the Von Mises stress may still exceed the yield stress in the 'Elastic' cobalt region and so this process must be performed again until the yield radius is equal to the 'Plastic' cobalt radius. Due to the recursive nature of the solution, it cannot be calculated by solving a single set of simultaneous equations and has to be performed manually. The input and output yield radii to and from the Maxima calculation are plotted against one another and the true yield radius is found where the two values are equal indicated by the intersection of this line with the $y = x$ line in figure 5.61 (solved for three values of α). The Von Mises stress in the cobalt (equation 5.7) varies as a function of $\frac{1}{r^3}$ and so decreases rapidly as distance from the centre increases. At small values of graphite expansion, this results in the stresses in the cobalt being low enough that the yield radius is within the graphite particle thereby dictating that none of the cobalt yields. As the graphite particle expands, the yield radius also expands and eventually extends into the cobalt pool. At this point, the cobalt yields, stress is transferred to the diamond causing it to fracture and catastrophic graphitisation follows. The source of the incubation period is therefore suggested to be the time required for the graphite particle to grow sufficiently for the yield radius to expand into the cobalt.

In section 5.4.1, increasing the temperature was shown to decrease the incubation period and in section 5.4.2.6, adding a group VII transition metal element to the binder was shown to increase it. Using the assumption that the transition from elastic to plastic deformation in the binder phase is the origin of the incubation period, these two observed behaviours can be explained by examining the effect of varying the yield stress of the binder on the yield radius. Figure 5.63 shows the difference between the yield radius (calculated by setting the Von Mises stress to the yield stress and solving for the radius using the 'Fully Elastic' regime, equation 5.9) and the radius of the graphite particle.

$$r_{yield} = \sqrt[3]{\frac{6\mu B_{Co}}{\sigma_y}} \tag{5.9}$$

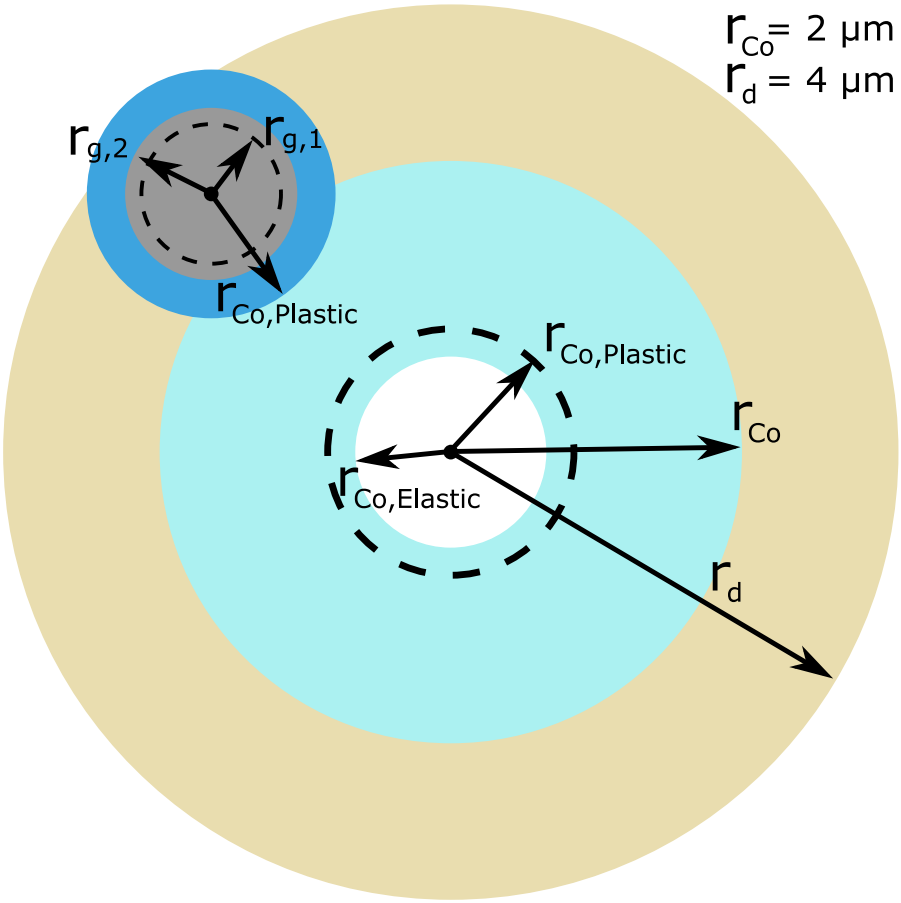

Figure 5.60: Schematic representation of the "Plastic Shell Regime" solution. r_d and r_{Co} are the diamond and cobalt outer radii and are equal to 4 µm and 2 µm as before. r_{g1} and r_{g2} are the original (5 nm) and expanded graphite radii as before. $r_{Co,Elastic}$ is the radius at which the Von Mises stress in the cobalt is calculated to exceed the yield stress using the "Fully Elastic Regime" solution. It is also the radius of the hole left in the cobalt shell after this cobalt-graphite particle has been removed from it. $r_{Co,Plastic}$ is the radius of the cobalt-graphite particle after the graphite has expanded and the amount of cobalt determined by $r_{Co,Elastic}$ has been re-plated back onto it.

(where μ is one of the Lamé constants, B_{Co} is one of the elastic parameters and σ_y is the yield stress of the cobalt). If the difference is negative, this indicates that the yield radius lies within the graphite particle and the cobalt does not yield. The point at which yield first occurs can therefore be determined by the point at which the curve first crosses the x-axis. The graph shows that increasing the yield stress requires the graphite to reach a greater size before yield first occurs. From figure 5.56 it can be seen that as the graphite grows larger within the elastic regime (pre-yield), the compressive hydrostatic stress within it increases and so

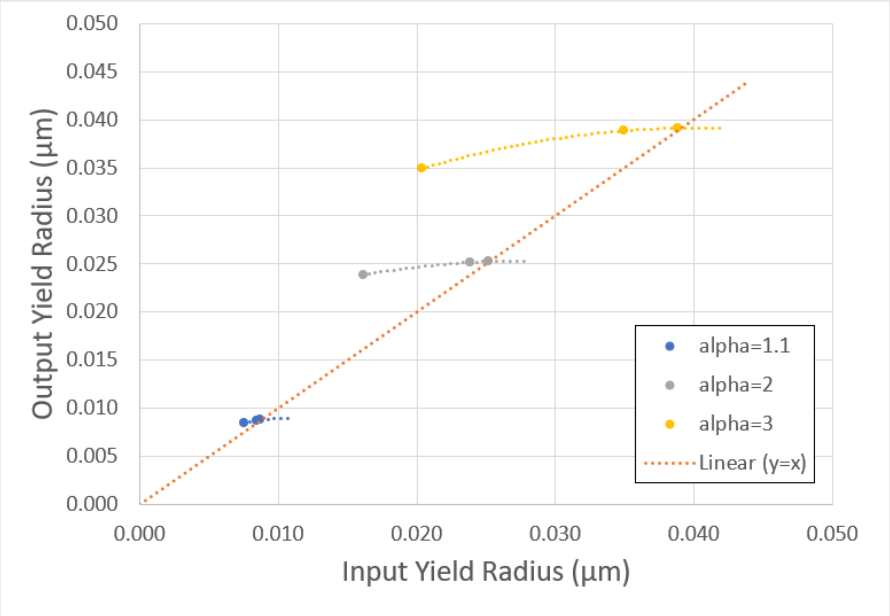

Figure 5.61: This graph shows the iterative nature of calculating the yield radius using the 'Fully Elastic Regime" solution (x-axis) and then re-calculating the yield radius with the "Plastic Shell" solution (y-axis). This process was repeated 3 times until the input yield radius was roughly equal to the output. A quadratic trendline was applied to these data points and the point where the two values were equal calculated and this was taken to be the value of the yield radius.

by combining these two pieces of data, a graph can be plotted for the hydrostatic stress in the graphite when yielding first occurs against the yield stress of the binder (figure 5.64). By substituting in a hydrostatic stress of $-3.95\,\text{GPa}$ (indicated by the horizontal red line) and solving for the yield stress, it is found that above a yield stress of $4.85\,\text{GPa}$, the binder will not be able to yield as by the time it is just on the point of plastically deforming, the hydrostatic stress in the graphite is large enough to push it into the diamond stable region of its phase diagram making it thermodynamically unfavourable to continue growing. As such, the binder will never leave the elastic regime, stress cannot be transferred onto the diamond and so catastrophic graphitisation will never occur. This shows that the higher the yield stress of the binder the longer the incubation period will be and it predicts that if the yield stress is high enough, catastrophic graphitisation will never occur.

This hypothetical mechanism can be related to the observed experimental behaviour of PCD heated to different temperatures and as a function of binder

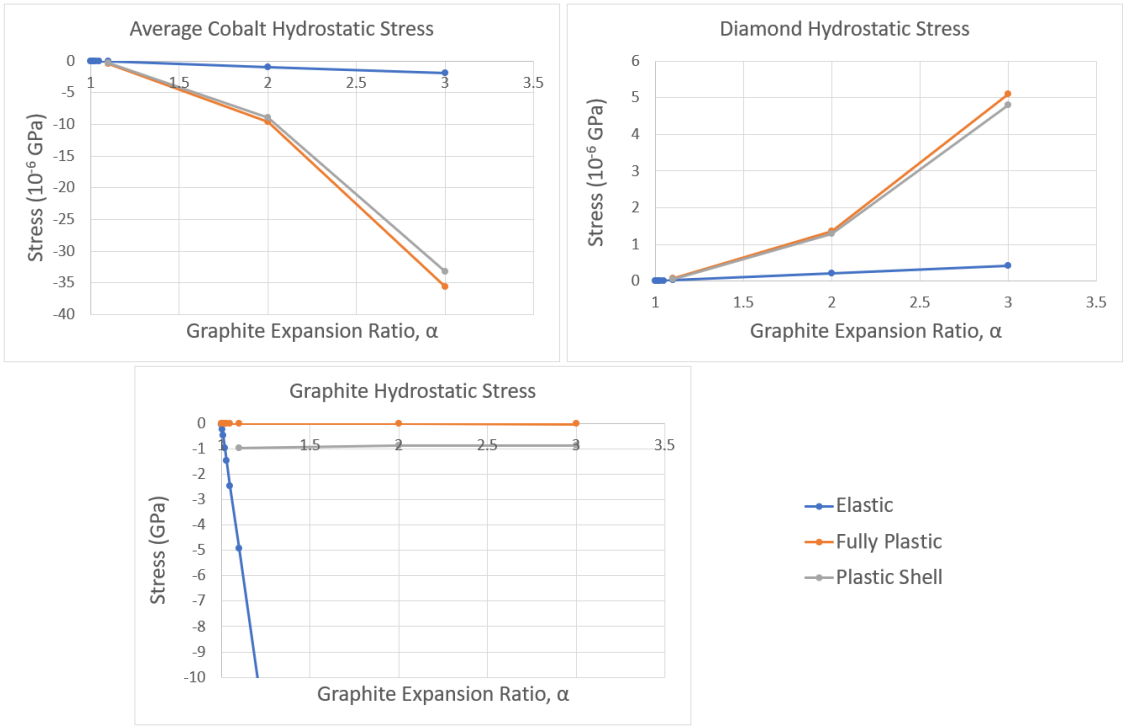

Figure 5.62: Graphs showing the effect of the "Plastic Shell" solution compared to the "Elastic" and "Fully Plastic" regimes. Changing from 'Fully Plastic" to "Plastic Shell" makes very little difference to the cobalt and diamond hydrostatic stresses but greatly reduces the hydrostatic stress in the graphite particle.

chemistry. The hardness of WC-Co cermets has been shown to decrease as the temperature increases[155]. As hardness is closely related to resistance to plastic deformation, it is likely that this is partly caused by a degradation of the yield stress of the binder and so increasing the temperature of the PCD would be expected to reduce the yield stress of the binder and hence the amount of time between heating and the onset of graphitisation. The neutron diffraction experiments in section 5.4.1 showed that increasing the temperature decreased the length of the incubation period. Konyashin *et al.*[156] showed that adding the aforementioned group VII transition metal element to the binder of WC-Co cermets "reduced the hot-hardness reduction"; in other words that the addition of this element increased the yield stress at any given temperature. Furthermore, the Additive also increases the melting temperature of its alloy with cobalt[157]. As flow stress increases the further away the temperature is from the melting point, the Additive will increase the flow stress of cobalt at any given temperature. It would therefore be

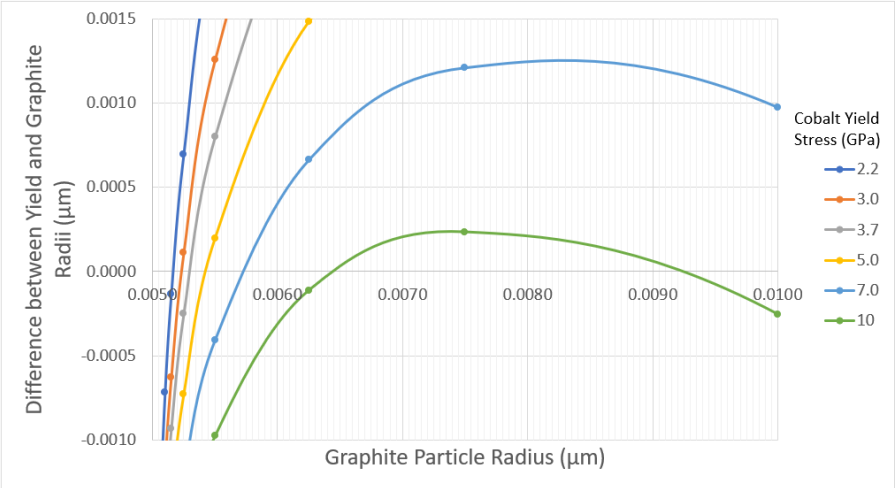

Figure 5.63: Graph showing the effect of changing the yield stress on yield radius. The y-axis shows the difference between the yield radius and the outer graphite particle radius. If this difference is less than zero, this means that yield radius is within the graphite particle and as the Von Mises stress only decreases with increasing distance from the centre (as a function of $\frac{1}{r^3}$) this means that none of the cobalt will yield. The graph therefore shows that increasing the yield stress of the cobalt eventually results in the cobalt binder not yielding which means that the cobalt will stay in the "Elastic Regime", the graphite hydrostatic stress will remain very high and it will eventually stop forming, preventing stress transfer to the diamond and protecting it from fracture and subsequent catastrophic graphitisation.

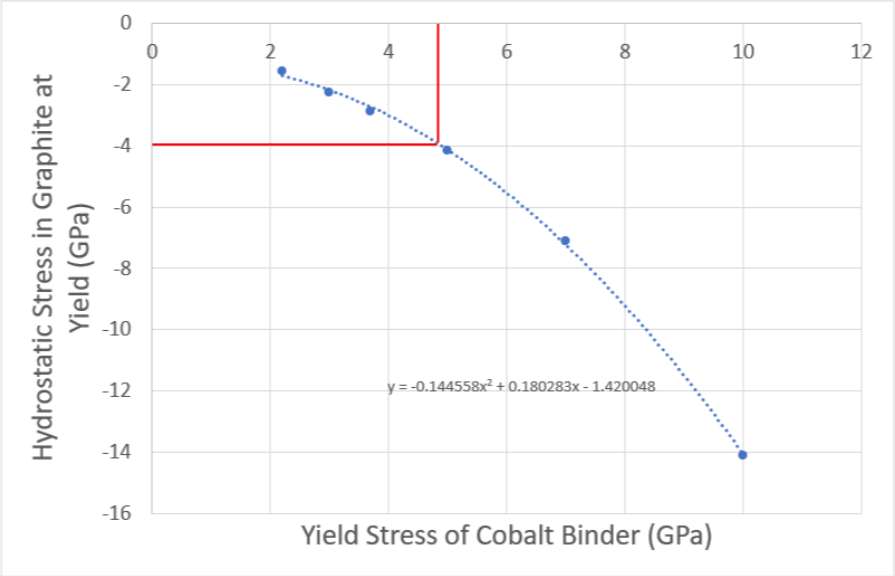

Figure 5.64: Graph showing the necessary yield stress of the cobalt binder for the hydrostatic stress in the graphite to exceed its limit of stability (−3.94 GPa) by the time the yield radius begins to exceed the graphite particle radius. This will mean that if the cobalt yield stress exceeds 4.85 GPa, the binder pool will remain in the "Elastic Regime" and catastrophic graphitisation will not be able to occur.

expected that the incubation period would be longer the more Additive the binder contained and the laboratory x-ray diffraction experiments in section 5.4.2.6 did indeed show this. These two findings validate the proposed mechanism behind the incubation period before catastrophic graphitisation occurs and its dependence on the temperature and binder chemistry that has been shown experimentally.

5.4.4.3 Effect of Carbon Leaving Solution

So far, graphite has been assumed to form from carbon dissolved in the cobalt binder phase but this has not been taken account of mathematically. Equation 5.1 shows the relationship between dissolved carbon content and the cobalt lattice parameter and so reducing the carbon content will cause a contraction in the lattice parameter that will influence the stresses in each phase. Using this equation, an equation can be defined for the change in radius of the cobalt particle for a given size of graphite particle formed:

$$\frac{\Delta r_{Co}}{r_{Co}} = \frac{0.12}{3.6} \frac{{r_g}^3}{{r_{Co}}^3} \frac{\rho_g M_{Co}}{\rho_{Co} M_g} \tag{5.10}$$

where r_{Co} and r_g; ρ_{Co} and ρ_g; M_{Co} and M_g are the radii, densities and molar masses of the cobalt and graphite respectively. This can then be applied to the boundary conditions between the cobalt and graphite and, diamond and graphite phases to test its effect on the stresses.

During the purely 'elastic regime', the graphite hydrostatic stress is only affected a negligible amount. Figures 5.65 and 5.66 show the effect on the cobalt and diamond hydrostatic stresses. Although a large effect appears showing the cobalt moving into tension and diamond into compression (as would be expected if the cobalt attempts to contract and is restricted from doing so by the diamond), this only becomes significant above a graphite expansion ratio of 3, by which time the cobalt has been shown to yield and move into the plastic regime anyway. As such, the conclusions are not changed during the 'elastic regime'.

When considering the effect of the cobalt lattice parameter reduction on the plastic stresses, figure 5.67 shows the graphite, cobalt and diamond hydrostatic and

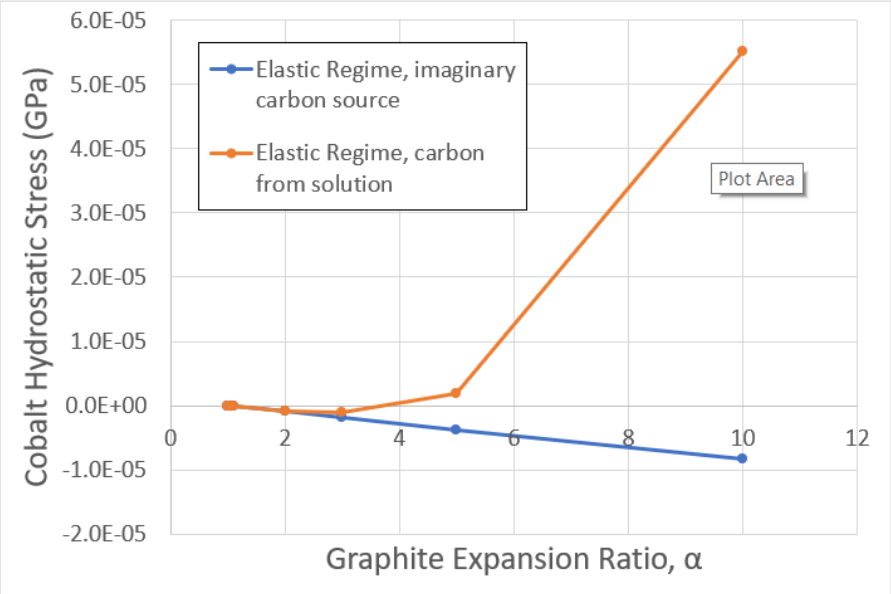

Figure 5.65: Graph showing the effect of including the cobalt contraction that would be caused by carbon coming out of solution on the cobalt hydrostatic stress predicted by the "Elastic Regime". At low expansion ratios, the difference between the stresses predicted is low but as the graphite gets bigger, the stresses deviate by a large amount. However, the point at which this happens is already past the point at which the transition to the "Plastic Regime" would have occurred.

diamond hoop stress (at the edge of the cobalt pool) as a function of graphite particle size for carbon coming from an imaginary source versus coming out of solution. The reduction of all of the stress is very similar and minimal and so it is concluded that the source of the carbon can be ignored and that considering it to come from an imaginary source is suitable for the purpose of the calculations made in this section.

5.4.4.4 Possible Causes of Temperature Drop

Energy of Formation The only phases forming around the temperature drop are graphite, η-carbide and tungsten carbide. As previously mentioned, carbon formation is thought to be associated with a release of energy. The carbides are also predicted to have negative formation energies (indicating exothermic reactions) of $-16.4\,\mathrm{kJ\,mol^{-1}}$, $-13.5\,\mathrm{kJ\,mol^{-1}}$ and $-7.7\,\mathrm{kJ\,mol^{-1}}$ for WC, Co_6W_6C and Co_3W_3C respectively when formed from elemental species. Small positive formation energies are predicted for both η-carbides from reaction pathways involving elemental cobalt

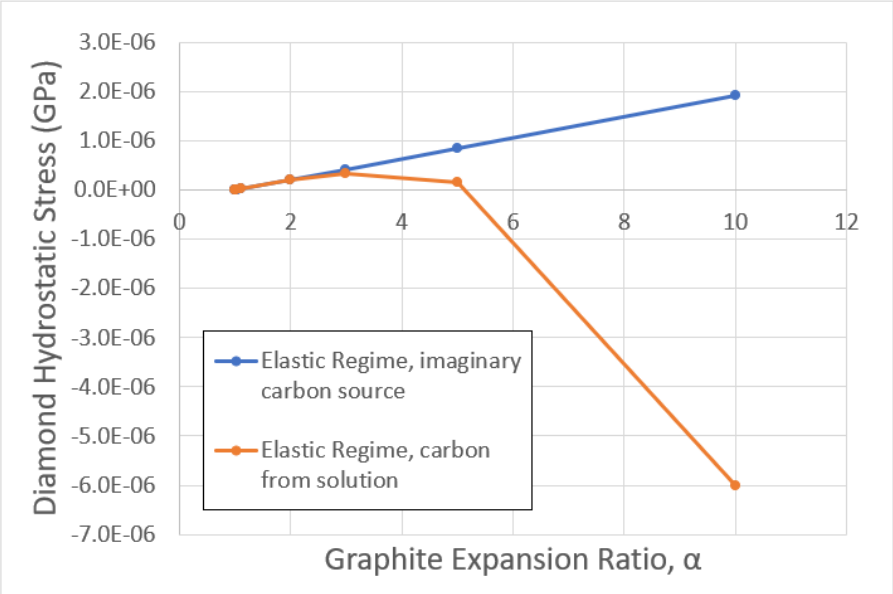

Figure 5.66: Graph showing the effect of including the cobalt contraction that would be caused by carbon coming out of solution on the diamond hydrostatic stress predicted by the "Elastic Regime". At low expansion ratios, the difference between the stresses predicted is low but as the graphite gets bigger, the stresses deviate by a large amount. However, the point at which this happens is already past the point at which the transition to the "Plastic Regime" would have occurred.

and WC but the increases in weight percentages do not correlate well enough with the drop in temperature for this to be likely.

New Surface Area In the conventional theory of fracture mechanics, the energy required for the creation of the new surface area associated with a crack is supplied by the stored mechanical energy of the system. For example, in a tensile test, the grips are allowed to do work as the crack propogates and new surface area is created thereby supplying the energy required. In the experiments described in the current section, although work is stored in the system in the form of elastic strain energy in the residual stresses, the form of the work supplied to the system is thermal and so it is suggested that this could be the source for the energy required to create the new surface area when catastrophic graphitisation occurs. To assess whether this was a reasonable suggestion or not, the total new surface area created per unit volume due to catastrophic graphitisation was estimated from figure 5.68 (a FIB cross-section of a sample heated to the point of catastrophic graphitisation) by adding up the

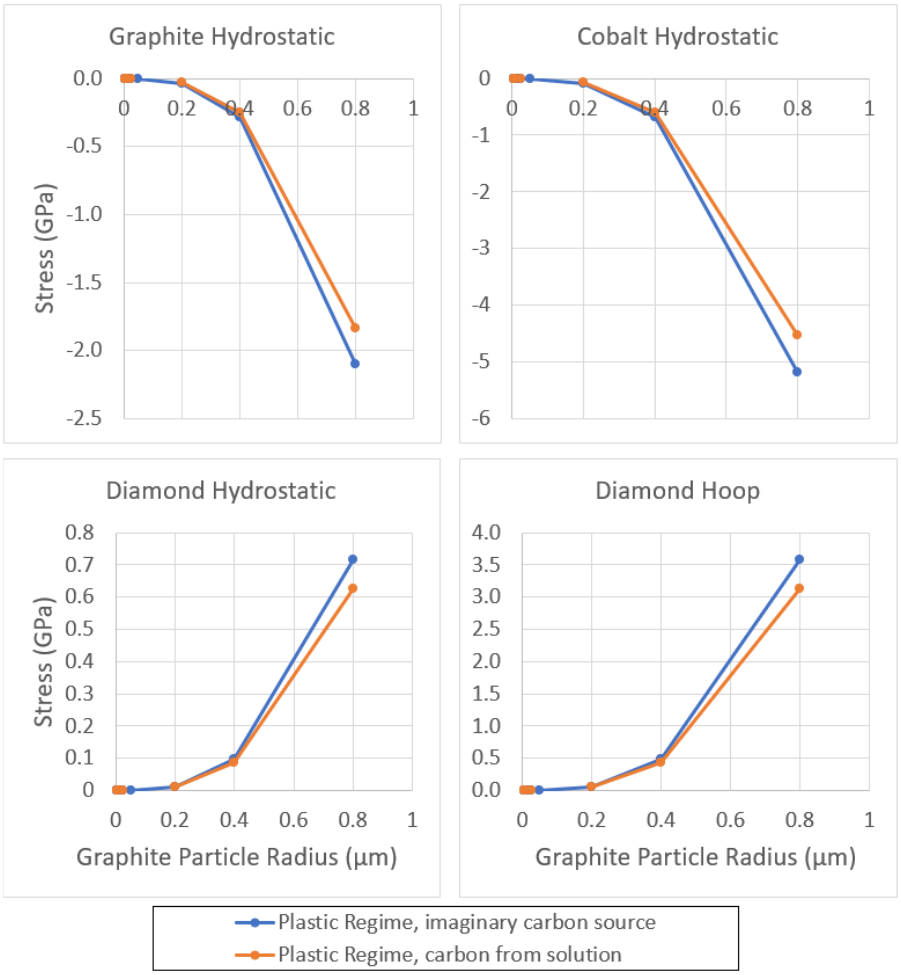

Figure 5.67: Graph showing the effect of including the cobalt contraction that would be caused by carbon coming out of solution on the graphite, cobalt and diamond hydrostatic and diamond hoop stresses calculated by the "Plastic Regime". The difference is low even up to graphite radii of 0.8 µm and so it is determined that this adjustment can be neglected.

total length of cracks intersecting the plane of the image and scaling this area density up to a volume density by assuming the same density of cracks in all three spatial dimensions giving a "new surface area density" of 2.9 $\mu m^2\,\mu m^{-3}$. The surface energies of the diamond {100}, {110} and {111} surfaces are given as 6.23, 6.26 and 5.11 $J\,m^{-2}$ respectively[158] and using an average of these values, the amount of energy needed to create the new surface area was calculated as 0.58 J. Assuming that all of this energy was provided by heat, the temperature drop is given by:

$$\Delta T = \frac{Q}{mc} \tag{5.11}$$

where Q is the heat energy transferred, m is the mass of the sample (0.12 g) and c is the heat capacity (2250 J/kgK[159] at 800 °C). The predicted temperature drop is just over 2 °C which is quite a bit lower than the 8 °C drop measured. This calculation assumed that all of the cracks were perfectly flat surfaces so roughening could increase the surface area and hence produce a predicted temperature drop closer to that measured. To get an accurate surface area value, a BET isotherm measurement could be taken.

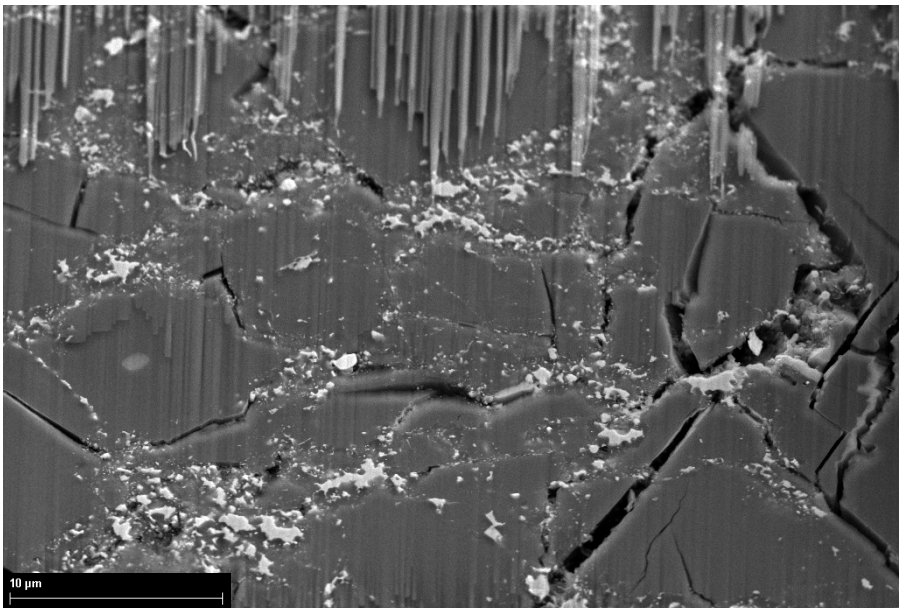

Figure 5.68: FIB cross-section of a highly cracked PCD sample after it has been heated and graphitised indicating that a large amount of new surface area will be generated when catastrophic graphitisation occurs.

Strain Release Local heating at a crack tip due to the plastic work done in deforming the material here is a well studied phenomenon[160]. However, another temperature changing effect due to the release of elastic strain is described by the thermoelastic effect[161]. Fuller *et al.*[162] first reported a transient cooling effect in response to the fracture of glassy polymers but a more detailed explanation was given by by Rittel[163] in the context of a moving crack front relative to a stationary thermocouple. Linear elastic fracture mechanics describes the tensile stress-field around a crack tip with a central plastic zone to prevent the necessity of infinite stresses. When the crack advances through a point (such as a thermocouple), the

thermoelastic effect predicts that the material will be cooled due to the release of the tensile strain ahead of the crack-tip. Using a thermocouple embedded in brittle PMMA, Rittel measured this thermoelastic cooling effect followed by the heating due to the passage of the plastic zone (both temperature changes were on the order of 10s of degrees over 10s to 100s of milliseconds). In the case of diamond, the plastic zone at the crack tip will be small as its size is inversely proportional to the yield stress and so it is likely that the thermoelastic cooling will be greater than the thermoplastic heating. In light of this it is possible that the passage of many crack fronts past the embedded thermocouple due to the disintegration of PCD due to catastrophic graphitisation could cause a cooling effect of approximately 10 °C over time scale of several seconds as was seen in this experiment.

5.4.4.5 Unexplained Phenomena

Although the model presented accounts for a large number of the behaviours seen when polycrystalline diamond is heated, there are two phenomena that it cannot account for in its current form.

Firstly, when PCD is leached, all of the cobalt from large, interconnected binder pools is dissolved away by the acid. This leaves smaller, isolated binder pools trapped within the diamond matrix and even when this material is heated to 850 °C for 3 hours, these binder pools do not catastrophically graphitise. A potential hypothesis was that smaller binder pools experience a higher hydrostatic stress in the graphite causing its growth to become thermodynamically unfavourable before the particle has a chance to become big enough to cause the binder around it to yield. However, the hydrostatic stress in the graphite phase and the yield radius of the cobalt remain relatively unchanged with decreasing binder size. In fact, the model predicts that these small binder pools will fracture the diamond surrounding them at smaller graphite particle sizes than bigger pools. The diamond hoop stress decreases with the inverse cube of the distance from the centre of the pool meaning that the diamond interface will be under greater hoop stresses for smaller binder pools. Furthermore, the residual binder pool in the leached material was of a similar

size to those seen to graphitise in the unleached material. There are two main possibilities that could explain why the model doesn't account for this behaviour. The spherical symmetry assumed in the model is not representative of the true microstructure - graphite particles actually form near the edge of binder pools rather than the centre, the larger binder pools aren't perfectly spherical and are interconnected and more than one graphite nucleus generally forms in each binder pool. This breaking of spherical symmetry makes it impossible to perfectly model the stresses in the binder pools using a purely analytical model and therefore a finite element model may be more appropriate. Secondly, there may be an issue with the assumption of the amount of carbon dissolved in the binder pools, this also may not necessarily be uniform for all sizes of binder pool. Smaller pools will have a lower total amount of carbon even if they have the same per unit volume. The smaller binder pools may therefore not have enough carbon dissolved in them to form a sufficiently sized graphite particle to cause enough stress in the surrounding diamond to cause catastrophic graphitisation. It is therefore suggested that a less simplified model, such as a finite element model, is used to examine how the stresses develop in a more representative microstructure.

The second phenomenon is highlighted in figures 5.32 and 5.33 however this was only observed in one instance. These figures show that when the PCD was heated in much smaller steps over a longer time period, the decrease in cobalt lattice parameter happens over a long period of time and starts a long time before measurable graphitisation occurs but the increase in diamond lattice parameter still occurs over a short period of time right around the point where catastrophic graphitisation is occurring. As it is thought that this stress is related to the fracturing of diamond and the precise nature of the transition from graphite nucleus formation to fracture of the diamond and catastrophic graphitisation is unknown, the explanation behind this phenomena will likely explain the decoupling of the diamond and cobalt stresses and so further work should be undertaken.

5.4.4.6 Summary of Key Points

- Stress due to the formation of graphite is deemed to be the likely cause of the observed behaviour of the cobalt and diamond lattice parameters.
- An elastic model that approximates plastic behaviour in the cobalt predicts the stresses in the diamond and cobalt phases with good agreement with those measured from the changes in lattice parameters.
- The time taken to grow a graphite nucleus to a size that causes plastic deformation in the surrounding cobalt is suggested as the origin of the incubaton period.
- The length of the graphitisation incubation period is suggested to be controlled by the yield stress of the cobalt binder.
- The mechanism by which nucleus graphite formation transitions to catastrophic graphitisation remains unclear.

5.4.5 The Effect of Graphitisation on Mechanical Properties

Figure 5.69 shows the strengths of samples of G12-M-HP (blue), G17-M-HP (orange) and G27-M-HP (grey) after 0, 1.5 and 3 hours of heating at 800 °C. After 1.5 h of heating, the strengths have been reduced by factors of 2.7, 2.2 and 2.3 respectively. After 3 h of heating, the strength is essentially reduced to zero with samples becoming friable to the point of crumbling during handling. Figure 5.70 shows one possible reason for the reduction in strength. Cobalt from pools that break the surface of the PCD has been extruded and has potentially reacted with residual oxygen in the vacuum chambre in which they were heated. These pools have now become voids which will act as very large surface flaws during bending strength tests. The voids in the surface of the G12-M-HP sample appear to be slightly smaller than the other two which may explain why this material has retained a slightly higher strength. However, for the G17-M-HP and G27-M-HP materials, the surfaces

appear similar making it difficult to explain the difference in strength between the two samples. An explanation similar to that accounting for the residual strengths of Hertzian indented samples in section 2.1.1.4 can be applied to understand the larger drop in strength of the finer grained G12-M-HP material. If the strength is originally controlled by the size of the grains (as they act as the critical flaws), the finer grained material will have a higher starting strength and a greater relative increase in flaw size if the new flaws introduced are independent of the original grain size. In larger grained materials, the difference between the size of the original grains and the new flaws introduced will be smaller and therefore represent a proportionally smaller reduction in strength.

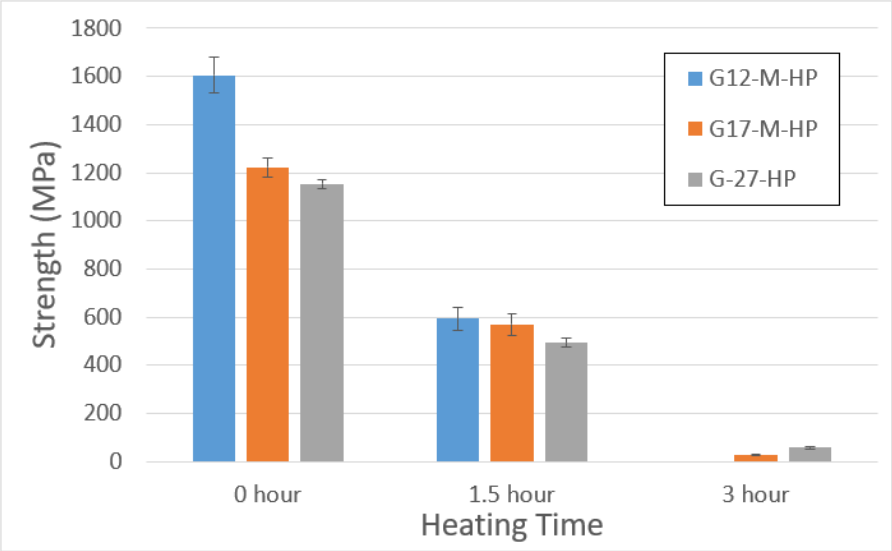

Figure 5.69: Graph showing the strengths of samples of G12-M-HP (blue, fine grained), G17-M-HP (orange, medium grained) and G27-M-HP (grey, coarse grained) samples after 0, 1.5 and 3 h of heating at 800 °C. The strengths are reduced by an approximate factor of 2-3 after 1.5 h of heating and to essentially zero after 3 h.

Figure 5.71 shows a comparison of the microstructures of unheated, 1.5 h heated and 3 h heated samples made from G27-M-HP material. The samples heated for 3 h show numerous, large graphite particles within the binder pools (panel 'a)'), graphite that has begun to form from the diamond grains (the boundary between the graphite and diamond is highlighted with red arrows in panel 'b)') and cracks with very large openings (cyan arrows, panel 'b)'). These cracks are numerous and connect most graphitised binder pools together like those seen in previous sections

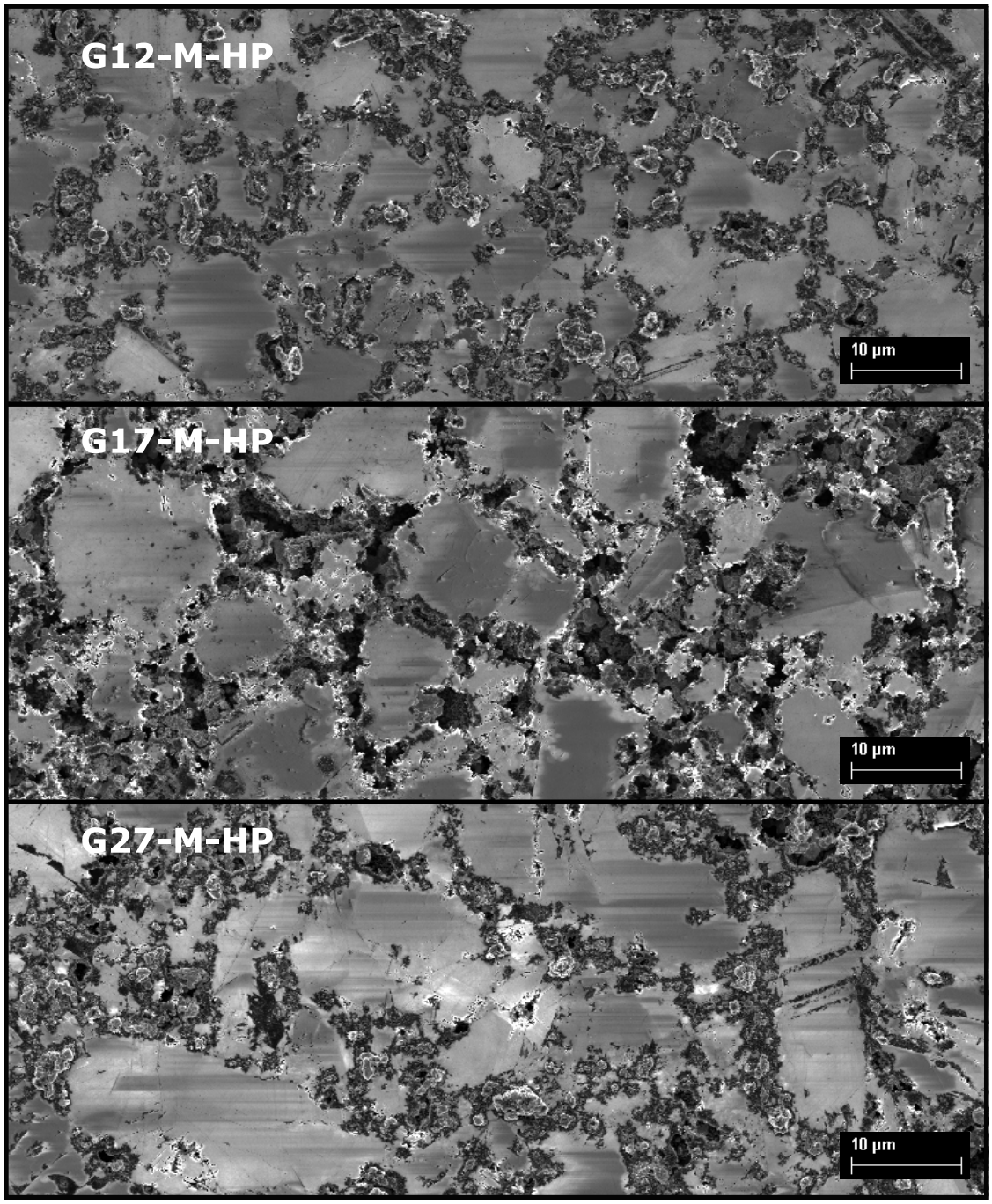

Figure 5.70: Secondary electron image of the tensile surfaces of G12-M-HP (top), G17-M-HP (middle) and G27-M-HP (bottom) materials that have been heated for 1.5 h showing that a significant amount of binder has been removed during heating which will have caused the flaw size to increase quite significantly, potentially explaining the drop in strength observed in figure 5.69. The electron micrographs in this figure were obtained by Jesse Singh, (DPhil candidate, Department of Materials, University of Oxford).

and explain the drastic drop in strength as the material has essentially turned into a loosely held-together powder. In panel 'a)' of the 1.5 h heated sample, small graphite

particles similar to the nucleus graphite seen in figure 5.40 can be seen within the binder pools (green arrows). The surprising result here is that cracks with small openings can also be seen emanating from binder pools with graphite particles in them in this sample (orange arrows, panel 'b)') but catastrophic graphitisation has not occurred. These microcracks were only seen in one binder pool in the whole FIB cross-section but this only represents a very small volume out of the entire sample so it is difficult to know how wide-spread these are. The graphite particles present do appear larger than those in figure 5.40 (from the synchrotron sample that was heated but not allowed to graphitise) and this would put a larger stress on the surrounding diamond explaining why it has cracked. These results show that there may also be a time dependence and/or temperature dependence on catastrophic graphitisation occurring after the growth of the nucleus graphite has caused the surrounding diamond to fracture. As all samples experienced 2–3 fold drops in strength after being heated for 1.5 h it seems likely that these microfractures are present in all of the samples and are the main cause of the drop in strength observed.

5.5 Conclusions

Neutron diffraction experiments showed that there is an incubation period before large-scale graphitisation of the PCD occurs whose length decreases as the temperature the PCD is heated to increases. Laboratory X-ray diffraction experiments showed that this incubation period is also sensitive to the binder chemistry and that there is a group VII transition metal element that can be added to the binder to increase the thermal stability of PCD. SEM analysis of these samples showed that graphite nuclei were forming during this incubation period at a level below the detection limit of the diffraction techniques. Although the literature on the transformation of diamond to graphite catalysed by cobalt is very sparse, two mechanisms of graphite formation involving cobalt (albeit from non-diamond sources of carbon) were identified. Dissolution-reprecipitation involves carbon dissolving in cobalt and reprecipitating out as graphite and the direct transformation mechanism is less well understood. In pure diamond, graphite has been shown to form from

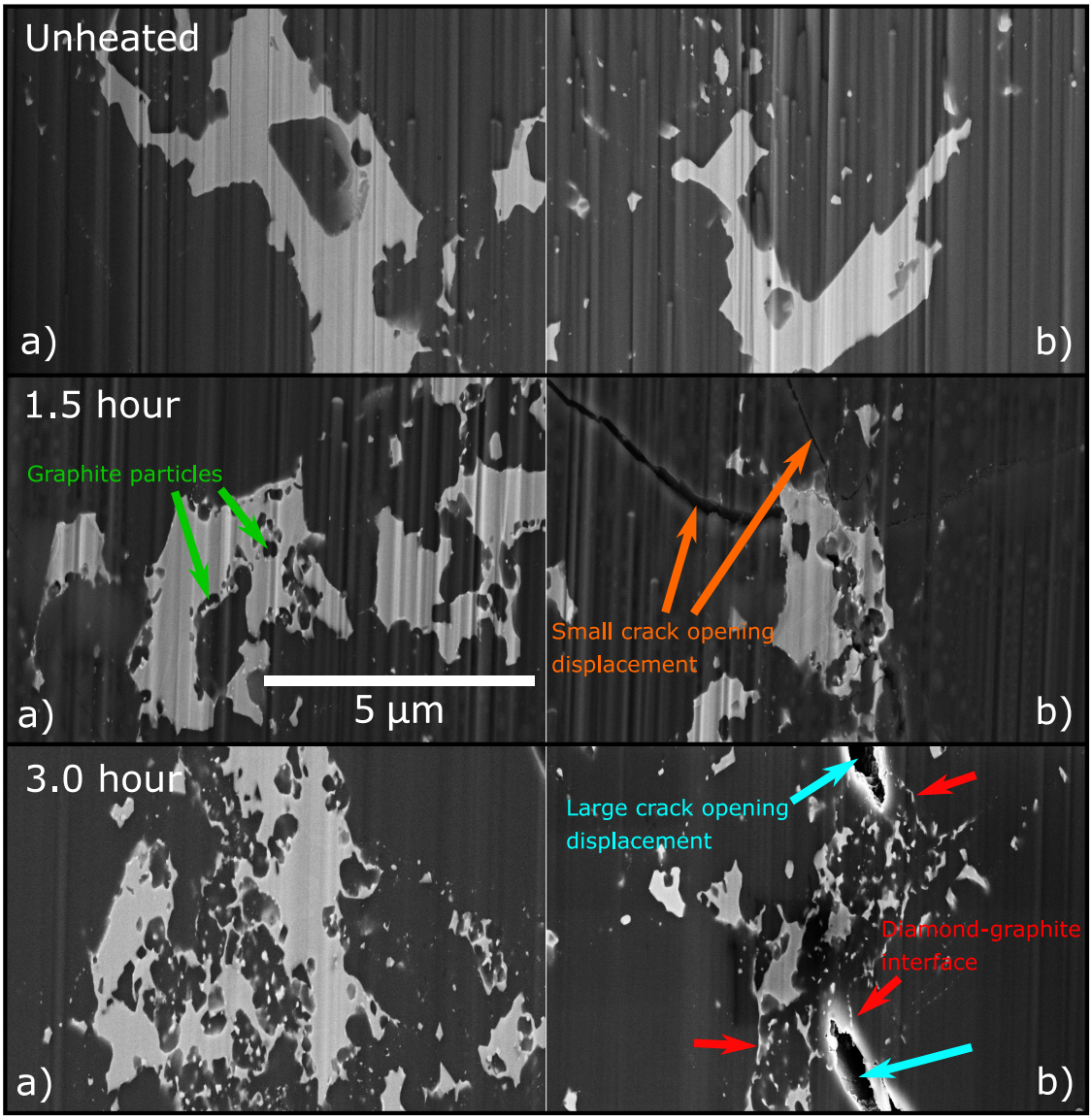

Figure 5.71: FIB cross-sections comparing the microstructures of samples of G27-M-HP after 0 (top), 1.5 (middle) and 3 h of heating at 800 °C. Small graphite particles within the binder pools (green arrows) and cracks with small opening displacements (orange arrows) can be seen emanating from them after 1.5 h of heating. After 3 h of heating, a significant amount of graphitisation has occurred and cracks with large opening displacements (cyan arrows) can be seen connecting graphitised binder pool regions.

graphite nucleus nests that propagate graphite growth into the bulk of the diamond along ⟨112⟩ directions. This form of graphite growth is associated with a large transformation strain and is retarded by high pressures. In-situ TEM experiments showed graphite nucleating from η-carbide particles and growing by a mechanism that appears to be similar to the ⟨112⟩-direction mechanism and it is suggested that

these are the graphite nuclei that were observed growing during the incubation period. Synchrotron X-ray diffraction experiments showed large fluctuations in the cobalt and diamond lattice parameters before large-scale graphitisation occurred and it was suggested that this was due to the stress caused by expansion of growing graphite nuclei within the cobalt binder pools. An elastic model was suggested that accounted for the direction and magnitude of the lattice parameter fluctuations observed. A modification of this model to account for plastic deformation in the cobalt surrounding the growing graphite particle predicted an incubation period before stress would be transferred to the diamond, causing fracture and allowing large-scale graphitisation that was sensitive to the yield stress of the binder (predicting the dependences on temperature and binder chemistry observed). At much higher temperatures, after large-scale graphitisation has already taken place, a mechanism of graphite growth that appears to be dissolution-reprecipitation was seen operating in an in-situ heating TEM experiment. Although the graphite nucleus growth appears to be by the $\langle 112 \rangle$, direct transformation mechanism, the evidence for this is less than clear and so further research is suggested. Finally, nucleus graphite growth is suggested to have a highly detrimental effect on the mechanical properties of PCD even before diffraction-detectable "catastrophic" graphitisation has occurred.

5.6 Further Work

So far, only a small number of tests have been carried out showing the dependence of the incubation period on temperature (and binder chemistry) and the inability of the furnace to heat to an accurate temperature in the synchrotron diffraction experiments prevented quantitative analysis. It is recommended for a large sample set to be heated to and held at a variety of temperatures in the range 750 to 850 with multiple data points per temperature to account for sample-to-sample variability. From this, a temperature-time diagram for the incubation period could be derived to better understand its cause. Also, samples with variable degrees of leaching should be heated in a similar manner to better understand why the residual cobalt appears to have a greater resistance to graphitisation than the cobalt in the unleached material.

To better understand the mechanism behind graphite nucleation, another in-situ heating TEM experiment should be performed but with the sample being quenched right after graphite is seen to nucleate. Performing electron diffraction on the graphite nucleus and surrounding diamond could validate or refute the suggestion that graphite is growing by the {112} plane mechanism during this stage. As it seems there are many newly discovered phenomena occurring all at once in the in-situ TEM experiment, it is suggested that a model microstructure be made by creating a layer of cobalt trapped between two pristine chemical vapour deposition-grown diamonds (similarly to the work of Ramirez *et al.* in figure 2.26) to try to simplify the system as much as possible. This sample would then be made into a TEM lamella and heated in-situ in the TEM to observe the graphitisation process. Another point of interest would be to create PCD microstructures completely devoid of η-carbide particles to see if these are necessary for graphite nucleation.

The model presented in this thesis is of a very simplified representation of the microstructure of PCD. Finite element modelling of more representative microstructures (including isolated and interconnected binder pools) should be used to create more complex stress models. The biggest deviation from reality of the model used here is that the graphite has to grow at the centre of the particle. Investigating how this changes the stress distribution may help understand why the isolated pools are more resistant to fracture and catastrophic graphitisation.

By creating larger mechanical test specimens, heating for the required time and temperature and then polishing away the surface layer of material, the effect of binder removal from this surface layer and its impact on the strength can be avoided. It is suggested to repeat the mechanical tests described in this section using such a sample preparation technique to eliminate this undesirable effect from the results. Furthermore, a larger range of heating times (less than the time required to cause catastrophic graphitisation) should be used to see if the degradation in mechanical properties is sudden or gradual.

Appendices

A

Simultaneous Equations for Residual Stress

The following appendix gives the full treatment of the simultaneous equations that are generated with equation 4.17 that are omitted from the main body of the text (section 4.5.3) for ease of readability.

The mean, hydrostatic, elastic strain in the matrix (diamond) is written as:

$$\epsilon_m = P_i f_i \int_T^{T_0} \alpha_d - \alpha_{Co}\, dT \tag{A.1}$$

where a_i is the lattice parameter of the leached or unleached material, a_0 is the stress-free reference lattice parameter, f_i is the volume fraction of diamond for the leached or unleached material, α_d and α_{Co} are the thermal expansion coefficients for the diamond and cobalt and P_i is the prefactor given by the expression:

$$P_i = \frac{E_{Co}(1-2\nu_{Co})}{(1-f)E_d(1-3\nu_{Co}) + E_{Co}[f(1-2\nu_d) + \frac{1}{2}(1+\nu_d)]} \tag{A.2}$$

where E_d, ν_d and E_{Co}, ν_{Co} are the Young's moduli and Poisson's ratios of the diamond and cobalt respectively.

At this point, the adjustment is made to convert the strain in the matrix into the strain in the diamond as the leached "'matrix" contains both voids and diamond as per equation 4.14.

$$\epsilon_m = P_i f_i N_i \int_T^{T_0} \alpha_d - \alpha_{Co}\, dT \tag{A.3}$$

For the leached material:

$$N_l = \frac{1-2\nu_d}{E_d}\frac{E_m}{1-2\nu_m} \tag{A.4}$$

where subscript m refers to the elastic constants of the leached matrix (both diamond and voids) that are modified by equations 4.15 and 4.16 to account for the voids. For the unleached material, $N_u = 1$ as no such modification has to be made.
As the thermal expansion coefficients were found to be represented by linear equations in terms of the temperature, T, they are written as:

$$\begin{aligned} \alpha_d &= A_d T + B_d \\ \alpha_{Co} &= A_{Co} T + B_{Co} \end{aligned} \tag{A.5}$$

The integral in equation A.1 becomes:

$$\begin{aligned} I &= \int_T^{T_0} A_d T + B_d - A_{Co} - B_{Co}\, dT \\ &= \left(\frac{A_d - A_{Co}}{2}\right) T_0^2 + (B_d - B_{Co})\, T_0 + \left(\frac{A_{Co} - A_d}{2}\right) T^2 + (B_{Co} - B_d)\, T \end{aligned} \tag{A.6}$$

where T_0 is the stress-free temperature and T is the measurement temperature.
The strain in the diamond can also be written by comparing the lattice parameter of the leached and unleached materials to the imaginary stress-free reference sample:

$$\epsilon_u = \frac{a_u - a_0}{a_0} \text{ and } \epsilon_l = \frac{a_l - a_0}{a_0} \tag{A.7}$$

These two expressions are rearranged for a_0 and equated to each other giving:

$$a_u\,(\epsilon_l + 1) - a_l\,(\epsilon_u + 1) = 0 \tag{A.8}$$

substituting in the previous expressions for the strain and rearranging gives:

$$I\,(a_u N_l P_l f_l - a_l P_u f_u) = 0 \tag{A.9}$$

Finally, substituting the expanded expression for I back into this equation gives a quadratic in terms of the stress-free temperature:

$$\left(\frac{A_d - A_{Co}}{2}\right) T_0^2 + (B_d - B_{Co})\, T_0 + \left(\frac{A_{Co} - A_d}{2}\right) T^2 + (B_{Co} - B_d)\, T + \frac{a_u - a_l}{a_u N_l P_l f_l - a_l P_u f_u} = 0 \tag{A.10}$$

which can be solved to give a value for the stress-free temperature, T_0.

B

Extrapolation of Elastic Constants to High Temperature

The calculations in chapter 4 required values of elastic constants for diamond and cobalt up to 1480 °C. The present appendix illustrates how these values were obtained.

B.1 Young's Modulus and Poisson's Ratio

Bulk (K) and shear (G) moduli were calculated from the elastic stiffness constants for both Voigt[164] and Reuss[165] bounds and an average of the two was taken to obtain the correct values for a polycrystalline material from the single crystal values as per the work of Hill[166].

Voigt bound:

$$K_V = \frac{c_{11} + 2c_{12}}{3}$$

$$G_V = \frac{c_{11} - c_{12} + 3c_{44}}{5}$$

Reuss bound:

$$K_R = \frac{1}{3s_{11} + 6s_{12}}$$

$$G_R = \frac{15}{12s_{11} - 12s_{12} + 9s_{44}}$$

where s_{ij} are the elastic compliance constants which are calculated from the elastic stiffness constants as follows:

$$s_{11} = \frac{c_{11} + c_{12}}{(c_{11} - c_{12})(c_{11} + 2c_{12})}$$

$$s_{12} = \frac{-c_{12}}{(c_{11} - c_{12})(c_{11} + 2c_{12})}$$

$$s_{44} = \frac{1}{c_{44}}$$

Voigt-Reuss-Hill average:

$$K_H = \frac{K_V + K_R}{2}$$

$$G_H = \frac{G_V + G_R}{2}$$

Poisson's ratio and Young's Modulus are then calculated from the Voigt-Reuss-Hill elastic moduli as follows:

$$\nu = \frac{3K_H - 2G_H}{G_H + 6K_H}$$

$$E = 3K_H(1 - 2\nu)$$

B.2 Diamond

Zouboulis and Grimsditch measured the three independent elastic stiffness constants (c_{11}, c_{12} and c_{44}) of diamond using a Brillouin scattering technique in the temperature range 300–1600 K (27–1327 °C)[167]. They found that each of the constants obeyed the following relation in this temperature regime:

$$c_{ij} = C_0 + C_2\left(T^2 - 300^2\right) \tag{B.1}$$

where the values of C_0 and C_2 are given in table B.1. The values of C_0 were taken from ref [168] and the values of C_2 were measured in the work of Zouboulis and Grimsditch.

The values obtained from the literature covered the required temperature range for the stress-free temperature calculations (up to 900 °C) but an extrapolation had

	C_0 GPa	C_2 10^{-6} GPa K^{-2}
c_{11}	1080.4	-29 ± 8
c_{12}	127.0	-3 ± 18
c_{44}	576.6	-22 ± 7

Table B.1: Values for the coefficients used to calculate the three independent elastic stiffness constants for diamond using equation B.1 from Zouboulis and Grimsditch[167].

to be performed to obtain values of the elastic constants at 1480 °C for the calculation involving the sintering temperature in section 4.5.5. The values of Young's modulus and Poisson's ratio as a function of temperature are given in table B.2.

Temperature (°C)	Young's Modulus (GPa)	Poisson's Ratio
27	1116	0.0827
200	1115	0.0828
400	1110	0.0832
600	1103	0.0837
700	1098	0.0840
800	1093	0.0844
900	1087	0.0849
1480	1037	0.0889

Table B.2: Young's modulus and Poisson's ratio for diamond as a function of temperature calculated with equation B.1 with the coefficients in table B.1.

B.3 Cobalt

For the elastic properties of cobalt, the values for the specific cobalt-tungsten-carbon allow found in PCD were not available. The data therefore had to be taken from a combination of pure cobalt and cobalt-iron alloys. Figure B.1 shows data from Nadal *et al.*[169] (orange points, pure cobalt) who calculated the shear modulus of cobalt between 250 and 700 °C and from Wazzan *et al.*[170] (blue points, cobalt-6 at% iron) who calculated the three independent elastic stiffness constants (c_{11}, c_{12} and c_{44}) in the range 0–315 °C. Good agreement can be seen between the two data sets with a slight deviation around 400 °C due to the hysteresis caused by the hcp-fcc phase transition that occurs here. Wazzan *et al.* also measured the first independent elastic stiffness constant (c_{11}) of Co-6at%Fe up to 1150 °C which is

shown in figure B.2. As it appears to be linear up to this temperature and due to the good agreement between data sets seen in figure B.1, all three elastic stiffness constants were extrapolated linearly over the entire temperature range of interest.

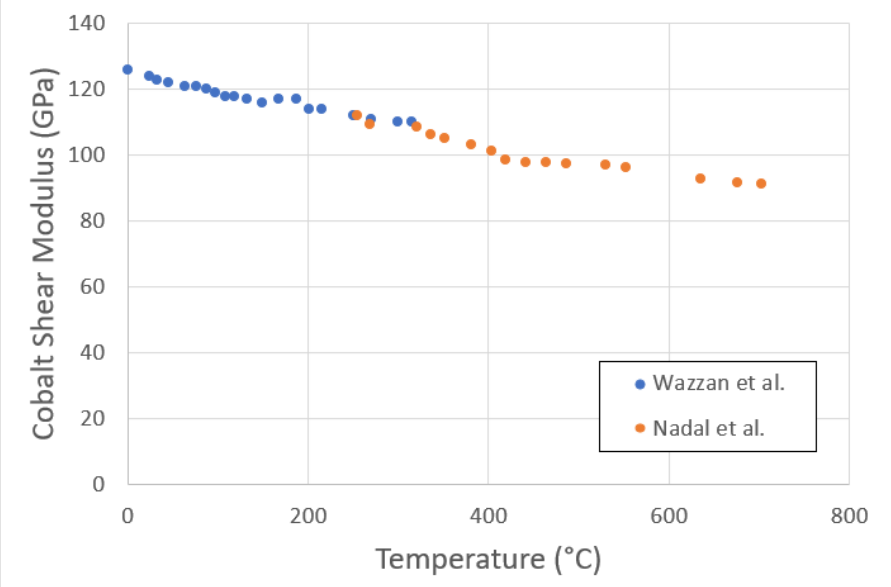

Figure B.1: Literature values for the shear modulus of pure cobalt (orange points, Nadal *et al.*[169]) and Co-6at%Fe (blue points, Wazzan *et al.*[170]. Good agreement is seen between the data where it crosses over and the shear modulus appears to decrease linearly with temperature.

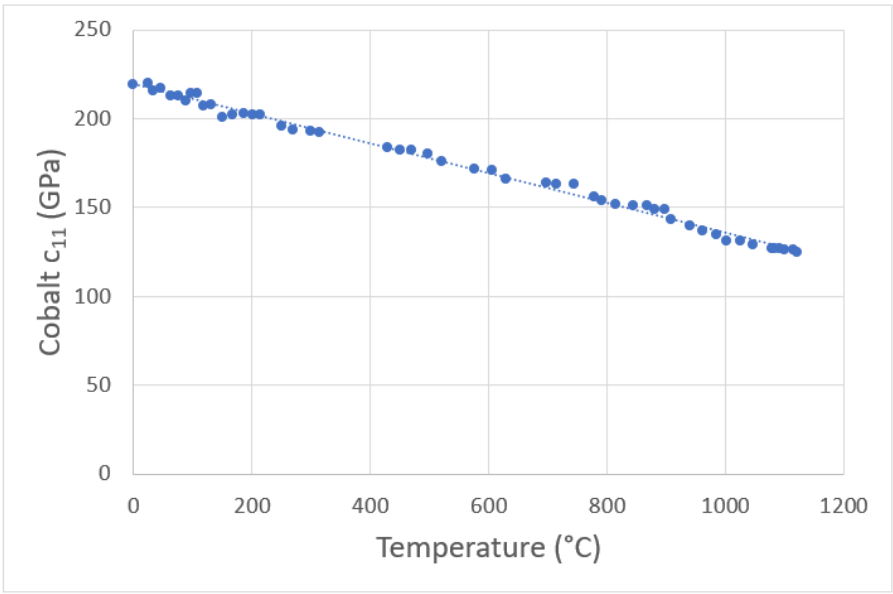

Figure B.2: First independent elastic stiffness constant (c_{11}) for Co-6at%Fe as a function of temperature measured by Wazzan *et al.*[170]. It appears to continue to decrease linearly past the values measured in figure B.1 up to 1150 °C.

The Young's modulus and Poisson's ratio values as a function of temperature are given in table B.3.

Temperature (°C)	Young's Modulus (GPa)	Poisson's Ratio
27	177	0.325
200	166	0.321
400	153	0.316
600	140	0.310
700	134	0.306
800	128	0.302
900	121	0.297
1480	83	0.241

Table B.3: Young's modulus and Poisson's ratio for cobalt as a function of temperature calculated by linearly extrapolating the data in figure B.1

B.3.1 Liquid Cobalt

The bulk modulus of liquid cobalt near the melting point is given by three authors. These values vary quite considerable and are all above that predicted for cobalt from the extrapolation of solid values up to the melting point. These values are for pure cobalt rather than the alloy composition used in the present work and there is no evidence to suggest that the bulk modulus should increase on melting and so the extrapolated value has been used in calculations in this work.

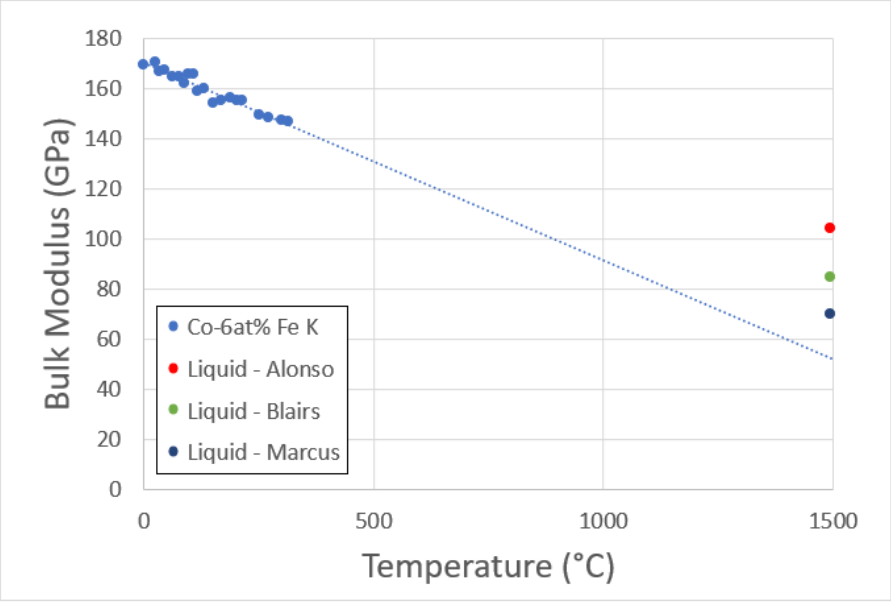

Figure B.3: Values for the bulk modulus of cobalt (6% Fe) extrapolated to the melting point. Also shown are three values of the bulk modulus of liquid pure cobalt at the melting point measured by Alonso and Silbert (red)[171], Blairs (green)[172] and, Marcus (dark blue)[173].

C

Equations Used in the Calculation of Stresses During Graphitisation

The following section shows the equations used to calculate the stresses in the elastic models described in section 5.4.2. All of the equations were derived using the elastic solutions for a system with spherical symmetry based on the boundary conditions of each example. After these simultaneous equations were established, they were solved computationally using the Maxima software package to find the elastic parameters A_i and B_i that can be used to calculate the stresses for each phase using:

Radial displacement as a function of distance from the centre:

$$U_r = Ar + \frac{B}{r^2} \tag{C.1}$$

Radial stress:

$$\sigma_{rr} = A_i\left(2\mu + 3\lambda\right) - \frac{4\mu B_i}{r^3} \tag{C.2}$$

Hoop stresses:

$$\sigma_{\theta\theta} = \sigma_{\phi\phi} = A_i\left(2\mu + 3\lambda\right) + \frac{2\mu B_i}{r^3} \tag{C.3}$$

C.1 Fully Elastic Regime

These equations describe the case of a graphite particle expanding within a cobalt particle within a diamond shell where the cobalt is assumed not to have yielded and all deformation is purely elastic as illustrated in figure 5.54 which is also reproduced here.

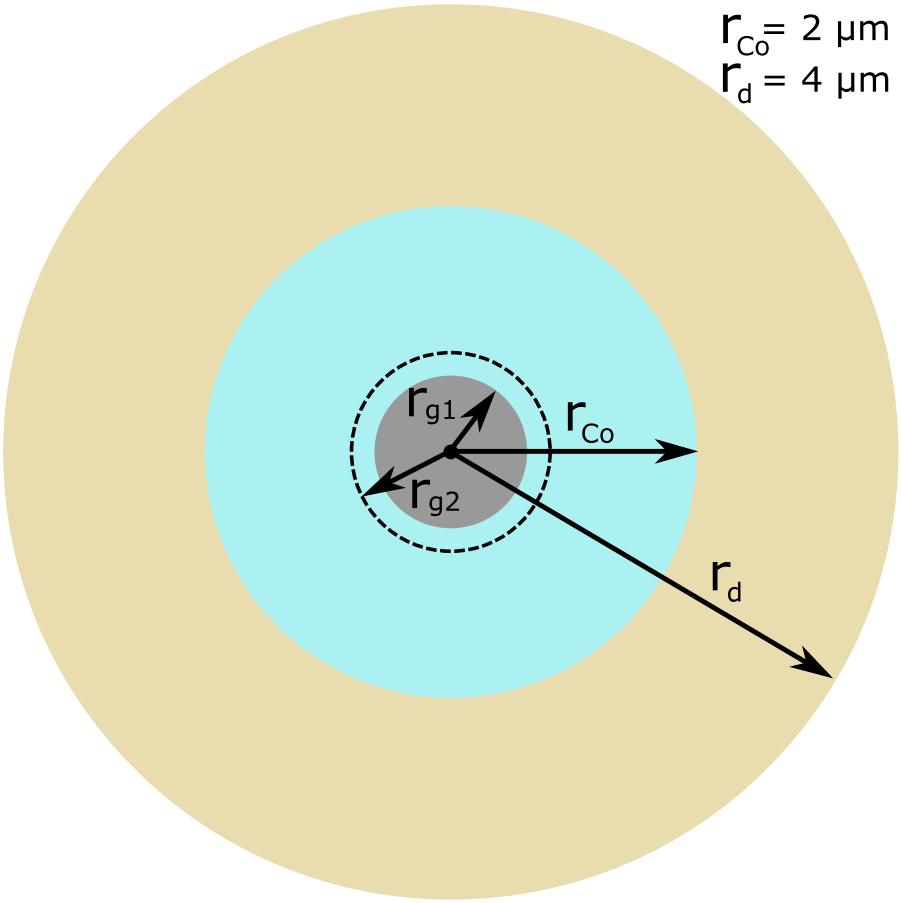

Figure C.1: Schematic representation of the "Fully Elastic Regime" solution. r_d is the outer diamond shell radius and was 4 µm. r_{Co} is the outer cobalt particle radius and was 2 µm. r_{g1} is the initial graphite particle radius which was 5 nm and r_{g2} is the radius of the graphite particle after it has expanded.

$$A_{Co} r_{g1} + \frac{B_{Co}}{r_{g1}^2} = r_{g1}(\alpha - 1) + A_g r_{g1} + \frac{B_g}{r_{g1}^2} \tag{C.4}$$

$$A_{Co}(2\mu_{Co} + 3\lambda_{Co}) - \frac{4\mu_{Co} B_{Co}}{r_{g1}^3} = A_g(2\mu_g + 3\lambda_g) \tag{C.5}$$

$$A_{Co} r_{Co} + \frac{B_{Co}}{r_{Co}^2} = A_d r_{Co} + \frac{B_d}{r_{Co}^2} \tag{C.6}$$

$$A_{Co}(2\mu_{Co} + 3\lambda_{Co}) - \frac{4\mu_{Co} B_{Co}}{r_{Co}^3} = A_d(2\mu_d + 3\lambda_d) - \frac{4\mu_d B_d}{r_{Co}^3} \tag{C.7}$$

$$A_d(2\mu_d + 3\lambda_d) = \frac{4\mu_d B_d}{r_d^3} \tag{C.8}$$

The terms used in the above equations are defined as follows: $\boldsymbol{A_{Co}}$, $\boldsymbol{B_{Co}}$, $\boldsymbol{A_d}$, $\boldsymbol{A_g}$, $\boldsymbol{B_g}$: Constants for cobalt, diamond and graphite phases. $\boldsymbol{\alpha}$: Ratio of expanded graphite size to original graphite size ($\alpha = \frac{r_{g2}}{r_{g1}}$). $\boldsymbol{r_{g1}}$, $\boldsymbol{r_{g2}}$: Original and expanded graphite particle radii. $\boldsymbol{\mu_{Co}}$, $\boldsymbol{\lambda_{Co}}$, $\boldsymbol{\mu_d}$, $\boldsymbol{\lambda_d}$, $\boldsymbol{\mu_g}$, $\boldsymbol{\lambda_g}$: Elastic Lamé constants for cobalt, diamond and graphite. $\boldsymbol{r_{Co}}$: Outer radius of cobalt particle, position of cobalt-diamond interface. $\boldsymbol{r_d}$: Outer radius of diamond shell.

C.2 Fully Plastic Regime

The equations below describe the situation where the cobalt has fully yielded and is transferring stress onto the surrounding diamond shell. Although these equations do not inherently account for plasticity, the assumption that the cobalt is allowed to fully relax stress-free before being reinserted into the misfitting hole in the diamond is meant to approximate yielding. This case is originally described by figure 5.57 and is reproduced below.

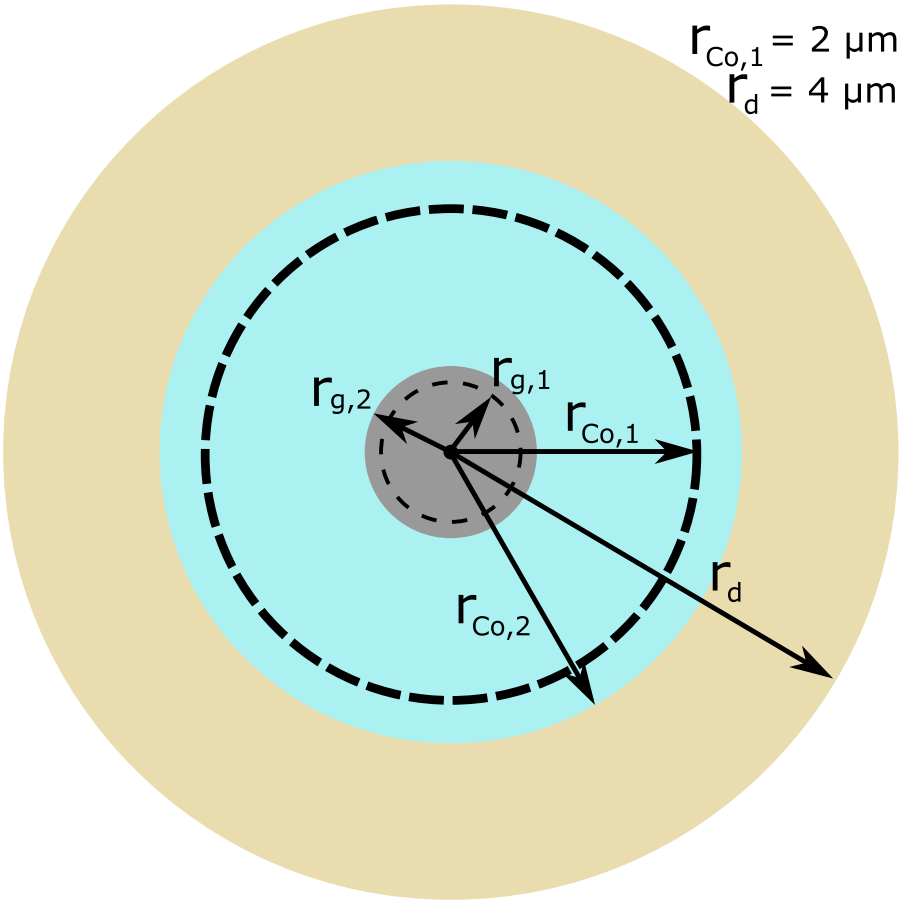

Figure C.2: Schematic representation of the "Fully Plastic Regime" solution. r_d is the outer radius of the diamond shell and is equal to 4 µm as before. $r_{Co,1}$ is the initial radius of the cobalt particle (and the radius of the hole left in the diamond shell) and is equal to 2 µm as before. r_{g1} is the radius of the initial graphite particle (5 nm) and r_{g2} is the expanded graphite radius. $r_{Co,2}$ is the radius of the cobalt-graphite particle after the cobalt has been re-plated onto the expanded graphite particle and will be greater than $r_{Co,1}$.

$$A_d\left(2\mu_d + 3\lambda_d\right) = \frac{4\mu_d B_d}{r_d^3} \tag{C.9}$$

$$A_d r_{Co1} + \frac{B_d}{r_{Co1}^2} = r_{Co2} - r_{Co1} + A_{Co} r_{Co2} + \frac{B_{Co}}{r_{Co2}^2} \tag{C.10}$$

$$A_{Co} r_{g2} + \frac{B_{Co}}{r_{g2}^2} = A_g r_{g2} \tag{C.11}$$

$$A_{Co}\left(2\mu_{Co} + 3\lambda_{Co}\right) - \frac{4\mu_{Co} B_{Co}}{r_{g2}^3} = A_g\left(2\mu_g + 3\lambda_g\right) \tag{C.12}$$

$$A_{Co}\left(2\mu_{Co} + 3\lambda_{Co}\right) - \frac{4\mu_{Co} B_{Co}}{r_{Co2}^3} = A_d\left(2\mu_d + 3\lambda_d\right) - \frac{4\mu_d B_d}{r_{Co1}^3} \tag{C.13}$$

The definition of terms are as in section C.1 with the addition of $\boldsymbol{r_{Co1}}$ being the initial cobalt radius before graphite expansion (and the size of the hole in the diamond shell) and and $\boldsymbol{r_{Co2}}$ being the radius of the graphite-cobalt particle after the cobalt has been re-plated onto the expanded graphite particle, stress-free.

C.3 Plastic Shell

The equations below describe the case of the cobalt yielding between its interface with the graphite and a radius determined by where the Von Mises stress exceeds the yield stress in the cobalt. This causes a shell of plastically deformed material to exist surrounding the graphite particle that exists within an elastically deforming cobalt particle within a diamond shell. Figure 5.60 shows this in section 5.4.4.2 and is reproduced below.

$$r_{Co_P} = \sqrt[3]{r_{Co_E}^3 + r_{g2}^3 - r_{g1}^3} \tag{C.14}$$

$$A_d\left(2\mu_d + 3\lambda_d\right) = \frac{4\mu_d B_d}{r_d^3} \tag{C.15}$$

$$A_{Co_E} r_{Co_E} + \frac{B_{Co_E}}{r_{Co_E}^2} = r_{Co_P} - r_{Co_E} + A_{Co_P} r_{Co_P} + \frac{B_{Co_P}}{r_{Co_P}^2} \tag{C.16}$$

$$A_{Co_P} r_{g2} + \frac{B_{Co_P}}{r_{g2}^2} = A_g r_g \tag{C.17}$$

$$A_{Co_P}\left(2\mu_{Co} + 3\lambda_{Co}\right) - \frac{4\mu_{Co} B_{Co_P}}{r_{g2}^3} = A_g\left(2\mu_g + 3\lambda_g\right) \tag{C.18}$$

$$A_{Co_P}\left(2\mu_{Co} + 3\lambda_{Co}\right) - \frac{4\mu_{Co} B_{Co_P}}{r_{Co_E}^3} = A_{Co_E}\left(2\mu_{Co} + 3\lambda_{Co}\right) - \frac{4\mu_{Co} B_{Co_E}}{r_{Co_E}^3} \tag{C.19}$$

$$A_{Co_E}\left(2\mu_{Co} + 3\lambda_{Co}\right) - \frac{4\mu_{Co} B_{Co_E}}{r_{Co}^3} = A_d\left(2\mu_d + 3\lambda_d\right) - \frac{4\mu_d B_d}{r_{Co}^3} \tag{C.20}$$

$$A_{Co_E} r_{Co} + \frac{B_{Co_E}}{r_{Co}^2} = A_d r_{Co} + \frac{B_d}{r_{Co}^2} \tag{C.21}$$

The definition of terms are as in section C.1 with the following differences. $\boldsymbol{r_{Co_P}}$ is the outer radius of the plastic shell of cobalt after it has been re-plated stress-free onto the expanded graphite particle. $\boldsymbol{r_{Co_E}}$ is where the cobalt transitions from plastic to elastic deformation (before it is allowed to relax) as calculated by equation 5.9. $\boldsymbol{A_{Co_E}}$, $\boldsymbol{B_{Co_E}}$, $\boldsymbol{A_{Co_P}}$ and $\boldsymbol{B_{Co_P}}$ are the elastic parameters for the elastic and

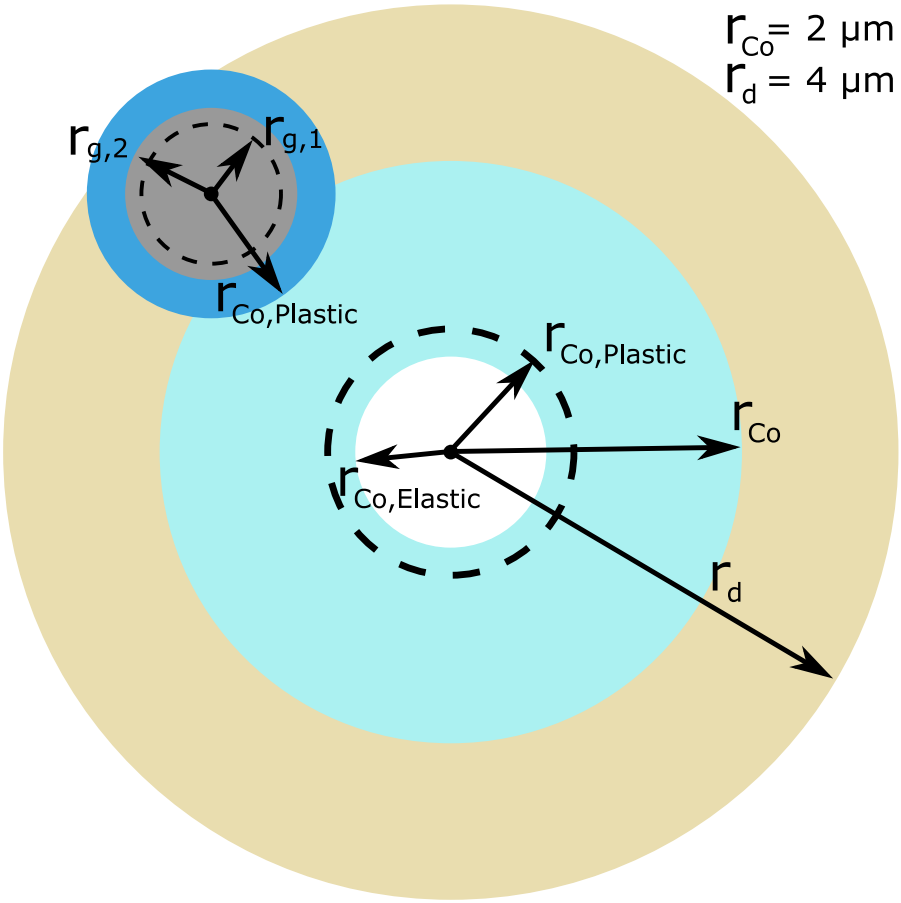

Figure C.3: Schematic representation of the "Plastic Shell Regime" solution. r_d and r_{Co} are the diamond and cobalt outer radii and are equal to 4 µm and 2 µm as before. r_{g1} and r_{g2} are the original (5 nm) and expanded graphite radii as before. $r_{Co,Elastic}$ is the radius at which the Von Mises stress in the cobalt is calculated to exceed the yield stress using the "Fully Elastic Regime" solution. It is also the radius of the hole left in the cobalt shell after this cobalt-graphite particle has been removed from it. $r_{Co,Plastic}$ is the radius of the cobalt-graphite particle after the graphite has expanded and the amount of cobalt determined by $r_{Co,Elastic}$ has been re-plated back onto it.

plastic cobalt regions respectively. $\boldsymbol{r_{Co}}$ is the outer radius of the cobalt particle and the position of the diamond-cobalt interface.

References

[1] Smithson Tennant. “On the Nature of the Diamond.” In: *Philosophical Transactions of the Royal Society of London* 87 (1797), pp. 123–127.

[2] H Moissan. “Nouvelles expériences sur la reproduction du diamant”. In: *Comptes Rendus* 118 (1894), pp. 320–326.

[3] P W Bridgman. “Synthetic Diamonds”. In: *Scientific American* 193.5 (1955), pp. 42–46.

[4] A T Collins. “The Hannay Diamonds”. In: *Industrial Diamond Review* (1975), pp. 434–437.

[5] F P Bundy et al. “Man-Made Diamonds”. In: *Nature* 175.4471 (1955), pp. 642–643.

[6] H P Bovenkirk et al. “Preparation of Diamond”. In: *Nature* 184.4693 (1959), pp. 1094–1098.

[7] A R Badzian and A Klokocki. “On the Catalytic Growth of Synthetic Diamonds”. In: *Journal of Crystal Growth* 52 (1981), pp. 843–847.

[8] H. T. Hall. “Sintered Diamond: A Synthetic Carbonado”. In: *Science* 169.3948 (1970), pp. 868–869.

[9] H. Katzman and W. F. Libby. “Sintered Diamond Compacts with a Cobalt Binder”. In: *Science* 172.3988 (1971), pp. 1132–1134.

[10] R. H. Wentorf Jr. and W. A. Rocco. “Diamond Tools for Machining”. Patent US3745623 A (US). July 1973.

[11] P. Philbin and S. Gordon. “Characterisation of the wear behaviour of polycrystalline diamond (PCD) tools when machining wood-based composites”. In: *Journal of Materials Processing Technology* 162-163 (2005), pp. 665–672.

[12] Y Wang et al. “Study of the wear mechanisms of PCD tools in high-speed milling of Al–Si alloy”. In: *Advanced Materials Research* 381 (2012), pp. 16–19.

[13] D. Kim, A. Beal, and P. Kwon. “Effect of Tool Wear on Hole Quality in Drilling of Carbon Fiber Reinforced Plastic–Titanium Alloy Stacks Using Tungsten Carbide and Polycrystalline Diamond Tools”. In: *Journal of Manufacturing Science and Engineering* 138.3 (2015), pp. 0310061–11.

[14] Federico Bellin et al. “The current state of PDC bit technology: Part 1”. In: *World Oil* 231.09 (2010), pp. 41–46.

[15] Federico Bellin et al. “The current state of PDC bit technology: Part 3”. In: *World Oil* 231.11 (2010), pp. 67–71.

[16] S. Jahanmir, M. Ramulu, and P. Koshy. *Machining of Ceramics and Composites*. Manufacturing Engineering and Materials Processing. Taylor & Francis, 1999, p. 7.

[17] J. A. Arsecularatne, L. C. Zhang, and C. Montross. "Wear and tool life of tungsten carbide, PCBN and PCD cutting tools". In: *International Journal of Machine Tools and Manufacture* 46.5 (2006), pp. 482–491.

[18] D H Wang et al. "Cutting Edge Wear of Tungsten Carbide Tool in Continuous and Interrupted Cutting of a Polymer Composite". In: *Materials and Manufacturing Processes* 10.3 (1995), pp. 493–508.

[19] J. C. Walmsley and A. R. Lang. "Transmission electron microscopic observations of deformation and microtwinning in a synthetic diamond compact". In: *Journal of Materials Science Letters* 2.12 (1983), pp. 785–788.

[20] J. C. Walmsley and A. R. Lang. "Characteristics of diamond regrowth in a synthetic diamond compact". In: *Journal of Materials Science* 23.5 (1988), pp. 1829–1834.

[21] Johan Ewald, Iakovos Sigalas, and Johannes Henoch. "Int . Journal of Refractory Metals and Hard Materials Characterisation of thermally degraded polycrystalline diamond". In: *International Journal of Refractory Metals and Hard Materials* 48 (2015), pp. 286–292.

[22] R. L. Mehan and L. E. Hibbs. "Thermal degradation of sintered diamond compacts". In: *Journal of Materials Science* 24 (1989), pp. 942–950.

[23] H.P. Bovenkerk and P.D. Gigl. "Temperature resistant abrasive compact and method for making same". US Patent 4,224,380. Sept. 1980.

[24] D. McNamara. "The mechanical and fracture properties fo polycrystalline diamond as a function of microstructure". PhD thesis. National University of Ireland, 2015.

[25] Chengliang Liu et al. "Effect of removing internal residual metallic phases on wear resistance of polycrystalline diamond compacts". In: *International Journal of Refractory Metals and Hard Materials* 31 (2012), pp. 187–191.

[26] A. Lammer. "Mechanical properties of polycrystalline diamonds". In: *Materials science and technology* 4.11 (1988), pp. 949–955.

[27] J E Field. "The mechanical and strength properties of diamond." In: *Reports on progress in physics. Physical Society (Great Britain)* 75.12 (2012), p. 126505.

[28] P. D. Gigl. *High-Pressure Science and Technology*. Ed. by K. D. Timmerhaus. Vol. 1. Plenum Press, 1979, pp. 914–922.

[29] D. C. Roberts. "Syndite – its mechanical and physical properties". In: *Industrial Diamond Review* 39 (1979), pp. 237–241.

[30] R. W. Rice. *Fracture mechanics of ceramics*. Ed. by R. C. Bradt. Vol. 1. Plenum Press, 1974, pp. 323–345.

[31] S. Ozbayraktar. "PCD Sintering Model". In: *De Beers Industrial Diamond Technical Note* (1997).

[32] Shane A. Catledge et al. “Micro-raman stress investigations and X-ray diffraction analysis of poly crystalline diamond (PCD) tools”. In: *Diamond and Related Materials* 5.10 (1996), pp. 1159–1165.

[33] F.G. Marro et al. “Damage induced by monotonic and cyclic spherical indentation in polycrystalline diamond (PCD)”. In: *International Journal of Refractory Metals and Hard Materials* 49 (2015), pp. 292–301.

[34] Dan Belnap and Anthony Griffo. “Homogeneous and structured PCD/WC-Co materials for drilling”. In: *Diamond and Related Materials* 13.10 (2004), pp. 1914–1922.

[35] Marin Petrovic, Alojz Ivankovic, and Neal Murphy. “The mechanical properties of polycrystalline diamond as a function of strain rate and temperature”. In: *Journal of the European Ceramic Society* 32.12 (2012), pp. 3021–3027.

[36] R. Morrell et al. “Meso-scale mechanical testing methods for diamond composite materials”. In: *International Journal of Refractory Metals and Hard Materials* 28.4 (2010), pp. 508–515.

[37] D. McNamara et al. “The influence of microstructure on the fracture statistics of polycrystalline diamond and polycrystalline cubic boron nitride”. In: *Ceramics International* 40.8 PART A (2014), pp. 11543–11549.

[38] F. García-Marro et al. “Contact damage and residual strength in polycrystalline diamond (PCD)”. In: *Diamond and Related Materials* 65 (2016), pp. 131–136.

[39] D. Miess and G. Rai. “Fracture toughness and thermal resistance of polycrystalline diamond compacts”. In: *Materials Science and Engineering: A* 209.1-2 (1996), pp. 270–276.

[40] Tze Pin Lin, George A. Cooper, and Michael Hood. “Measurement of the fracture toughness of polycrystalline diamond using the double- torsion test”. In: *Journal of Materials Science* 29 (1994), pp. 4750–4756.

[41] A. Shyam and E. Lara-Curzio. “The double-torsion testing technique for determination of fracture toughness and slow crack growth behavior of materials: A review”. In: *Journal of Materials Science* 41.13 (2006), pp. 4093–4104.

[42] R. B. Tait, P. R. Fry, and G. G. Garrett. “Review and evaluation of the double-torsion technique for fracture toughness and fatigue testing of brittle materials”. In: *Experimental Mechanics* 27.14 (1987).

[43] M. Petrovic et al. “Role of rate and temperature on fracture and mechanical properties of PCD”. In: *Key Engineering Materials* 452 (2011), pp. 153–156.

[44] D. McNamara et al. “Fracture toughness evaluation of polycrystalline diamond as a function of microstructure”. In: *Engineering Fracture Mechanics* 143 (2015), pp. 1–16.

[45] D Taylor. “Crack modelling: A technique for the fatigue design of components”. In: *Engineering Failure Analysis* 3.2 (1996), pp. 129–136.

[46] R. Damani, R. Gstrein, and R. Danzer. “Critical Notch-Root Radius Effect in SENB-S Fracture Toughness Testing”. In: *Journal of the European Ceramic Society* 16.7 (1996), pp. 695–702.

[47] P.D. Warren. “Determining the fracture toughness of brittle materials by Hertzian indentation”. In: *Journal of the European Ceramic Society* 15.3 (1995), pp. 201–207.

[48] V. R. Howes and S. Tolansky. “Pressure crack-figures on diamond faces I. The octahedral face”. In: *Proceedings of the Royal Society A* 230.1182 (1955), pp. 287–293.

[49] S. Tolansky and A. Halperin. “Oriented Ring Cracks on Diamond”. In: *Proceedings of the Physical Society B* 67.6 (1954), pp. 473–476.

[50] B R Lawn and H Komatsu. “The nature of deformation around pressure cracks on diamond”. In: *Philos. Mag.* 14.February (1966), pp. 689–699.

[51] J. E. Field and C. J. Freeman. “Strength and fracture properties of diamond”. In: *Philosophical Magazine A* 43.3 (1981), pp. 595–618.

[52] F. C. Roesler. “Brittle Fractures near Equilibrium”. In: *Proceedings of the Physical Society B* 69.10 (1956), pp. 981–992.

[53] L. E. Hibbs and M. Lee. “Some aspects of the wear of polycrystalline diamond tools in rock removal processes”. In: *Wear* 46.1 (1978), pp. 141–147.

[54] Tze Pin Lin et al. “Wear and failure mechanisms compact bits of polycrystalline diamond”. In: *Wear* 156 (1992), pp. 133–150.

[55] D. Miller and A. Ball. “Rock drilling with impregnated diamond microbits - an experimental study”. In: *International Journal of Rock Mechanics and Mining Sciences* 27.5 (1990), pp. 363–371.

[56] D. Miller and A. Ball. “The wear of diamonds in impregnated diamond bit drilling”. In: *Wear* 141 (1991), pp. 311–320.

[57] R. H. Wentorf, R. C. DeVries, and F. P. Bundy. “Sintered superhard materials”. In: *Science* 208 (1980), pp. 873–880.

[58] H. J. Osburn. “Wear of rock cutting tools”. In: *Powder Metallurgy* 12.24 (1969), pp. 471–502.

[59] K. J. Dunn and M. Lee. “The fracture and fatigue of sintered diamond compact”. In: *Journal of Materials Science* 14 (1979), pp. 882–890.

[60] F. J. Brett, T. M. Warren, and S. M. Behr. “Bit whirl - a new theory of PDC bit failure”. In: *Society of Petroleum Engineers* 5.4 (1990), pp. 275–281.

[61] “Quality and wear behavior of graded polycrystalline diamond compact cutters”. In: *International Journal of Refractory Metals and Hard Materials* 56 (2016), pp. 87–95.

[62] Johan Ewald Westraadt, Iakovos Sigalas, and Johannes Henoch Neethling. “Characterisation of thermally degraded polycrystalline diamond”. In: *International Journal of Refractory Metals and Hard Materials* 48 (2015), pp. 286–292.

[63] Cornelius J. Pretorius et al. “Tool wear behaviour and workpiece surface integrity when turning Ti-6Al-2Sn-4Zr-6Mo with polycrystalline diamond tooling”. In: *CIRP Annals - Manufacturing Technology* 64.1 (2015), pp. 109–112.

[64] David J. Schrock et al. “Phase Dependent Tool Wear in Turning Ti-6Al-4V Using Polycrystalline Diamond and Carbide Inserts”. In: *Journal of Manufacturing Science and Engineering* 136.4 (2014), p. 041018.

[65] Q. S. Bai et al. “Study on wear mechanisms and grain effects of PCD tool in machining laminated flooring”. In: *International Journal of Refractory Metals and Hard Materials* 22.2-3 (2004), pp. 111–115.

[66] Y. Li, X. L. Han, and X. Q. Wang. “Research on mechanical properties and test methods of polycrystalline diamond”. In: *Diamond and Abrasives Engineering* 5 (2001), pp. 27–30.

[67] Tze-Pin; Lin, Michael; Hood, and George A. Cooper. “Residual stresses in polycrystalline diamond compacts”. In: *Journal of the American Ceramic Society* 77.6 (1994), pp. 1562–68.

[68] A. D. Krawitz et al. “Residual stresses in polycrystalline diamond compacts”. In: *International Journal of Refractory Metals and Hard Materials* 17.1 (1999), pp. 117–122.

[69] “High-pressure, high-temperature plastic deformation of sintered diamonds”. In: *Diamond and Related Materials* 59 (2015), pp. 95–103.

[70] HongSheng Jia et al. “Effects of initial crystal size of diamond powder on surface residual stress and morphology in polycrystalline diamond (PCD) layer”. In: *Science China Physics, Mechanics and Astronomy* 54.1 (2011), pp. 98–101.

[71] Feng CHEN et al. “Thermal residual stress of polycrystalline diamond compacts”. In: *Transactions of Nonferrous Metals Society of China (English Edition)* 20.2 (2010), pp. 227–232.

[72] “A study on PDC drill bits quality”. In: *Wear* 298-299.1 (2013), pp. 32–41.

[73] R. M. Erasmus et al. “Application of Raman spectroscopy to determine stress in polycrystalline diamond tools as a function of tool geometry and temperature”. In: *Diamond and Related Materials* 20.7 (2011), pp. 907–911.

[74] Hongsheng Jia et al. “HPHT preparation and Micro-Raman characterization of polycrystalline diamond compact with low residual stress”. In: *Science China Physics, Mechanics and Astronomy* 53.8 (2010), pp. 1445–1448.

[75] Pin-lu Cao et al. “Optimization design and residual thermal stress analysis of PDC functionally graded materials *”. In: *Journal of Zhejiang University SCIENCE A* 7.8 (2006), pp. 1318–1323.

[76] Ken Bertagnolli and Roger Vale. *Understanding and controlling residual stresses in thick polycrystalline diamond cutters for enhanced durability.* Tech. rep. 2000, pp. 1–9.

[77] Declan McNamara et al. “A Raman spectroscopy investigation into the influence of thermal treatments on the residual stress of polycrystalline diamond”. In: *International Journal of Refractory Metals and Hard Materials* 52 (2015), pp. 114–122.

[78] L. E. Jr. Hibbs. “Unpublished research”. General Electric Corporate Research and Development, Schenectady, New York, Contract No. Sandia 13-9406. Apr. 1981.

[79] Alfonso Ortega and David A Glowka. “Studies of the frictional heating of polycrystalline diamond compact drag tools during rock cutting”. In: *SPE Annual Technical Conference and Exhibition*. New Orleans, Sept. 1982.

[80] M.V. Sneddon and D.R. Hall. “Polycrystalline Diamond: Manufacture, Wear Mechanisms, and Implications for Bit Design”. In: *Journal of Petroleum Technology* 40.12 (1988), pp. 1593–1601.

[81] S. G. Moseley, K. P. Bohn, and M. Goedickemeier. “Core drilling in reinforced concrete using polycrystalline diamond (PCD) cutters: Wear and fracture mechanisms”. In: *International Journal of Refractory Metals and Hard Materials* 27.2 (2009), pp. 394–402.

[82] “Measurement of forces, temperatures and wear of PDC cutters in rock cutting”. In: *Wear* 169.1 (1993), pp. 9–24.

[83] E. A. Burgemeister. “Thermal conductivity of natural diamond between 320 and 450 K”. In: *Physica B+C* 93.2 (1978), pp. 165–179.

[84] O. A. Voronov, E. S. Chebotareva, and E. N. Yabolev. “Unknown”. In: *Soviet Journal of Superhard Materials* 9 (1987), p. 10.

[85] F. S. Phinney. “Graphitization of Diamond”. In: *Science* 120.3114 (1954), pp. 393–394.

[86] T. Evans and D. H. Sauter. “Etching of diamond surfaces with gases”. In: *Philosophical Magazine* 6.63 (1961), pp. 429–440.

[87] V. R. Howes. “The graphitization of diamond”. In: *Proceedings of the Physical Society* 80.3 (1962), pp. 648–662.

[88] T. Evans and P. F. James. “A study of the transformation of diamond to graphite”. In: *Proceedings of the Physical Society B* 277.1961 (1963), pp. 260–269.

[89] G. Davies and T. Evans. “Graphitization of Diamond at Zero Pressure and at a High Pressure”. In: *Proceedings of the Royal Society A* 328 (1972), pp. 413–427.

[90] H. J. Rodewald. “Beiträge zur Polymorphie der im Sinne von W. Hückel artfremde Gitter bildenden Modifikationen V. Zur Graphitisierung des Diamanten”. In: *Helvetica Chimica Acta* 43.6 (1960), pp. 1657–1666.

[91] C. Pantea et al. “High pressure study of graphitization of diamond crystals”. In: *Journal of Applied Physics* 91.4 (2002), pp. 1957–1962.

[92] Roman A. Khmelnitsky and Alexey A. Gippius. “Transformation of diamond to graphite under heat treatment at low pressure”. In: *Phase Transitions* 87.2 (2014), pp. 175–192.

[93] “Oxidation kinetics of type 2A natural diamond [100] and [111] surfaces by TG”. In: *Thermochimica Acta* 192.C (1991), pp. 321–326.

[94] Q. Sun and M. Alam. “Relative Oxidation Behavior of Chemical Vapor Deposited and Type IIa Natural Diamonds”. In: *Journal of The Electrochemical Society* 139.3 (1992), pp. 933–936.

[95] Asao Oya and H. Marsh. “Review Phenomena of catalytic graphitization”. In: *Journal of Materials Science* 17 (1982), pp. 309–322.

[96] Asao Oya and Sugio Otani. “CATALYTIC GRAPHITIZATION OF CARBONS BY VARIOUS METALS”. In: *Carbon* 17 (1979), pp. 131–137.

[97] A. Oya and S. Otani. “Three phase catalytic graphitization of a phenolic resin carbon by use of nickel particles”. In: *Carbon* 16.2 (1978), pp. 153–154.

[98] A. Oberlin and J. P. Rouchy. “Transformation des carbones non graphitables par traitement thermique en presence de fer”. In: *Carbon* 9.1 (1971).

[99] “Graphite formation by the dissolution-precipitation of carbon in cobalt, nickel and iron”. In: *Carbon* 13.2 (1975), pp. 111–113.

[100] T. J. Konno and R. Sinclair. “Crystallization of amorphous carbon in carbon-cobalt layered thin films”. In: *Acta Metallurgica Et Materialia* 43.2 (1995), pp. 471–484.

[101] A. G. Ramírez, T. Itoh, and R. Sinclair. “Crystallization of amorphous carbon thin films in the presence of magnetic media”. In: *Journal of Applied Physics* 85.3 (1999), pp. 1508–1513.

[102] Satoshi Tomita et al. “Formation of Co filled carbon nanocapsules by metal-template graphitization of diamond nanoparticles”. In: *Journal of Applied Physics* 88.9 (2000), pp. 5452–5456.

[103] I. S. Raju and J. C. Newman Jr. *Improved stress-intensity factors for semi-elliptical surface cracks in finite-thickness plates*. Tech. rep. San Francisco, USA, 1977.

[104] Stefan Strobl et al. “Surface crack in tension or in bending - A reassessment of the Newman and Raju formula in respect to fracture toughness measurements in brittle materials”. In: *Journal of the European Ceramic Society* 32.8 (2012), pp. 1491–1501.

[105] Stefan Strobl et al. “Corrigendum to“surface crack in tension or in bending – A reassessment of the Newman and Raju formula in respect to fracture toughness measurements in brittle materials” [J. Eur. Ceram. Soc. 32 (8) (2012) 1491–1501] (S0955221912000258) (10.1016/j.jeurceramsoc.2012.01.011))”. In: *Journal of the European Ceramic Society* 38.1 (2018), pp. 355–358.

[106] Andrew Norton. “Measuring and understanding grain boundary properties of engineering ceramics”. PhD thesis. University of Oxford, 2013.

[107] G. R. Irwin. “Analysis of Stresses and Strains Near the End of a Crack Traversing a Plate”. In: *Journal of Applied Mechanics* 24 (1957), pp. 361–364.

[108] R. Nilen. Private Communication. GIC, Harwell, UK, 2016.

[109] Amanda McKie et al. “Suppression of abnormal grain growth in fine grained polycrystalline diamond materials (PCD)”. In: *International Journal of Refractory Metals and Hard Materials* 41 (2013), pp. 66–72.

[110] Taek Jung Shin et al. “The mechanism of abnormal grain growth in polycrystalline diamond during high pressure-high temperature sintering”. In: *Diamond and Related Materials* 13.3 (2004), pp. 488–494.

[111] L. N. Devin et al. “Resistance to cracking of hard-metal composite materials”. In: *Soviet Powder Metallurgy and Metal Ceramics* 21 (1982), pp. 419–423.

[112] L S Nui et al. “STRESS FIELD NEAR A LARGE BLUNTED TIP V-NOTCH CRITICAL NOTCH STRESS INTENSITY FACTOR”. In: 49.3 (1994), pp. 325–335.

[113] T. Fett and D. Munz. *Stress Intensity Factors and Weight Functions*. Computational Mechanics Publications. Southampton, 1997.

[114] B Y S Ramaseshan. "The Cleavage Properties of Diamond". In: *Proceedings of the Indian Academy of Sciences - Section A* 111 (1946), pp. 114–121.

[115] B. Roebuck, E. A. Almond, and A. M. Cottenden. "The influence of composition, phase transformation and varying the relative F.C.C. and H.C.P. phase contents on the properties of dilute CoWC alloys". In: *Materials Science and Engineering* 66.2 (1984), pp. 179–194.

[116] Jeffrey M Wheeler et al. "The effect of size on the strength of FCC metals at elevated temperatures : annealed copper". In: *Philosophical Magazine* 96.32-34 (2016), pp. 3379–3395.

[117] J. M. Tarragó et al. "Mechanical deformation of WC-Co composite micropillars under uniaxial compression". In: *International Journal of Refractory Metals and Hard Materials* 54 (2016), pp. 70–74.

[118] Varley F. Sears. "Appendix. Neutron Scattering Lengths and Cross Sections". In: *Neutron News* 3.3 (1992), pp. 26–37.

[119] B. D. Cullity. *Elements of X-ray Diffraction*. Ed. by M. Cohen. Second. Addison-Wesley Series in Metallury and Materials. Addison-Wesley, 1959, p. 482.

[120] H. M. Rietveld. "A profile refinement method for nuclear and magnetic structures". In: *Journal of Applied Crystallography* 2.2 (1969), pp. 65–71.

[121] Alan A. Coelho. "TOPAS and TOPAS-Academic: An optimization program integrating computer algebra and crystallographic objects written in C++: An". In: *Journal of Applied Crystallography* 51.1 (2018), pp. 210–218.

[122] R. B. Larson A. C. and. Von Dreele. *General Structure Analysis System (GSAS)*. Tech. rep. Los Alamos National Laboratory, USA, 2000.

[123] P. Zeeman and Harvey B. *Over den invloed eener magnetisatie op den aard van het door een stof uitgezonden licht*. Plotnick Collection of the History of Quantum Mechanics and the Theory of Relativity. Koninklijke Akademie van Wetenschappen te Amsterdam, 1896.

[124] M. W. Dale. "Coulour Centres on Demand in Diamond". PhD thesis. University of Warwick, 2015.

[125] Yiming Zhang, Julian R G Evans, and Shoufeng Yang. "Corrected Values for Boiling Points and Enthalpies of Vaporization of Elements". In: *Journal of Chemical Engineering* 56 (2011), pp. 328–337.

[126] G. W. C. Kaye and T. H Laby. *Tables of physical and chemical constants*. Sixteenth. Addison-Wesley Series in Metallury and Materials. London, UK: Longman, 1995.

[127] G. Bouquet and B. Dubois. "Influence of the f.c.c. phase retained at room temperature on the mechanical properties of cobalt". In: *Scripta Metallurgica* 12 (1978), pp. 1079–1081.

[128] Victor J. Kehrer and Henry Leidheiser. "The phase transformation of cobalt as observed on single crystals". In: *The Journal of Chemical Physics* 21.3 (1953), p. 570.

[129] Nick Wain, Paolo G. Radaelli, and Richard I. Todd. "In situ neutron diffraction study of residual stress development in MgO/SiC ceramic nanocomposites during thermal cycling". In: *Acta Materialia* 55.13 (2007), pp. 4535–4544.

[130] "Neutron diffraction measurements of residual stresses in alumina/SiC nanocomposites". In: *Acta Materialia* 45.4 (1997), pp. 1791–1800.

[131] J. K. Mackenzie. "The elastic constants of a material containing spherical holes". In: *Proceedings of the Physical Society B* 63 (1950), pp. 2–11.

[132] P. J. Wray. "Predicted volume change behavior accompanying the solidification of binary alloys". In: *Metallurgical Transactions B* 7.4 (1976), pp. 639–646.

[133] R Earnshaw. "The casting shrinkage of cobalt-chromium alloys". In: *Australian Dental Journal* 3 (1958), pp. 159–170.

[134] Deng Jianxin et al. "Friction and wear behavior of polycrystalline diamond at temperatures up to 700 °c". In: *International Journal of Refractory Metals and Hard Materials* 29.5 (2011), pp. 631–638.

[135] Jeffery L Tallon and A Wolfenden. "Temperature dependence of the elastic constants of aluminum". In: *J. Phys. Chem. Solids* 40 (1979), pp. 831–837.

[136] D. Mari et al. "Residual stress in WC-Co measured by neutron diffraction". In: *Materials Science and Engineering A* 209.1-2 (1996), pp. 197–205.

[137] C. M. Fernandes and A. M.R. Senos. "Cemented carbide phase diagrams: A review". In: *International Journal of Refractory Metals and Hard Materials* 29.4 (2011), pp. 405–418.

[138] Minoru Taya et al. "Toughening of a Particulate-Reinforced Ceramic-Matrix Composite by Thermal Residual Stress". In: *Journal of the American Ceramic Society* 73.5 (1990), pp. 1382–1391.

[139] R. Nilen. Private Communication. GIC, Harwell, UK, 2016.

[140] A. A. Griffith. "The Phenomena of Rupture and Flow in Solids". In: *Philosophical Transactions of the Royal Society of London A* 221 (1921), pp. 163–198.

[141] A. R. Lang et al. "On the dilatation of synthetic type Ib diamond by substitutional nitrogen impurity". In: *Philosophical Transactions of the Royal Society of London. Series A: Physical and Engineering Sciences* 337 (1991), pp. 497–520.

[142] R. Tait. Private Communication. Cape Town, UK, 2019.

[143] T. H. Becker, T. J. Marrow, and R. B. Tait. "An Evaluation of the Double Torsion Technique". In: *Experimental Mechanics* 51.9 (2011), pp. 1511–1526.

[144] "Transition metal solubilities in WC in cemented carbide materials". In: *Journal of the American Ceramic Society* 94.2 (2011), pp. 605–610.

[145] "Structural, electronic and magnetic properties of η carbides (Fe3W3C, Fe6W6C, Co3W3C and Co6W6C) from first principles calculations". In: *Physica B: Condensed Matter* 404.20 (2009), pp. 3544–3549.

[146] O. J. Kleppa and K. C. Hong. "New applications of high-temperature solution calorimetry 1. Enthalpy of the diamond-to-graphite transformation and enthalpy of formation of Mn5C2 at 1320 K". In: *The Journal of Chemical Thermodynamics* 10.3 (1978), pp. 243–248.

[147] F. P. Bundy. “Direct conversion of graphite to diamond in static pressure apparatus”. In: *The Journal of Chemical Physics* 38.3 (1963), pp. 631–643.

[148] José García et al. “Cemented carbide microstructures: a review”. In: *International Journal of Refractory Metals and Hard Materials* 80.August 2018 (2019), pp. 40–68.

[149] “Nickel in hardmetals”. In: *International Journal of Refractory Metals and Hard Materials* 11.3 (1992), pp. 137–149.

[150] N.S. Wheeler. “Microstructural characterization of cobalt-tungsten coated graphite fibers”. In: *Journal of Research of the National Institute of Standards and Technology* 100.6 (1995), p. 641.

[151] Samuel A. Humphry-Baker and William E. Lee. “Tungsten carbide is more oxidation resistant than tungsten when processed to full density”. In: *Scripta Materialia* 116 (2016), pp. 67–70.

[152] Maxima. *Maxima, a Computer Algebra System. Version 5.34.1.* 2014. URL: `http://maxima.sourceforge.net/`.

[153] Q Jiang, J C Li, and G Wilde. “The size dependence of the diamond-graphite transition”. In: *Journal of Physics: Condensed Matter* 12 (2000), pp. 5623–5627.

[154] L. S. Sigl and H. F. Fischmeister. “On the fracture toughness of cemented carbides”. In: *Acta Metallurgica* 36.4 (1988), pp. 887–897.

[155] A. B. Platov. “Temperature dependence of the hardness of tungsten-cobalt hard alloys”. In: *Poroshkovaya Metallurgiya* 3.9 (1962), pp. 63–68.

[156] I. Konyashin et al. “WC-Co-Re cemented carbides: Structure, properties and potential applications”. In: *International Journal of Refractory Metals and Hard Materials* 78.July 2018 (2019), pp. 247–253.

[157] I. N. Chaporova and Z. N. Sapronova. *Theory and Practice of Cemented Carbide Applications*. Moscow, Russia, 1991, pp. 12–15.

[158] Jian Min Zhang et al. “Anisotropy analysis of the surface energy of diamond cubic crystals”. In: *Surface and Interface Analysis* 35.10 (2003), pp. 805–809.

[159] Andrew C. Victor. “Heat capacity of diamond at high temperatures”. In: *The Journal of Chemical Physics* 36.7 (1962), pp. 1903–1911.

[160] G. I. Taylor and H. Quinney. “The Latent Energy Remaining in a Metal after Cold Working”. In: *Proceedings of the Royal Society A: Mathematical, Physical and Engineering Sciences* 143.849 (1934), pp. 307–326.

[161] V. A. Lubarda. “On thermodynamic potentials in linear thermoelasticity”. In: *International Journal of Solids and Structures* 41.26 (2004), pp. 7377–7398.

[162] K. N. G. Fuller, P. G. Fox, and J. E. Field. “The temperature rise at the tip of fast-moving cracks in glassy polymers”. In: *Proceedings of the Royal Society A* 341 (1975), pp. 537–557.

[163] D. Rittel. “Experimental Investigation of Transient Thermoelastic Effects in Dynamic Fracture”. In: *J. Mech. Phys. Solids* 35.972 (1998), pp. 2959–2973.

[164] Woldemar Voigt. *Lehrbuch der kristallphysik*. Vol. 962. Teubner Leipzig, 1928.

[165] A. Reuss. “Berechnung der Fließgrenze von Mischkristallen auf Grund der Plastizitätsbedingung für Einkristalle .” In: *ZAMM - Journal of Applied Mathematics and Mechanics / Zeitschrift für Angewandte Mathematik und Mechanik* 9.1 (1929), pp. 49–58.

[166] R. Hill. “The elastic behaviour of a crystalline aggregate”. In: *Proceedings of the Physical Society. Section A* 65.5 (1952), pp. 349–354.

[167] “Temperature dependence of the elastic moduli of diamond: A Brillouin-scattering study”. In: *Physical Review B - Condensed Matter and Materials Physics* 57.5 (1998), pp. 2889–2896.

[168] R. Vogelgesang et al. “Brillouin and Raman scattering in natural and isotopically controlled diamond”. In: *Physical Review B - Condensed Matter and Materials Physics* 54.6 (1996), pp. 3989–3999.

[169] M. H. Nadal, C. Hubert, and R. Oltra. “High temperature shear modulus determination using a laser-ultrasonic surface acoustic-wave device”. In: *Journal of Applied Physics* 106.2 (2009).

[170] A. R. Wazzan et al. “Temperature dependence of the single-crystal elastic constants of Co-rich Co – Fe alloys”. In: *Journal of Applied Physics* 44.5 (1973), pp. 2018–2024.

[171] J. A. Alonso and M. Silbert. “Surface Energy of Liquid Transition Metals Related to Bulk Compressibility and Thickness”. In: *Physics and Chemistry of Liquids* 17.3 (1987), pp. 209–214.

[172] S. Blairs. “Review of data for velocity of sound in pure liquid metals and metalloids”. In: *International Materials Reviews* 52.6 (2007), pp. 321–344.

[173] Yizhak Marcus. “On the compressibility of liquid metals”. In: *Journal of Chemical Thermodynamics* 109 (2017), pp. 11–15.